

MARIAN KREYER

STRONGLY INTERACTING FERMI-FERMI MIXTURES OF DY
AND K: MONTE CARLO SIMULATIONS AND TRAPPING
POTENTIAL CONTROL



STRONGLY INTERACTING FERMI-
FERMI MIXTURES OF DY AND K:
MONTE CARLO SIMULATIONS AND
TRAPPING POTENTIAL CONTROL

A PhD THESIS

BY

MARIAN KREYER, MSc

SUBMITTED TO THE FACULTY OF MATHEMATICS, COMPUTER
SCIENCE, AND PHYSICS



IN PARTIAL FULFILLMENT OF THE REQUIREMENTS FOR THE
DEGREE OF

DOCTOR OF PHILOSOPHY (PhD)

CARRIED OUT AT THE INSTITUTE OF EXPERIMENTAL PHYSICS

UNDER THE SUPERVISION OF
UNIV.-PROF. DR. RUDOLF GRIMM

INNSBRUCK, APRIL 2023

Ich musste mich vergleichen einem Bergsteiger, der, ohne den Weg zu kennen, langsam und mühselig hinaufklimmt, oft umkehren muss, weil er nicht weiter kann, der bald durch Überlegung, bald durch Zufall neue Wegspuren entdeckt, die ihn wieder ein Stück vorwärts leiten, und endlich, wenn er sein Ziel erreicht, zu seiner Beschämung einen königlichen Weg findet, auf dem er hätte herauffahren können, wenn er gescheidt genug gewesen wäre, den richtigen Anfang zu finden.

— Hermann von Helmholtz [1]

ABSTRACT


Ultracold gases with strong interactions have been studied to a great extent with the help of Feshbach resonances, and have been used as precisely controllable models for other systems that are not easily accessible experimentally. Fermionic gases are especially interesting, because they can be used to simulate many-body physics present in primordial matter, neutron stars, atomic nuclei or condensed matter systems, particularly superconductors. Since interactions in cold fermions are in general only present if the particles are not identical, most experiments have been working with two spin states of a single atomic species. Changing the number ratio of the two spins can lead to interesting new pairing phenomena, some of which have been studied extensively in recent years. Mass-imbalanced systems have been theoretically predicted to exhibit new exotic interaction regimes and phases that go beyond the physics of spin mixtures.

This thesis reports on the efforts to realize a strongly interacting mass-imbalanced Fermi-Fermi mixture of Dy and K that features collisional stability as well as tunability of interaction strength and trapping geometry. Feshbach resonances have become a ubiquitous tool to control the interaction strength in ultracold gases. With the identification of a broad Feshbach resonance close to 217 G, we were able to realize a resonantly interacting sample of Dy and K. A detailed characterization of the resonance was conducted to extract relevant parameters. In the expanding mixture, the resonant interspecies interaction causes a hydrodynamic behavior which leads to a bimodal density profile. The influence of mass-imbalance and other experimental parameters on the hydrodynamic expansion have been studied with the help of a Monte Carlo simulation, and the results have been found to be in good agreement with the experimental data. The simulation model has been developed and characterized as part of this thesis and can serve as a model to gain understanding of other interesting phenomena that might occur in our mixture, e.g. inversion of the aspect ratio in the hydrodynamic expansion or the influence of the R^* parameter for closed-channel resonances.

In order to control the trapping potential of the constituents of our mixture we developed two methods to accurately measure the Dy polarizability with the help of K as a well-known reference species. The first method is based on measuring the sloshing mode frequency in a standard red-detuned optical dipole trap at the typical wavelength of 1064 nm. The second method employs modulation spectroscopy in optical lattices to be able to measure the polarizability also on the blue-detuned side of optical resonances. This has been used to characterize the Dy polarizability around its 626-nm intercombination line, which will be useful for species-specific

manipulation of atoms in the Dy-K mixture. In order to control the spatial properties of the trapping potential, techniques involving digital micromirror devices have been prepared and tested, resulting in highly uniform flat-top profiles that can be used to study homogeneous systems, as well as profiles featuring linear intensity gradients that would enable optical gravity compensation schemes.

PUBLICATIONS

The following list contains publications that emerged during this thesis in chronological order. The symbol  indicates publications that are part of and directly discussed within the thesis.

-  C. Ravensbergen, V. Corre, E. Soave, M. Kreyer, S. Tzanova, E. Kirilov, and R. Grimm, *Accurate Determination of the Dynamical Polarizability of Dysprosium*. Phys. Rev. Lett. **120**, 223001 (2018)
- Cornelis Ravensbergen, Vincent Corre, Elisa Soave, Marian Kreyer, Emil Kirilov, and Rudolf Grimm, *Production of a Degenerate Fermi-Fermi Mixture of Dysprosium and Potassium Atoms*. Phys. Rev. A **98**, 063624 (2018)
-  C. Ravensbergen, E. Soave, V. Corre, M. Kreyer, B. Huang (黄博), E. Kirilov and R. Grimm, *Resonantly Interacting Fermi-Fermi Mixture of ^{161}Dy and ^{40}K* . Phys. Rev. Lett. **124**, 203402 (2020)
-  Marian Kreyer, Jeong Ho Han, Cornelis Ravensbergen, Vincent Corre, Elisa Soave, Emil Kirilov, and Rudolf Grimm, *Measurement of the Dynamic Polarizability of Dy Atoms near the 626-nm Intercombination Line*. Phys. Rev. A **104**, 033106 (2021)
- E. Soave, V. Corre, C. Ravensbergen, J. H. Han, M. Kreyer, E. Kirilov, R. Grimm, *Low-field Feshbach resonances and three-body losses in a fermionic quantum gas of Dy-161*. Ukr. J. Phys. **67**, 334 (2022)
- Zhu-Xiong Ye, Alberto Canali, Elisa Soave, Marian Kreyer, Yaakov Yudkin, Cornelis Ravensbergen, Emil Kirilov, and Rudolf Grimm, *Observation of low-field Feshbach resonances between ^{161}Dy and ^{40}K* . Phys. Rev. A **106**, 043314 (2022)

CONTENTS

I INTRODUCTION

| | | |
|-----|--|----|
| 1 | OVERVIEW | 3 |
| 1.1 | From "Super"... | 3 |
| 1.2 | ...to "Ultra" | 4 |
| 1.3 | From Balanced to Imbalanced Fermi-Fermi Mixtures | 5 |
| 1.4 | The Dy-K Experiment | 8 |
| 2 | CONTENTS OF THIS THESIS | 11 |

II INTERACTIONS IN THE DY-K MIXTURE

| | | |
|-------|--|----|
| 3 | SCATTERING AND FESHBACH RESONANCES IN QUANTUM GASES | 15 |
| 3.1 | Basic Scattering Theory | 15 |
| 3.2 | Feshbach Resonances | 17 |
| 4 | PUBLICATION: RESONANTLY INTERACTING FERMI-FERMI MIXTURE OF ^{161}DY AND ^{40}K | 19 |
| 4.1 | Introduction | 20 |
| 4.2 | Sample Preparation | 22 |
| 4.3 | Interaction Characterization | 22 |
| 4.4 | Hydrodynamic Expansion | 23 |
| 4.5 | Lifetime | 26 |
| 4.6 | Discussion and Conclusion | 28 |
| 4.7 | Supplemental Material | 29 |
| 4.7.1 | Feshbach Resonance Scenario | 29 |
| 4.7.2 | Decay | 37 |
| 4.7.3 | Interaction-induced Contraction | 40 |
| 5 | MONTE CARLO SIMULATIONS FOR HYDRODYNAMIC MIXTURES | 45 |
| 5.1 | Simulation Model | 45 |
| 5.1.1 | General Method | 46 |
| 5.1.2 | Validation Tests | 52 |
| 5.2 | Hydrodynamic Expansion | 57 |
| 5.2.1 | Comparison with Experimental Data | 57 |
| 5.2.2 | Scaling, Timesteps and Robustness Against Missed Collisions | 61 |
| 5.2.3 | Effects of Experimental and Physical Parameters | 63 |
| 5.2.4 | Aspect Ratio Inversion | 66 |
| 5.3 | The Effect of R^* | 67 |
| 5.3.1 | Shift of the Resonance Center | 67 |
| 5.3.2 | Increased Thermalization Rate | 69 |

| | | |
|--|--|-----|
| 5.4 | Possible Extensions and Limitations of the Model | 72 |
| 5.4.1 | Harmonic Potentials | 72 |
| 5.4.2 | Collision Rate and Species Separation | 73 |
| 5.4.3 | Collective Oscillations | 76 |
| 5.4.4 | The Effect of Quantum Statistics | 81 |
| 5.4.5 | Summary | 81 |
| III FLAT AND ARBITRARY POTENTIALS FOR ATOM MIXTURES | | |
| 6 | MOTIVATION | 85 |
| 6.1 | Trapping Techniques | 85 |
| 6.2 | Atomic Polarizability | 86 |
| 6.3 | Harmonic Potentials and Exotic Phases | 89 |
| 6.4 | Box Traps and Arbitrary Potentials | 91 |
| 6.5 | Contents of Part III | 92 |
| 7 | PUBLICATION: ACCURATE DETERMINATION OF THE DYNAMICAL POLARIZABILITY OF DYSPROSIUM | 93 |
| 7.1 | Introduction | 94 |
| 7.2 | Dynamical Polarizability | 95 |
| 7.3 | Experimental Setup | 97 |
| 7.4 | Systematic Effects | 98 |
| 7.5 | Determination of the Polarizability | 101 |
| 7.6 | Discussion and Conclusion | 102 |
| 7.7 | Supplemental Material | 103 |
| 7.7.1 | Absence of Density Effect on Oscillation Frequency | 103 |
| 7.7.2 | Damping of Oscillations | 104 |
| 7.7.3 | Error Budget of the Frequency Ratio Measurement | 106 |
| 7.7.4 | Measurement of the Tensor Contribution | 106 |
| 8 | PUBLICATION: MEASUREMENT OF THE DYNAMIC POLARIZABILITY OF DY ATOMS NEAR THE 626-NM INTERCOMBINATION LINE | 109 |
| 8.1 | Introduction | 110 |
| 8.2 | Methods | 111 |
| 8.2.1 | Sample Preparation | 112 |
| 8.2.2 | Measuring the Lattice Depth of ^{161}Dy | 114 |
| 8.2.3 | Calibration Measurements with Potassium | 115 |
| 8.3 | Results | 116 |
| 8.3.1 | Anisotropic Polarizability | 116 |
| 8.3.2 | Determination of the Natural Linewidth | 119 |
| 8.4 | Demonstration of Optical Dipole Trapping | 120 |
| 8.5 | Conclusion and Outlook | 122 |
| 8.6 | Appendix A: Lattice Depth Extraction for Potassium | 123 |
| 8.7 | Appendix B: Systematic Uncertainties from Angle Determination | 124 |

| | | |
|--|---|-----|
| 9 | OPTICAL POTENTIAL SHAPING WITH A DMD | 127 |
| 9.1 | Preliminary Considerations | 127 |
| 9.1.1 | Uniformity Requirement | 127 |
| 9.1.2 | Techniques for Shaping the Intensity Distribution | 128 |
| 9.2 | Basic Methods and Technical Details | 130 |
| 9.2.1 | Digital Micromirror Devices | 130 |
| 9.2.2 | Direct Imaging | 131 |
| 9.2.3 | Grayscale Algorithm | 133 |
| 9.2.4 | Input and Transformation | 134 |
| 9.2.5 | Red-Detuned Flat Traps | 135 |
| 9.3 | Noise Treatment | 139 |
| 9.3.1 | Camera Noise | 139 |
| 9.3.2 | Flat-Field Correction | 140 |
| 9.3.3 | Coherent Light and Interference | 143 |
| 9.3.4 | Digital Lowpass Filter | 144 |
| 9.4 | Feedback Algorithm | 144 |
| 9.5 | Best Achieved Flat Profile | 146 |
| 9.6 | Linear Optical Gradients | 149 |
| | | |
| IV A LOOK IN THE MIRROR AND A LOOK AHEAD | | |
| 10 | CONCLUSION | 153 |
| 11 | CURRENT STATE AND WHAT'S NEXT FOR THE DY-K EXPERIMENT | 155 |
| | | |
| | BIBLIOGRAPHY | 157 |
| | ACKNOWLEDGEMENT | 181 |

ABBREVIATIONS AND ACRONYMS

| | |
|------|------------------------------------|
| AOD | acousto-optic deflector |
| AOM | acousto-optic modulator |
| BCS | Bardeen-Cooper-Schrieffer |
| BEC | Bose-Einstein condensate |
| CoM | center-of-mass |
| DFG | degenerate Fermi gas |
| DMD | digital micromirror device |
| DP | dynamical polarizability |
| DSMC | direct simulation Monte Carlo |
| DSNU | dark signal non-uniformity |
| FFLO | Fulde-Ferrell-Larkin-Ovchinnikov |
| FPN | fixed pattern noise |
| LC | liquid crystal |
| LDA | local density approximation |
| mBEC | molecular Bose-Einstein condensate |
| MD | molecular dynamics |
| MOT | magneto-optical trap |
| NA | numerical aperture |
| ODT | optical dipole trap |
| PRNU | photo response non-uniformity |
| PSF | point spread function |
| RMS | root-mean-square |
| SL | Superlorentzian |
| SLM | spatial light modulator |
| TOF | time-of-flight |
| UV | ultraviolet |

Part I

INTRODUCTION

OVERVIEW

1.1 FROM "SUPER"...

In the beginning of the 20th century, the observations of two “super” phenomena were posing new fundamental questions to physicists. In his experiments with mercury in 1911, H.K. Onnes noticed that its electrical resistance would suddenly vanish below a temperature of 4.2 K, allowing current to flow freely through the material [2]. The discovery of what he later called “superconductivity” would earn him the Nobel Prize in Physics in 1913. Although Onnes already used liquid helium as a coolant, it would take until 1938, when a sudden change in the viscosity of liquid helium-4 was observed at a critical temperature of $T_c = 2.17$ K [3, 4]. This ability to flow without friction led to the term “superfluid”, in analogy to the already studied superconductivity. But while the latter phenomenon was still not understood well, superfluidity was quickly linked to Bose-Einstein condensation [5] on the microscopic level. The Bose-Einstein condensate (BEC) is a prediction of the Bose-Einstein statistics [6, 7], which describe how an ensemble of indistinguishable particles with integer spin (bosons) occupy the available energy states in a system. At low temperatures, they macroscopically populate the lowest energy state, behaving like a big macro-particle. With the Fermi-Dirac statistics [8, 9], a similar description exists for half-integer particles (fermions), which include also the electrons in a metal such as mercury. However, as a direct consequence of the Pauli exclusion principle, identical fermions do not occupy the same single-particle state, preventing the condensation process. Instead, at zero temperature, the particles will fill up all available energy states up to the Fermi energy E_F .

It took another 20 years, until 1957, when Bardeen, Cooper and Schrieffer recognized that with attractive interactions between two electrons of opposite spin, loosely bound pairs could be formed below a critical temperature. These composite bosons, called Cooper pairs, were then allowed to condense, yielding a microscopic description of superconductivity in the Bardeen-Cooper-Schrieffer (BCS) theory [10, 11]. Within this framework it was expected that also the fermionic helium-3 should exhibit superfluidity at even lower temperatures as in its bosonic counterpart. This was finally verified in 1972 after the observation of two phase transitions [12, 13], although in this case the underlying mechanism required a more elaborate theoretical explanation [14].

Since then, the development of experiments and theoretical descriptions and predictions went hand in hand. In particular, the role of interaction between two

particles was studied intensely. The strength of this interaction can be described by the scattering length a . A negative value of a indicates attractive interaction, as in the case of BCS pairing, while a is positive when the interaction is repulsive. It was found that in the latter case, two fermions can enter bound dimer states, which are bosonic and can consequently undergo condensation into a BEC. These two phases are linked by the regime of strong interactions in between, and it was later found that by changing a , it is possible to cross from one end of the spectrum to another while the whole system stays superfluid. Interestingly, this happens without an abrupt phase transition. This is nowadays known as the BEC-BCS crossover and has been studied extensively throughout the years (see for example in Ref. [15]).

Part of the great interest in this field comes from the fact, that when a approaches infinity, the system enters a universal regime. Here the properties of the system only depend on its temperature and density, but the details of the interaction potential drop out of the description. Examples of such systems are neutron stars [16, 17] or the quark-gluon plasma [18–20] (a state of matter describing the universe shortly after the big bang). However, such systems can often not be studied and controlled directly, making the development and testing of new theories demanding, and thus many open questions remain.

Additionally, since the first historic observations of superconductivity in mercury, materials with far higher critical temperatures T_c have been identified. Recently, with the synthesis of exotic materials, T_c even approached room-temperature, however only in combination with pressures in the range of several hundreds of GPa [21]. Naturally, materials with superconducting conditions at feasible temperatures and pressures would find widespread applications in science and industry. While the BCS theory can explain low-temperature Type I superconductivity, the underlying mechanisms of Type II or high- T_c superconductors are still not understood. Experimentally, condensed matter systems are still hard to study on a microscopic level, since the timescales of the underlying processes lie in the range of attoseconds, a result of their high Fermi energies and densities. However, nowadays, physicists try to push the boundaries of and gain insight in the field of strongly interacting fermions by employing quantum simulators and conducting experiments with ultracold atomic quantum gases. Ultracold gases have become extremely controllable, and feature lower densities, therefore shifting the timescales of the dynamics to the range of micro- to milliseconds, making them an ideal test bed.

1.2 ...TO "ULTRA"

Throughout the 20th century, with a deeper understanding of quantum phenomena, science was advancing rapidly. With the development of the laser [22] and using its light in techniques to trap and cool atoms [23–25] to temperatures of tens of

nK, the field of ultracold atoms was born. Ultimately, this led to the realization of conditions, where quantum effects occur, culminating in the first direct observations of an atomic BEC. In 1995, two groups at JILA and MIT simultaneously succeeded in condensing a gas of ^{87}Rb and ^{23}Na atoms [26, 27]. Owing to the fact that because of the Pauli principle, thermalization in a low-temperature gas of fermions is suppressed, the first degenerate Fermi gases (DFGs) were only observed 4 years later. ^{40}K was cooled to degeneracy by using two spin states by the group in JILA [28], while another two years later the groups at Rice University and in Paris used the bosonic ^7Li to sympathetically cool ^6Li [29, 30].

By now, with the development of additional experimental techniques, ultracold atoms have become extremely controllable. This includes the ability to change the temperature, particle number and density, trapping geometry and dimensionality, and interaction strength, as well as techniques to bring the systems out of their equilibrium state and study their response. As a result, a Bottom-Up approach is possible, where simple systems are studied and then made more and more complex to tackle not yet understood phenomena. In particular, the ability to control the interaction strength of the system by the use of Feshbach resonances should be highlighted [31, 32]. Around such resonances, by changing the magnetic field strength B , the scattering length a can be precisely tuned, going from attractive to repulsive and from weak to strong interactions.

Consequently, this was used extensively to study the effects of interaction on various properties of thermal and condensed bosonic systems, as well as the formation of molecules. However, attractive interactions can lead to an instability of a BEC, leading to its collapse [33–35]. Additionally, when three atoms come together, two of them can bind into a molecule with the help of the third, setting free their molecular binding energy as kinetic energy, which can lead to loss and heating of the gas. This has been studied extensively, and it has been shown that the rate with which such collisions occur scales as a^4 [36–38], and in the degenerate regime is even enhanced by Bose statistics. This makes experiments with strongly interacting bosons extremely difficult.

1.3 FROM BALANCED TO IMBALANCED FERMI-FERMI MIXTURES

In contrast to bosons, because of the Pauli principle, fermions behave quite differently. On the one hand, identical fermions can not interact via s-wave collisions. This means that for gases at low temperatures, where other partial wave contributions vanish, originally two spin states had to be used to have an interacting sample. On the other hand, this also leads to increased stability against three-body loss [39–42]. This opened up the ability to reach strong interactions [43] between the two spin states and study the BEC-BCS crossover in great depth.

After the first experiments observed the formation of Feshbach molecules from fermionic atoms [40, 41, 44, 45], several groups succeeded in the realization of a molecular Bose-Einstein condensate (mBEC) almost simultaneously [46–48]. Soon after, condensation of fermionic pairs was also observed on resonance and in the BCS side [49]. The superfluidity at the crossover was then studied extensively through collective modes [50, 51] and hydrodynamic behavior [52], although the direct observation of superfluidity only came with the observation of vortices [53]. Furthermore, the pairing gap as a distinctive feature of Fermi pairing was measured with radio-frequency spectroscopy [54].

In the center of Feshbach resonances, where the scattering length diverges, the gas enters the unitarity limit. In this so-called universal regime, the interparticle distance becomes the only relevant length scale remaining [55]. The interparticle interaction then does not depend on the microscopic details of the interaction potential anymore. Hence, insights from highly controllable ultracold atom experiments can be applied to other inaccessible universal systems like neutron stars or the quark gluon plasma [20]. Unsurprisingly, many experiments focused on the thermodynamic properties of the universal Fermi gas [56–58]. Another interesting aspect was the characterization of the temperature dependence of first sound [59, 60] and the observation of second sound [61].

Originally, early experiments with spin mixtures were carried out with roughly equal atom numbers in both states. However, possible pairing mechanisms in the case of mismatched Fermi surfaces were also discussed, for example for superconductors in strong external fields. In this case, the external field couples to the spin of the electrons, resulting in separated Fermi surfaces of the two opposite spins. Furthermore, in the core of neutron stars, high-density quark mixtures are proposed to be present. Here, a mismatch between the Fermi surfaces of quark flavors can appear as a result of their different masses and charges, and can lead to color-superconductivity, which was proposed to have relevance to astrophysics [19]. However, such systems remain difficult to study directly.

Therefore, the next logical and experimentally easy to implement step was to change the atom number ratio (or polarization P of the system) and study its effect on the pairing mechanism and phase diagram of the mixture. In the opposite extreme to the equal-numbered case, a single species Fermi gas, no pairing is possible. The absence of interactions because of Pauli blocking leads to the textbook example of an ideal gas. But after adding just a few atoms of a second species, this minority component acts as an impurity. With attractive interactions, a quasiparticle is formed with nearby majority component atoms, forming the Fermi polaron [62]. Together with its bosonic counterpart [63], the polaron and its properties were studied extensively [64].

The question arises, how and when superfluidity occurs between these two regimes. In the case of equal spin numbers, Cooper pairs form between atoms

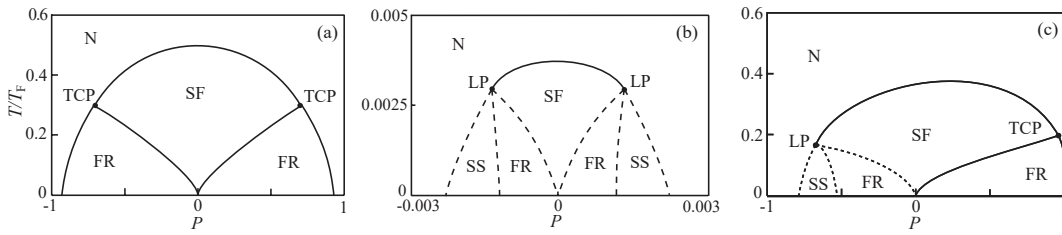


Figure 1.1: Phase diagrams of imbalanced Fermi gases as a function of polarization P and temperature T . (a) and (b) show the equal mass case at strong ($1/k_F a = 0$) and weakly attractive interactions ($1/k_F a = -3$), respectively. (c) shows the phase diagram for a mass ratio of 6.7 in the strongly interacting limit. N normal state, SF superfluid state, FR forbidden region, SS supersolid, TCP tricritical point, LP Lifshits point. Figure adapted from Ref. [70].

from the two opposing sides of the Fermi surface of the two spin states, where the addition of their equal but oppositely directed momentum results in a pair of zero net momentum. Generally, all atoms can pair up, resulting in the creation of a superfluid throughout the whole sample. However, with unequal atom numbers, this is not the case anymore, resulting in a transition to the normal state for increasing polarization [65], or in the formation of a superfluid core surrounded by a normal Fermi gas [66, 67]. The theoretical calculated phase diagram of such a spin mixture at strong interactions can be seen in Fig. 1.1(a), where the temperature was rescaled by the Fermi temperature $T_F = E_F/k_b$. Here, a tricritical point occurs where the superfluid, phase separated (referred to as forbidden region FR) and normal phases meet. Extensive theoretical studies on the phase diagram for different interaction regimes show that they can be substantially modified, with the occurrence of new, exotic phases. For example, for larger polarization, where the Fermi surfaces are mismatched, pairing between atoms of unequal momenta can be favorable. This results in pairs with non-zero total momentum and an inhomogeneous superfluid order parameter, as has been shown independently by Fulde and Ferrell (FF) [68], and Larkin and Ovchinnikov (LO) [69], who considered the aforementioned case of superconductors in external magnetic fields. As the LO state features a modulated density, it is also associated with a supersolid state. Fig. 1.1(b) shows a spin mixture at weakly attractive interactions, where the formation of a supersolid phase accompanied by a Lifshits point was predicted [70]. However, as the Fulde–Ferrell–Larkin–Ovchinnikov (FFLO) states are believed to appear only in a very small phase space region [71], and the required extremely low temperatures are hard to reach in experiments, it is still elusive experimentally.¹

¹ Experiments with exotic organic superconductors using nuclear magnetic resonance measurements [72] and measurements of their heat capacity [73] have found indicators of the FFLO state, however a direct microscopic confirmation is missing.

As a second possibility to introduce imbalance to a mixture, a second atomic species with a different mass can be used. In such a mass-imbalanced case, the $T - P$ phase diagram is modified even more, as is shown in 1.1(c). It is not symmetric with respect to the polarization anymore, and the supersolid phase is only found at a majority of light particles. Remarkably, the temperature associated to the supersolid phase and Lifshits point is now about two orders of magnitude higher, which puts it at conditions realistic to reach with current ultracold atom experiments [74].

As another striking effect, the interaction between particles can be substantially modified by the mass-imbalance. While for identical fermions at low temperatures the p -wave centrifugal barrier prevents the three-body recombination to dimers and subsequent loss of particles, at a mass ratio from 13.6 and higher, this barrier no longer exists, at resonance leading to an occurrence of an infinite number of bound trimer states under the Efimov effect [75]. A second, different, p -wave trimer state is present for a mass ratio of 8.2 onward for strong repulsive interactions.

With the combination of the two originally degenerate species Li and K, a first system was available to try to study the effects of mass imbalance [76–78]. The hydrodynamic expansion of the strongly interacting mixture could be observed [79], as well as the effect of the mass ratio on three-body interactions [80]. However, because of the narrow nature of the Feshbach resonances in this system, no strong loss suppression is present [81]. Additionally, there is also a two-body inelastic decay process [82]. The resulting limited lifetime is a major complication for the investigation of ground-state properties of this mass-imbalanced mixture.

1.4 THE DY-K EXPERIMENT

In recent years, additionally to the relatively simple alkali species Li and K, several other fermionic species have been brought to degeneracy, including Cr [83], Sr [84] and Yb [85]. In the tradition of transitioning to more complicated systems, focus was also laid on the lanthanides Er [86] and Dy [87]. Their complex electronic structure, featuring a partially filled, submerged $4f$ shell and consequently a high magnetic moment of 9 and $10\mu_B$, respectively, gives rise to several interesting aspects. Most notably, they exhibit long-range anisotropic dipole-dipole interactions, which can be used as an additional control parameter. The effect of the long-range nature of the interaction is that all partial waves participate and contribute to the scattering process, even at low temperatures [88]. As a consequence, a single-species polarized dipolar Fermi gas still exhibits interaction at low temperatures [89], nevertheless making it possible to reach degeneracy [86, 90]. Another striking feature, originating from the anisotropic nature of their interactions, is that Er and Dy exhibit extremely dense Feshbach spectra [91, 92]. However, combined also with the high magnetic moment, this demands a high level of control and accuracy on the magnetic field.

Aside from its effect on the interaction properties, the complicated electronic structure also results in a dense spectrum of optical transitions, featuring both broad and narrow closed transitions at wavelengths accessible with current laser technology [93–96]. These have, for example, been used to reach sub- μK temperatures already before evaporative cooling, enabling a rapid BEC and DFG production. With the wide field of new phenomena and experimental techniques the lanthanides offer, they have recently found a lot of interest in the cold atom community. Most notably are perhaps the pursuit and observation of self-bound quantum droplets and ultimately the supersolid phase [97–99].

Within the need for a new strongly interacting mass-imbalanced Fermi-Fermi mixture, the combination of Dy and K stands as a good candidate. The mass ratio of about 4 is expected to result in a reasonable effect on the interaction properties, while at the same time staying away from the lossy trimer states occurring at higher ratios. It is expected that the mixture exhibits a sufficient suppression of inelastic decay [81].

Although the dense Feshbach spectrum of Dy increases the difficulty in terms of magnetic field control, the reasonable assumption is that this will result in usable interspecies Feshbach resonances at moderate field strengths [100], as opposed to mixtures with closed-shell atoms like Sr [101] and Yb [102, 103]. Furthermore, dysprosium's efficient cooling strategies offer an advantage as compared to Cr and the challenges imposed by its level structure [104]. In comparison to the very similar Er, Dy stands out because of its two fermionic isotopes, doubling the chances of realizing a strongly interacting mixture.

CONTENTS OF THIS THESIS

This thesis has been realized in the Innsbruck Dy-K experiment and was started shortly after the move-in into a new lab. I was therefore present in the early stages of the experiment, facing mostly technical challenges. As we have seen in the brief history of ultracold gases, two main ingredients for a successful experiment are the ability to control the system and to have methods to gain understanding of the measured data. My work is therefore divided into two directions.

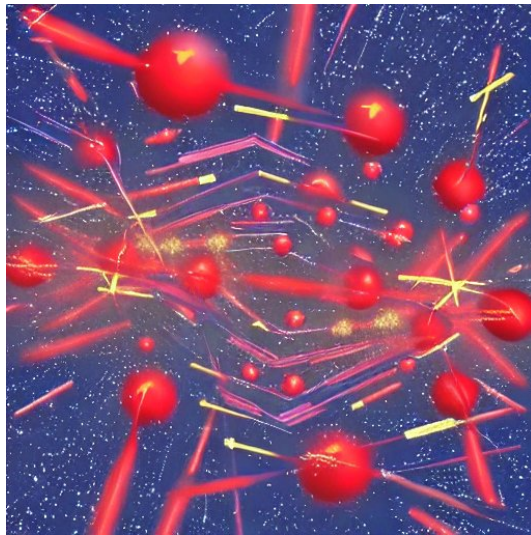
Part II of this thesis is centered around our initial effort to realize a resonantly interacting Fermi gas. Chapter 3 serves as a short introduction to interactions in a gas and how these interactions can be controlled with the use of Feshbach resonances. As a first step in the experiment, we developed techniques to produce deeply degenerate Fermi mixtures of Dy and K, the details of which are described in our publication in Ref. [105]. Building on these results, we identified a set of Feshbach resonances close to 217 gauss, which lead to the creation of a resonantly interacting Fermi-Fermi mixture of Dy and K. Our findings are reported in Chapter 4. As one of the techniques to identify the center of the resonances, we used hydrodynamic expansion of the two clouds. To understand the experimental data, we developed a Monte Carlo simulation to solve the Boltzmann equation. The details of this simulation are summarized in Chapter 5.

Part III focuses on the aspect of controlling the system by shaping the properties of the optical trapping potential. In Chapter 6 I will introduce the atomic polarizability as the quantity that describes the response of an atom in an off-resonant light field, and I will motivate why the realization of a flat trapping potential is interesting for our experiment and in general for the hunt for exotic phases. Since the atomic polarizability strongly depends on the wavelength of the trapping light, we measured the response of dysprosium to the light at wavelengths close to 1064 nm and around 626 nm. The results of these measurements are reported in Chapters 7 and 8. Chapter 9 focuses on the experimental techniques used to shape arbitrary potentials with a spatial light modulator.

The thesis is then concluded in Part IV with a summary on the work that has been carried out during my time as a PhD student, and an outlook of what is next for the Dy-K experiment.

Part II

INTERACTIONS IN THE DY-K MIXTURE



AI interpretation of simulations of colliding gas particles, created by Stable Diffusion [106].

SCATTERING AND FESHBACH RESONANCES IN QUANTUM GASES

Interactions and scattering in ensembles of particles are an important aspect of current scientific research. This is especially pronounced in fermionic systems, where interactions enable the formation of superfluids, the basis of many interesting physical phenomena, e.g. superconductivity. In the field of ultracold atoms, Feshbach resonances can be used to control interactions, which, among other techniques, enable the systematic study of superfluidity and other related phenomena. In this chapter I will only shortly touch on the wide subject of interactions to give a brief introduction to the basic concepts appearing and used in this part of the thesis. For a more extensive discussion, I refer to the References [32, 107, 108].

In general, in a dilute ultracold atomic gas, two-body collisions dominate over other interaction processes with more constituents, because the limited density leads to a suppression of the probability of three or more particles coming close to each other. At large distances r between two atoms, the interaction potential is dominated by the attractive van der Waals potential, which is approximately proportional to $-1/r^6$, whereas at short distances on the order of the Bohr radius a_0 the repulsive interaction of the two electron clouds leads to a hard-core repulsion. The formal treatment of atoms moving in this interaction potential is very tedious and complicated in the case of a gas with high atom numbers. However, in an ultracold gas, the de Broglie wavelength of the atoms is large, on the order of $10000 a_0$, meaning that the atoms often do not explore the fine details of the interaction potential. Under this assumption, the potential can be described by another potential that is easy to solve to understand the scattering process, for example a spherical well potential.

3.1 BASIC SCATTERING THEORY

In scattering theory, the system of two colliding particles is usually described as a single particle of energy E , reduced mass μ and relative wavevector \mathbf{k} in the relative coordinate system with potential $V(r)$. The magnitude of the wavevector is given by $k = \sqrt{2\mu E/\hbar^2}$. In the asymptotic cases, the particle enters as a plane wave $e^{i\mathbf{k}\mathbf{r}}$ and leaves the process in a superposition of the incident wave and an outgoing scattered, spherical wave

$$\Psi(\mathbf{r}) \rightarrow e^{i\mathbf{k}\cdot\mathbf{r}} + f(\mathbf{k}', \mathbf{k}) \frac{e^{ikr}}{r}. \quad (3.1)$$

Here, $f(\mathbf{k}', \mathbf{k})$ is called the scattering amplitude and describes scattering from an incident wave with \mathbf{k} into direction \mathbf{k}' . Assuming a central potential, we can employ a partial wave expansion of the wave function with respect to the angular momentum l . In the limit of ultracold gases, the collision energies are so small that s -wave interactions ($l = 0$) dominate over all other partial wave contributions. Then

$$f \approx f_s = \frac{1}{k \cot \delta_s - ik'} \quad (3.2)$$

which means that the outgoing wave gets a phase shift δ_s . For low momenta we use the expansion

$$k \cot \delta_s \approx -\frac{1}{a} + r_{\text{eff}} \frac{k^2}{2}, \quad (3.3)$$

where we define the effective range r_{eff} of the potential and the (s -wave) scattering length

$$a = \lim_{k \rightarrow 0} \frac{\tan \delta_s}{k}. \quad (3.4)$$

With this we can rewrite

$$f(k) = \frac{1}{-\frac{1}{a} + \frac{1}{2}r_{\text{eff}}k^2 - ik} \quad (3.5)$$

and finally arrive at the scattering cross section for s -wave collisions

$$\sigma = 4\pi |f(k)|^2 = \frac{4\pi}{\left(\frac{1}{a} - \frac{1}{2}r_{\text{eff}}k^2\right)^2 + k^2}. \quad (3.6)$$

Let's now discuss the behavior of σ in some special cases. In general, r_{eff} depends on the details of the interaction potential. However, in ultracold gases the de Broglie wavelength $2\pi/k$ is often much bigger than the effective range, $1/k \gg |r_{\text{eff}}|$, which means that the atoms do not sample the fine details of the potential. In this case, simpler pseudo potentials can be used to describe the scattering process, and the cross section reduces to the universal form

$$\sigma = \frac{4\pi a^2}{1 + a^2 k^2}. \quad (3.7)$$

For very low momenta $|ka| \ll 1$, the scattering length is enough to describe the scattering process, with the corresponding low-energy cross section

$$\sigma = 4\pi a^2. \quad (3.8)$$

In the opposing limit $|ka| \gg 1$, the cross section is momentum limited and reduces to

$$\sigma = \frac{4\pi}{k^2}. \quad (3.9)$$

In this so-called unitarity limit, the scattering length drops out of the description of the scattering process. The interaction is then entirely governed by k and universal for many different physical systems, which makes this regime very interesting to explore in highly controllable ultracold atom experiments.

3.2 FESHBACH RESONANCES

The scattering length a and the effective range depend on the nature and details of the interaction potential. However, it turns out that a shows a resonance behavior whenever the energy of the two free particles is close to the energy of a bound state in another potential. This is also the underlying principle of the Feshbach resonances, which provide an important tool to control the scattering length in cold atom experiments. Again, for an in-depth discussion of the mechanisms behind Feshbach resonances the reader is referred to Refs. [32, 107].

In the description of the Feshbach mechanism, the coupled two-channel picture is often used. Two free atoms at a large distance in their interaction potential are said to be in the open (or entrance) channel. However, other (closed) channels exist that differ in their electron configuration and therefore their energy, and can support a bound state. Since the different channels have different magnetic moments, their energy difference depends on the magnetic field strength B . Thus, by changing B , open and closed channel can be shifted in their relative energy, such that the energy of the free atoms is close to the energy of the bound state in the closed channel. In this scenario, the scattering length shows a resonance behavior which can be described by

$$a(B) = a_{\text{bg}} \left(1 - \frac{\delta}{B - B_0} \right). \quad (3.10)$$

The background scattering length a_{bg} summarizes the effect of off-resonant scattering processes, as well as contributions from other nearby Feshbach resonances, and depends on the interaction potential. B_0 indicates the resonance center, where the scattering length diverges. The resonance width δ depends on a_{bg} and determines the position of a zero-crossing of the scattering length at $B = B_0 + \delta$.

Close to the resonance, the incoming scattering state couples to the bound molecular state of the closed channel, and the scattering state becomes a dressed state, consisting of contributions from both channels. In the case of an open-channel dominated resonance, the closed channel can be eliminated by assuming a single channel model with an attractive spherical well potential. In this simple description, the three parameters a_{bg} , δ and B_0 are enough to fully characterize the Feshbach resonance. The universal regime can then be accessed if $|ka| \gg 1$ and we can use Eq. (3.9) to compute the scattering cross section. Furthermore, for $a > 0$ the atoms enter the molecular state whose binding energy in the universal range is given by $E_b = -\frac{\hbar^2}{2\mu a^2}$.

However, in some cases the resonance is dominated by the closed channel and the single channel model is not enough to describe the scattering process. In this case, another, fourth parameter $R^* = -r_{\text{eff}}/2$ has to be introduced [109], and the cross section takes the form of Eq. (3.6). However, even for narrow resonances the universal regime can be recovered for $|a| \gg R^*$.

Feshbach resonances have become an invaluable tool for experimentalists, because they allow to accurately control the interaction of the atoms and thus access different physical phenomena. Especially the universal regime offers the possibility to study other physical systems with the well-developed tools of ultracold atom experiments. Therefore, one of the first steps in experiments with new species is to search for suitable Feshbach resonances, if possible "broad" (i. e. entrance-channel dominated) ones. Chapter 4 features a publication where we investigated a Dy-K resonance close to 217 G. In the characterization of this resonance, we used methods that rely on the hydrodynamic expansion and thermalization of the two species, two phenomena that depend on the scattering cross section. To understand the experimental data, we developed a Monte Carlo simulation that numerically solves the Boltzmann equation and allows to make some predictions for the experiment. The details of this simulation are described in Chapter 5.

PUBLICATION: RESONANTLY INTERACTING FERMI-FERMI
MIXTURE OF ^{161}DY AND ^{40}K

Published as:

C. Ravensbergen, E. Soave, V. Corre, M. Kreyer, B. Huang (黄博), E. Kirilov and R. Grimm.

Phys. Rev. Lett. **124**, 203402 (2020)

Author contribution: The author took a supporting role in the process of acquiring and analyzing the data described in this publication as well as contributed to the writing of the manuscript. The author took a leading role in the development of the Monte Carlo simulation.

Changes with respect to the original publication: Subsection headlines have been added.

We report on the realization of a Fermi-Fermi mixture of ultracold atoms that combines mass imbalance, tunability, and collisional stability. In an optically trapped sample of ^{161}Dy and ^{40}K , we identify a broad Feshbach resonance centered at a magnetic field of 217 G. Hydrodynamic expansion profiles in the resonant interaction regime reveal a bimodal behavior resulting from mass imbalance. Lifetime studies on resonance show a suppression of inelastic few-body processes by orders of magnitude, which we interpret as a consequence of the fermionic nature of our system. The resonant mixture opens up intriguing perspectives for studies on novel states of strongly correlated fermions with mass imbalance.

4.1 INTRODUCTION

Ultracold Fermi gases with resonant interactions have attracted a great deal of attention as precisely controllable model systems for quantum many-body physics [15, 110–112]. The interest spans across many different fields, from primordial matter, neutron stars and atomic nuclei to condensed-matter systems, and in particular concerning superfluids and superconductors [113]. Corresponding experiments in ultracold Fermi gases require strong s -wave interactions, which can be realized based on Feshbach resonances [32] in two-component systems. The vast majority of experiments in this field relies on spin mixtures of fermionic atomic species, which naturally imposes equal masses. Beyond this well-established situation, theoretical work has predicted fermionic systems with mass imbalance to favor exotic interaction regimes [114]. Mass-imbalanced systems hold particular promise [74, 115] in view of superfluid states with unconventional pairing mechanisms, most notably the elusive FFLO state [68, 69, 116].

A key factor for experiments on resonantly interacting Fermi gases is the collisional stability that arises from a suppression of inelastic loss processes at large scattering lengths. This effect is a result of Pauli exclusion in few-body processes at ultralow energies [42, 117]. To act efficiently in an experiment, the suppression requires a broad s -wave Feshbach resonance with a sufficiently large universal range [75, 117]. For the mass-balanced case, suitable resonances exist in spin mixtures of ^6Li or ^{40}K , and such systems are used in many laboratories worldwide. In a mass-imbalanced fermion system, the same suppression effect can be expected [118]. However, the only s -wave tunable Fermi-Fermi system realized so far is the mixture of ^6Li and ^{40}K [79, 80], for which the Feshbach resonances [77, 82, 119] are too narrow to enable strong loss suppression [81].

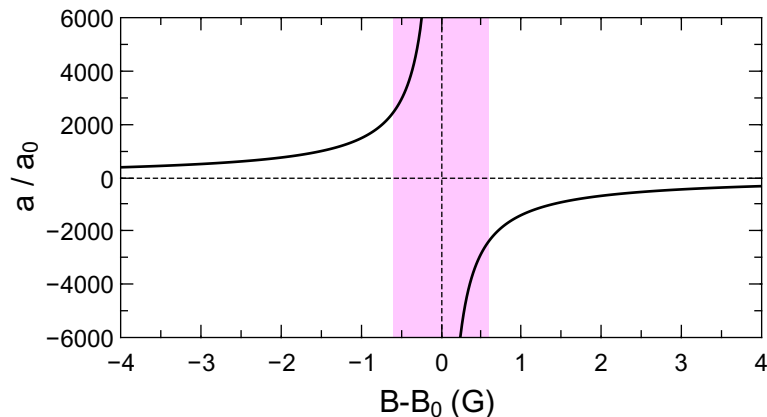


Figure 4.1: Interspecies scattering length a for ^{161}Dy - ^{40}K near the broad Feshbach resonance centered at $B_0 \approx 217$ G. The shaded region indicates the regime where a exceeds all other relevant length scales (see text).

The advent of submerged-shell lanthanide atoms in the field of ultracold quantum gases [86, 87, 120, 121] has considerably enhanced the experimental possibilities. While most of the current work focuses on interactions that result from the large magnetic dipole moment or the complex optical transition structure, the availability of additional fermionic atoms is of great interest in view of novel ultracold mixtures and strongly interacting systems [122, 123]. We have recently introduced the mixture of ^{161}Dy and ^{40}K [105, 124] as a candidate for realizing a collisionally stable, strongly interacting Fermi-Fermi mixture. Many narrow Feshbach resonances can be expected for such a system as a result of anisotropic interatomic interactions [100, 125]. However, the key question in view of future experiments has remained, whether suitable broad resonances would exist.

In this Letter, we report on a broad Feshbach resonance in the ^{161}Dy - ^{40}K mixture with its center found near 217 G. We have identified this resonance (see Fig. 4.1) as the strongest one in a scenario of three overlapping resonances (Sec. 4.7), with the other two at 200 G and 253 G. Some weak (only few mG wide) interspecies resonances do also exist in the relevant region, but they can be ignored for understanding the general structure of the broad scenario. We have characterized the three resonances by interspecies thermalization measurements, as reported in detail in Sec. 4.7. Close to the center of the strongest resonance, the tunability of the interspecies s -wave scattering length can be well approximated by

$$a = -\frac{A}{B - B_0} a_0, \quad (4.1)$$

where a_0 is Bohr's radius. Our best knowledge of the pole position and the strength parameter is $B_0 = 217.27(15)$ G and $A = 1450(230)$ G, see Sec. 4.7.

4.2 SAMPLE PREPARATION

The starting point of our experiments is a degenerate mixture of ^{161}Dy and ^{40}K , prepared in a crossed-beam optical dipole trap according to the procedures described in our earlier work [105]. Evaporative cooling is performed at a low magnetic field of 225 mG. Both species are in their lowest hyperfine and Zeeman substates, which excludes two-body losses. The transfer of the system into the high-field region above 200 G is challenging, because many Dy intraspecies [91, 126] and Dy-K interspecies resonances have to be crossed in a fast ramp of the magnetic field. To minimize unwanted losses, heating, and excitations of the trapped cloud we proceed in two steps. Within a few ms, we ramp up the magnetic bias field to 219.6 G¹, where the system is given a time of a few 10 ms to settle and establish thermal equilibrium. We then apply a very fast (2-ms) small-amplitude ramp to the target field, where the experiments are carried out. Throughout the whole sequence after evaporation, a magnetic levitation field is applied to compensate for the relative gravitational sag of both species [105]. In this way, we reach typical conditions of $N_{\text{Dy}} = 20\,000$ and $N_{\text{K}} = 8\,000$ atoms at a temperature of $T = 500\text{ nK}^2$ in a slightly elongated trap (aspect ratio ~ 2) with mean oscillation frequencies of $\bar{\omega}_{\text{Dy}}/2\pi = 120\text{ Hz}$ and $\bar{\omega}_{\text{K}}/2\pi = 430\text{ Hz}^3$ and depths corresponding to $3.5\text{ }\mu\text{K}$ and $10\text{ }\mu\text{K}$, respectively. With Fermi temperatures of $T_F^{\text{Dy}} = 290\text{ nK}$ and $T_F^{\text{K}} = 750\text{ nK}$, our experimental conditions are near-degenerate of ($T/T_F^{\text{Dy}} = 1.7$ and $T/T_F^{\text{K}} = 0.65$).

4.3 INTERACTION CHARACTERIZATION

Interaction regimes near resonance can be discussed by comparing the scattering length with other relevant length scales. To characterize the interaction strength on resonance, where scattering is limited by unitarity [127, 128], we define a length scale corresponding to the inverse wave number of the relative motion $1/\bar{k}_{\text{rel}} = \hbar/(m_r\bar{v}_{\text{rel}})$, where $\bar{v}_{\text{rel}} = \sqrt{8k_B T/(\pi m_r)}$ is the mean relative velocity and m_r denotes the reduced mass. The typical interparticle distance sets another length scale, for which we adopt a common definition for two-component Fermi gases, $d = (3\pi^2 n_{\text{tot}})^{-1/3}$, where n_{tot} is the total number density of both species in the trap center. For our typical experimental parameters, we obtain $1/\bar{k}_{\text{rel}} \approx 2100 a_0$ and $d \approx 2500 a_0$. The scattering length exceeds $1/\bar{k}_{\text{rel}}$ in a magnetic field range of roughly $\pm 0.7\text{ G}$. In this resonant interaction regime, scattering is dominated by the

-
- 1 At 219.6 G interspecies thermalization is sufficiently fast and Dy background losses show a pronounced minimum.
 - 2 Thermometry is based on time-of-flight images taken at high magnetic fields in regions where interspecies interactions are weak.
 - 3 The ratio of the trap frequencies for K and Dy is essentially determined by the mass ratio and the polarizability ratio, which results in a $\bar{\omega}_{\text{K}}/\bar{\omega}_{\text{Dy}} = 3.60$ [124].

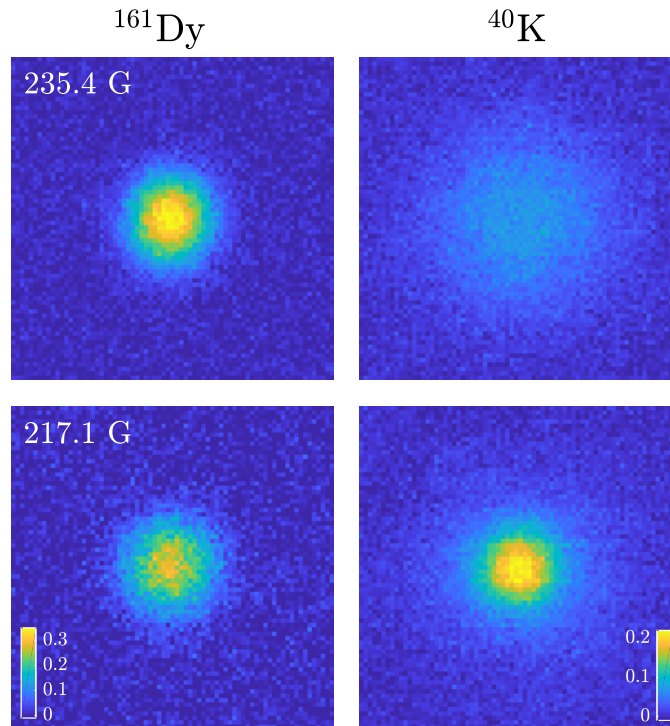


Figure 4.2: Comparison of the expansion of the mixture for weak (upper) and resonant (lower) interspecies interaction. The absorption images show the optical depth for both species (Dy left, K right) after a time of flight of 4.5 ms. The field of view of all images is $240 \mu\text{m} \times 240 \mu\text{m}$.

unitarity limitation. In addition to that, the values of $1/\bar{k}_{\text{rel}}$ and d are similar, which means that the system is in the crossover between weak and strong interactions. A further length scale is set by the effective range of the resonance [32]. Its value is presently unknown because of the yet undetermined magnetic moment of the molecular state underlying the resonance, but we expect the effective range (Sec. 4.7) to be rather small in comparison to realistic values of the scattering length and the interparticle spacing, so that the interaction physics will be dominated by universal behavior.

4.4 HYDRODYNAMIC EXPANSION

A striking effect of the resonant interspecies interaction shows up in the expansion of the mixture. In the experiments, the sample was released from the trap right after switching to the target field strength. The absorption images in the upper row of Fig. 4.2 illustrate the case of weak interactions ($a \approx -40 a_0$), realized at $B = 235.4 \text{ G}$. Here the expansion takes place in a ballistic way and, as expected from the mass

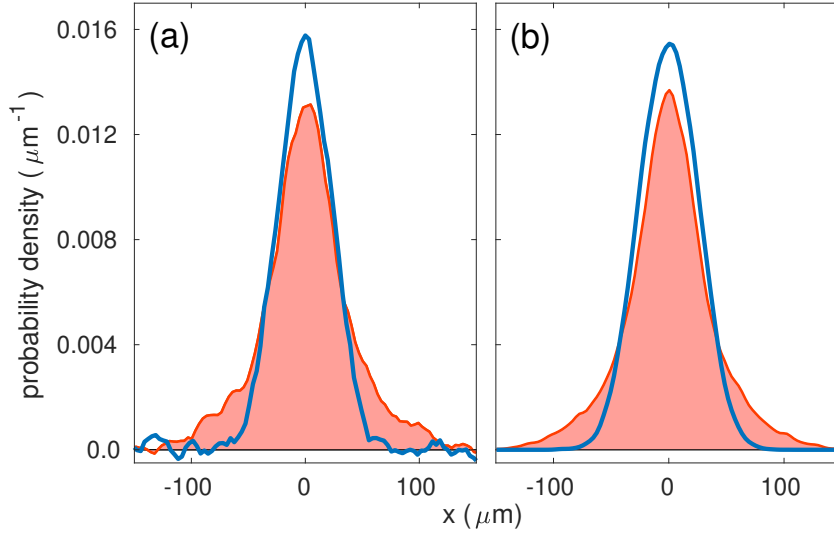


Figure 4.3: Profiles of the hydrodynamically expanding mixture for resonant interaction, (a) experimentally observed and (b) from a corresponding Monte-Carlo simulation. Shown are the probability densities of doubly-integrated profiles for both Dy (solid blue lines) and K (red curve with filling).

ratio, the K component expands much faster than the Dy component. In contrast, in the resonant case (images in the lower row of Fig. 4.2) both components expand with similar sizes. Evidently, the interaction between the two species slows down the expansion of the lighter species and accelerates the expansion of the heavier species. Such a behavior requires many elastic collisions⁴ on the timescale of the expansion and thus can be interpreted as a hallmark of hydrodynamic behavior.

A closer inspection of the spatial profiles of the hydrodynamically expanding mixture reveals an interesting difference between the heavy and the light species; see profiles in Fig. 4.3. While the Dy cloud essentially keeps its near-Gaussian shape, the K cloud (initially about twice smaller than the Dy cloud) develops pronounced side wings. Apparently, the mixture forms a hydrodynamic core surrounded by a larger cloud of ballistically expanding lighter atoms.

To elucidate the origin of this surprising effect we have carried out a Monte-Carlo simulation [129], accounting for the classical motion and the quantum-mechanically resonant collisional cross section, which is only limited by the finite relative momentum of a colliding pair [127, 128]. For our near-degenerate conditions, we neglect Pauli blocking and interactions beyond two-body collisions. The simulation results in Fig. 4.3(b) reproduce the experimental profiles (a) without any free parameter.

⁴ We estimate the collision rate for a K atom in the center of the Dy cloud by considering the resonant elastic scattering cross section $\sigma_{\text{res}} = 4\pi/\bar{k}_{\text{rel}}^2$, the Dy peak number density \hat{n}_{Dy} , and the mean relative velocity \bar{v}_{rel} . For our typical conditions, $\hat{n}_{\text{Dy}}\sigma_{\text{res}}\bar{v}_{\text{rel}} \approx 10^4 \text{ s}^{-1}$.

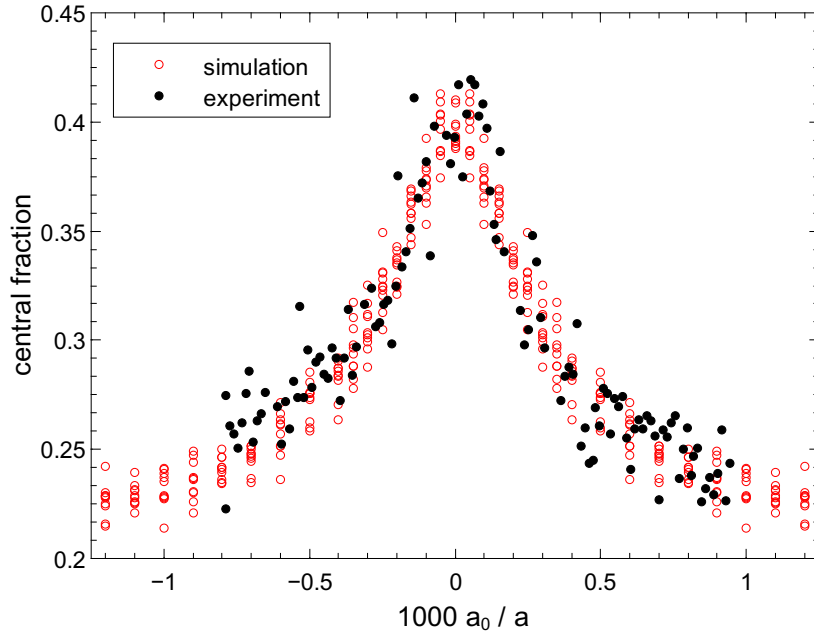


Figure 4.4: Enhancement of the central fraction of K atoms in the expanding mixture. Experimental results for the resonance behavior (filled black symbols) are shown in comparison with Monte-Carlo simulation results (red open symbols).

The simulation confirms our interpretation in terms of a hydrodynamic core, where both species collide with each other at a large rate, surrounded by a ballistically expanding cloud of light atoms. The physical mechanism for the formation of the latter is the faster diffusion of lighter atoms, which can leak out of the core and, in the absence of the other species, begin to move ballistically. We point out that this bimodality effect is not an experimental imperfection, but a generic feature in the hydrodynamic expansion of a mass-imbalanced mixture.

To investigate the dependence of the hydrodynamic expansion on the scattering length, we recorded two-dimensional expansion profiles (such as in Fig. 4.2) for various values of B in a 2-G wide range around the resonance center. We focus our analysis on the K profiles as they reveal the hydrodynamic core, while the Dy profiles only show a slight increase in width. As a quantitative measure we define the “central fraction” as the fraction of K atoms in a circle of particular radius. For the latter we use the $\sqrt{2}\sigma$ -width of the non-interacting Dy cloud ($\sim 34 \mu\text{m}$ at a 4.5-ms time of flight). We find a marked increase of the central fraction from its non-interacting background value 0.22 to a resonant peak value of about 0.40. As a function of the magnetic detuning $B - B_0$, the central fraction shows a pronounced resonance behavior, which closely resembles a Lorentzian curve. From a fit we derive the center $B_0 = 217.04\text{G}$ and a width (half width at half maximum) of 0.37 G.

We finally use Eq. (4.1) with the fixed value $A = 1450$ G to convert the magnetic detuning scale into an inverse scattering length and plot the data as shown in Fig. 4.4.

For comparison, we have also employed our Monte-Carlo approach to calculate the central fraction as a function of the scattering length. Figure 4.4 shows the simulation results (red open symbols) together with the experimental data (black closed symbols). We find that the simulation reproduces the experimental observations very well. This agreement between experiment and theory strongly supports our qualitative and quantitative understanding of both the resonance scenario and the expansion dynamics.

For a precise determination of the resonance center, measurements based on the hydrodynamic expansion can in general provide much sharper resonance features than simple thermalization [130]. While our expansion measurement yielded 217.04(1) G for the resonance center B_0 , the thermalization measurement (Sec. 4.7) resulted in a value of 217.27(15) G, somewhat higher and with a statistical uncertainty more than an order of magnitude larger. Whether the apparent deviation is a pure statistical effect (about 1.5σ), whether it is caused by magnetic-field control issues⁵, or whether there are unknown systematic effects behind it requires further investigation. We note that anisotropic expansion effects in our nearly spherical trap remain very weak and are barely observable. The anisotropic expansion of a hydrodynamic, strongly interacting Fermi-Fermi system has been studied in our earlier work on a resonant ${}^6\text{Li}$ - ${}^{40}\text{K}$ mixture [79].

4.5 LIFETIME

We now turn our attention to the lifetime of the mixture in the resonance region. In general, we find the magnetic-field dependence of losses to exhibit a very complex behavior, see Sec. 4.7. Both Dy-K interspecies and Dy intraspecies losses show strong fluctuations with a variation of the magnetic field. A broad loss feature appears about 0.5 G below the 217-G resonance, where the scattering length is very large and positive. This feature closely resembles observations made in spin mixtures of ${}^6\text{Li}$ [39, 131, 132] and ${}^{40}\text{K}$ [130], which have been understood as a signature of the formation of weakly bound dimers. In addition to this broad feature, additional narrower structures appear, which make the experiment very sensitive to the particular choice of the magnetic field. Nevertheless, several good regions exist close to the center of the broad Feshbach resonance under conditions, where losses are relatively weak and s -wave scattering is deep in the unitarity-limited regime.

⁵ Day-to-day fluctuations, drifts in the calibration, and residual ramping effects may cause magnetic-field uncertainties of the order of 100 mG.

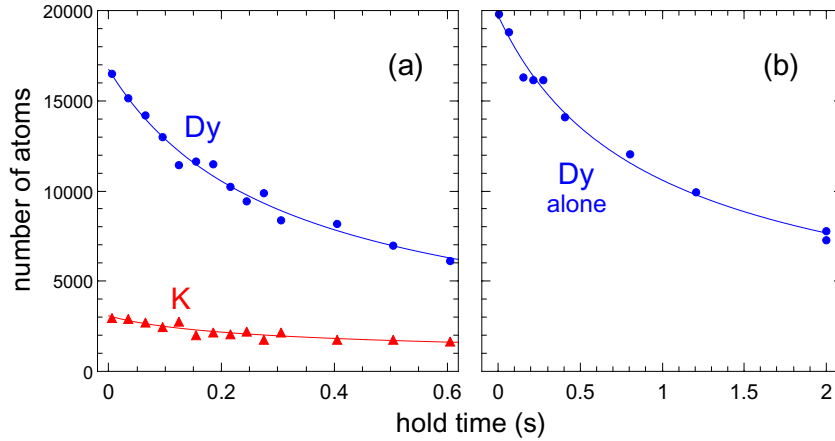


Figure 4.5: Decay of the resonant Dy-K mixture (a) in comparison with a pure Dy sample (b) at magnetic field $B = 217.5$ G, very close to the resonance pole. The solid lines show fits by a phenomenological model, see Sec. 4.7.

As an example for long lifetimes attainable in the resonance region, Figure 4.5 shows a set of measurements taken at field strength of 217.5 G, for which we estimate a large negative scattering length of $-3000 a_0$ or even larger. We have fitted and analyzed the decay of the atom numbers following the procedures detailed in Sec. 4.7. For the number of K atoms, our data show an initial time constant of about 350 ms. If we attribute this decay completely to K-Dy-Dy (K-K-Dy) three-body processes, we obtain the upper limits of $4 \times 10^{-25} \text{ cm}^6/\text{s}$ ($3 \times 10^{-25} \text{ cm}^6/\text{s}$) for the event rate coefficients. These values are very small compared with other resonant three-body systems that do not involve identical fermions. In Feshbach-resonant Bose-Bose [133–135] or Bose-Fermi mixtures [136–140], event rate coefficients have been measured exceeding $10^{-23} \text{ cm}^6/\text{s}$, i.e. at least two orders of magnitude more. In preliminary experiments [141] on Bose-Fermi mixtures of Dy-K (bosonic isotope ^{162}Dy), we have also observed a dramatic increase of resonant three-body losses by orders of magnitude. We attribute the low values of the three-body rate coefficients and thus the long lifetimes in our Fermi-Fermi system to the Pauli suppression of inelastic losses [42, 117, 118].

The decay of the Dy component in the mixture, displayed in Fig. 4.5(a) by the blue data points and the corresponding fit curve, shows a peculiar behavior. Since we find that about 10 times more Dy atoms are lost as compared to K atoms, three-body interspecies collisions may only explain a small fraction of Dy losses. As Figure 4.5(b) shows, Dy alone exhibits losses even without K being present, but much weaker. Interpreting these losses as Dy intraspecies losses, gives values for the event rate coefficient of $3.4 \times 10^{-25} \text{ cm}^6/\text{s}$ in the presence of K, but only $0.8 \times 10^{-25} \text{ cm}^6/\text{s}$ without K (Sec. 4.7). These observations point to an unknown mechanism, in which K atoms somehow catalyze the decay of Dy

without directly participating in the loss processes. A possible mechanism may be due to elastic collisions with K atoms causing residual evaporation. We tested this in our experiments by recompressing the trap, but did not observe significant changes in the observed loss behavior. Another hypothesis is based on a spatial contraction (density increase) of the Dy cloud caused by strong interaction effects with K atoms. Considering the zero-temperature limit, we have developed a model (Sec. 4.7) for such an effect, but its applicability is questionable at the temperatures of our present experiments. The explanation of the mysterious enhancement of Dy losses induced by K remains a task for future experiments.

4.6 DISCUSSION AND CONCLUSION

Already our present experiments, carried out near quantum degeneracy ($T/T_F^K \approx 0.65$), demonstrate that mass imbalance can make a qualitative difference in the physical behavior of a strongly interacting fermion mixture. The bimodality observed in the hydrodynamic expansion profile of the lighter component is seemingly similar to observations in population-imbalanced spin mixtures near the superfluid phase transition [142]. However, while in the latter case bimodality signals superfluidity, the reason is a different one in our case. Detailed understanding of the expansion dynamics of a Fermi-Fermi mixture in different classical and quantum regimes is thus essential for interpreting the expansion profiles in future work aiming at superfluid regimes. For reaching lower temperatures and deeper degeneracy, work is in progress to eliminate heating in the transfer from low to high magnetic fields and to implement an additional evaporative cooling stage that takes advantage of the large elastic scattering cross section close to the resonance. The experimental challenge is to realize similar degeneracy conditions near the 217-G resonance as we have achieved at a low magnetic field [105]. With some improvements, conditions for superfluid regimes seem to be attainable. To give an example, a Lifshitz point [70, 115] in the phase diagram, where zero momentum pairs become unstable, may be expected at a temperature corresponding to about 15% of the Fermi temperature of the heavy species⁶.

In conclusion, we have shown that the ^{161}Dy - ^{40}K mixture possesses a broad Feshbach resonance offering favorable conditions for experiments on strongly interacting fermion systems with mass imbalance. In particular, the system features a substantial suppression of inelastic losses near resonance, which is a key requirement for many experiments. Novel interaction regimes, including unconventional superfluid phases, seem to be in reach.

⁶ Note that in Ref. [115] temperatures are given in units of a reduced Fermi temperature, which at the Lifshitz point is a factor of 3.4 higher than the Fermi temperature of the heavy species.

4.7 SUPPLEMENTAL MATERIAL

4.7.1 Feshbach Resonance Scenario

To date, no theoretical model is available that would describe the scattering properties of our Dy-K mixture. Our experimental characterization in the region of interest therefore relies on a combination of various observables, like the positions of resonance poles and zero crossings, and measurements of the interspecies thermalization time. Our basic model assumption is a scenario of three partially overlapping s -wave Feshbach resonances.

Wide-range Thermalization Scan

Figure 4.6 shows a thermalization scan over the wide magnetic field range from 155 to 255 G. After evaporatively cooling the mixture at low magnetic fields down to a temperature of about $1.3 \mu\text{K}$, a short period (60 ms) of species-selective parametric heating by trap power modulation was applied to increase the temperature of the 1.4×10^4 K atoms to about $4 \mu\text{K}$, leaving the temperature of the 2.9×10^4 Dy atoms essentially unchanged. For carrying out the measurements in the high-field region, we then quickly (within 12 ms) ramped up the magnetic field to the variable target field, where (partial) thermalization took place. After a hold time of 50 ms, the magnetic field was quickly (within 1 ms) ramped to 235.4 G. At this field, chosen for thermometry, the interspecies interaction is very weak and the sample expands ballistically after release from the trap. Temperatures were measured by standard time-of-flight imaging.

The thermalization scan reveals a scenario dominated by three broad Feshbach resonances, at the centers of which very fast interspecies heat exchange occurs and the temperatures become nearly equal. The corresponding positions are located near 200, 217, and 253 G (see solid arrows in Fig. 4.6). While the first resonance (near 200 G) is quite strong and has considerable overlap with the 217-G resonance (second resonance), the third resonance (near 253 G) is clearly weaker and well separated from the two other ones. Further, much narrower resonances exist (dashed arrows), with negligible effect on the overall scenario. The resonance near 217 G is the strongest one and thus the feature of main interest in our present work.

Model of Three Overlapping Resonances

The magnetic-field dependence of the scattering length in a scenario of overlapping Feshbach resonances, assuming a constant background a_{bg} , can be represented by the product formula [143, 144]

$$a(B) = a_{\text{bg}} \prod_{i=1}^n \frac{B - c_i}{B - p_i}, \quad (4.2)$$

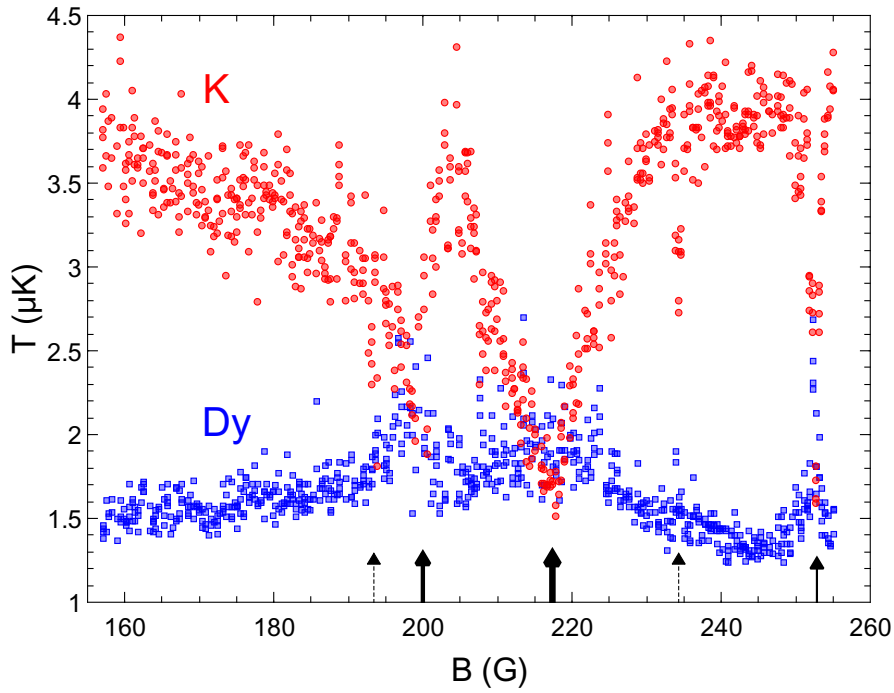


Figure 4.6: Thermalization scan revealing magnetic-field dependent resonances in interspecies elastic scattering. The mixture is initially prepared in a non-equilibrium situation, where the ^{161}Dy component ($1.3\ \mu\text{K}$) is much colder than the ^{40}K component ($4\ \mu\text{K}$). Within a short hold time of 50 ms, interspecies thermalization is observed. Fast thermalization is found to reach essentially equal temperatures at three points (solid arrows), which reveals the existence of three relatively broad Feshbach resonances. Indications of further, much narrower resonances are observed as well (two examples marked by dashed arrows). The broadest resonance, centered near 217 G is the one of main interest for the creation of strongly interacting Fermi-Fermi systems.

where the parameters p_i and c_i denote the positions of the poles and zero crossings, respectively. A straightforward transformation gives the equivalent sum formula [144]

$$a(B) = a_{\text{bg}} \left(1 - \sum_{i=1}^n \frac{\delta_i}{B - p_i} \right) \quad (4.3)$$

with

$$\delta_i = (c_i - p_i) \prod_{j \neq i}^n \frac{c_j - p_i}{p_j - p_i}. \quad (4.4)$$

A practical advantage of the product formula is that it explicitly contains the positions c_i of the zero crossings, which are often good observables in an experiment [145, 146]. An advantage of the sum formula is that the parameters δ_i provide a measure for the relative strengths of the different resonance contributions. In the case of a single, isolated resonance $\delta_1 = c_1 - p_1$ corresponds to the common definition [32] of the Feshbach resonance width.

Determination of Poles and Zero Crossings

The poles (zero crossings) associated with Feshbach resonances can be identified as points of fastest (slowest) thermalization in scans like the one shown in Fig. 4.6. We have carried out further scans with higher resolution in narrower magnetic field ranges near the resonance centers, and obtained values $p_1 = 200.1(2)$ G and $p_2 = 217.27(15)$ G for the poles of the two broadest resonances. Here, because of the fast thermalization, we used short hold times of 50 ms (15 ms) for the determination of p_1 (p_2).

For the observation of zero crossings, close to which thermalization is very slow, long hold times are favorable. In a scan with a hold time of 1.2 s, we determined the position $c_1 = 203.0(2)$ G for the zero crossing between the poles p_1 and p_2 .

The third resonance (near 253 G) is found in a region where the local background scattering length is very small. This is a consequence of the near cancellation of the the global background scattering length a_{bg} by the effect of the two broad resonances. While the pole position p_3 can be determined in a straightforward way from the point of fastest thermalization, a determination of the two zero crossings c_2 and c_3 solely based on the observation of thermalization minima turns out to be rather inaccurate. We therefore investigated thermalization in a wide range covering c_2 , p_3 , and c_3 and analyzed the resulting data based on the model introduced in Ref. [147] and applied to our mixture in [105] (see also Sec. 4.7.1).

The model is based on the assumption of thermalization described by an exponential decrease of the temperature difference with increasing hold time, with a relaxation rate being proportional to the elastic scattering cross section and thus

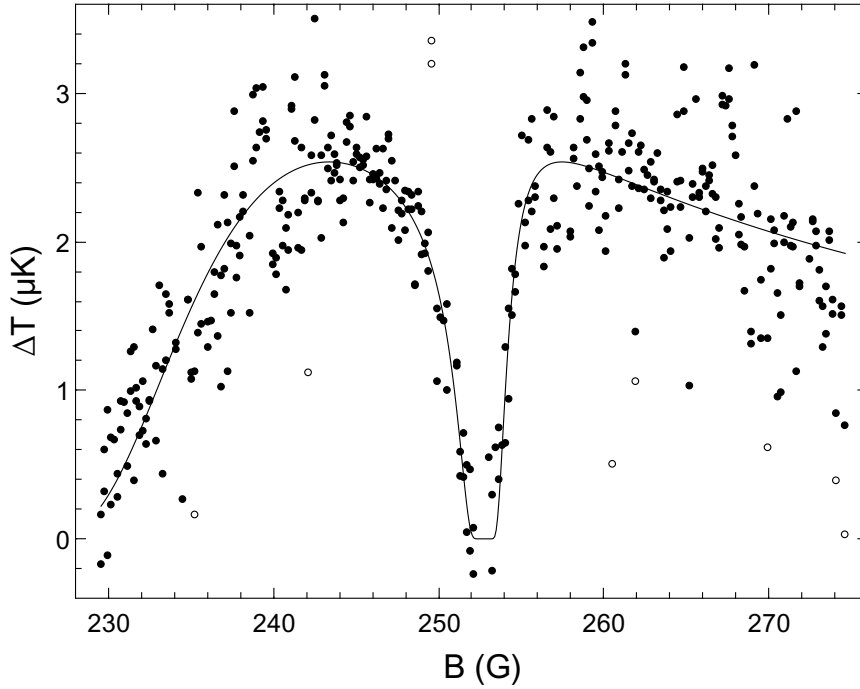


Figure 4.7: Thermalization scan in the region of the third resonance. The temperature difference ΔT was measured for a long hold time of 1.2 s. The solid line represents a fit based on the thermalization model described in the text, from which we obtain the pole position (minimum of ΔT) and the positions of the two neighboring zero crossings (maxima). Note that we have applied a rejection algorithm based on repeated application of Chauvenet's criterion [148] to reduce the effect of outliers and barely resolved narrow Feshbach on the fit. This removed 17 data points (open symbols) of in total 393 data points and resulted in very robust parameter values.

being proportional to $a^2(B)$. The temperature difference $\Delta T = T_K - T_{Dy}$ can then be written as a function of the magnetic field strength,

$$\Delta T(B) = \Delta T_0 \exp[-Ca^2(B)], \quad (4.5)$$

where ΔT_0 is the initial temperature difference. The parameter C is proportional to the hold time and further determined by a combination of the experimental parameters, as described in Refs. [105, 147].

The measurements in Fig. 4.7 were taken in a wide range between 229 and 275 G under similar initial conditions as in Fig. 4.6, but with a much longer hold time of 1.2 s. Thermometry was performed in the same way as in Fig. 4.6. We fitted the data based on the thermalization model [Eq. (4.5)] and the product formula [Eq. (4.2)] for $a(B)$. The parameters p_1 , p_2 , and c_1 were fixed to their separately determined

Table 4.1: Parameters characterizing the scenario of three overlapping resonances. The given 1σ uncertainties include the fit errors and estimates for model-dependent errors. Additional magnetic-field uncertainties from the calibration and from day-to-day fluctuations are estimated on the order of 0.1 G.

| i | p_i (G) | c_i (G) | δ_i (G) |
|-----|------------|-----------|----------------|
| 1 | 200.1(2) | 203.0(2) | 7.9(7) |
| 2 | 217.27(15) | 243.4(4) | 24.6(6) |
| 3 | 252.79(8) | 257.5(4) | 1.2(1) |

values (see above discussion). The fit (solid curve in Fig. 4.7) yielded the parameter values $p_3 = 252.79(8)$ G, $c_2 = 243.4(4)$ G, and $c_3 = 257.5(4)$ G.

The complete set of resonance parameters p_i and c_i for our three-resonance model is summarized in Table 4.1. Based on Eq. (4.4), we also calculated the parameters δ_i , which characterize the strengths of the resonances. The resulting values (last column) confirm that the second resonance is the strongest one. The first resonance is about three times weaker, and the third resonance is about 20 times weaker than the strongest one.

Background Scattering Length

Having determined the poles and zero crossings describing our three-resonance scenario, the remaining task is to determine the background scattering length a_{bg} , which is left as the only unknown quantity in Eqs. (4.2) and (4.3). For this purpose, we carried out thermalization measurements in a similar way as described in Ref. [105]. We selected magnetic field regions, where thermalization takes place on experimentally convenient timescales and which are free of narrow Feshbach resonances, and determined the absolute values $|a(B)|$ of the scattering length for nine different values of the magnetic field strength. The corresponding signs uniquely follow from our three-resonance model. In this way, we obtained the nine measured values shown in Fig. 4.8. We finally fitted Eq. (4.2) to these data points with a_{bg} being the only free parameter. This yields the value of $a_{\text{bg}} = +59(3) a_0$, where the given uncertainty includes the fit error and the effect of the uncertainties in the resonance parameters p_i and c_i .

We estimate that systematic uncertainties in the experimental parameters (mainly uncertainties in the atom numbers and trap frequencies) and model-dependent errors result in an additional relative uncertainty of 15%, which dominates the error budget. Therefore, our final result for the background scattering length in the 200-G region is $a_{\text{bg}} = +59(9) a_0$. It is interesting to note that our previous measurement [105], which was carried out at a low magnetic field of 430 mG, gave

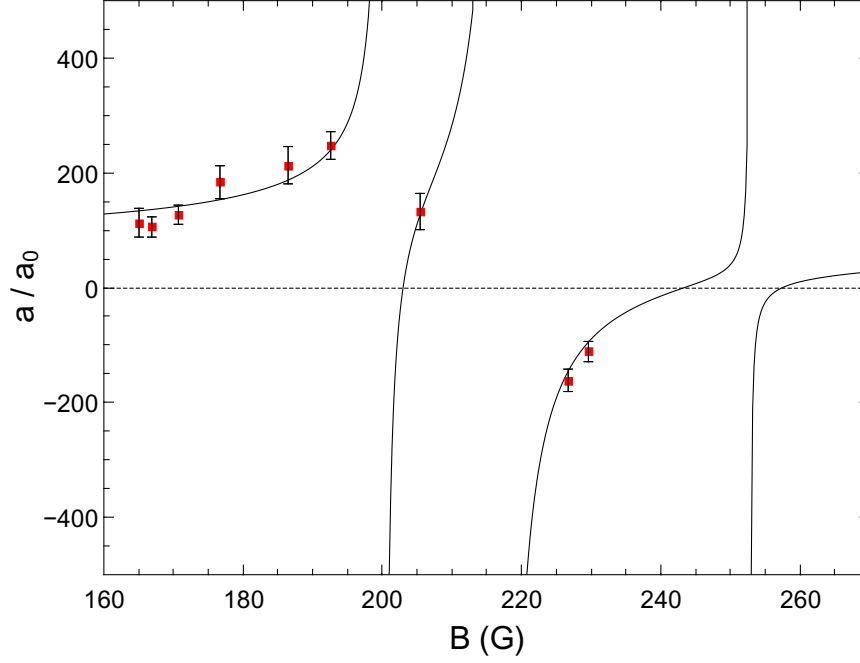


Figure 4.8: Magnetic-field dependence of the scattering length in the range of interest. The solid lines represent our model of three overlapping Feshbach resonances, with all parameters being determined experimentally. The experimental data points result from measurements of the scattering cross section by interspecies thermalization.

essentially the same value ($|a_{bg}| \approx 60 a_0$), although the background scattering length may slowly vary with the magnetic field.

Analysis of Thermalization Measurements

The basic idea of our cross-species thermalization measurements to determine the Dy-K elastic scattering cross section (see example in Fig. 4.9) is the same as reported in [105], but here we have to deal with the additional complication that strong Dy losses occur during the thermalization process.

Our model was originally introduced in [147] and can be expressed in terms of a differential equation for the temperature difference $\Delta T = T_K - T_{Dy}$,

$$\frac{d}{dt} \Delta T = -\sigma_{el}^2 \frac{\zeta q}{3\pi^2} \frac{m_{Dy} \bar{\omega}_{Dy}^3}{k_B T_{Dy}} (N_{Dy} + N_K) \Delta T, \quad (4.6)$$

where $\sigma_{el} = 4\pi a^2$ is the cross section for elastic Dy-K collisions and

$$\zeta = 4m_{Dy}m_K / (m_{Dy} + m_K)^2 \quad (4.7)$$

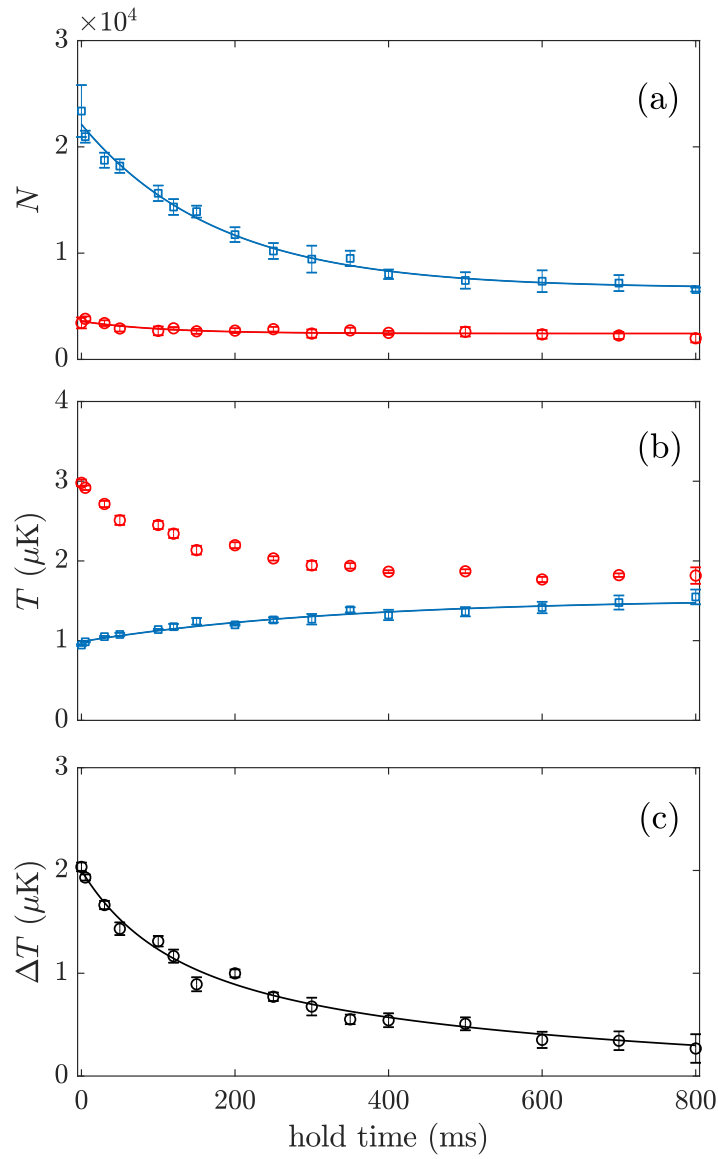


Figure 4.9: Example for cross-species thermalization ($B = 229.5$ G) and the fit analysis to extract a value for $|a|$. (a) Observed time evolution of the atom numbers N_{Dy} (blue open squares) and N_{K} (red open circles) together with fits by simple exponential functions with a constant offset. (b) Time evolution of the temperatures T_{Dy} and T_{K} ; the increasing Dy temperature is again fitted by a simple heuristic model function. (c) Evolution of the temperature difference $\Delta T = T_{\text{K}} - T_{\text{Dy}}$ with a numerical fit based on Eq. (4.6).

accounts for the effect of mass imbalance in the collisional energy transfer. The factor q depends on the ratio of polarizabilities, masses, and temperatures [105]. Under our experimental conditions, this factor can be well approximated by a constant $q = 1.45$.

A typical data set for the time evolution of the atom numbers N_{Dy} , N_{K} and the temperatures T_{Dy} , T_{K} is shown in Fig. 4.9(a) and (b). As a first step in the analysis, we independently fit the observed decay of N_{Dy} , the slow decrease of N_{K} , and the increase in T_{Dy} with simple exponential model functions, which we generally find to describe the data well. As a second step, we fit a numerical solution of Eq. (4.6) to the decreasing temperature difference ΔT , with the evolution of T_{Dy} and $N_{\text{Dy}} + N_{\text{K}}$ described by the fit functions obtained before. Figure 4.9(c) illustrates that the fit with the two free parameters σ_{el} and ΔT_0 matches the experimental data very well. For our specific example ($B = 229.5 \text{ G}$, $\bar{\omega}_{\text{Dy}}/2\pi = 180 \text{ Hz}$), we obtain a best estimate for σ_{el} corresponding to $|a| = 87 a_0$.

217-G Resonance: Strength and Universal Range

For the experiments described in the main text, we are mainly interested in the interspecies scattering length near the pole of the 217-G resonance. Here, the scattering length can be well approximated by

$$a(B) = -\frac{A}{B - B_0} a_0, \quad (4.8)$$

where $B_0 = p_2 = 217.27(15) \text{ G}$ and $A = \delta_2 a_{\text{bg}}/a_0 = +1450(230) \text{ G}$.

For discussing the character of this Feshbach resonance in terms of entrance-channel or closed-channel dominated behavior [32], it is useful to introduce a characteristic length as defined by the range parameter [109]

$$R^* = \frac{\hbar^2}{2m_r a_0 \delta\mu A}. \quad (4.9)$$

Here $m_r = 32.04 \text{ a.m.u.}$ is the reduced mass and $\delta\mu$ the (unknown) differential magnetic moment. The universal range of a Feshbach resonance is reached if $|a| \gg R^*$, which also represents a necessary condition for a strong Pauli suppression of few-body losses [81].

The properties of the molecular states underlying our Feshbach resonances are currently unknown and require further in-depth investigation. For now, to get an idea of the universal range, we use a conservative guess for the differential magnetic moment $\delta\mu = 0.1 \mu_{\text{B}}$, where μ_{B} is Bohr's magneton. This yields $R^* \approx 300 a_0$ as a conservative estimate for the range parameter. We thus conclude that the universality condition $|a| \gg R^*$ is rather easy to fulfill near the pole of our 217-G Feshbach resonance. We note that also the many-body condition $k_F R^* \ll 1$ for universality in a fermionic system (Fermi wave number k_F) is well fulfilled under realistic conditions.

4.7.2 Decay

Overview of Losses in the Resonance Region

The loss scan in Fig. 4.10 presents an overview of the complex magnetic-field dependence of losses in the region of the 217-G resonance. Here the number of Dy and K atoms was recorded after a hold time of 150 ms in the trap at a constant magnetic field. Interspecies losses show up as correlated features in the loss spectra of both species.

A broad loss feature appears for both species about 0.5 G below the resonance center, where we estimate a scattering length of roughly $+3000 a_0$. This feature resembles observations made in spin mixtures of ${}^6\text{Li}$ [39, 131, 132] and ${}^{40}\text{K}$ [130] and indicates the formation of weakly bound dimers, which after secondary collisions decay to deeply bound molecular states. The fact that such losses appear not at the center of the resonance, but on the side with large positive scattering length, is intrinsic to two-component fermion systems near broad Feshbach resonances with strong Pauli suppression of inelastic few-body processes.

The loss spectrum also reveals several narrow interspecies features. Some of them appear as resolved resonances, but other structures rather resemble a fluctuating background. In between features of increased losses, good regions can be identified where the lifetime exceeds 100 ms. Besides interspecies losses, we have observed intraspecies losses for Dy. This can be seen from the background atom number ($N_{\text{Dy}} \approx 9500$) in Fig. 4.10, which is a factor of 2.5 below the initial atom number. These Dy losses generally show a fluctuating background behavior, as observed in [126].

From the timescale of losses (on the order of 100 ms), we conclude that recombination processes are no problem for experiments on short time scales (typically below 10 ms), such as the hydrodynamic expansion studied in the main text. For experiments on longer timescales, however, it may be important to choose good spots, where both intraspecies and Dy interspecies losses are minimized. The data of Fig. 5 in the main text were recorded on such a spot at 217.5 G.

Model for Fitting Decay Curves

For extracting three-body rate coefficients from atom number decay curves, one has to take into account the heating of the sample [38]. Our simple model to avoid this complication is based on the initial behavior near $t = 0$, which can be characterized by the initial number $N_0 = N(t = 0)$ and the initial decay rate $1/\tau = -\dot{N}(0)/N(0)$. To extract optimum values for these parameters from a fit to the observed decay, we follow a heuristic approach based on the differential equation

$$\frac{\dot{N}}{N_0} = -\frac{1}{\tau} \left(\frac{N}{N_0} \right)^\alpha, \quad (4.10)$$

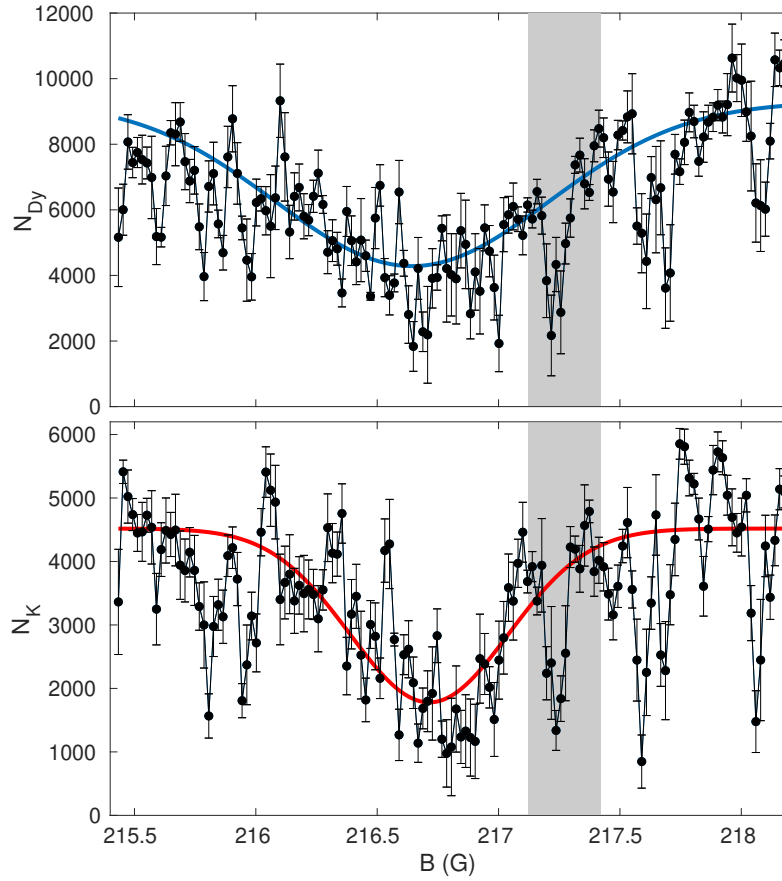


Figure 4.10: Loss scan in the resonance region. The plots show the number of Dy atoms (upper panel) and K atoms (lower panel) left in the trap ($\bar{\omega}_{\text{Dy}} = 2\pi \times 130 \text{ Hz}$) after a hold time of 150 ms at a fixed magnetic field. The initial atom numbers are $N_{\text{Dy}} = 24\,000$ and $N_{\text{K}} = 6\,000$, and the initial temperature is $T = 500 \text{ nK}$. The solid lines are Gaussian fits to the broad loss feature, excluding narrow loss features. The shaded region indicates the 1σ -uncertainty in our knowledge of the pole position of the strong 217-G resonance.

where the phenomenological exponent α is a fit parameter, which absorbs possible heating and other effects. We find that the solution

$$N(t) = \frac{N_0}{\alpha^{-1} \sqrt{1 + (\alpha - 1) t/\tau}} \quad (4.11)$$

fits our loss curves for all single- and mixed-species cases very well and is thus applied to all cases discussed in the present work. The calculation of rate coefficients is then based on the values for the fit parameters N_0 and τ .

Decay of K in the Mixture

Here we analyze losses of K observed in the Dy-K mixture in terms of three-body processes and extract upper limits for the corresponding rate coefficients. Three-body decay of K alone is known to be very weak and can be neglected here.

We first assume that losses are caused by processes involving one K and two Dy atoms. This leads to the loss equation

$$\dot{N}_K = -K' \int d^3r n_K n_{\text{Dy}}^2. \quad (4.12)$$

We approximate the number density distributions n_i ($i = \text{K}, \text{Dy}$) in the harmonic trap (mean frequencies $\bar{\omega}_i$) by thermal Gaussian distributions with spatial widths $\sigma_i = \bar{\omega}_i^{-1} \sqrt{k_B T / m_i}$. After integration we obtain

$$\frac{\dot{N}_K}{N_K} = -K' N_{\text{Dy}}^2 \left(\frac{\sigma'}{2\pi\sigma_K\sigma_{\text{Dy}}} \right)^3, \quad (4.13)$$

where $\sigma' = (\sigma_K^{-2} + 2\sigma_{\text{Dy}}^{-2})^{-1/2}$.

In an analogous way, we now assume that losses are caused by processes involving two K atoms and one Dy atom (two K atoms lost per event). This leads to the loss equation

$$\dot{N}_K = -2K'' \int d^3r n_K^2 n_{\text{Dy}}, \quad (4.14)$$

which after integration simplifies to

$$\frac{\dot{N}_K}{N_K} = -K'' N_K N_{\text{Dy}} \left(\frac{\sigma''}{2\pi\sigma_K\sigma_{\text{Dy}}} \right)^3, \quad (4.15)$$

where $\sigma'' = (2\sigma_K^{-2} + \sigma_{\text{Dy}}^{-2})^{-1/2}$.

To obtain values (upper limits) for the event rate coefficients, we analyze the decay curves displayed in Fig. 5(a) in the main text. By using the above fit model, we extract values for the initial K decay time $\tau = -N_K / \dot{N}_K = 350(150)$ ms, the initial K atom number $N_K = 3100(200)$, and the initial Dy atom number $N_{\text{Dy}} = 16\,700(400)$.

From Eqs. (4.13) and (4.15) and the experimental parameters ($\omega_{\text{Dy}} = \omega_{\text{K}}/3.6 = 2\pi \times 130 \text{ Hz}$, $T = 540 \text{ nK}$) we finally obtain

$$K' \approx 4 \times 10^{-25} \text{ cm}^6/\text{s} \quad (4.16)$$

$$K'' \approx 3 \times 10^{-25} \text{ cm}^6/\text{s} \quad (4.17)$$

as upper limits for the interspecies three-body event rate coefficients.

Decay of Dy

Here we analyze the observed Dy decay (data shown in Fig. 5 of the main text) under the assumption that these losses are caused by collisions of three Dy atoms. The corresponding loss equation reads

$$\dot{N}_{\text{Dy}} = -3K_3 \int d^3r n_{\text{Dy}}^3, \quad (4.18)$$

which after integration simplifies to

$$\frac{\dot{N}_{\text{Dy}}}{N_{\text{Dy}}} = -3K_3 N_{\text{Dy}}^2 \left(\frac{1}{2\pi\sqrt{3}\sigma_{\text{Dy}}^2} \right)^3. \quad (4.19)$$

From the fit to the Dy decay shown in Fig. 5(a) of the main text, we extract $\tau = 320(50) \text{ ms}$ and $N_{\text{Dy}} = 16700(400)$ and obtain the value

$$K_3 = 3.4(5) \times 10^{-25} \text{ cm}^6/\text{s} \quad (4.20)$$

for the event rate coefficient. Analyzing the data in Fig. 5(b) of the main text in the same way, with the fit yielding $\tau = 1000(150) \text{ ms}$ and $N_{\text{Dy}} = 19700(400)$, we obtain the value

$$K_3 = 8.1(1.2) \times 10^{-26} \text{ cm}^6/\text{s}. \quad (4.21)$$

The fact that the former value (with K present) is about four times larger cannot be explained by three-body loss events involving K atoms, as their contribution is too weak. However, our data show that K atoms somehow catalyze Dy losses. The underlying mechanism is currently not understood.

4.7.3 *Interaction-induced Contraction*

Here we introduce a model that describes the contraction of the mixture induced by the resonant interaction in the unitarity limit under the assumption of zero temperature. The results point to a possible mechanism how the presence of K atoms can enhance three-body losses in the Dy component.

Theoretical Model

We calculate the number density distributions $n_{\text{Dy}}(r)$ and $n_{\text{K}}(r)$ of the trapped interacting species in the Thomas-Fermi limit, in which kinetic energy terms related to density variations can be neglected and the local density approximation can be applied. This also allows us to reduce the situation to a spherical trap; the solutions can then be scaled to the real, anisotropic trap.

The functional for the total energy can be written as

$$E = \int d^3r (U_{\text{Dy}}n_{\text{Dy}} + U_{\text{K}}n_{\text{K}} + \epsilon_{\text{Dy}} + \epsilon_{\text{K}} + \epsilon_{\text{int}}), \quad (4.22)$$

where $U_{\text{Dy}}(r) = \frac{1}{2}m_{\text{Dy}}\bar{\omega}_{\text{Dy}}^2 r^2$ represents the Dy trap potential and

$$\epsilon_{\text{Dy}} = \frac{3}{10}(6\pi^2)^{2/3} \frac{\hbar^2}{m_{\text{Dy}}} n_{\text{Dy}}^{5/3} \quad (4.23)$$

denotes the kinetic energy density of Dy without interaction. For the K component, U_{K} and ϵ_{K} are defined analogously.

For the interaction energy density we use the approximation

$$\epsilon_{\text{int}} = -b \times \frac{3}{10}(6\pi^2)^{2/3} \frac{\hbar^2}{2m_{\text{r}}} \frac{n_{\text{Dy}}n_{\text{K}}}{(n_{\text{Dy}}^2 + n_{\text{K}}^2)^{1/6}}. \quad (4.24)$$

This expression was introduced in [114] to fit the equation of state of a non-superfluid mass-balanced system [149]. Remarkably, we noticed that the same expression also provides a very good fit to the equation of state for the imbalanced mixture with mass ratio 40/6, which was published in [150]. The only difference seems to be a slight difference in the optimum value of the prefactor b . While $b = 1.01$ provides an optimum fit for the mass-balanced case [114], we found the slightly higher value $b = 1.04$ for the mass-imbalanced (40/6) case. In the representation of Eq. (4.24), the interaction term seems to be nearly independent of the mass ratio. Therefore, we are confident that it can be readily applied also to our mass ratio of 161/40.

The number density distributions $n_{\text{Dy}}(r)$ and $n_{\text{K}}(r)$ are found by minimizing the energy functional. This is done by varying the densities with the gradient descent method under the constraint that the atom numbers N_{Dy} and N_{K} are fixed. We represent the densities on a spatial grid, of which the step size is below 10^{-3} of the typical Thomas-Fermi radius of the clouds. The number of iterations in the minimization algorithm guarantees a relative precision of 10^{-4} for number densities and derived quantities.

Density Increase and Loss Enhancement

Figure 4.11 shows the effect of interaction for $N_{\text{K}}/N_{\text{Dy}} = 0.12$, which has been chosen to demonstrate that even a small fraction of K atoms can have a considerable

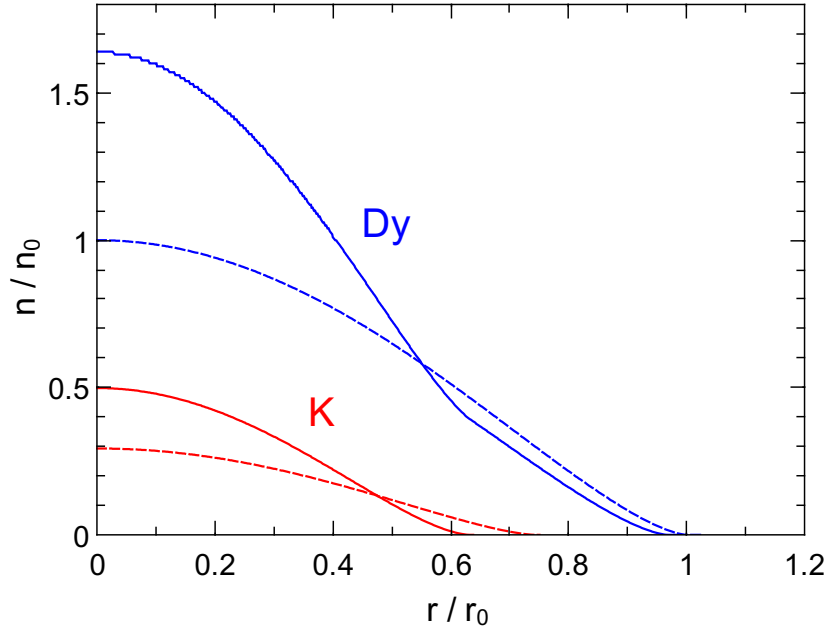


Figure 4.11: Radial density distributions for the Dy and K components, with (solid lines) and without (dashed lines) interaction for a number ratio $N_K/N_{\text{Dy}} = 0.12$. All profiles are normalized to the quantities r_0 and n_0 , which represent the Thomas-Fermi radius and the central density of the non-interacting Dy component, respectively.

effect. The interaction-induced contraction is clearly seen in profiles. The central Dy (K) density is increased by a factor of 1.64 (1.70). To quantify the total enhancement of three-body decay of Dy and K within the whole trap, we relate the total three-body decay rate to the case without interspecies interaction (Thomas-Fermi profile n_{TF}), and define the corresponding factors

$$\beta_i \equiv \frac{\int d^3r n_i^3(\mathbf{r})}{\int d^3r n_{\text{TF},i}^3(\mathbf{r})}, \quad (4.25)$$

where $i = \text{Dy}, \text{K}$. These factors can describe both the effect of attractive ($\beta > 1$) or repulsive ($\beta < 1$) interaction in the mixture, but here we focus on the case of the strong attraction on resonance. By numerical integration of the cubed density profiles of the two species we obtain $\beta_{\text{Dy}} = 2.07$ and $\beta_{\text{K}} = 2.85$. It is remarkable that the presence of a relatively small minority component of K can have such a large effect on the profile and thus three-body recombination rate of the majority component of Dy.

Within the assumptions of our model, the enhancement factor depends only on the atom number ratio N_K/N_{Dy} and the trap frequency ratio $\bar{\omega}_K/\bar{\omega}_{\text{Dy}}$. Since, in our experiments, the latter is fixed to a value of 3.6, we can draw universal curves

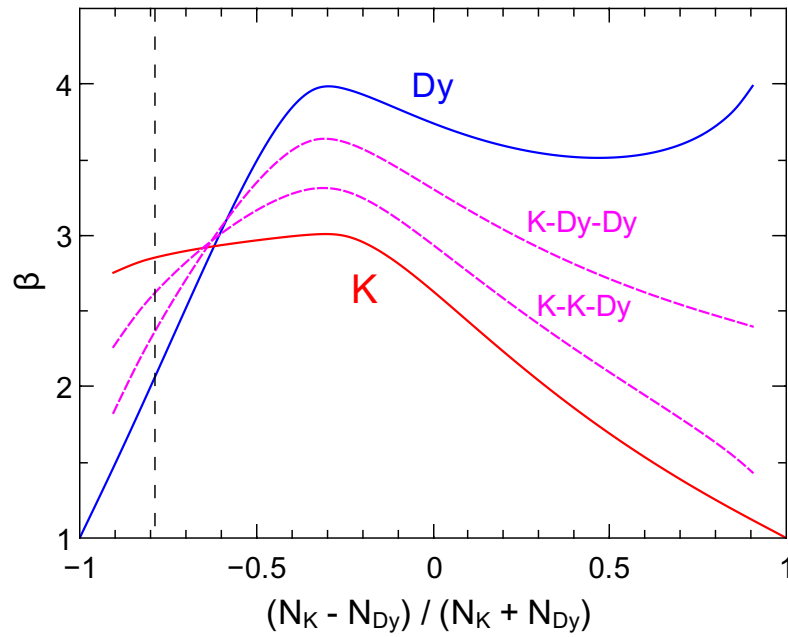


Figure 4.12: Enhancement factors for three-body recombination as a function of the global polarization. The solid curves refer to intraspecies three-body collisions of Dy and K, while the dashed curves refer to interspecies processes involving both atoms. The vertical dashed line corresponds to the situation shown in Fig. 4.11.

for β_{Dy} and β_{K} as a function of the global polarization $(N_{\text{K}} - N_{\text{Dy}})/(N_{\text{K}} + N_{\text{Dy}})$; see Fig. 4.12. The solid line that represents the Dy case shows a maximum value of about $\beta_{\text{Dy}} = 4$ for a polarization of -0.7 ($N_{\text{K}}/N_{\text{Dy}} = 0.54$), which highlights the possible strength of the effect.

MONTE CARLO SIMULATIONS FOR HYDRODYNAMIC MIXTURES

For our goal to realize a strongly interacting Fermi-Fermi mixture, extensive Feshbach scans were performed to find suitable broad interspecies Feshbach resonances, as for example described in our previous publications in Chapter 4 or Ref. [151]. An indication of strong interactions was observed when switching off the trap and letting the two species expand freely at the center of a Feshbach resonance. Contrary to the non-interacting case, the expansion is slowed for potassium and the size of the two clouds after expansion was similar, hinting at a hydrodynamic behavior. However, density and temperature of the samples precluded an explanation in terms of superfluid hydrodynamics, instead we expected the behavior to be the result of a large number of collision events, so-called collisional hydrodynamics. To better understand our system and test this hypothesis, a numerical simulation of the system was developed. Direct simulation Monte Carlo (DSMC) [152–154] and molecular dynamics (MD) schemes [155, 156] have been used extensively to investigate the behavior of gaseous and liquid systems and connected engineering problems [157–161], in biochemistry [162], and recently also in the context of ultracold atomic gases [129, 163–165]. Here, we have used a modified version of these approaches as a test model to better understand our particular problem. In this chapter the general working principle of the simulation is explained and compared to other DSMC algorithms. Furthermore, its behavior is characterized and possible extensions and limitations are discussed.

5.1 SIMULATION MODEL

The goal of the simulation is to show that a simple short-range two-body collision model as described in Chapter 3 can reproduce the observed hydrodynamic behavior. To this end, the simulation models the interaction of particles as collisions of hard spheres. This simple model is enough to reproduce behavior like thermalization, hydrodynamic expansion, or other in-trap dynamics in real systems, which can be used as a reference. In this section, the employed methods and details of the simulation will be explained and some simple validation tests are performed.

5.1.1 General Method

We consider the evolution of an ensemble of particles in the normal phase. For our double-species experiment the real-space and velocity-space evolution is described by a phase space density f_i for each species $i \in \{\text{K, Dy}\}$ that satisfies the space-homogeneous Boltzmann equation

$$\frac{\partial f_i}{\partial t} + \mathbf{v} \nabla_{\mathbf{r}} f_i = I_{\text{coll}}(f_i, f_j). \quad (5.1)$$

Here, $f_i(\mathbf{r}, \mathbf{v}, t)$ is the phase space density at position \mathbf{r} and velocity \mathbf{v} at time t . The collision properties of the system enter in the collision integral $I_{\text{coll}}(f_i, f_j)$. Since exact solutions to the Boltzmann equation only exist in some cases, different numerical and approximation approaches have been developed for this problem, see for example Ref. [166] and references therein.

The basic principle of the numerical treatment of the Boltzmann equation with molecular dynamics (MD) [155] and direct simulation Monte Carlo (DSMC) schemes [153] is that the computation of one time step Δt can be split into two processes. In the absence of collisions, Eq. (5.1) reduces to the equation of motion

$$\frac{\partial f_i}{\partial t} + \mathbf{v} \nabla_{\mathbf{r}} f_i = 0, \quad (5.2)$$

which can be solved analytically in free space. Then, the contribution of collisions can be included as a second step by calculating the collision integral

$$I_{\text{coll}}(f_i, f_j) = \int d^3 v_j \int d\Omega \frac{d\sigma}{d\Omega} |\mathbf{v}_i - \mathbf{v}_j| (f'_i f'_j - f_i f_j). \quad (5.3)$$

It describes elastic collisions between two particles with initial velocities \mathbf{v} and final velocities \mathbf{v}'_i , the phase space density after the collision $f'_i = f_i(\mathbf{r}, \mathbf{v}'_i, t)$, and a differential cross section $\frac{d\sigma}{d\Omega}$. This split step method is a valid assumption, as long as Δt is much smaller than the mean time between collisions. However, the computation of $I_{\text{coll}}(f_i, f_j)$ can be costly.

One possibility to facilitate the calculation of Eq. (5.3) is to sample f with individual particles, which can interact with each other. In this so-called test particle method, each particle is represented by a position vector \mathbf{r} and a velocity vector \mathbf{v} , the values of which are initialized with a random number generator reproducing f .¹ Then, for each time step, first, the new position coordinates and velocities are calculated for each particle. In the free expansion case, the new position is simply given by

$$\mathbf{r}(t + \Delta t) = \mathbf{r}(t) + \mathbf{v} \Delta t, \quad (5.4)$$

¹ Depending on the shape of f , this can be done with a uniform random number generator, a Gaussian random number generator or the acceptance-rejection method [167].

and the velocities remain unchanged because of the lack of any potential gradients. This step can be changed to include the influence of gravity and optical or magnetic potentials.

In the second step, the collision process is modeled. In our special case, we only consider short-range interactions between atoms from different species, since intraspecies interactions are suppressed for fermions at low temperatures.² The collision of two atoms itself is modeled as the fully elastic s -wave collision of two hard spheres, by transforming their velocities into the center-of-mass (CoM) system $\mathbf{v}_{i,\text{CoM}} = \mathbf{v}_i - \mathbf{v}_{\text{CoM}}$, and rotating the CoM velocities into a random direction by multiplying with the random unit vector \mathbf{e}_R . The velocity vectors after the collision are then given by

$$\mathbf{v}'_K = \mathbf{v}_{\text{CoM}} + \mathbf{e}_R v_{K,\text{CoM}}, \quad (5.5)$$

and

$$\mathbf{v}'_{\text{Dy}} = \mathbf{v}_{\text{CoM}} - \frac{m_K}{m_{\text{Dy}}} \mathbf{e}_R v_{K,\text{CoM}}, \quad (5.6)$$

where

$$\mathbf{v}_{\text{CoM}} = \frac{m_K \mathbf{v}_K + m_{\text{Dy}} \mathbf{v}_{\text{Dy}}}{m_K + m_{\text{Dy}}}. \quad (5.7)$$

This collision process is isotropic, and energy and momentum conserving. However, it does not include any quantum statistical effects (like Pauli blocking), which is a good approximation for our thermal or only near-degenerate system.³

Selection of Collision Pairs

Test particle simulation models used to compute the Boltzmann equation are usually divided in how they select the collision pairs. In our particular problem we treat the atoms as hard spheres with a size given by the collisional cross section. At strong interactions, e.g. close to or at the center of a Feshbach resonance, we have to use the finite relative momentum limited quantum mechanical cross section

$$\sigma = \frac{4\pi a^2}{1 + a^2 k^2}, \quad (5.8)$$

where a is the interspecies scattering length and $k = \mu v_r / \hbar$ is the relative momentum of the collision pair, with reduced mass μ and relative velocity v_r .

² In the case of K, the relevant temperature for p -wave collisions is $k_B T_p = \hbar^2 / m r_0^2 \approx k_B \times 300 \mu\text{K}$ [107], consequently these collisions are suppressed at the typical temperatures of the experiment. In the case of fermionic Dy, because of universal dipole scattering [87, 89], the intraspecies cross section is $\sigma_{\text{D,Dy}} = \frac{32\pi}{15} a_{\text{D,Dy}}^2 = 7.2 \times 10^{-16} \text{ m}^2$, with $a_{\text{D,Dy}} = 195 a_0$ [105, 168], which is much smaller than the typical cross section near an interspecies Feshbach resonance.

³ The relevant temperature scale for this is the Fermi temperature T_F . At our typical experimental conditions T_F is on the order of 100 nK, well in the regime where s -wave interactions are dominating.

In MD simulations [155] with hard sphere interactions the motion of the particles is tracked and a collision is happening if the relative distance between two particles is smaller than the radius of the cross section. This results in the requirement

$$|\mathbf{r}_i - \mathbf{r}_j| < 2 \frac{a}{\sqrt{1 + a^2 k^2}}, \quad (5.9)$$

where $\mathbf{r}_{i,j}$ is the position of the particles. Typically, to determine when and between which particles the next collision is happening, the points in time of closest approach are calculated for each possible pair. Between collisions the particles can move freely, so the particle motion is propagated to the closest of these points in time and if the collision condition is satisfied, the collision is performed. Then the next collision pair is determined. For each time step, this calculation has to be done for each possible pair, subsequently the computational effort scales as $\mathcal{O}(N^2)$, with N being the number of simulated particles. In our two species experiment this would lead to $N_K \times N_{Dy}$ calculations, which is impractical for large atom numbers. The advantage of MD simulations on the other hand is that they do not require many assumptions but are still able to reproduce the correct behavior of the gas.

In contrast, the DSMC method [153] employs a probabilistic approach. The coordinate space is divided into a grid of cells. If one limits the size of the cells to be smaller than the mean free path, instead of checking individually which pairs can collide, a statistically expected collision rate can be computed for each cell and the corresponding amount of collisions per timestep is performed randomly among the pairs of a cell. With this probabilistic approach it is not necessary to check all individual pairs, which greatly improves the computational scaling to $\mathcal{O}(N)$. However, as the variation of the collision rate is coarse-grained by the cell size, so is the resolution of processes that depend on the collision rate. This can limit the accuracy of DSMC results, especially when density and local collision rate vary over the sample [169–171]. Several elaborate schemes have been introduced to combat this, for example by introducing locally adaptive cell sizes and time steps [164].

As the DSMC approach relies on theoretical predictions to infer the number of collisions per cell and timestep, and we want to reproduce the behavior or the experiment without many assumptions, we have chosen an approach similar to the more fundamental MD method. Instead of calculating the point in time for the next collision, we use a constant timestep. For each timestep we check condition (5.9), but by assuming that only pairs of particles collide that are near each other, the volume can be divided into smaller cells into which the atoms get sorted [172]. Then, only pairs of atoms inside a particular cell have to be checked for the collision condition, which greatly reduces the number of required operations.

This approach is only valid if $\sqrt{\sigma}$ is smaller than the physical extent of the system. Furthermore, it may miss collisions of particles close to the cell border, which leads to a smaller collision rate. This issue can be partly solved by adding

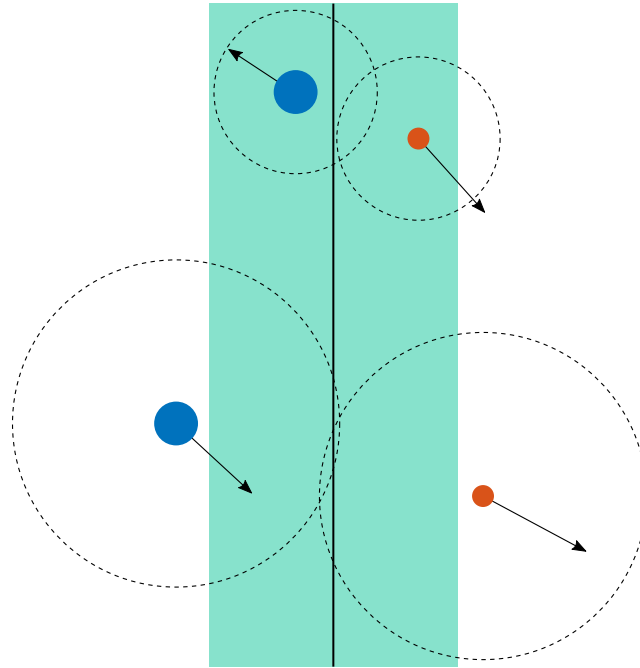


Figure 5.1: Schematic of the collision detection and cells. Dy (blue) and K (red) atoms can collide if their spheres with radius calculated from Eq. (5.8) (dashed circles) overlap. Checking all possible pairs of the two ensembles is very expensive. Dividing the space into cells (vertical line) and only checking pairs in those cells is more efficient, however collisions on the border can be missed. This can be circumvented by overlapping the cells (teal area). Still then it is possible that pairs outside the overlap, which have a low relative velocity and therefore a large cross section, are missed.

an overlap to the cells (see Fig. 5.1) that is on the order of the mean of $\sqrt{\sigma}$. At low scattering length, where the influence of the relative momentum term is small, this approach works well, however, when it becomes significant, the overlap can soon become larger than the cell size and even the sample size, which again degrades the performance. In practice we adapt the number of cells (and therefore their size) such that the overlap does not exceed the cell size. In extreme cases this can mean that only one cell is used.

Even with cell division, in some cases the atom number in the experiment might be so high that the computation time becomes infeasibly long. In this case, a macro-particle approach is useful. Each of the N_{sim} simulated particles then represents s atoms, where $s = N/N_{\text{sim}}$ is the scaling parameter between experiment and simulation.⁴ This approach speeds up the simulation on the order of s^2 , because

⁴ It should also be added that in low atom number systems, $s \ll 1$ can be used to simulated more particles and therefore reduce the effect of random noise from the discretization of f .

less particle pairs have to be checked for the collision condition. To still get the correct collision rate, the cross section has to be multiplied by s as well to $\sigma' = s\sigma$ and the collision condition is computed with σ' . However, s can not be chosen arbitrarily high. On the one hand, a too small simulated particle number leads to a coarse sampling of f and therefore a reduced accuracy of the simulation. On the other hand, the scaled cross section at some point approaches the spatial size of the system, which can also lead to problems.

Initialization, Timesteps and Blocking Time

For the simulation of our double-species experiment, for each species N_i position vectors \mathbf{r} and N_i velocity vectors \mathbf{v} are generated in the beginning, where N_i is the particle number per species. The initial values for \mathbf{v} are distributed in equilibrium according to the Maxwell-Boltzmann distribution

$$f(\mathbf{v}) \propto e^{-\frac{(\mathbf{v}-\mu_v)^2}{2\sigma_v^2}}. \quad (5.10)$$

We generate them with a Gaussian random number generator, where the parameters for the mean μ_v and width σ_v are calculated according to the experimental parameters. In particular, we require

$$\sigma_v = \sqrt{\frac{k_B T}{m}}, \quad (5.11)$$

where T is the starting temperature of the sample and m is the mass of one atom. Usually, μ_v is 0 but can be set to a non-zero value to account for an initial CoM motion.

The distribution of \mathbf{r} depends on the physical system that is studied. In a harmonic dipole trap, in the case of a thermal sample, the number density is Gaussian, so we again use a Gaussian random number generator with

$$\sigma_r = \sigma_v / \omega, \quad (5.12)$$

where ω is the angular trapping frequency. Also here, μ_r can be used to shift the cloud relative to the trap center and simulate out of equilibrium situations. In contrast, in a box potential we use uniformly distributed random positions and require that $r < r_b$, where r_b is the radius of the box trap.

Other technical parameters of the simulation, e.g. the time step Δt , can be inferred from the values of T , m and ω . As mentioned before, the split-step approach works well as long as Δt is much smaller than the mean time between collisions. To estimate the mean time between collisions, we look at the collisional volume $\overline{\sigma v_r}$ that is swept by one particle moving through space per unit time, with the mean relative velocity

$$\overline{v_r} = \sqrt{\frac{8}{\pi}(\sigma_{v,K}^2 + \sigma_{v,Dy}^2)}, \quad (5.13)$$

as given by the Maxwell-Boltzmann distribution of the relative velocities of two species of particles with a mean speed as given in Eq. (5.11). At unitarity, the mean cross-section reduces to

$$\bar{\sigma} = \frac{4\pi}{\bar{k}^2}, \quad (5.14)$$

with

$$\bar{k} = \frac{\mu \bar{v}_r}{\hbar} \quad (5.15)$$

being the mean relative k vector and μ the reduced mass. For a thermal gas in a harmonic trap we calculate the number density in the trap center for each species

$$n_0 = \frac{1}{(\sqrt{\pi}\sigma_r)^3}. \quad (5.16)$$

For a single particle moving through this density we can calculate the mean time between collisions as

$$\bar{t}_c = \frac{1}{\bar{\sigma}\bar{v}_r n_0} \simeq 30 \mu\text{s}. \quad (5.17)$$

This value was calculated using the parameters of the experiment in Sec. 4.2 (see also Table 5.1). Δt should then be chosen to be smaller than 30 μs .

To get the correct number of collisions in the simulation, Δt should also be chosen such that no collisions are missed. For this we calculate the time it takes a pair to move through the collisional volume with radius

$$r_c = \sqrt{\frac{\bar{\sigma}}{\pi}}. \quad (5.18)$$

At unitarity, this reduces to

$$r_c = \frac{2}{\bar{k}} = 2 \frac{\hbar}{\mu \bar{v}_r}, \quad (5.19)$$

and the time to move through this volume is given by

$$t = 4 \frac{\hbar}{\mu \bar{v}_r^2}. \quad (5.20)$$

To not miss any collisions, the timestep should be chosen so small that even fast particles can not move through their collisional volume during Δt . In this case we can make a conservative choice of

$$v_r \gtrsim 5 \bar{v}_r, \quad (5.21)$$

which covers the majority of pairs with high relative velocity. This results in

$$\Delta t \lesssim \frac{1}{6} \frac{\hbar}{\mu \bar{v}_r^2} \simeq 1 \mu\text{s} \quad (5.22)$$

as an upper bound for the time step, which also fulfills the requirement for the split-step method.

In our implementation it is possible that the same pair is detected to collide again in the next timestep after a collision if it did not yet travel out of the collisional volume. This can be prevented by blocking this collision to happen for a time t_b , which is again given by the time it takes the pair to travel through the collisional volume. An estimate for t_b can be found by assuming

$$\frac{\bar{v}_r}{3} < v_r < \frac{\bar{v}_r}{2}, \quad (5.23)$$

which covers the majority of slow pairs. This assumption ensures that the majority of pairs should have traveled through their respective collisional volume and gives an estimated transfer time of

$$t_b \simeq 25 \frac{\hbar}{\mu \bar{v}_r^2} \simeq 150 \mu\text{s}, \quad (5.24)$$

which is then used to block a pair of atoms from colliding again. t_b can also be calculated for each pair individually by explicitly calculating v_r after the collision. In homogeneous systems, the blocking time can also be computed analytically from the trajectories of the two particles.

Here, we have calculated these parameters for the resonantly interacting conditions given in Chapter 4. Following the same reasoning, the values can be adjusted for different interaction strengths and temperatures. In practice the value of Δt can not always be chosen overly conservatively, as the overall computation time scales inversely proportional to Δt .

5.1.2 Validation Tests

To validate the working principles of the simulation described in the last section we apply them to a simple system of a mixture of two interacting species in a box potential. We can then compare the simulation results to theoretical predictions.

Scattering Rate

As a first step, we consider the mean collision rate Γ_C , which in a homogeneous system takes the form

$$\Gamma_C = \sigma \bar{v}_r \frac{N_K N_{Dy}}{V}, \quad (5.25)$$

where $V = 4\pi r_b^3/3$ is the volume of the box with radius r_b . We then compare this to the recorded collision rate Γ_{sim} obtained by the simulation. Here we use the boxing technique but no scaling. Figure 5.2 shows the accumulated total number

of collisions over time of an exemplary run with $N_K = N_{\text{Dy}} = 2000$ atoms at a temperature of $T_K = T_{\text{Dy}} = 1 \mu\text{K}$ in a box with $r_b = 10.7 \mu\text{m}$, where the collision process was altered to not change the velocities of the particles. This is to test the collision detection scheme and avoid errors that could arise from a change in the phase space density. The scattering length was set to $1000 a_0$ and the unitarity limit was disregarded. The accumulated collision number can be fitted with a linear function to extract the mean collision rate from the slope. In this particular case, the fit result of $8.591(2) \times 10^5 \text{ s}^{-1}$ deviates slightly from the theoretical value $\Gamma_C = 8.638 \times 10^5 \text{ s}^{-1}$. However, the standard deviation over 20 simulation runs is about 1.6%, which closely matches what we would expect when assuming a Poissonian error in counting the collisions.

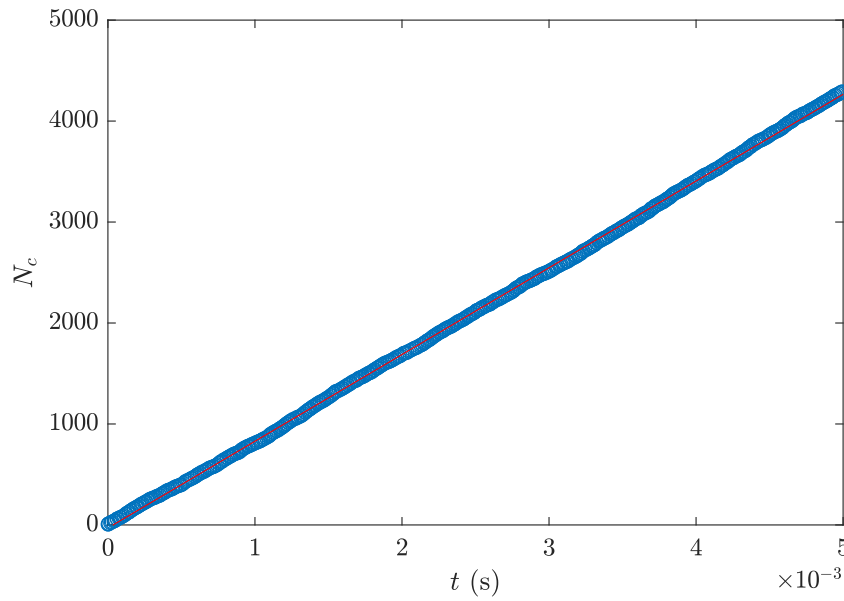


Figure 5.2: Accumulated number of collisions in a box without changing the particle velocities. The red line shows a linear fit. The fit result for $\Gamma_{\text{sim}} = 8.591(2) \times 10^5 \text{ s}^{-1}$ agrees well with the theoretical prediction of $8.638 \times 10^5 \text{ s}^{-1}$ within the statistical variation over multiple simulation runs.

We now investigate the behavior of the scattering rate for different scattering lengths. With increasing interaction strength, as a becomes comparable to the interparticle distance, the recorded scattering rate Γ_{sim} starts to differ from the theoretical prediction. Figure 5.3 shows $\Gamma_{\text{sim}}/\Gamma_C$ as a function of the diluteness parameter $\eta = a(N/V)^{1/3}$ in two cases. First we again only counted detected scattering events (without changing the particle velocities) to verify the correct implementation of the collision detection scheme. In this case, $\Gamma_{\text{sim}}/\Gamma_C$ drops as $1 - a/r_b$. This can be explained as a finite size effect by considering atoms close to the potential walls. Because their scattering volume extends to outside of the

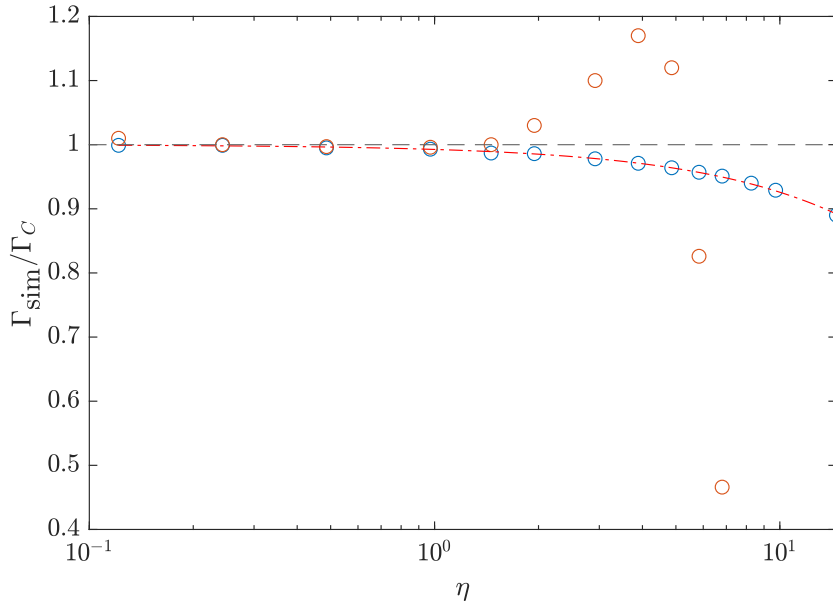


Figure 5.3: Ratio of simulated collision rate to theoretical prediction depending on the diluteness of the gas. Blue shows simulations where only collision events were counted but to verify the collision detection scheme the particle velocities were not changed. The red dash-dotted line shows a $1 - b\eta$ fit to this dataset. Light red circles show simulations where the particle velocities were also changed in the collision process.

potential, where no collision partners are present, their individual scattering rate is diminished. In contrast, Eq. (5.25) assumes an infinite homogeneous system.

Figure 5.3 also shows $\Gamma_{\text{sim}}/\Gamma_C$ in a situation where the collision actually changes the particle velocities. In this case, starting at about $\eta = 1$, Γ_{sim} increases until it is almost 20% higher than the theoretical prediction, and drops rapidly after. The finite size effect can not account for this. Instead, at high densities, the assumption of uncorrelated Boltzmann distributions is not necessarily true anymore, see for example Chapter 16 in Ref. [173]. A correlation between neighboring particles might exist because of multiple recent collisions. Furthermore, the sum of all scattering volumes is approaching the spatial size of the system, which effectively reduces the free volume, and therefore increases the scattering rate. A third effect is that at some point the particles are packed so closely that free motion is not possible anymore. The particles then effectively get screened by their neighbors and are prevented to interact with particles further away, which reduces the scattering rate. These processes, to some extent, should be physical and not an artifact of the simulation. Indeed, mathematical models for these processes exist and have been tested on real gases [173], but in combination with the finite size of the simulated system, no model could be found that reproduces the simulation results. For example,

the finite size effect can be amplified if the gas is dense, because the particles get pushed closer to the borders of the potential walls and therefore more of their collisional volume lies in particle-free areas. Furthermore, if the atoms can not move freely anymore, the blocking time essentially limits the number of collisions, because the atoms are not allowed to interact with their neighbors after a collision, but can also not move freely to find new interaction partners. It is therefore not completely clear, which part of the behavior can be considered realistic and which part is a result of the simulation model. However, most of these phenomena appear at conditions where other descriptions like mean-field theory should be used to describe the behavior of the gas. An integration of the mean-field concept to the test-particle method has been done in Ref. [174].

Thermalization

As a second check, thermalization curves can be taken to provide further insight into the mixture and extract valuable information from measurements. DSMC algorithms have already been used in the field of ultracold atoms to investigate cross-species and cross-dimensional thermalization in harmonic traps [129, 163], providing a vital check of theoretical models.

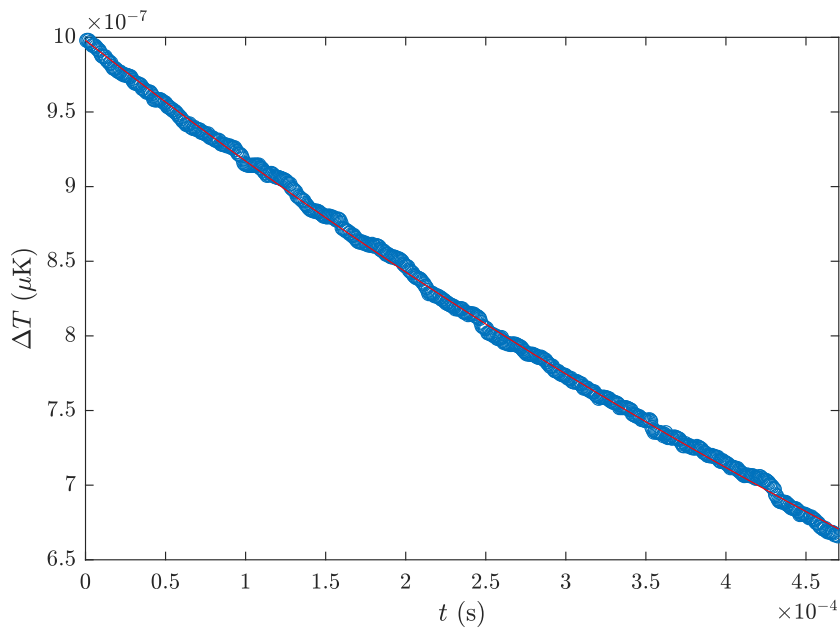


Figure 5.4: Exemplary evolution of ΔT during thermalization of Dy and K. The red line shows a fit after Eq. (5.30). The fit result for this particular run of $\tau_{th,f} = 1.184(1) \times 10^{-3}$ s is slightly higher than the theoretical prediction of 1.176×10^{-3} s, but agrees well within the statistical standard deviation over multiple runs.

To investigate thermalization between two species with different temperatures, we consider the average energy transfer per collision

$$\langle \Delta E \rangle = \zeta k_B (T_K - T_{Dy}), \quad (5.26)$$

where the factor

$$\zeta = \frac{4m_K m_{Dy}}{(m_K + m_{Dy})^2} \approx 0.638 \quad (5.27)$$

accounts for the mass imbalance of the mixture. For a thermal gas in a box, the average energy per particle is given as

$$\langle E \rangle = \frac{3}{2} k_B T, \quad (5.28)$$

and with these expressions one arrives at a differential equation for the difference in temperature $\Delta T = T_K - T_{Dy}$ [147, 175],

$$\frac{d}{dt} \Delta T = -\frac{2}{3} \zeta \frac{N_K + N_{Dy}}{N_K N_{Dy}} \Gamma_C \Delta T. \quad (5.29)$$

The behavior of ΔT is near exponential (because of the dependence of Γ_C on temperature) and for short times can be approximated by

$$\Delta T(t) = \Delta T(0) e^{-t/\tau_{th}}, \quad (5.30)$$

where

$$\tau_{th} = \frac{3}{2\zeta} \frac{N_K N_{Dy}}{N_K + N_{Dy}} \frac{1}{\Gamma_C} \quad (5.31)$$

is the thermalization time. Figure 5.4 shows the evolution of ΔT of an exemplary simulation run with $N_K = N_{Dy} = 5000$, $T_K = 1.5 \mu\text{K}$, $T_{Dy} = 0.5 \mu\text{K}$ and $r_b = 10.7 \mu\text{m}$. The simulation was again carried out with the boxing technique and without scaling. To record T_K and T_{Dy} we calculate the kinetic energy for each particle per species from its velocity, take the average and convert to temperature according to Eq. (5.28). The thermalization time is then extracted by fitting the exponential function in Eq. (5.30) to ΔT . This yielded a mean thermalization time of $1.04(5) \tau_{th}$, where the number in parentheses is the standard deviation over 50 repetitions. Depending on the fit interval, the simulation systematically gives slightly higher results for $\tau_{th,f}$, which can be explained by the dependence of Γ_C and τ_{th} on the temperatures of the two gases [129]. The collision rate is about 14% lower when the clouds are thermalized compared to the beginning of the simulation, which causes the thermalization time to be longer when extracted from a fit that reaches from simulation start until thermalization. In conclusion, the results for Γ_C and τ_{th} of the developed simulation algorithm agree well with theory predictions.

5.2 HYDRODYNAMIC EXPANSION

After the validation of the simulation method, it can now be used to simulate the dynamics in the experiment and compare the results to the experimental results. We can also use it to investigate the dependence on parameters that can not easily be changed in the experiment.

5.2.1 Comparison with Experimental Data

As stated in Chapter 4, the algorithm was primarily developed and used to simulate an interacting mixture of K and Dy expanding out of the harmonic dipole trapping potential after it was turned off. In the experiment, the expansion of K was seemingly slowed down by the interaction with Dy and its profile was different from the expected Gaussian profile. This effect varied with the interaction strength and therefore with the magnetic field, and can be used to extract some information about the Feshbach resonance, such as the resonance position. It furthermore provided a check of our calibration of the scattering length.

The upper panels of Fig. 5.5 show a non-interacting, thermalized sample of Dy and K after release from the trap. As can be seen, K is much more dilute than Dy, a result of the faster expansion caused by its lower mass. The radial number density of a non-interacting thermal gas expanding from a spherical symmetric trap with trapping frequency ω is given by⁵

$$n(r, t) = \frac{N}{\sqrt{2\pi}r(t)} e^{-\frac{r^2}{2r^2(t)}} \quad (5.32)$$

with the $1/e$ -radius at time t

$$r(t) = \sqrt{\sigma_r^2 + \sigma_v^2 t^2}. \quad (5.33)$$

To quantify the slowing effect, we define a central fraction C as the ratio of atoms inside a circle with radius $\sqrt{2}r_{\text{Dy}}(t)$ to the total atom number (marked green in Fig. 5.5). For a non-interacting gas of Dy atoms, this gives

$$C_{\text{Dy}} = \frac{1}{N_{\text{Dy}}} \int_0^{\sqrt{2}r_{\text{Dy}}(t)} n_{\text{Dy}}(r, t) r dr = 1 - e^{-1} \approx 0.63. \quad (5.34)$$

In general, for any other non-interacting species (in our case K) with the same temperature, the fraction of atoms in the same circle defined by the Dy expansion will be

$$C_{\text{K}}(t) = \frac{1}{N_{\text{K}}} \int_0^{\sqrt{2}r_{\text{Dy}}(t)} n_{\text{K}}(r, t) r dr = 1 - e^{-\frac{\omega_{\text{K}}^2}{\omega_{\text{Dy}}^2} \frac{m_{\text{K}}}{m_{\text{Dy}}} \frac{1+(\omega_{\text{Dy}}t)^2}{1+(\omega_{\text{K}}t)^2}}. \quad (5.35)$$

⁵ To be able to compare to the experimental absorption imaging pictures, the 3D-profile was already integrated along the imaging direction and the azimuth angle.

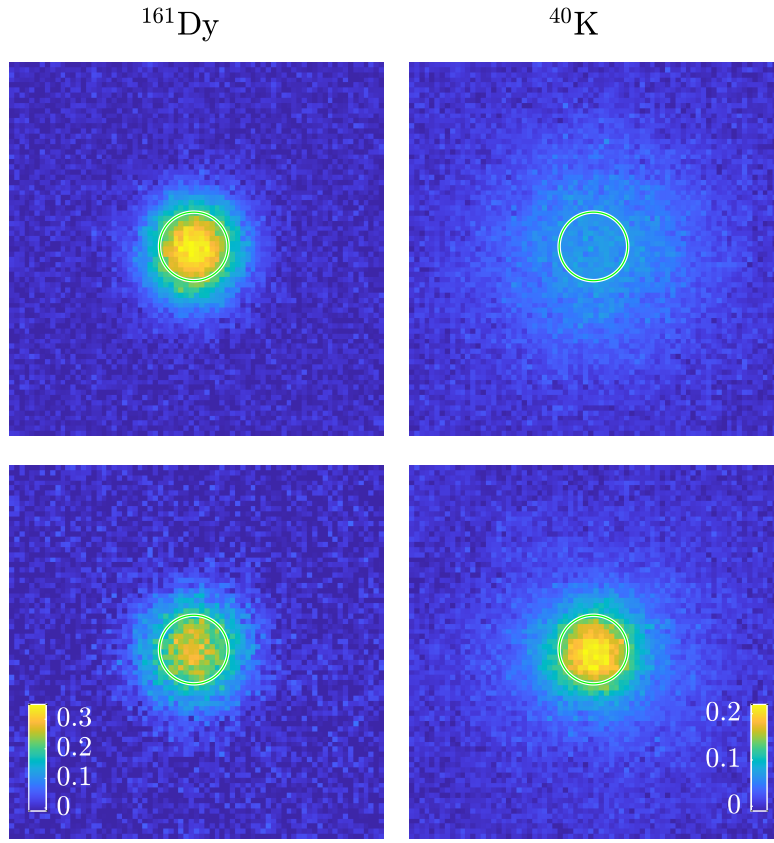


Figure 5.5: Absorption imaging pictures of non-interacting (upper panels) and resonantly interacting samples (lower panels) of Dy and K in time-of-flight imaging. The green circle indicates the $\sqrt{2}r_{\text{Dy}}$ border.

The dependence on the ratios of masses and trap frequencies can be understood in terms of the faster expansion of light particles and the initial size of the samples in the trap. For the experimental parameters given in Tab. 5.1, we expect $C_{\text{K}} \approx 0.24$ in the case of no interactions. In contrast, the experimentally observed C_{K} in the strongly interacting regime was larger than the theoretical value, which hints at a strong drag effect caused by many collision events with the slower expanding Dy. This can also be seen in the lower panels of Fig 5.5, where the K cloud suddenly appears much more dense compared to the non-interacting case.

To verify if the observed behavior could be explained by a hydrodynamic expansion, we used the Monte Carlo simulation and replaced the box potential with a free-space propagation of the particles right after release from a harmonic trapping

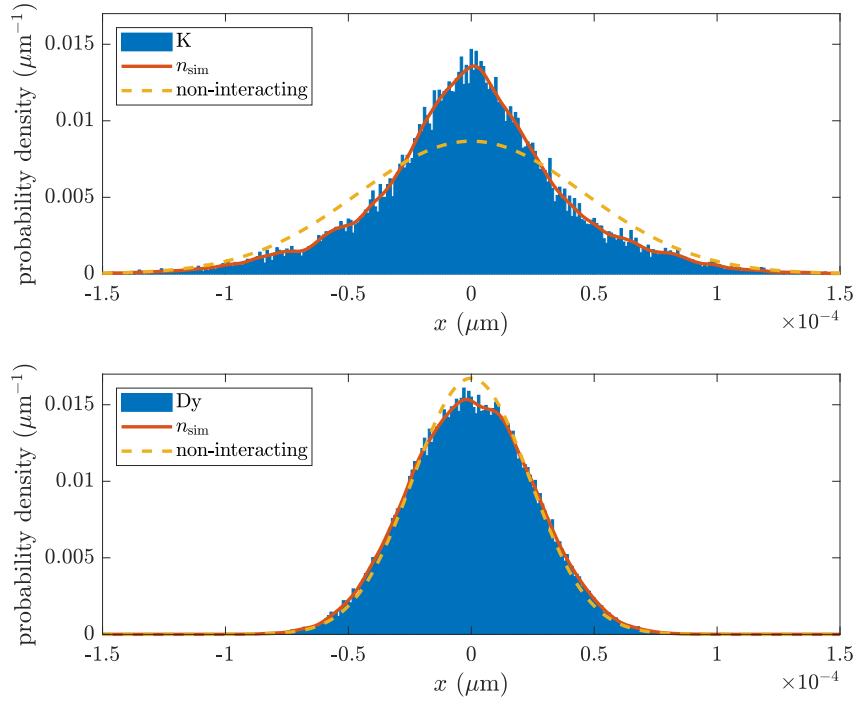


Figure 5.6: Examples of simulated profiles for K and Dy obtained by using the same parameters as in the experiment. Binning the positions of the particles to 1 nm large bins gives the probability density shown in blue. Red shows a convolution of the bin counts with a Gaussian. The orange dashed line shows the expected profile after expansion with no interactions.

potential. As a result, we get two sets of coordinates in space corresponding to the particle distribution.

The simulation was computed with the parameters listed in Table 5.1. As in the experiment, the clouds were thermalized and had a temperature of $T_K = T_{Dy} = 0.5 \text{ } \mu\text{K}$. The simulation was carried out with $N_K = 8000$ and $N_{Dy} = 22000$ atoms. The particle distributions were generated according to a gas in a spherical harmonic trap with $\omega_{Dy} = 2\pi \times 120 \text{ Hz}$ and $\omega_K = 3.6 \omega_{Dy}$. Then, the particle distributions were evolved in free space in the universal regime ($a = \infty$), where the cross section is fully limited by the finite relative momentum of the collision pair. The time-of-flight (TOF) of the mixture was $t_{TOF} = 4.5 \text{ ms}$, after which the particle distribution was recorded. To be able to compare the simulation to the experimental profiles, histograms are created from the discretized locations of the particles. Since the resolution of the imaging system in the experiment is limited, every atom contributes one point spread function to the image. To account for this, a histogram of the positions of the simulated point-like particles is convoluted with

a Gaussian profile with a width of $3 \mu\text{m}$. Figure 5.6 shows exemplary histograms converted to linear density and the corresponding reconstructed and theoretical non-interacting linear density profiles. While the profile of dysprosium is still very close to its non-interacting shape, the potassium profile is much more narrow and deviates from a Gaussian curve. The central fraction of potassium is 0.40, as opposed to its non-interacting value of 0.22.⁶ A comparison of experimental and simulated profiles can be found in Fig. 4.3.

To check the model for the dependence of the scattering length on the magnetic field given in Eq. (4.1), we made multiple simulations with varying a and compared their values for C_K with the results from the experiment, see Fig. 5.7. The error bars indicate the standard deviation over 10 simulation repetitions. The observations regarding the central fractions as well as the sizes of the clouds seem to be quantitatively well explained by the simulations, supporting our physical interpretation as a drag effect. Furthermore, the good agreement of the behavior of C_K with the interaction strength confirmed our calibration of the scattering length obtained by other means (thermalization curves and wide thermalization scans).

Table 5.1: Standard parameters used in the simulations for Fig. 5.7.

| | | | | | |
|------------------|-----------------|--------|-----------------|-------|-----------------|
| N_K | N_{Dy} | T_K | T_{Dy} | s | Δt |
| 8000 | 22000 | 500 nK | 500 nK | 5 | 1 μs |
| t_{TOF} | t_b | f_K | f_{Dy} | m_K | m_{Dy} |
| 4.5 ms | 150 ms | 432 Hz | 120 Hz | 40 u | 161 u |

⁶ In our publication [176], Chapter 4, the in-trap radius σ_r was disregarded in the definition of C_K , which leads to a value of $1 - e^{-m_K/m_{\text{Dy}}} \approx 0.22$ instead of 0.24. The rest of the calculations in this chapter have been made with the definition of Eq. (5.35), as the ratio of σ_r varies with the ratios of m and ω and affects the drag effect.

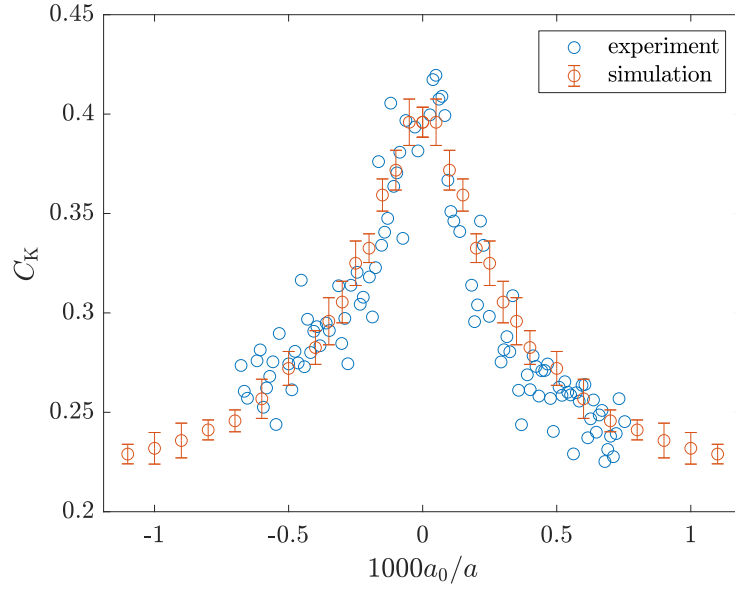


Figure 5.7: Comparison of C_K depending on the interaction strength for experiment and simulation.

5.2.2 Scaling, Timesteps and Robustness Against Missed Collisions

The simulations to support the experimental data for the publication [176] were originally carried out without the use of the sorting cells, because in the universal regime, due to the momentum limited cross section, two particles with low relative velocity can collide even if they are on two opposing ends of the cloud. These collisions would be missed when using the cell approach. Because this means testing all possible pairs for collision within every timestep, the simulation took about 48 h, which is too long to be able to scan parameters and gather enough data for statistical analysis. Therefore, different values for Δt and the scaling parameter s were investigated to speed up the computation. As this might also lead to missed collisions, to verify that the behavior of the hydrodynamic expansion was not affected, we conducted χ^2 tests of the histograms.

To test whether two runs give an equivalent result with respect to the statistical fluctuations, we use reduced χ^2 testing. We compare bins of two histograms, a_i and b_i , with the same total number of bins ν and same bin borders, and calculate the reduced chi-squared

$$\chi_\nu^2 = \frac{1}{\nu} \sum_i \frac{(a_i - Kb_i)^2}{a_i + K^2b_i}, \quad (5.36)$$

where K is a renormalization factor between simulations with different numbers of atoms. Since both bins are subject to statistical fluctuations, we have to add their standard deviations, which we assume to be Poissonian, quadratically in

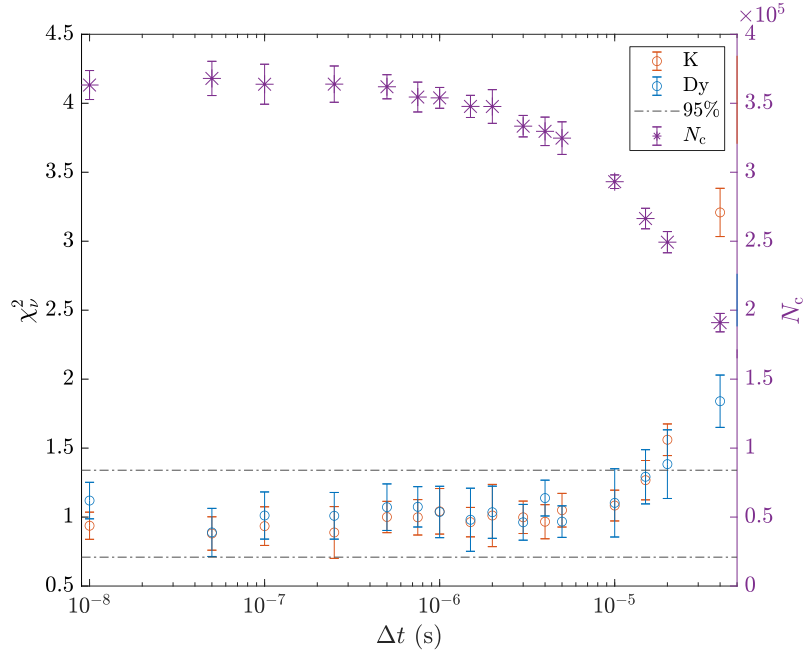


Figure 5.8: Reduced χ^2 and total number of recorded collisions N_c for a scan of the timestep Δt . The reduced χ^2 was calculated from histograms of the simulation profiles compared to a profile of a full simulation without sorting cells, $dt = 1 \mu\text{s}$ and $s = 1$.

the denominator. To determine equivalence, χ_v^2 is compared to the corresponding 95%-interval of the cumulative distribution function. The full simulation without sorting cells, $\Delta t = 1 \mu\text{s}$ and $s = 1$ was used as reference.

As the sorting cell approach results in a substantial performance increase, we first compared a run with 9 cells to the reference data. Interestingly, with $\chi_{v,K}^2 = 0.95(9)$ and $\chi_{v,Dy}^2 = 1.01(13)$ the data was fully consistent within the 95%-interval, although we know that some collisions are missed by this approach. The overlap between cells was calculated with the mean relative velocity \bar{v}_r , which means that pairs that are in different cells and have a small relative velocity were missed. This suggests that collisions between particles further away than the overlap do not contribute significantly to the slowing effect. We suspect that more collisions are happening than what is necessary for the hydrodynamic expansion, which makes the simulation quite robust against errors in the collision detection. This can also be seen in Fig. 5.8, which shows χ_v^2 and the number of total detected collisions N_c for different values of Δt . N_c starts to drop off before χ_v^2 increases beyond the 95%-interval.

Despite the fact that the usage of the scaling factor s can speed up the simulations drastically, it can also lead to problems with the scaled cross section and spatial

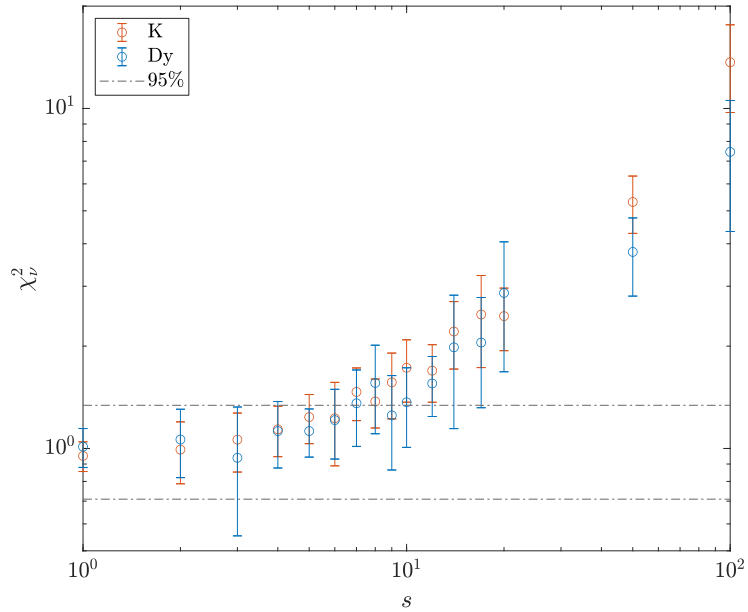


Figure 5.9: Reduced χ^2 as a function of the scaling factor s . Profiles were compared to a full simulation without sorting cells, $\Delta t = 1 \mu\text{s}$ and $s = 1$.

system size, and random fluctuations in the initialization of the simulated particles are more pronounced at low N_{sim} . Figure 5.9 illustrates the influence of s on the simulated profiles. χ_r^2 leaves the 95%-interval at a scaling factor of 10. At this point, there are only 800 K and 2200 Dy particles left in the simulation, which is already a coarse sampling of the Boltzmann distributions. Furthermore, with increasing s , the size of σ approaches the spatial system size, leading to the effects described in Sec. 5.1.2. For $s = 5$ the profiles are not distinguishable from the full simulation, while there is still roughly a 25-fold speedup in computation time. For larger spatial system sizes with more atoms, larger values for s should be possible.

5.2.3 Effects of Experimental and Physical Parameters

For a more involved analysis of the effects of parameters like mass, in-trap size, particle number etc., we now look at the behavior of the central fraction. To illustrate the effect of the scanned parameter, simulations were carried out on resonance and with no interaction, with the other parameters as in Tab. 5.1. A comparison of the non-interacting simulations with Eq. (5.35) serves as another check of the initialization and propagation methods. Each data point was simulated 10 times, with the error bars indicating the standard deviation.

From Eq. (5.35), it is clear that the mass ratio and the trap frequency ratio, which both enter in the in-trap size σ_r , will influence C_K in the non-interacting case.

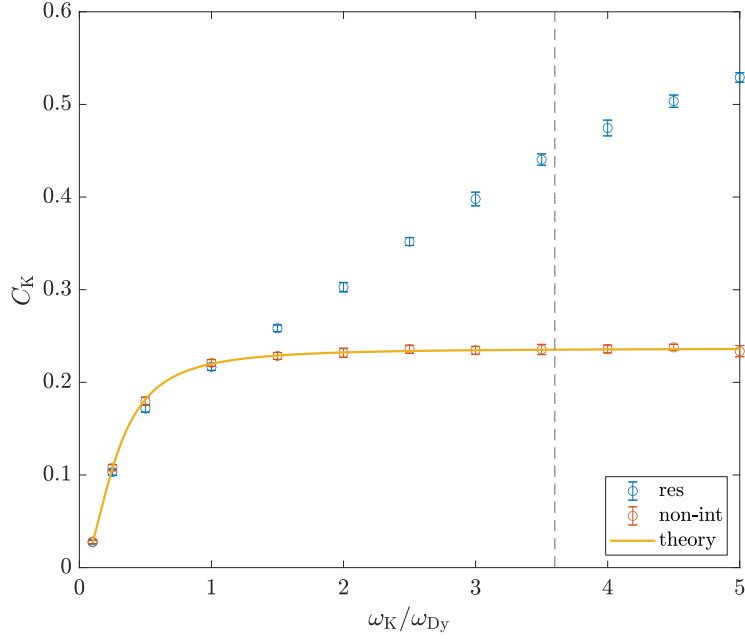


Figure 5.10: C_K depending on the ratio of trapping frequencies. The vertical dashed line indicates the frequency ratio in the experiment.

However, since a change in σ_r influences the number density and therefore the collision rate, they will also have an additional effect on C_K in the interacting case.

For Fig. 5.10, the ratio of trap frequencies ω_K/ω_{Dy} was scanned, with all other parameters used as in the experiment. C_K follows the non-interacting theory below a frequency ratio of 1. At this point, the initial size of K is about twice the size of Dy , which means that from the start, many atoms are already outside the influence of the Dy atoms. As a result, first, fewer atoms can actually be slowed, and second, the collision rate and therefore the drag force in the center is reduced. The higher the frequency ratio, the smaller the initial size of K, which means that more atoms will experience the stronger slowing effect. C_K then grows roughly linearly with ω_K/ω_{Dy} , as the K cloud gets immersed into the Dy cloud more and more. In the experiment, $\omega_K/\omega_{Dy} = 3.6$ (indicated by the dashed line), corresponding to $\sigma_{r,K} = 0.56\sigma_{r,Dy}$, which explains most of what we see in the experiment.

In Fig. 5.11, the mass of the second species (K) was scanned, once for a trap frequency ratio of 3.6 as in the experiment, and once with the trapping frequency of the second species adjusted as $\omega_K = \omega_{Dy}\sqrt{m_{Dy}/m_K}$. In this way, σ_r is equal for both species and the effect of the mass on the expansion is isolated. In comparison, the effect of the trapping frequency on σ_r is substantially higher than the effect of the masses on both σ_r and σ_v , as can be seen at the vertical dashed lines, which corresponds to the mass ratio used in the experiment. For higher mass ratios, in

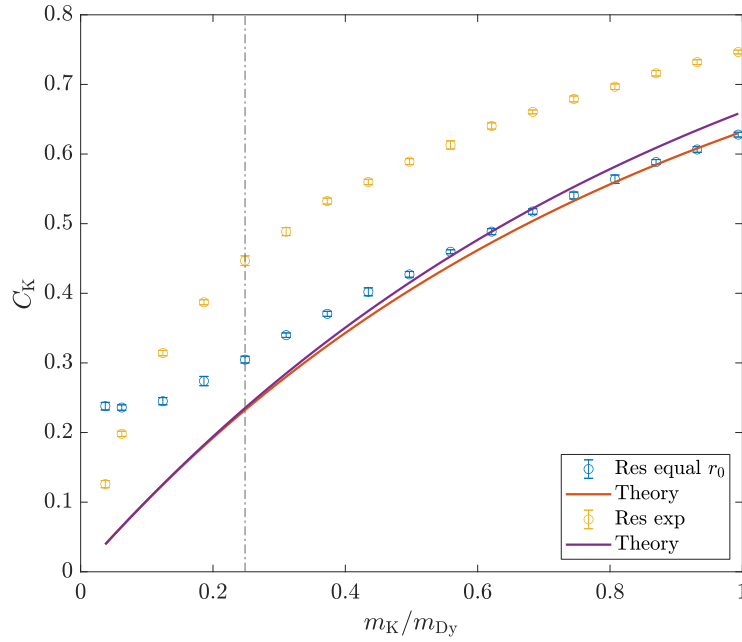


Figure 5.11: C_K depending on the mass ratio. To differentiate the effect of the mass on the initial size σ_r and the initial mean velocity v_0 , ω_K was adjusted such that σ_r is equal for both species. In comparison, in the experimental case of $\omega_K = 3.6 \omega_{Dy}$, the difference to the non-interacting case is much higher.

the size-matched case, there is almost no difference in the expansion of the two species to the non-interacting case. For lower mass ratios, the central fraction seems to level off to a constant value. In contrast, in the case of a fixed frequency ratio, the size of the light species becomes larger than the heavy one at ratios below about 0.08, leading to a vanishing slowing effect.

As the number ratio also influences the density and therefore collision rate, we scanned the number of Dy atoms (see Fig. 5.12). With more Dy atoms than K atoms, C_K is behaving close to a power law and recovers the non-interacting behavior only at a very large imbalance of K atoms. In this case, there are just not enough Dy atoms to provide sufficiently many collisions to slow down the large number of K atoms.

In conclusion, the trapping frequency ratio and therefore the initial size ratio is the most influential, however the other parameters have to be chosen accordingly to see a pronounced effect in the experiment. Since the mass ratio can not be chosen freely, in extreme cases such as the Dy-Li mixture, it is important to tune the other parameters accordingly.

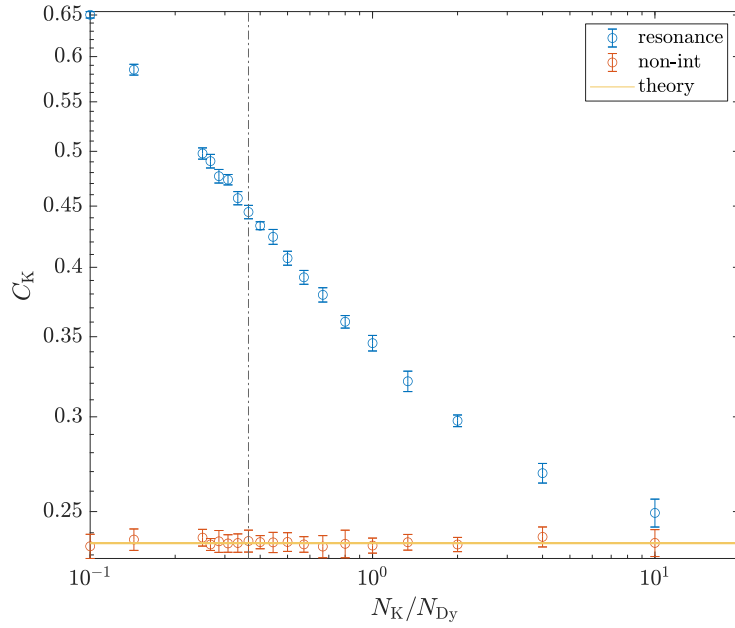


Figure 5.12: C_K depending on the number ratio with other parameters as in the experiment. The vertical dashed line marks the number ratio used in the experiment.

5.2.4 Aspect Ratio Inversion

Another hallmark of hydrodynamic behavior is the inversion of the aspect ratio of the clouds in asymmetric traps [43, 79, 177]. In our experiment we did not observe this effect due to the trap being almost spherically symmetric. In the simulations, this effect can be reproduced when the starting samples are created with varying σ_r in x , y and z directions, which corresponds to different trapping frequencies in these directions.

The left side of Fig. 5.13 shows the evolution of the aspect ratio $\epsilon = r_{x,y}/r_z$ during expansion for an interacting and a non-interacting mixture. The initial aspect ratio of the trap was $\omega_z/\omega_{x,y} = 1/5$. In the non-interacting case, the aspect ratio approaches unity for long expansion times, as the cloud is thermalized in all directions. In contrast, in the interacting case, the aspect ratio is inverted as a result of the redistribution of kinetic energy to the axis with the largest density gradient. The maximum value of $\epsilon_K = 1.11(3)$ is different from the value of 2.44 expected from hydrodynamic scaling theory [178, 179], probably because the density drops during expansion, which causes the mixture to transition to the collisionless regime. To tackle this issue in an experiment with rubidium, a two-phase model was developed with a mean-field approach in Ref. [177], where the expansion is described by a hydrodynamic expansion followed by a collisionless expansion. But since the situation of this single-species experiment is different to our two-species

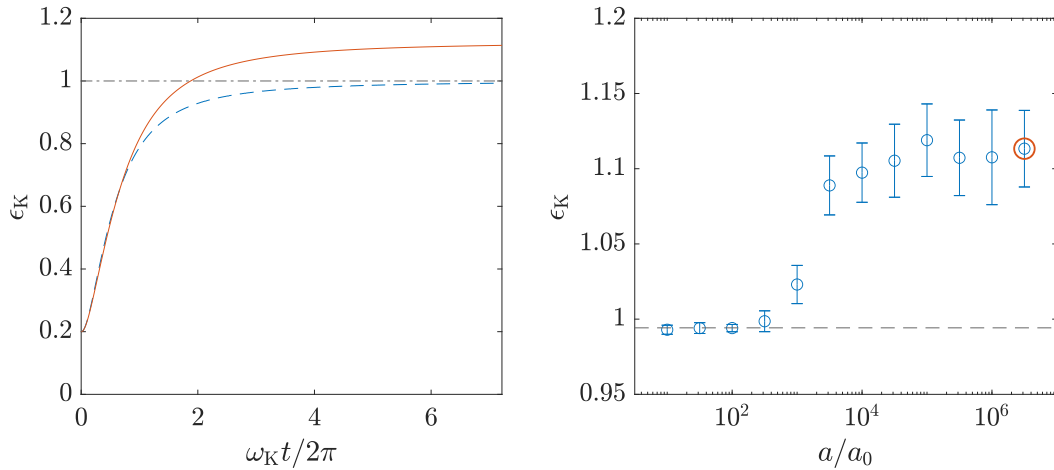


Figure 5.13: Left side: evolution of the aspect ratio of potassium during expansion for a non-interacting mixture (dashed blue line) and on resonance (solid red line). Right side: dependence of the aspect ratio on the scattering length after 16.7 ms of expansion. The red circle marks the result for the data shown as solid line on the left side and the dashed line indicates the theoretical result for a non-interacting mixture.

case, where the mass imbalance affects the expansion speed and the initial in-trap sizes of the two species, the model is not directly applicable to our situation.

5.3 THE EFFECT OF R^*

So far, the simulations were carried out with the unitarity-limited cross section as in Eq. (5.8), which is a good description in the case of entrance-channel dominated Feshbach resonances such as the 217-G resonance. However, as described in Chapter 3, a fourth parameter R^* is necessary to fully describe the interaction in the case of a closed-channel dominated resonance. Under certain conditions, the resulting effects can have an impact on the accuracy of the experimental data, but can also be turned to an advantage.

5.3.1 Shift of the Resonance Center

In the case of closed-channel dominated resonances, the cross section takes the form

$$\sigma = \frac{4\pi}{\left(\frac{1}{a} + R^*k^2\right)^2 + k^2}. \quad (5.37)$$

The position of the maximum of σ is then shifted away from the resonance center, to a detuning on the attractive side, where $a = -1/(R^*k^2)$. In a recent publica-

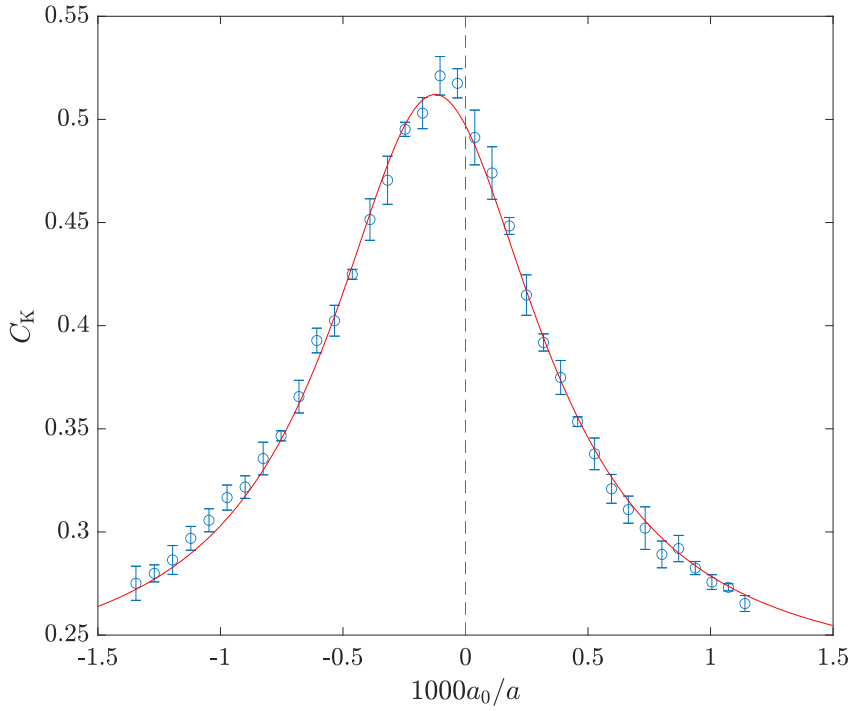


Figure 5.14: Behavior of the K central fraction after hydrodynamic expansion near a resonance with $R^* = 643 a_0$. The red line shows a Lorentzian fit, the dashed line indicates the resonance pole, where the scattering length diverges.

tion [151], we were able to characterize several other Feshbach resonances at lower fields. Among those, a resonance at 7.29 G is particularly interesting for us, as it combines accurate magnetic tunability and a universally interacting regime. With the help of a measurement of the binding energy of Feshbach molecules on the repulsive side, we can extract the value of R^* to be $643(30) a_0$.

As in Chapter 4, we used hydrodynamic expansion and thermalization measurements to identify the pole of the resonance. The observed hydrodynamic expansion data was again compared to the Monte Carlo simulation, both with and without including R^* in the cross section. Figure 5.14 shows the simulated effect of R^* in the hydrodynamic expansion. The peak position of the slowing effect on K is shifted towards negative scattering length. Furthermore, the feature becomes slightly asymmetric. As a result, the Lorentzian model used for fitting does not agree well with the data, but it indicates a shift of the center position to $a \approx -8.0(3) \times 10^3 a_0$. In the experiment, this amounts to a shift of about 3 mG, which is roughly the level of magnetic field stability that we currently achieve. However, with other combinations of R^* and absolute width of the resonance, this effect should be kept in mind, since it could lead to a sizable disagreement in the results for the pole

position obtained with other methods, such as measurements of the binding energy of the molecular state.

5.3.2 Increased Thermalization Rate

Another effect caused by R^* can manifest itself when considering thermalization between two species. While the unitarity-limited cross section is greatly reduced for high-energy pairs (i.e. pairs with a high relative velocity), R^* can in turn enhance the cross section for a certain velocity class of pairs with

$$k_{\sigma}^* = \frac{1}{R^*} \sqrt{-\frac{R^*}{a} - \frac{1}{2}}. \quad (5.38)$$

Subsequently, the energy-dependent scattering rate features a resonance at

$$k_{\Gamma}^* = \frac{1}{\sqrt{6R^*}} \sqrt{-\frac{2R^*}{a} - 1 + \sqrt{1 + \frac{4R^*}{a} + \left(\frac{4R^*}{a}\right)^2}}. \quad (5.39)$$

Since R^* is fixed by the resonance, the value of k_{Γ}^* can be tuned by varying a . It could be desirable to tune k_{Γ}^* in such a way that the scattering rate for high-energy pairs is substantially enhanced, especially in situations, where many atoms of one species are used to sympathetically cool few atoms of another species.

In the second mixture experiment in the Grimm group, known as the FeLiKx experiment, large samples of fermionic lithium are used to sympathetically cool either ^{40}K or ^{41}K , in order to prepare cold Fermi-Fermi or Fermi-Bose mixtures. In the case of the bosonic potassium isotope, the details of the experimental sequence are described in Ref. [140]. The evaporation is carried out utilizing the resonance between the first and third spin state of Li [180, 181], with scattering lengths $a_{\text{Li,Li}} \approx -635 a_0$ and $a_{\text{Li,K}} \approx 60 a_0$. The low interspecies scattering length leads to comparatively long thermalization times, and therefore long evaporation sequences. When evaporating the sample close to the interspecies resonance later used in the experiment [140, 182], $a_{\text{Li,K}}$ could be tuned to achieve faster thermalization. The question arose to what extent the resonance's value of $R^* = 2241 a_0$ influences the thermalization dynamics.

Figure 5.15 shows a test of such a scenario in the case of a Li-K mixture. For this simulation, a similar setup as in Section 5.1.2 was used, with $N_{\text{Li}} = 3333$, $N_{\text{K}} = 1000$, $T_{\text{Li}} = 100$ nK and $T_{\text{K}} = 280$ nK chosen to reflect the conditions in the experiment. The thermalization time τ was then extracted by fitting the model in Eq. (5.30) to the data. This was done once with $R^* = 0$ and once for $R^* = 2241 a_0$ [140, 183]. Figure 5.15 shows the variation of τ in both scenarios, and the ratio of these thermalization times with a . Around $-6000 a_0$, thermalization happens faster, by up to 30% in the narrow-resonance scenario, whereas in the

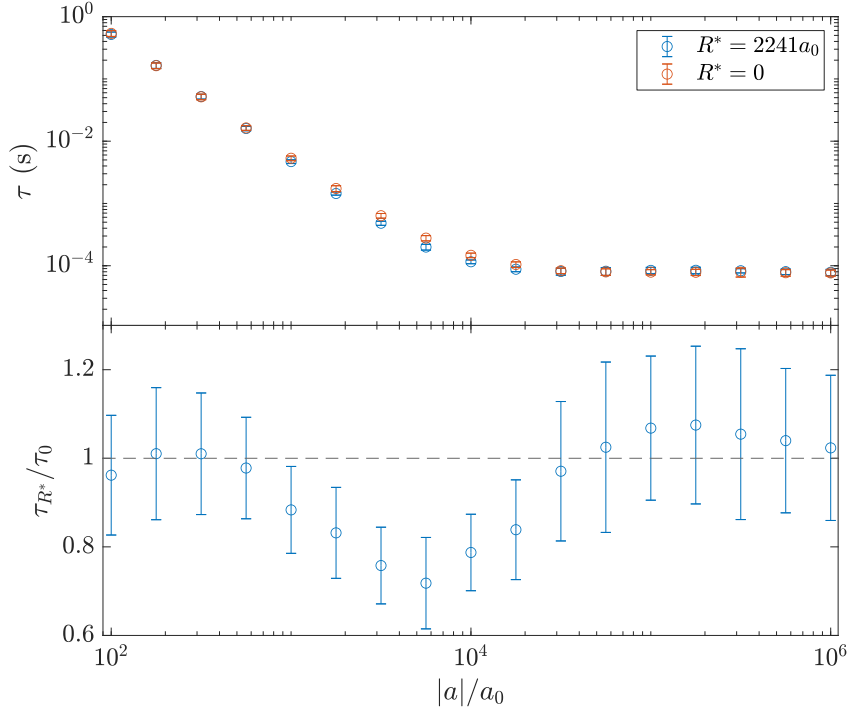


Figure 5.15: Upper panel: thermalization times in the attractive regime for a narrow resonance with $R^* = 2241 a_0$ and a broad resonance with $R^* = 0$. The lower panel shows the ratio of the thermalization times for narrow (τ_{R^*}) and broad resonances (τ_0).

weakly interacting regime, the difference is negligible. In the universally limited regime, thermalization is slightly slower, although the effect is comparable to the error bar.

The question arises, if faster thermalization can be attributed to only an overall increase of scattering rates. The upper panel of Fig. 5.16 shows the ratio of scattering rates of the two scenarios. In the region around $-6000 a_0$ the scattering rate is increased by up to 25% for the narrow resonance, whereas for higher scattering lengths it is slightly decreased. As the 25% higher scattering rate is not enough to fully account for the 30% reduction in thermalization time, we turn to the mean energy transfer per collision.

According to Eq. (5.29) we can extract the mean energy transfer per collision in the simulation

$$\langle \Delta E \rangle_{\text{sim}} = \frac{3}{2} k_B (T_K - T_{\text{Li}}) \frac{N_K N_{\text{Li}}}{N_K + N_{\text{Li}}} \frac{1}{\tau \Gamma_C} \quad (5.40)$$

from the measured values for the thermalization time τ and scattering rate Γ_C . The data is shown in the lower panel of Fig. 5.16, normalized to the theoretical value $\langle \Delta E \rangle = \zeta k_B (T_K - T_{\text{Li}})$ of Eq. (5.26). In the low-energy limit ($|ka| < 1$), the

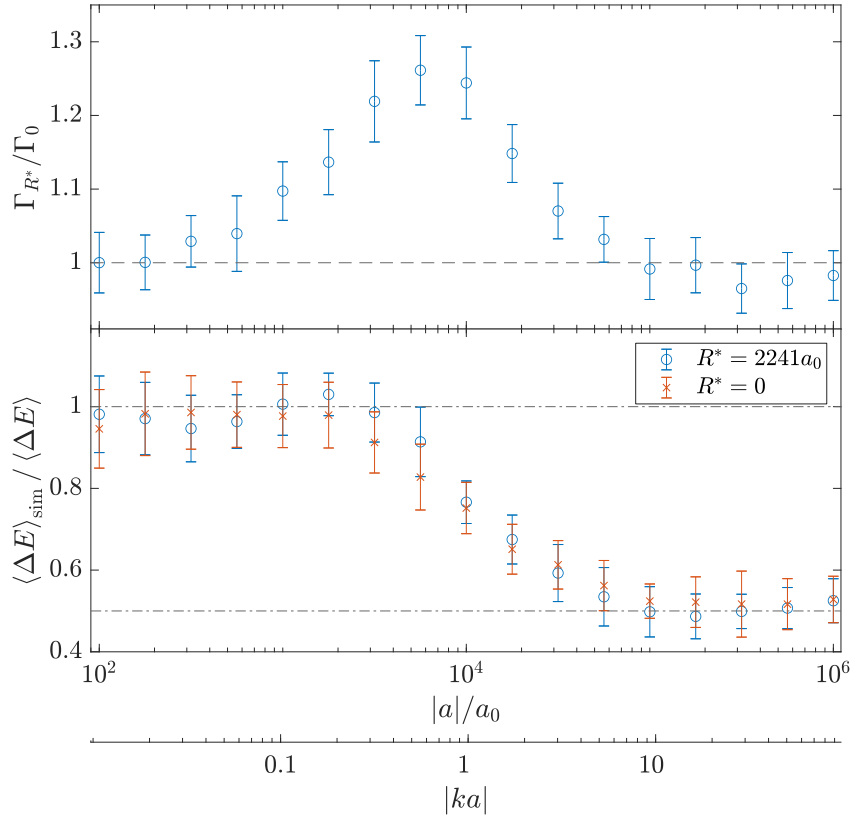


Figure 5.16: Evolution of the ratio of the scattering rates (upper panel) and energy transfer per collision (lower panel) over the scattering length for a narrow (blue) and a broad resonance (red). The average energy transfer per collision was extracted from the measured values of τ and Γ_C and then normalized to the theoretical result for $\langle \Delta E \rangle$ (see text). Dash-dotted lines indicate the theoretical values in the low-energy (1) and in the universal regime (1/2), respectively

simulation recovers the theoretical value, whereas in the unitarity regime ($|ka| > 1$), the mean energy transfer per collision drops to half of that value [175, 184]. Since the increase of the scattering rate in the narrow-resonance scenario comes from a selective promotion of collisions with certain energies, $\langle \Delta E \rangle_{\text{sim}}$ is also modified. For this particular scenario, the mean energy transfer per collision is increased by up to 10% in the region around $-4000 a_0$, which, together with the increased scattering rate, explains the 30% reduction in thermalization time. Even though the statistical variation in this data set does not allow for a clear statement, this behavior is consistent with a Monte Carlo evaluation of the integral in Eq. (5.3) multiplied with ΔE [129, 184].

In conclusion, in this particular case, the thermalization rate is enhanced by up to 30% due to the narrow nature of the resonance, which is a small gain compared to

the improvement over three orders of magnitude when going from the background scattering length to close to resonance. At the scattering length of $-6000 a_0$ the maximum of the scattering rate is shifted from $1.71 \bar{v}_r$ for the broad resonance to $1.93 \bar{v}_r$ for the narrow resonance, a relatively small shift. By going further away from the resonance center, the maximum can be shifted to even higher velocities, which might be beneficial when (forced) evaporative losses are present as in the FeLiKx experiment. In this case it could be possible to prevent losses of high-energy atoms of the hot minority component through enhanced thermalization. Evaporation dynamics have been modeled with DSMC simulations [163], but exceed the scope of this thesis.

5.4 POSSIBLE EXTENSIONS AND LIMITATIONS OF THE MODEL

So far, systems were studied in free-space or in a homogeneous trapping potential with infinitely hard walls. However, the algorithm can be extended to work also in an arbitrary trapping potential V . Furthermore, it would be possible to modify the collision process to include quantum statistics. Here, we discuss possible extensions and limitations of the model, for example at dense conditions.

5.4.1 Harmonic Potentials

To include other trapping potentials, the calculation of the first simulation step is replaced with an appropriate numerical method to solve the differential equation of motion. In the Dy-K experiment, the trapping potential is generated from optical dipole traps with a Gaussian beam profile. As a good approximation, in the central region the potential takes the form

$$V_i(r) = \frac{1}{2} m_i \omega_i^2 r^2, \quad (5.41)$$

where ω_i is the angular trapping frequency per species. To solve the classical equations of motion of the particles in an external potential, the velocity Verlet algorithm [185] has been used in MD and DSMC schemes. The propagation of $\mathbf{r}(t_n)$ and $\mathbf{v}(t_n)$ to $t_{n+1} = t_n + \Delta t$ is done according to

$$\begin{aligned} \mathbf{v}(t_{n+1/2}) &= \mathbf{v}(t_n) - \nabla V(r(t_n)) \Delta t / 2m \\ \mathbf{r}(t_{n+1}) &= \mathbf{r}(t_n) + \mathbf{v}(t_{n+1/2}) \Delta t \\ \mathbf{v}(t_{n+1}) &= \mathbf{v}(t_{n+1/2}) - \nabla V(r(t_{n+1})) \Delta t / 2m. \end{aligned} \quad (5.42)$$

The Verlet integrator is a symplectic integrator, which means that it conserves energy and the volume in phase space, which will become especially important when quantum statistics are considered. The global error for \mathbf{r} and \mathbf{v} is of order $\mathcal{O}(\Delta t^2)$.

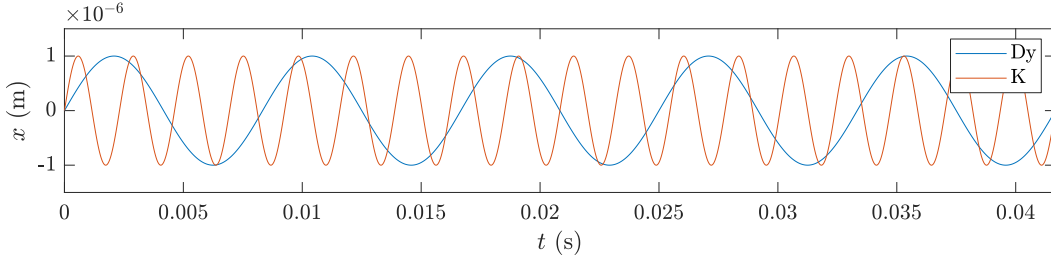


Figure 5.17: CoM motion of Dy and K without interactions when starting the simulation with a finite CoM velocity.

Here we have assumed an isotropic trap, but the simulation can be generalized to different trapping frequencies in three directions.

The easiest way to verify the correct behavior of the integrator is to look at the sloshing mode in the non-interacting mixture. In this case, the collision integral is 0, and we are left with the second order differential equation for the motion in the trapping potential for each particle, which can be solved analytically. The sloshing mode is also used in real experiments to characterize the trapping potential, as it does not depend on intraspecies interactions. Fig. 5.17 shows the CoM motion of the two species, when the cloud is given a finite uniform CoM velocity at the start. The simulation reproduces the uncoupled sinusoidal oscillations, which are the analytic solution to the uncoupled harmonic oscillator differential equation, quantitatively very well. Furthermore, if a breathing mode is excited, this would hint at a problem with the initialization of position and velocity of the particles.

5.4.2 Collision Rate and Species Separation

A second check of the correct behavior in the trap can be done by comparing the measured scattering rate to the theoretical scattering rate

$$\Gamma_C = \bar{n}\sigma\bar{v}_r. \quad (5.43)$$

In the case of a harmonic trap, the overlap integral takes the form

$$\bar{n} = \int n_K n_{Dy} d^3r = \frac{N_K N_{Dy}}{\left(2\pi \left(\sigma_{r,K}^2 + \sigma_{r,Dy}^2\right)\right)^{3/2}}. \quad (5.44)$$

Interestingly, what we find here is qualitatively different from what we saw in the box potential. As can be seen in Fig. 5.18, for a dilute gas and the low-energy cross section $\sigma = 4\pi a^2$,⁷ the simulated scattering rate agrees well with the theoretical

⁷ Note that here the low-energy cross section was used to be able to easily recognize problems with the simulation. The universal cross section will be limited by the relative momentum of collision pairs,

prediction, whereas for dense gases, $\Gamma_{\text{sim}}/\Gamma_C$ drops proportionally to $(a/\bar{r}_{\text{rel}})^{-3}$. This behavior is the same, whether the collisions were only counted without actually changing the particle's velocities, or if the velocities were also modified. As in the case of the box trap before, we assume that this is in part due to the scattering length exceeding the sample size, as well as an effective limitation of the scattering rate by the blocking time. Evidently, the simulation, as well as the theoretical prediction of the scattering rate, lose their validity here, however, quantum effects become relevant anyways when the scattering length approaches the inter-particle distance. These strongly correlated systems should be treated with other theoretical descriptions.

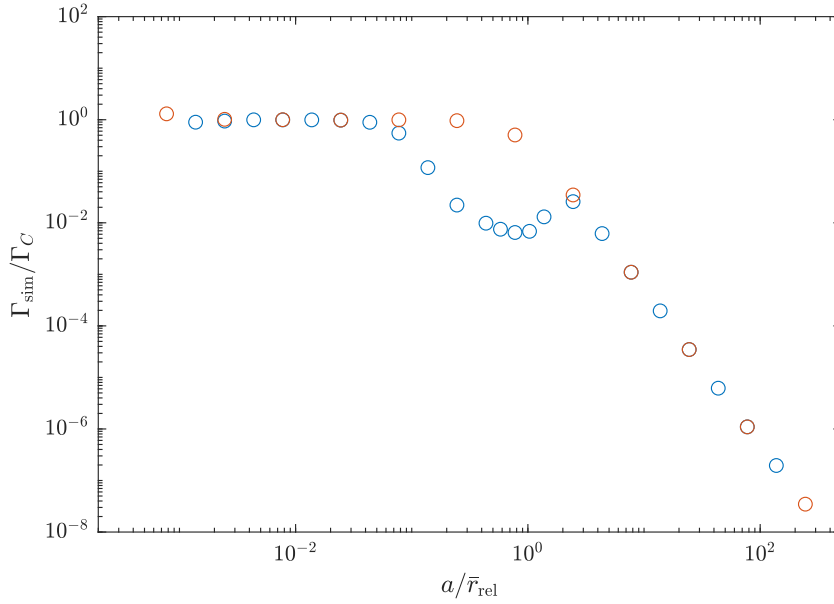


Figure 5.18: Behavior of the simulated collision rate depending on the ratio of scattering length a to mean relative distance \bar{r}_{rel} . Blue shows a full simulation, whereas for the points in red, only the collisions were counted without changing the velocities of the colliding particles.

In the intermediate regions, however, the simulations performing the full collision exhibit a strong reduction of the collision rate that is not present in the counting case. This suggests that the collisions alter the atomic distribution f far away from its equilibrium value. We check this by looking at the evolution of the number of collisions $N_c(t)$ and the radial profiles at different times during the simulation. Figure 5.19 shows an example at a scattering length of $9.5 \times 10^4 a_0$. At the start of the simulation, after the initialization of the equilibrium atomic distribution

which makes the identification of problems more difficult in some cases, as the radius of the cross section depends on the individual particles, and some effects are smeared out in the thermodynamic average.

according to Boltzmann statistics, the scattering rate is close to the case where we only count collisions for a few ms, after which $N_c(t)$ flattens. Coincidentally, the radial distribution of the particles changes, concentrating K in the middle of the trap with an outer shell of Dy. After 15 ms the clouds have fully separated, with a distance roughly equal to $\sqrt{\sigma/\pi}$, the diameter of the interaction spheres. From this point on, the scattering rate settles to a constant value much smaller than the theoretical prediction. We assume that this is a result of the reduced spatial overlap and non-thermal velocity distribution. In this case, the sample cannot be described by the uncorrelated equilibrium distributions f anymore, and the Boltzmann equation fails to make accurate predictions.

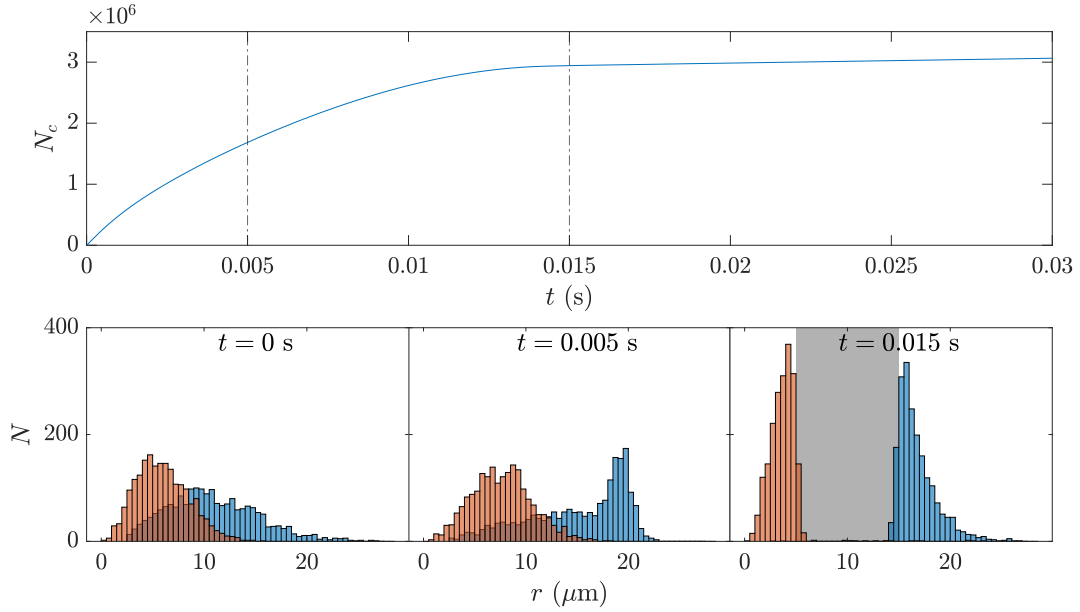


Figure 5.19: Evolution of the number of collisions N_c with time (upper panel), and the radial profiles of Dy (blue) and K (red) at different points in time (lower panels). The gray shaded area indicates $\sqrt{\sigma/\pi}$ at the scattering length of $9.5 \times 10^4 a_0$ used in this simulation, which matches the separation of the two species.

This species separation can be understood in terms of a competition between the trapping forces and the interspecies interaction, which is repulsive in the hard sphere model. Since K experiences a much stiffer trap in this scenario ($\omega_K/\omega_{Dy} = 3.6$), it is concentrated in the center, whereas Dy is expelled to the outer regions. The separation breaks down if $\sqrt{\sigma/\pi}$ becomes larger and pushes Dy further outside to a point where the restoring force of the trap overcomes the interaction, at which the collision rate recovers the values obtained by only counting collisions. This behavior can be reversed by changing the trapping frequencies of the two species to a point where $\sigma_{r,K} > \sigma_{r,Dy}$. Note again that this was carried out using the low-energy

cross section with a large value of the scattering length. With a temperature of the sample of $T = 0.5 \mu\text{K}$, we are well into the unitarity regime, where the cross section is limited by the relative momentum. Using the unitary cross section will lead to a similar effect of changing the overlap, but will smear out the borders of the separation, therefore making it harder to identify the mechanism limiting the scattering rate.

Although a similar species separation has been observed and extensively studied with two BECs [186, 187], where the ratio of inter- to intraspecies interactions determines the (im-)miscibility of the mixture, the promoting intraspecies interactions are not present in our simulation. This hints at a fundamental problem either with the hard sphere interaction picture itself or our treatment of it. Although here the low-energy cross section was used to make this effect more visible, the same effect happens, to a lesser extent, when using the universally limited cross section. Since in this case the effective scattering length depends on k and is different for each pair, the separation is more washed out.

This behavior starts to appear in a regime, where Pauli blocking should prevent the formation of the dense core. Indeed, models that include quantum statistical effects [165] and mean-field potentials [174] do not show such a behavior in trap. However, the collision model employed in these works computes the closest approach of two colliding particles before the collision and allows the particles to penetrate the hard sphere.

5.4.3 *Collective Oscillations*

In the case of non-zero interspecies interaction, we expect that oscillations can be excited by the momentum transfer between the two species. If one species is given a kick, the collisions should excite some oscillation also in the other species. The response of the system depends on the number of collisions per oscillation period.

In the so-called collisionless regime, only few collisions happen during a full oscillation period, which will transfer only some small amount of momentum. The trapping potential then forces the species to oscillate with their own trapping frequency. This can be seen in the upper left panel of Fig. 5.20. In this case, both species will oscillate at their respective trapping frequency.

When the collision rate per atom Γ_C becomes much bigger than ω , this is called the collisional hydrodynamic regime.⁸ The atom is colliding so often that the trapping force can not lead to an oscillation with the bare trapping frequency. Instead, the two samples oscillate locked together, with a new combined frequency different from the trapping frequencies. This can be seen in the lower left panel in

⁸ It should be noted that hydrodynamic behavior is also present in a superfluid, where it is not a result of the high collision rate, but the long-range order in the one-body (bosons) and two-body (fermions) densities [111].

Fig. 5.20. In the hydrodynamic regime, the motion can be described by solving the hydrodynamic equations with a scaling Ansatz [188], arriving at a coupled mode frequency

$$\omega_h = \sqrt{\frac{N_K m_K \omega_K^2 + N_{Dy} m_{Dy} \omega_{Dy}^2}{N_K m_K + N_{Dy} m_{Dy}}}. \quad (5.45)$$

In the case of equal numbers of atoms for both species and our standard trapping frequencies of $\omega_{Dy} = 2\pi \times 120$ Hz and $\omega_K = 3.6 \omega_{Dy}$, we calculate $\omega_h = 2\pi \times 220.6$ Hz, which is reproduced by the simulation.

Between the collisionless ($\omega \gg \Gamma_C$) and the hydrodynamic regime ($\omega \ll \Gamma_C$), there is a crossover which features strong damping of the oscillations. Theoretically, collective oscillations throughout the crossover have been studied by solving the Boltzmann equation with different techniques, including Monte Carlo methods [165, 189, 190] or the method of averages [189]. By employing a linearization of f and a relaxation time approximation [191], a set of coupled differential equations can be obtained, with which the different modes and also the crossover regime can be studied.

Interestingly, it was found that the behavior of the system can also be modeled by extending the harmonic oscillator differential equations for the center of mass position of the two gases with a phenomenological friction term that couples the two systems via their velocities [192–194]:

$$\begin{aligned} x''_{Dy} &= -\omega_{Dy}^2 x_{Dy} - \frac{F_d}{N_{Dy} m_{Dy}} \\ x''_K &= -\omega_K^2 x_K + \frac{F_d}{N_K m_K}. \end{aligned} \quad (5.46)$$

The drag force F_d takes the form [194]

$$F_d = \underbrace{\frac{4}{3} \frac{m_K m_{Dy}}{m_K + m_{Dy}} \bar{n} \bar{\sigma} \bar{v}_r}_{\alpha} (x'_{Dy} - x'_K), \quad (5.47)$$

where $\bar{n} = \int n_K n_{Dy} d^3r$ is the overlap integral. The hereby defined coefficient α depends on the collision rate and therefore the interaction strength between the two species, and has a dimension of mass per time. This phenomenological model reproduces the result of Ref. [192] in the case of equal mass and atom numbers for the two species.

A comparison of the simulation and the phenomenological model with matched parameters can be seen in Fig. 5.20, with the value for γ_K/ω_K extracted from the simulated scattering rate. In the collisionless (upper panels) and the hydrodynamic regime (lower panels), the two approaches agree very well. However, the aforementioned species separation (see Sec. 5.4.2) strongly influences the behavior

in the intermediate regime (middle panels). Initially, the scattering rate is high enough to exhibit a locked but strongly damped oscillation that closely matches the phenomenological model, but the separation slowly starts to form. After about 0.01 s the overlap is significantly reduced, leading to a lower collision rate, while the value of γ_K/ω_K drops from 14 to 1. This results in a decoupling of the two oscillations, while the phenomenological model maintains a locked oscillation with strong damping.

Figure 5.21 shows the spectrum of the center of mass position of K obtained by solving Eq. (5.46) for different values of α . As can be seen, in the collisionless regime where α is small, K only exhibits a very small oscillation at its own trapping frequency, excited by very few collisions with Dy. In between, the motion of the two species is strongly damped, as indicated by the width of the spectra. Figure 5.22 was obtained from the simulation and qualitatively shows the same behavior, even in the intermediate regime. However, because of the problems associated to the scattering rate and the species separation, a quantitative comparison, especially with regards to the interaction strength and drag force, is outside the scope of this thesis.

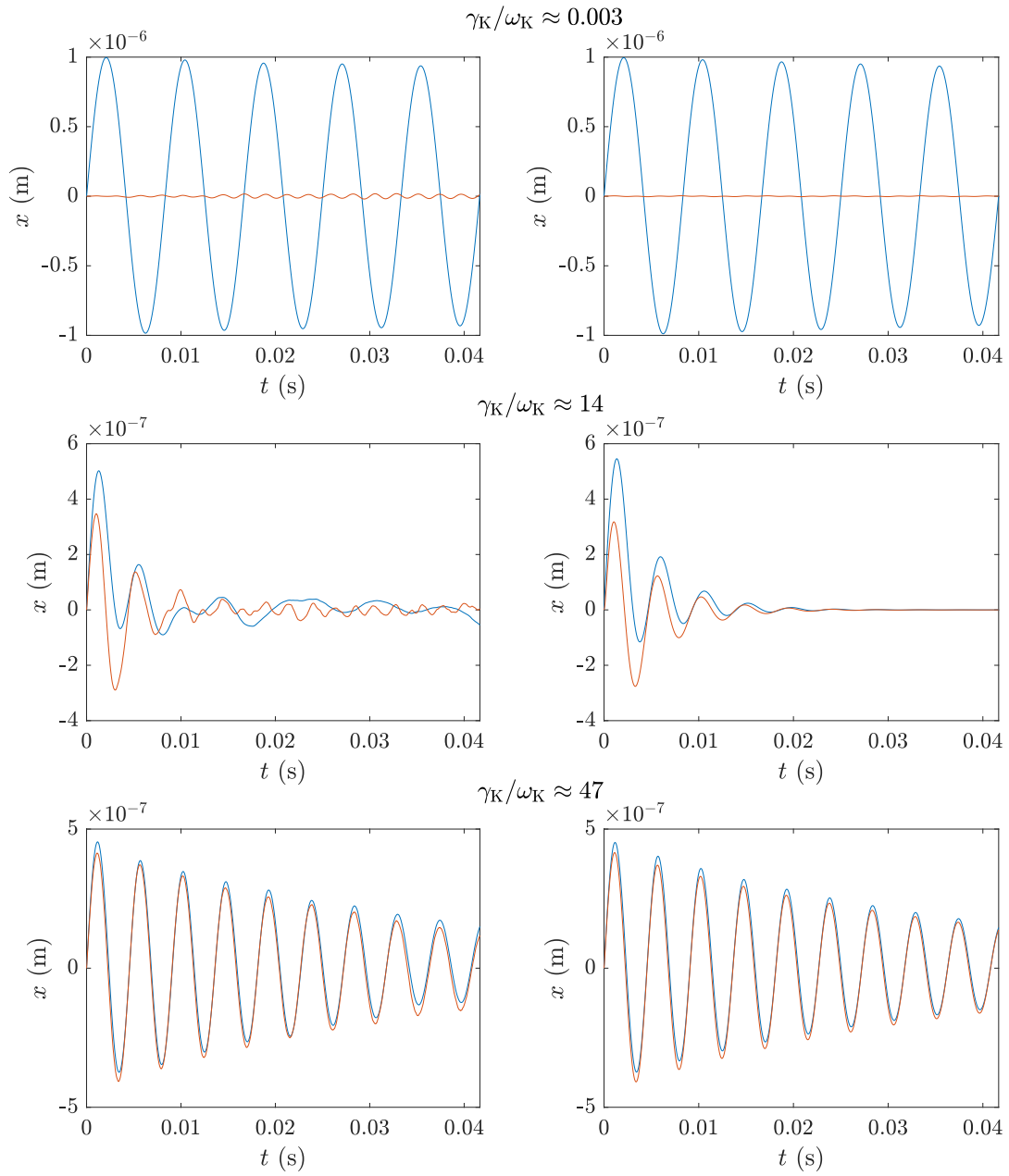


Figure 5.20: Example traces of Dy (blue) and K (red) CoM motion in the collisionless, intermediate and hydrodynamic regime (top to bottom), obtained from the simulation (left side) and differential equation in Eq. (5.46) (right side). The parameters for the differential equation were hand-matched to fit the behavior of the simulation.

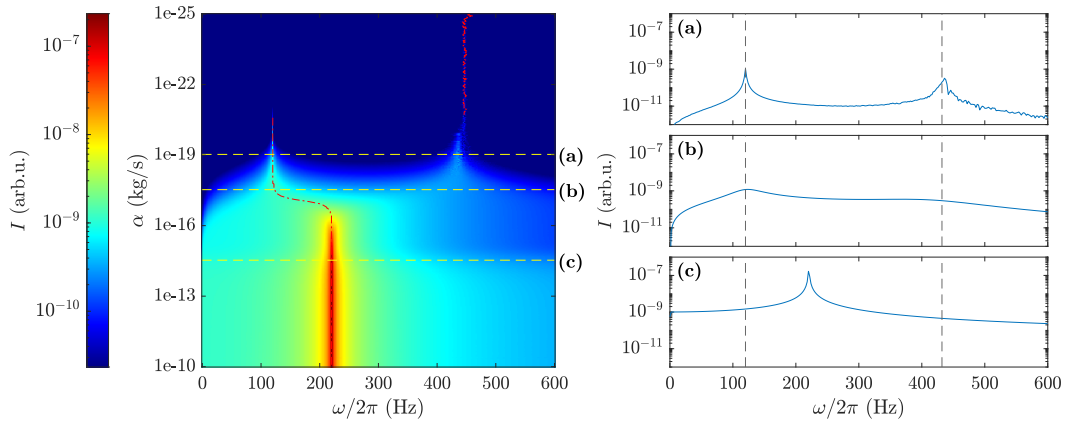


Figure 5.21: Fourier spectra of the K center of mass motion for different values of α . The red dashed line indicates the position of the highest frequency component. The right side shows spectra at specific values of α indicated by the dashed lines on the left. Vertical dashed lines in the spectra indicate the position of the trapping frequencies ω_K and ω_{Dy} .

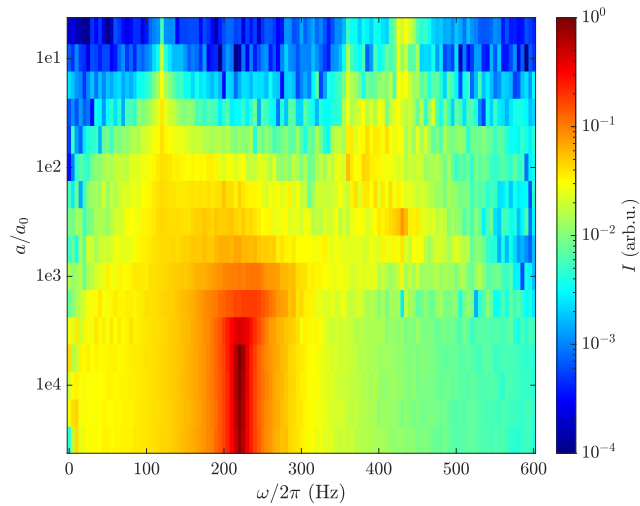


Figure 5.22: Simulated spectra for the K center of mass motion with varying interaction strength.

5.4.4 *The Effect of Quantum Statistics*

As we have seen now, many of the interesting phenomena appear at or close to regimes where quantum statistics are relevant. In the initial measurements of hydrodynamic expansion for the characterization of the Feshbach resonances, the clouds were only near-degenerate, and the level of degeneracy decreases as the clouds expand. As a result the current model without accounting for quantum statistics is a good approximation. As the experimental apparatus evolves, and a more deeply degenerate regime becomes accessible, the model should be extended to include quantum statistics.

In general, this can be done by extending the collision operator to [195, 196]

$$I_{\text{coll}}(f_i, f_j) = \int d^3v_j \int d\Omega \frac{d\sigma}{d\Omega} |\mathbf{v}_i - \mathbf{v}_j| \left[f'_i f'_j (1 \pm f_i)(1 \pm f_j) - f_i f_j (1 \pm f'_i)(1 \pm f'_j) \right]. \quad (5.48)$$

The $(1 \pm f'_i)(1 \pm f'_j)$ term includes the effect of Bose-Einstein (+) or Fermi-Dirac (−) statistics and enhances or prevents scattering in already occupied phase space-regions, respectively. When assuming that quantum statistical effects do not play any role, which is a reasonable approximation for our system in the expansion, the form of $I_{\text{coll}}(f_i, f_j)$ reduces to Eq. (5.3).

Solving the quantum collision integral requires knowledge about the phase-space density f' of the final state after the collision. Different methods have been implemented [163, 165, 197–199] to estimate f' from initial parameters or the test particle distribution, however, some require very high numbers of particles [200] to avoid errors from numerical fluctuations, which further increases the complexity and computation time of the simulations. Furthermore, for an in-depth study of collective oscillations it might be necessary to include an additional effective mean-field potential in the propagation of particles as well as in-medium effects in the scattering amplitude [174, 201].

5.4.5 *Summary*

This simulation was initially developed to better understand the data acquired by the experiment. After gaining good agreement between simulation and experiment, the model was subsequently extended to account for different starting parameters, and the calculations were refined to speed up the computation. The largest effect was obtained by sorting the atoms into cells for collision detection similar to the DSMC approach. The following careful check of the method in situations where an analytic description is available revealed its strengths and weaknesses.

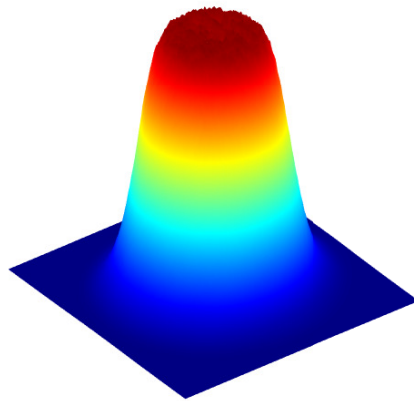
The model works well with dilute gases or free-space systems without external confinement, and provides a simple tool to gain understanding of the experiment, e.g. the expansion of an interacting sample. However, modeling the atoms as hard,

impenetrable spheres leads to problems in the case of dense samples, and it seems to not be sufficient anymore to only consider two-particle interactions. As discussed already, usually other methods are used for describing gases in such conditions, for example the mean-field approach, which can also account for n -body interactions. The hard sphere model can lead to nonphysical behavior, which should be kept in mind when choosing the parameters of the simulations. At this point it should also be noted that the closest-approach technique [165] and the DSMC method do not suffer from this problem. Indeed, it has been shown that DSMC methods can also work for regimes where the mean free path is much shorter than the relevant length scales of the system [159].

Since more sophisticated simulation models and theoretical frameworks already exist that avoid or properly address these problems, the extension of our approach seems unnecessary at this point. As a simple model to quickly gain a basic understanding of phenomena appearing in the experiment (e.g. the effect of the R^* parameter) it works reasonably well, but for more thorough analysis, a collaboration with theory groups will be more fruitful.

Part III

FLAT AND ARBITRARY POTENTIALS FOR ATOM MIXTURES



Experimental profile of a flat-top beam.

MOTIVATION

In many cases, the particular realization of the trapping potential for the atoms is a key ingredient determining the possible success of the experiment. This chapter gives a short introduction to optical trapping, why control over the trapping potential is desired in our experiment, and which particular geometries we are interested in.

6.1 TRAPPING TECHNIQUES

For neutral atoms, three different interactions can be used for trapping, which differ in their properties and area of application [202]. Traps relying on absorption-emission cycles of photons often form the first steps in an experimental sequence. They operate on wavelengths close to atomic transitions and have a strong trapping effect that can be more than 1000 times stronger than gravity, allowing them to capture even hot samples. However, the photon recoil from the re-emission process prevents cooling to low temperatures, and radiation trapping and light-assisted inelastic collisions limit the achievable density, making it hard to reach degenerate conditions with these traps [203–205].

Magnetic traps utilize the interaction of the atom's magnetic dipole moment with a magnetic field. High-field seeking atoms will move towards a maximum in magnetic field strength, whereas low-field seeking atoms move towards a minimum. Inhomogeneous fields with local minima can be generated easily with wire coils or permanent magnets, and this technique was therefore predominantly used in the early years of ultracold atomic physics [206]. However, the internal atomic state determines the coupling to the magnetic field and therefore the magnitude and sign of the trapping force (high-field or low-field seeking). Additionally, the trapping geometry is limited by the possible arrangements of coils or permanent magnets.

Optical dipole traps, the third option for trapping neutral atoms, usually operate at wavelengths further away from atomic transitions. The trapping force results from the electric dipole interaction of the atom with the light field. The corresponding potential energy of an atom in a light field of angular frequency ω is then given by

$$V(\mathbf{r}, \omega) = -\frac{2\pi a_0^3}{c} \tilde{\alpha}(\omega) I(\mathbf{r}). \quad (6.1)$$

The geometry or shape of the potential V is governed by the shape of the intensity distribution $I(\mathbf{r})$, which can be controlled to some extent.

The magnitude of the potential is influenced by $\tilde{\alpha}(\omega)$,¹ the real part of the dynamical polarizability (DP) of the atom. The polarizability is a measure of the ability of the electronic shells to rearrange in an external oscillating field, which therefore develop an electric dipole that couples to the field and changes the potential energy of the atom. It is in general strongly dependent on ω and its shape is determined by the atom's electronic transition spectrum and the atom's internal state. For positive values of $\tilde{\alpha}(\omega)$, the atom will seek areas with high optical intensity $I(\mathbf{r})$, and vice versa for negative values, which allows for great flexibility and tailored potentials. As we will see later, under the right conditions the polarizability can even be independent of the particular sub-state of the atoms, which allows for experiments studying the sub-state dynamics. For a sufficient detuning from an electronic transition, the absorption processes will be suppressed, but there will still be a significant dipole interaction. This greatly reduces the heating of the atomic sample and offers ideal conditions to reach low temperatures and to conduct experiments on the timescale of seconds. These properties have made optical dipole traps an ubiquitous tool in the field of ultracold atoms.

6.2 ATOMIC POLARIZABILITY

In quantum mechanics, the atomic polarizability operator is described as a 3×3 tensor $\tilde{\alpha}$ [207], and the Hamiltonian in dependence of the electric field \mathbf{E} is written as

$$H = -\frac{1}{2}\mathbf{E}^\dagger \tilde{\alpha} \mathbf{E}. \quad (6.2)$$

In some cases it is sufficient to consider only the diagonal terms of the 3×3 tensor to describe the atom-light interaction. This is then known as the scalar contribution, which is dominating especially for alkali atoms and far away from any atomic transitions. However, an anisotropy in the atom's electronic structure is expressed by the off-diagonal entries, which can be separated into a vectorial and a tensorial contribution.

When considering an atom in a state with orbital angular momentum quantum numbers J and m_J in a field with intensity $I(\mathbf{r}) = \frac{\epsilon_0 c}{2} |\mathbf{E}(\mathbf{r})|^2$, then the potential can be written in the separation [208]

$$V(\mathbf{r}, \omega) = \frac{-1}{\epsilon_0 c} I(\mathbf{r}) \left[\alpha_s(\omega) + |\mathbf{u}^* \times \mathbf{u}| \cos \theta_k \frac{m_J}{J} \alpha_v(\omega) + \frac{3m_J^2 - J(J+1)}{J(2J-1)} \times \frac{3 \cos^2 \theta_p - 1}{2} \alpha_t(\omega) \right]. \quad (6.3)$$

¹ In this representation, $\tilde{\alpha}(\omega)$ is defined as the dimensionless real part of the dynamical polarizability normalized to the atomic unit of polarizability.

Here \mathbf{u} stands for the polarization vector and θ_k (θ_p) denotes the angle between the propagation (polarization) axis of the field and the quantization axis. This leads to three polarizability coefficients for scalar (α_s), vector (α_v) and tensor (α_t) contributions, which can be calculated as

$$\begin{aligned}\alpha_s(\omega) &= -\frac{1}{\sqrt{3(2J+1)}} \Re \left(\alpha_J^{(0)}(\omega) \right) \\ \alpha_v(\omega) &= \sqrt{\frac{2J}{(J+1)(2J+1)}} \Re \left(\alpha_J^{(1)}(\omega) \right) \\ \alpha_t(\omega) &= \sqrt{\frac{2J(2J+1)}{3(J+1)(2J+1)(2J+3)}} \Re \left(\alpha_J^{(2)}(\omega) \right).\end{aligned}\quad (6.4)$$

The complex polarizability $\alpha_J^{(k)}(\omega)$ can be calculated by applying the sum-over-states approach and is given by

$$\begin{aligned}\alpha_J^{(k)}(\omega) &= \sqrt{2k+1} \sum_{J'} (-1)^{J+J'} \left\{ \begin{matrix} 1 & 1 & k \\ J & J & J' \end{matrix} \right\} |\langle J' \| \mathbf{d} \| J \rangle|^2 \\ &\quad \times \frac{1}{\hbar} \left(\frac{(-1)^k}{\omega_{J,J'} - i\frac{\Gamma_{J'}}{2} - \omega} + \frac{1}{\omega_{J,J'} - i\frac{\Gamma_{J'}}{2} + \omega} \right).\end{aligned}\quad (6.5)$$

This is a summation over the contribution of all transitions to states J' , with a reduced dipole transition element $|\langle J' \| \mathbf{d} \| J \rangle|^2$, where $\omega_{J,J'} = (E_{J'} - E_J)/\hbar$ is the transition frequency between states with energies E_J , and $\Gamma_{J'}$ denotes the natural line width of the excited state. The curly brackets indicate the Wigner 6- j symbol that incorporates the dipole selection rules.

As we have seen, the trapping potential relates to the real part \Re of Eq. (6.5), whereas the off-resonant scattering rate relates to the imaginary part \Im . Considering a laser frequency ω far away from the resonance frequency of a single transition, i.e. $|\omega_{J,J'} - \omega| \gg \Gamma_{J'}$, their dependence

$$\begin{aligned}\Re \left(\alpha_J^{(k)}(\omega) \right) &\propto \frac{2\omega_{J,J'}}{\omega_{J,J'}^2 - \omega^2} \\ \Im \left(\alpha_J^{(k)}(\omega) \right) &\propto \Gamma_{J'} \frac{\omega_{J,J'}^2 + \omega^2}{\left(\omega_{J,J'}^2 - \omega^2 \right)^2}\end{aligned}\quad (6.6)$$

shows that a large detuning is beneficial to keep the scattering rate low, while still retaining a trapping effect.

A few special cases of Eq. (6.3) and (6.5) have to be considered. Firstly, in the case of linearly polarized light, the vectorial contribution vanishes. Secondly, as for alkali atoms in their ground state, where the orbital angular momentum $J = 1/2$,

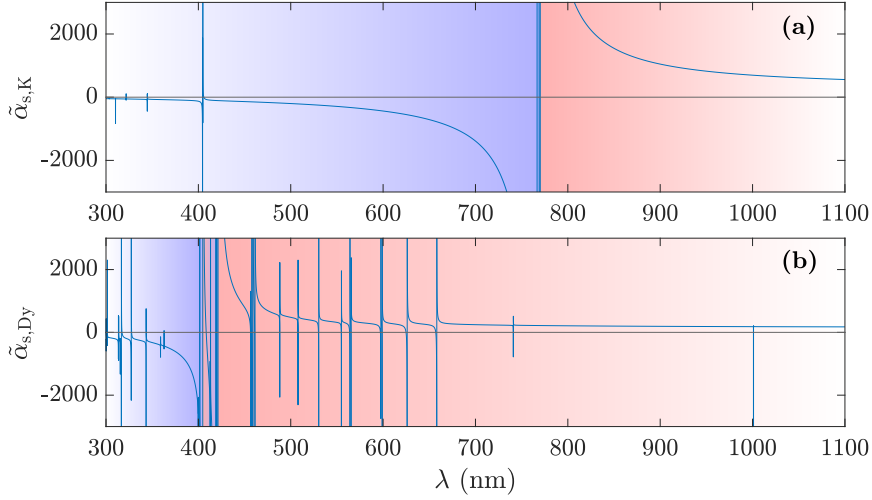


Figure 6.1: Calculated scalar polarizability of the K and Dy ground states, with data from [94, 210, 211]. Divergences in the polarizability appear at atomic transitions. Finite peak values are because of sampling errors. Blue (red) shading represents a mostly repulsive (attractive) interaction.

the tensor light shift vanishes, unless the detuning is on the order of the hyperfine splitting [207]. For other species, e.g., dysprosium, the tensorial contribution can be comparable to the scalar contribution. Thirdly, it is possible to reformulate this description in terms of the total angular momentum quantum number F , however, the difference is negligible for detunings larger than the hyperfine splitting [208]. Fourthly, the scaling terms in front of the vectorial and tensorial contributions in Eq. (6.3) are state dependent with m_J . This can be used for example to drive non-linear spin dynamics [209].

In our experiment, we focus on the case of linearly polarized light and atoms in the stretched state ($m_J = J$). We define

$$\tilde{\alpha}(\omega) = \tilde{\alpha}_s(\omega) + \frac{3 \cos^2 \theta_p}{2} \tilde{\alpha}_t(\omega) \quad (6.7)$$

as the dimensionless real part of the total dynamical polarizability normalized to the atomic unit of polarizability, with $\tilde{\alpha}_s$ and $\tilde{\alpha}_t$ the real parts of the scalar and tensorial contributions in the same normalization. Within a hyperfine manifold, $\tilde{\alpha}_s$ and $\tilde{\alpha}_t$ only depend on the wavelength.

Figure 6.1 shows a theoretical calculation of $\tilde{\alpha}_s$ for the K and Dy ground states in the range between 300 and 1100 nm. It is dominated by the broad transitions at 767 and 770 nm for K and 421 nm for Dy, however, the complex electronic arrangement of Dy results in many narrower transitions, and therefore a more complicated

structure of the polarizability. A standard wavelength for trapping is 1064 nm, as for most atoms this is far away enough from any transitions to avoid sizable scattering rates, while $\tilde{\alpha}(\omega)$ is still positive and large enough, and high-power lasers are readily available. That being said, over the typical tuning range of these lasers the ratio of polarizabilities of the two species remains almost constant at this wavelength, which limits the versatility of the experiment. However, with enough knowledge of the electronic structure, other wavelength ranges suitable for dipole trapping can be identified. For the combination of K and Dy, a blue detuning (repulsive interaction) for both species is possible below the 421 nm transition of Dy and the 405 nm transition of K, but generating enough optical power is difficult in this wavelength range. Another possibility is to use a wavelength close to and blue detuned to a Dy transition in the range between 450 and 767 nm. In this region the K polarizability is dominated by the D1 and D2 transitions and negative.

6.3 HARMONIC POTENTIALS AND EXOTIC PHASES

As already mentioned, the geometry or shape of the potential V is a direct result of the shape of the intensity distribution $I(\mathbf{r})$. In general, $I(\mathbf{r})$ can be chosen freely and shaped to some extent with some effort, however, most lasers and optical elements generate beams with a Gaussian intensity profile, which is a solution to the paraxial Helmholtz equation. Therefore, most dipole traps are realized by a Gaussian laser beam, which gives a confinement that is approximated very well around the center of the beam by a harmonic oscillator with potential energy

$$V(\mathbf{r}) = \frac{1}{2}m \left(\omega_x^2 x^2 + \omega_y^2 y^2 + \omega_z^2 z^2 \right) \quad (6.8)$$

in all three directions. Here, m is the mass of the atom and $\omega_{x,y,z}$ is the angular trapping frequency in the three directions. While this technique has been extensively used and refined throughout the last decades, the resulting potential often does not fit most manybody systems, e.g., condensed matter systems, which are usually uniform to some extent. In contrast, the density of a thermal gas in a harmonic trap has a Gaussian shape, as can be derived from the Maxwell-Boltzmann distribution. For fermionic gases below the Fermi temperature T_F , the local density approximation (LDA) can be used to estimate the density profile as

$$n(\mathbf{r}) = \frac{1}{6\pi} \left(\frac{2m}{\hbar^2} \right)^{3/2} [\mu - V(\mathbf{r})]^{3/2}, \quad (6.9)$$

where μ is the chemical potential. It is derived from the assumption that in a small (local) region of the trap, the density can be viewed as constant, as long as the potential is slowly varying. It is clear that for a harmonic potential, the density will exhibit a r^3 -behavior, meaning that the density will vary over the sample, locally changing the thermodynamic properties.

Although many methods have been developed to extract relevant properties from harmonically trapped gases, in some systems the confinement can alter the physical phenomena to be studied. For example, as we have seen in Section 1.3, the occurrence of exotic phases strongly depends on the polarization of the mixture. Generally, in a harmonic trap, the polarization varies locally across the trap, which corresponds to a line in the phase diagram. This can lead to different phases being present at different areas in the trap, for example, in the case of a spin-imbalanced mixture, a superfluid core and a partially polarized normal gas on the outside [66, 67]. In mass-imbalanced systems, where the polarizabilities of both species are generally different, the varying local population imbalance could even lead to a three-shell structure [212]. It is also proposed that a FFLO phase may exist at a certain radius or narrow shell in the trap [213]. While this can be an advantage because a broader phase space region can be probed at once, this also implies some problems.

To detect phase separation, in-situ imaging is required to be able to measure the polarization of the sample throughout the trap, because in time-of-flight imaging, the spatial information would be washed out. This results in the need for a good imaging system. To detect FFLO-type pairing in cold atom experiments, two methods were proposed [214]. In the pair projection technique, Cooper pairs are projected onto molecules, with which the total pair momentum can be determined after time-of-flight imaging [49]. In the other technique, correlations in the shot noise in time-of-flight images are studied [215]. While in the BCS case, the projected pairs have zero net momentum, FFLO-type pairing would show up at non-zero values. In the case of a uniform system, this leads to a pronounced peak in the projected pair momentum distribution at a certain momentum with value q . However, as in a harmonic potential the local atomic density and polarization both vary, the value of q changes locally as well. Time-of-flight imaging effectively averages all the different trap regions with changing q , leading to a smearing of the peak [216] and rendering the detection of the elusive FFLO phase hard.

As another example, near second order transitions, where the correlation length diverges, the LDA breaks down, which complicates theoretical descriptions [217]. On the more technical side, other measuring techniques that globally probe the system similar to time-of-flight imaging, such as Bragg, Rabi and Ramsey spectroscopy, also suffer from the mixing of signals from several trap regions with different densities and thermodynamic properties [217].

6.4 BOX TRAPS AND ARBITRARY POTENTIALS

Many of the aforementioned problems can be avoided by studying uniform systems experimentally, instead of relying on the well-tested Gaussian traps. As we still need to trap atoms in order to study them, box shaped potentials of the form

$$V(\mathbf{r}) = \begin{cases} 0 & r < r_b \\ V_b & r \geq r_b \end{cases}, \quad (6.10)$$

can be used. A box with radius r_b has a barrier of height V_b , which prevents the atoms to travel out of the trapping region. At the same time, Eq. (6.9) shows that $n(\mathbf{r})$ will be homogeneous in the central part of the box, circumventing many of the aforementioned problems.

Recently, many different techniques have been studied to achieve uniform trapping potentials in one to three dimensions. These involve, among others, time-averaged potentials, and beam shaping using holographic methods or amplitude masks with both red- and blue-detuned light. For an in-depth discussion of these techniques and experimental results obtained by using them, we point to two recent reviews [217, 218].

Beam shaping techniques have also been employed to realize other arbitrary potentials in cold atom experiments [218, 219]. These include the generation of tweezer arrays for quantum simulation [220], the preparation of the atomic density in a quantum simulator to realize a Fermi-Hubbard antiferromagnet [221], or the engineering of potentials to study transport phenomena with ultracold fermions [222].

As another interesting aspect, time averaged laser beams have been used to compensate gravity for cold atoms [223]. By modulating the position of the beam, an optical potential with a linear gradient along the direction of gravity was generated. With the right choice of $\tilde{\alpha}$ and I_0 , the effect of gravity on the atoms can be canceled. Such a technique is even more desirable in the case of mixtures of very different atomic species, like Dy and K in our case. The standard way to levitate atoms is to generate a linear magnetic gradient in the magnetic field \mathbf{B} in z -direction,

$$\frac{\partial B}{\partial z} = \frac{mg}{|\mu|}, \quad (6.11)$$

which depends on the magnetic moment μ and the mass m of the atom. Naturally, to levitate two species at the same value of the gradient, their ratio $|\mu|/m$ has to be equal, a condition that is rarely realized since μ is only tuneable by changing the atomic state. However, using an optical linear gradient, the condition now changes to $\tilde{\alpha}/m$ being equal for both species, which can be met by changing the wavelength of the laser. The optical levitation method has another advantage, especially for

systems with highly magnetic atoms, as for example Er and Dy. The Feshbach spectrum of these systems is very dense and also features very narrow resonances. As a result, it is important that the magnetic field is stable on the mG level to avoid heating of the sample and artificial broadening of narrow features. Magnetic levitation can add another source of magnetic noise to the system, which can become a problem if the hardware is not designed well enough. Furthermore, Dy exhibits a very chaotic Feshbach spectrum, where narrow features can be as small and as close together as a few mG. The necessary gradient for levitation can be large enough so that the field changes by a few mG over the extent of the sample, which can also possibly lead to broadening of those narrow features [224]. In general, because of the high magnetic moment of Dy, any problems with magnetic fields (field stability, noise, inhomogeneity...) will have considerable impact on the sample, which is why we want to avoid magnetic levitation.

6.5 CONTENTS OF PART III

The main motivation of this part was to develop techniques for our experiment to be able to produce arbitrary optical potentials, with a focus on flat traps for homogeneous systems and optical levitation. Trapping two species simultaneously requires that the sign of $\tilde{\alpha}(\omega)$ is equal for both species, either attractively or repulsively interacting with the light. However, other configurations can be used to realize species selective control also with Gaussian beams, which can help to realize superfluid conditions [225]. And as we have seen before in the case of optical levitation, it can be interesting to be able to tune the ratio $\tilde{\alpha}_K(\omega)/\tilde{\alpha}_{Dy}(\omega)$ precisely to the mass ratio. However, this requires a detailed knowledge about the spectrum of $\tilde{\alpha}(\omega)$, so Chapters 7 and 8 will feature two publications, in which we investigated $\tilde{\alpha}_{Dy}(\omega)$ at 1064 nm and around the dysprosium 626-nm resonance in more detail.

The detailed knowledge of the polarizability enables us to realize red- and blue-detuned dipole traps. To extend these traps from Gaussian to arbitrary intensity profiles we have chosen an approach involving the direct imaging of a digital micromirror device (DMD). In Chapter 9, I will describe the technical challenges and considerations concerning the design of such a system, as well as the results we were able to achieve in a test setup.

PUBLICATION: ACCURATE DETERMINATION OF THE
DYNAMICAL POLARIZABILITY OF DYSPROSIUM

Published as:

C. Ravensbergen, V. Corre, E. Soave, M. Kreyer, S. Tzanova, E. Kirilov, and R. Grimm.

Phys. Rev. Lett. **120**, 223001 (2018)

Author contribution: The author took a supporting role in the process of acquiring and analyzing the data described in this publication as well as writing the manuscript.

Changes with respect to the published version: Subsection headlines have been added.

We report a measurement of the dynamical polarizability of dysprosium atoms in their electronic ground state at the optical wavelength of 1064 nm, which is of particular interest for laser trapping experiments. Our method is based on collective oscillations in an optical dipole trap, and reaches unprecedented accuracy and precision by comparison with an alkali atom (potassium) as a reference species. We obtain values of 184.4(2.4) a.u. and 1.7(6) a.u. for the scalar and tensor polarizability, respectively. Our experiments have reached a level that permits meaningful tests of current theoretical descriptions and provides valuable information for future experiments utilizing the intriguing properties of heavy lanthanide atoms.

7.1 INTRODUCTION

The dipole polarizability is a quantity of fundamental importance in light-matter interaction, as it characterizes the linear response of a neutral particle to an electric field. The polarizability is related to other important physical quantities, like the van-der-Waals dispersion coefficient, and its knowledge is of great relevance for a deep understanding of many-electron systems, for example in heavy atoms, molecules, and clusters [226]. The static polarizability characterizes the response to a constant electric field by a single real number. The dynamical polarizability (DP) describes the response to an oscillating field and is represented by a complex frequency-dependent function. Naturally, the DP is much richer and contains much more information on the properties of a particle, in particular on its resonance behavior. While various different methods have been established to measure the static polarizability with high accuracy [227, 228], measurements of dynamic polarizabilities are notoriously difficult. Accurate laser-spectroscopic methods only provide access to differential polarizabilities, whereas other methods like deflection from a laser beam suffer from the problem of characterizing the interaction region well enough.

In the realm of ultracold atoms, both the real and imaginary part of the DP play an essential role for controlling the external and internal atomic degrees of freedom. The imaginary part is related to the absorption and scattering of light. The real part gives rise to Stark shifts, which are primarily utilized for constructing optical dipole traps [202] in a wide range of different geometries. Zero crossings of the DP, which occur at tune-out wavelengths, can be used to engineer species-selective traps [229]. Optical lattice clocks operate at a so-called magic wavelength, where the differential DP between the two relevant atomic states vanishes [230]. The DP

also enables coherent spin manipulation, which is the basis of many spin-orbit coupling schemes [231].

The optical manipulation of ultracold magnetic lanthanide atoms has attracted considerable interest [87, 120, 121, 232–237]. Their exceptional magnetic properties arise from a partially filled, submerged 4f shell. They feature a very rich atomic spectrum, including narrow optical transitions, and a large orbital angular momentum gives rise to substantial non-scalar contributions to the polarizability. These special properties make magnetic lanthanide atoms excellent candidates to implement advanced light-matter coupling schemes, such as spin-orbit coupling [126, 238], and to realize novel regimes of quantum matter. The electronic configuration makes advanced calculations of the DP very challenging and interesting [239–244]. To benchmark theoretical models, measurements are highly desirable with uncertainties on the percent level. Experimental results have been reported for dysprosium [120, 245, 246], thulium [241, 244] and erbium [247], in the latter case also demonstrating the anisotropic nature of the DP. However, all these measurements have been subject to large systematic uncertainties, imposed by the methods at hand.

In this Letter, we report on the accurate determination of the real part of the DP of a magnetic lanthanide atom at a wavelength of particular interest for cooling and trapping experiments. We investigate dysprosium atoms and utilize an idea often applied in precision metrology, performing a measurement relative to a known reference. As a reference species, we use potassium atoms, for which the DP is known on the permille level, and measure the trap frequencies of both species in the same single-beam optical dipole trap (ODT). The frequency ratio is then independent of major experimental systematics and imperfections. In a further set of experiments, we determine the tensor contribution to the DP.

7.2 DYNAMICAL POLARIZABILITY

The interaction of atoms with the electric field \vec{E} of laser light is described by the Hamiltonian $H = -\frac{1}{2}\vec{E}^\dagger \tilde{\alpha} \vec{E}$, where $\tilde{\alpha}$ is the dynamical polarizability tensor operator [207]. The energy shift for a given quantum state corresponds to the optical trapping potential and is

$$U(\mathbf{r}, \omega_L) = -\frac{2\pi a_0^3}{c} I(\mathbf{r}) \tilde{\alpha}(\omega_L), \quad (7.1)$$

where ω_L is the laser frequency, $I(\mathbf{r})$ the position-dependent intensity, a_0 the Bohr radius, and c the speed of light. Here we define $\tilde{\alpha}(\omega_L)$ as a dimensionless quantity corresponding to the real part of the DP of the quantum state of interest in atomic units (1 a.u. = $4\pi\epsilon_0 a_0^3$, where ϵ_0 is the vacuum permittivity). For a Gaussian laser

beam, the central region (trap depth \hat{U}) can be approximated by a harmonic potential. The corresponding radial trap frequency

$$\omega_r = \sqrt{\frac{4\hat{U}}{m\omega_0^2}} = \sqrt{\frac{16a_0^3}{c} \frac{P}{\omega_0^4} \frac{\tilde{\alpha}(\omega_L)}{m}} \quad (7.2)$$

is determined by the laser beam parameters (power P and waist w_0) and atomic properties (polarizability $\tilde{\alpha}$ and mass m) [202].

The DP can generally be decomposed into the three irreducible contributions $\tilde{\alpha}_S$, $\tilde{\alpha}_V$, and $\tilde{\alpha}_T$ (scalar, vector, and tensor polarizability), with weights depending on the angular momentum quantum numbers and the polarization of the trapping light. In our work, we focus on the elementary case of linearly polarized light and atoms in a stretched state ¹, where we can decompose $\tilde{\alpha}$ into

$$\tilde{\alpha}(\omega_L) = \tilde{\alpha}_S(\omega_L) + \frac{3\cos^2\theta - 1}{2} \tilde{\alpha}_T(\omega_L); \quad (7.3)$$

here θ is the angle between the polarization axis and the quantization axis, the latter being defined by the magnetic field. Note that within a hyperfine manifold $\tilde{\alpha}_S$ and $\tilde{\alpha}_T$ only depend on the wavelength.

The usual method to measure the dynamical polarizability in an ODT [120, 241, 244, 245, 247] is to determine the trap frequency ω_r by observing collective oscillations in a trap with a given power P and a well-defined waist w_0 , and to use Eq. (7.2). A major complication arises from the strong dependence $\tilde{\alpha} \propto w_0^4$. An accurate determination of w_0 at the position of the atoms is crucial, but very difficult to achieve in practice. In addition, any aberrations from an ideal Gaussian beam are not accounted for. Moreover, a real cloud with its finite spatial extent will experience some anharmonicity, which will alter the measured oscillation frequency. The combination of these systematic problems typically limits the accuracy of such DP measurements to a few 10% [247].

The above limitations can be overcome by referencing the trap frequency of the particle of interest (or state [248]) to a species with a known polarizability [249, 250]. Figure 7.1 illustrates the situation for two species in the same optical trapping field, where different potential depths result from the different polarizabilities. Within the harmonic trap approximation, the DP of the unknown species, in our case Dy, is then obtained as

$$\tilde{\alpha}_{\text{Dy}} = \tilde{\alpha}_{\text{K}} \frac{m_{\text{Dy}}}{m_{\text{K}}} \left(\frac{\omega_{\text{Dy}}}{\omega_{\text{K}}} \right)^2, \quad (7.4)$$

where $\tilde{\alpha}_{\text{K}}$ is the polarizability of the reference species (in our case K), and $m_{\text{Dy}}/m_{\text{K}}$ is the known mass ratio. Experimentally, one only has to measure the frequency

¹ Angular momentum projection on the quantization axis equals plus or minus the total angular momentum ($|m_J| = J$)

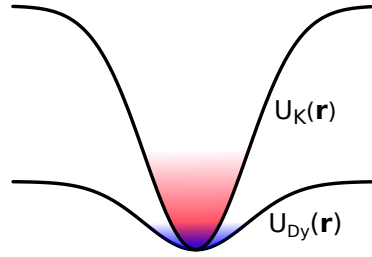


Figure 7.1: Schematic illustration of the species-dependent optical trapping potential U filled with potassium or dysprosium atoms in a beam with a Gaussian profile. Here, in the ideal case, the ratio T/\tilde{U} is equal for the two species, the atoms explore exactly the same region in the trap, and thus experience the same anharmonicity and beam aberrations.

ratio $\omega_{\text{Dy}}/\omega_{\text{K}}$, which eliminates the need to determine w_0 or P . This scheme also removes the effects of anharmonicity provided that the ratio of the temperature to the trap depth is the same for both species. In this ideal case, illustrated in Fig. 7.1, the two thermal clouds fill exactly the same region in the trap, and thus experience the same relative effect of anharmonicity. Introducing another species with a different mass may lead to a different gravitational sag and thus to a shift of the frequency ratio. This effect, however, can be suppressed by using a sufficiently deep and tight trap.

7.3 EXPERIMENTAL SETUP

In our experiments, we use the isotopes ^{164}Dy and ^{40}K , with a mass ratio $m_{\text{Dy}}/m_{\text{K}} = 4.102$. For trapping we use the standard near-infrared wavelength of 1064.5 nm. At this wavelength the polarizability of potassium is $\tilde{\alpha}_{\text{K}} = 598.7(1.1)$ [210, 251]². Based on the available theory values for Dy [239, 242], we can estimate $\tilde{\alpha}_{\text{K}}/\tilde{\alpha}_{\text{Dy}} \approx 3.2$ and $\omega_{\text{K}}/\omega_{\text{Dy}} \approx 3.6$.

We produce a thermal cloud of either ^{164}Dy or ^{40}K atoms in a single-beam ODT. For dysprosium, we employ a laser cooling and trapping scheme similar to Refs. [96, 237]. After loading the ODT and some evaporative cooling, we typically trap 10^6 atoms, spin-polarized in Zeeman substate $|J = 8, m_J = -8\rangle$, at about 8 μK . For potassium, after a sub-Doppler cooling stage [252] which also enhances ODT loading, we have 3×10^5 unpolarized ² atoms at $\sim 30 \mu\text{K}$. The trapping laser (Mephisto MOPA 18 NE) operates on a single longitudinal mode, is linearly

² At 1064.5 nm the polarizability of potassium is without any significant tensor contribution

polarized, and its power is actively stabilized. All measurements reported here are performed with $P = 2.5$ W, $w_0 \approx 30$ μm , and a magnetic field strength of 250 mG.

We measure the trap frequencies by exciting a CoM oscillation, the so-called sloshing or dipole mode. In a harmonic potential, this mode does not involve a compression of the cloud and the frequency is thus not affected by the interactions within the cloud or by its quantum statistics [253]. We excite a pure radial sloshing oscillation by displacing the trap position abruptly in the vertical direction using an acousto-optic modulator. The displacement amounts to approximately 2 μm , which is smaller than the in-trap radial cloud size of about $\sigma_r = 6$ μm . After a variable hold time we switch off the trap and perform standard TOF absorption imaging. The cloud position is extracted from the images by performing a one-dimensional Gaussian fit to a vertical slice taken from the central part of the elongated trap. Both species are imaged using the same optical path and camera.

A typical measurement run for both dysprosium and potassium is shown in Fig. 7.2. The magnetic field is chosen to be parallel to the polarization of the trapping light ($\theta = 0$), and therefore from Eq. (7.3) we get $\tilde{\alpha} = \tilde{\alpha}_S + \tilde{\alpha}_T$. We fit the oscillations with an exponentially damped sine wave to extract the frequency ω^{fit} and the damping time τ of the oscillation. The two species oscillate at different frequencies because of their different mass and polarizability. By relative scaling of the horizontal axes of Fig. 7.2 with the expected factor of 3.6 the oscillations exhibit a nearly identical behavior. This already confirms that the theoretical values of Refs. [239, 242] provide a good estimate for the Dy polarizability. The identical damping behavior, with $\omega^{\text{fit}}\tau$ being the same for both species, is consistent with our assumption that the main source of damping is dephasing resulting from the trap anharmonicity 7.7.

7.4 SYSTEMATIC EFFECTS

The measured frequency ratio exhibits a residual anharmonicity effect. After trap loading, plain evaporative cooling reduces the temperature to a certain fraction of the trap depth. This effect is similar, but not exactly equal for both species. We take this into account by a small correction to the dysprosium oscillation frequency. For a given potassium temperature T_K the corresponding dysprosium temperature would be $(\tilde{\alpha}_{\text{Dy}}/\tilde{\alpha}_K)T_K$. A deviation from this ideal value can be quantified by $\Delta T_{\text{Dy}} = T_{\text{Dy}} - (\tilde{\alpha}_{\text{Dy}}/\tilde{\alpha}_K)T_K$. The anharmonic frequency shift depends on the slope $\beta = d\omega_{\text{Dy}}/dT_{\text{Dy}}$, which gives a corrected frequency ratio

$$\frac{\omega_K}{\omega_{\text{Dy}}} = \frac{\omega_K^{\text{fit}}}{\omega_{\text{Dy}}^{\text{fit}} - \beta\Delta T_{\text{Dy}}}. \quad (7.5)$$

With this correction, Eq. (7.4) allows to determine $\tilde{\alpha}_{\text{Dy}}/\tilde{\alpha}_K$ in an accurate way.

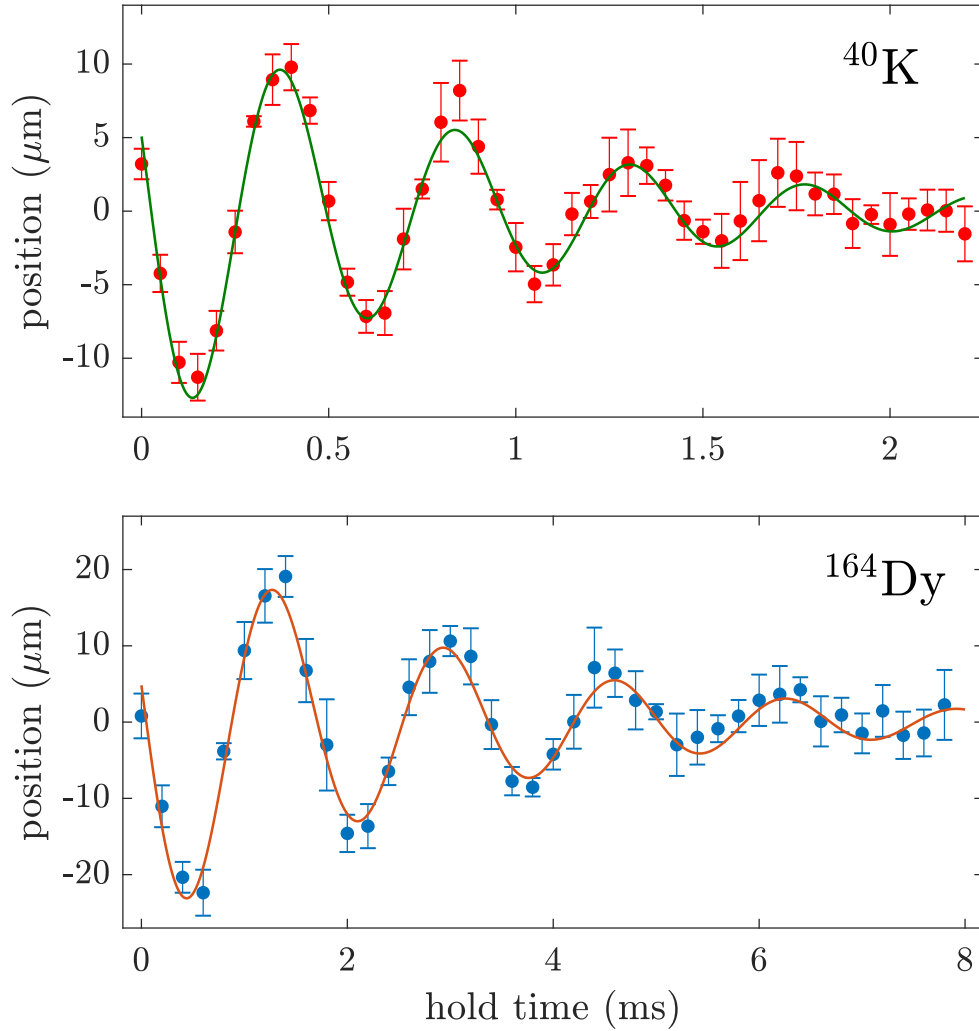


Figure 7.2: Radial sloshing mode oscillation for potassium and dysprosium. The cloud position after TOF is plotted against the hold time in the trap after the excitation. We obtain $\omega_{\text{K}}^{\text{fit}}/2\pi = 2140(10)$ Hz and $\omega_{\text{Dy}}^{\text{fit}}/2\pi = 601(2)$ Hz, $\tau_{\text{K}} = 0.8(1)$ ms and $\tau_{\text{Dy}} = 2.9(1)$ ms. The temperatures are $T_{\text{K}} = 36(3)$ μK and $T_{\text{Dy}} = 8.3(2)$ μK , and the TOF is 0.3 ms for K and 2 ms for Dy. Note that the time scales for K and Dy differ by a factor of 3.6. The error bars show the sample standard deviation of five individual measurements at the same hold time.

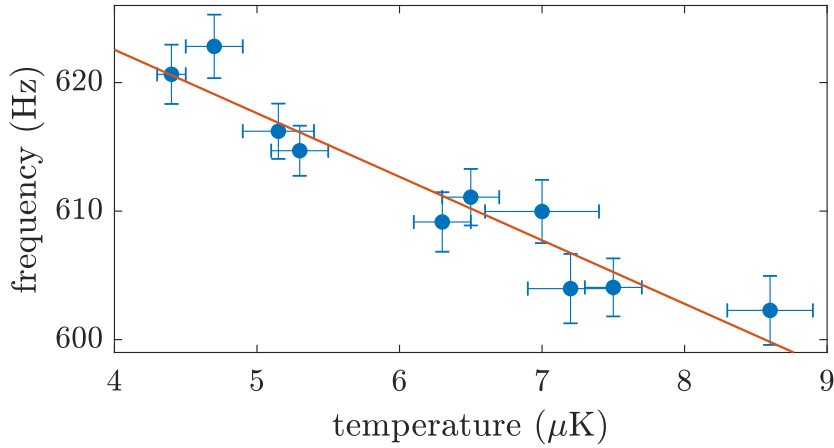


Figure 7.3: Anharmonicity effect on the trap frequency. The Dy CoM oscillation frequency is plotted as a function of the cloud temperature. The weighted linear fit takes both frequency and temperature errors into account, and for the displayed set of measurement yields a slope $\beta/2\pi = -5.1(7)\text{Hz}/\mu\text{K}$.

In order to determine β , we vary the temperature of the dysprosium atoms and measure the oscillation frequency. The temperature, determined by standard TOF expansion, is changed by an evaporation ramp down to a variable trap power followed by a re-compression to the standard power and a hold time for thermalization. We observe a frequency decrease with increasing temperature, as is shown in Fig. 7.3. From this set of measurements and a second one taken under similar conditions (not shown in Fig. 7.3), we obtain the combined result $\beta/2\pi = -4.5(4)\text{Hz}/\mu\text{K}$. Note that the anharmonicity shifts the measured Dy frequency, for our typical temperatures and trap depth, by about 5% as compared to the harmonic approximation of Eq. (7.2).

Possible remaining systematics affecting the frequency ratio could include density-dependent interactions, the finite excitation amplitude, and the effect of gravity. We do not observe a density dependence of the oscillation frequency of Dy when varying the atom number over a wide range 7.7, confirming that the frequency shift observed in Fig. 7.3 can be fully attributed to a change in temperature. The frequency ratio should not be affected by the excitation amplitude, because, for an equal amplitude, both species are affected in the same way. In addition, we varied the excitation amplitude for a single species (Dy) and we did not observe any significant shift for the amplitude used here. The estimated gravitational frequency shift in our trap is $\sim 0.1\%$ ³, which we neglect in our analysis. Moreover, we noticed that the fitted frequency may slightly depend (on the subpercent level) on the time

³ The relative frequency downshift caused by the gravitational sag can be approximated by: $-2(g/w_0\omega^2)^2$

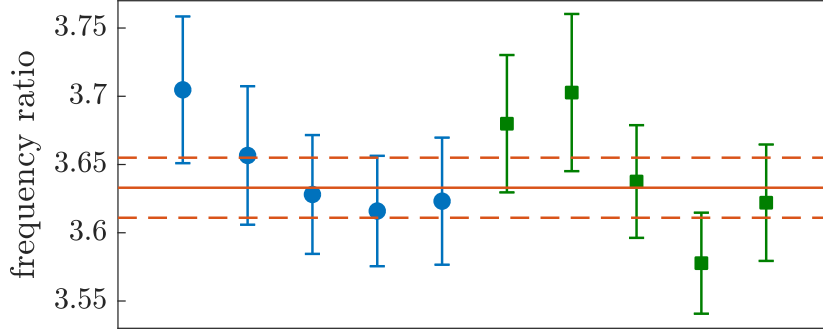


Figure 7.4: Repeated measurements of the frequency ratio ω_K/ω_{Dy} , including small anharmonicity corrections. The two symbols (blue dots and green squares) represent the data sets taken on two different days. The error bars include the fit errors of the frequency measurements and all uncertainties in the anharmonicity correction. Because of the latter, the uncertainties are partially correlated, which we properly take into account in our data analysis when combining the individual results. The solid line marks the final result $\omega_K/\omega_{Dy} = 3.632(22)$, with the dashed lines indicating the corresponding error range 7.7.

interval chosen for the analysis. To avoid systematic deviations in the comparison of both species, we choose the time intervals to follow the scaling factor of 3.6. With 0-2.2 ms for K and 0-8 ms for Dy, the intervals then correspond to about twice the respective $1/e$ damping time τ_K or τ_{Dy} .

7.5 DETERMINATION OF THE POLARIZABILITY

We now turn our attention to an accurate and precise determination of the frequency ratio ω_K/ω_{Dy} . We measure the potassium and dysprosium CoM oscillation frequency, in the same trap, in an alternating fashion to eliminate possible slow drifts over time, and repeat this 10 times. The resulting frequency ratios, including small anharmonicity corrections, are shown in Fig. 7.4. The data were taken on two different days, which were one week apart, and the consistency shows the robustness of the presented method. The differential anharmonicity effect from Eq. (7.5) yields a small correction of about 1.4% and 2.2% for the frequency ratio of the two data sets. The combined result for the frequency ratio is $\omega_K/\omega_{Dy} = 3.632(22)$; for details on the error budget see 7.7.

In a second set of experiments, we measure the frequency ratio $\omega_{\parallel}/\omega_{\perp}$ for Dy in a magnetic field parallel and perpendicular to the polarization of the laser field. In this way, we can identify the tensor part which is expected to be more than 100 times smaller [242] than the scalar part. Here we perform in total 11 pairs of measurements 7.7, alternating the angle θ between 0 and $\pi/2$. We obtain the

combined result $\omega_{\parallel}/\omega_{\perp} = 1.0070(24)$, which significantly deviates from one and thus reveals a tensor contribution.

From the measured frequency ratios and Eqs. (7.1-7.3), it is now straightforward to derive the polarizability ratios $(\tilde{\alpha}_S + \tilde{\alpha}_T)/\tilde{\alpha}_K = 3.217(40)$ and $(\tilde{\alpha}_S + \tilde{\alpha}_T)/(\tilde{\alpha}_S - \tilde{\alpha}_T/2) = 1.014(5)$. Solving for the scalar and tensor part and using the reference value for $\tilde{\alpha}_K$, we finally obtain $\tilde{\alpha}_S = 184.4(2.4)$ and $\tilde{\alpha}_T = 1.7(6)$.

Our result for the scalar polarizability lies between the two theoretical values of 180 a.u. [239] and 193 a.u. [242], being consistent with both of them within the corresponding error estimates of a few percent [254, 255]. For the small tensorial part, our result is consistent with the theoretical value of 1.34 a.u. [242].

7.6 DISCUSSION AND CONCLUSION

Already in its present implementation, the experimental uncertainty of our method to determine the DP of a magnetic lanthanide atom is smaller than the uncertainties of theoretical calculations. This, in turn, means that our new result already provides a benchmark and sensitive input for refined theoretical calculations. In extension of our work, much more information on the DP can be obtained by measuring at other optical wavelengths [247], which is straightforward to be implemented experimentally. Furthermore, experimental uncertainties may be reduced considerably by using the well-defined environment of optical lattices instead of macroscopic trapping schemes. Further advanced DP measurements could provide a wealth of accurate information on the interaction of light with atoms that feature a complex electronic structure, which would go far beyond the present state of the art.

The presented technique should also be largely applicable to the rapidly expanding field of ultracold molecules [256, 257], where diatomic molecules combining alkali and alkaline earth atoms are produced routinely in numerous labs. The increased complexity of the molecular structure, relative to its atomic constituents, renders the precise determination of the dynamic polarizability challenging. Another emerging field aims at direct laser cooling and trapping of more exotic molecules [258, 259], with the benefit of a larger ground state electric dipole moment or applicability to precision measurements. In such systems sympathetic cooling by ultracold alkali atoms [260, 261] or even by ultracold hydrogen has been proposed [262] as a route to reach quantum degeneracy. In all of the above experiments a spectroscopically well understood species exists either as a constituent forming the molecule or as a coolant, naturally enabling reference measurements of polarizability and other physical quantities.

In our future experiments, we are particularly interested in mass-imbalanced Fermi-Fermi mixtures and possible new superfluid pairing regimes [70, 74, 150, 263–267]. For the combination of ^{161}Dy and ^{40}K and not far from our present experimental conditions, a “magic” wavelength is expected to exist where the

polarizability ratio for the two species corresponds to the inverse mass ratio. An optical dipole trap operating at this particular wavelength would automatically match the Fermi surfaces of both species after deep evaporative cooling. Based on Refs. [239] and [242] for Dy and [210] for K, we would expect this wavelength to be at 982 nm or 954 nm, respectively, and our present measurement suggests it to be in between these two values. The precise location will be subject of further studies.

7.7 SUPPLEMENTAL MATERIAL

In Sections 7.7.1 and 7.7.2 we present measurements on Dy testing systematic effects introduced by atomic density and temperature. Section 7.7.3 provides additional information on our measurement of the tensor part of the polarizability of Dy. Section 7.7.4 reviews the different contributions to the uncertainty on our measurement of the polarizability of Dy.

7.7.1 Absence of Density Effect on Oscillation Frequency

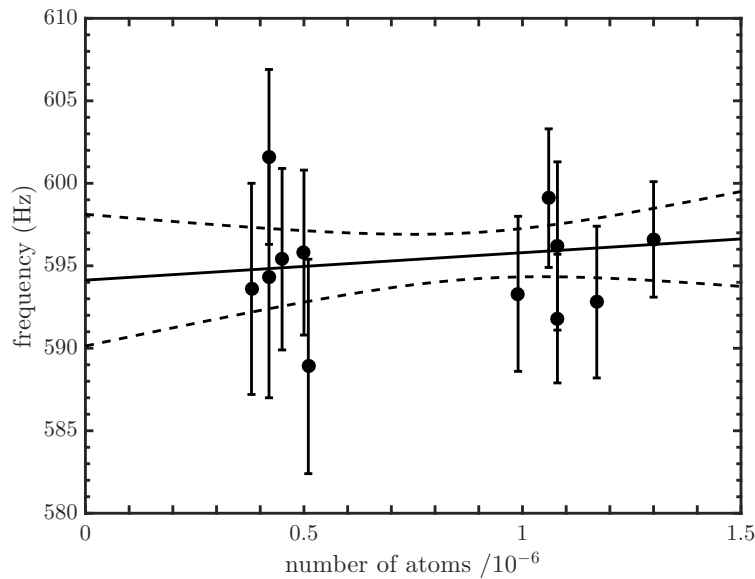


Figure 7.5: Test of the effect of atomic density on the oscillation frequency. The measured frequency is plotted against the atom number. The solid line is a linear fit, and the dashed line shows the 68% (1σ) confidence band.

Throughout our determination of the polarizability of Dy we assume that the frequency of the CoM oscillations is independent of the atomic density, as is expected in a harmonic potential. In this section we test this basic assumption by investi-

gating the effect of density on our frequency measurements. We prepare samples of largely different atom numbers and determine the frequency for the same trap depth as used in the main text. The atom number is controlled through the MOT loading time. We use a standard (reduced) loading time of 4 s (0.2 s), resulting in a cloud of about 1.1×10^6 (4.5×10^5) atoms. We measure alternately using one loading time, then the other one, and repeat the procedure to eliminate the effect of possible slow drifts. After each individual measurement the temperature of the cloud is measured by TOF expansion. Based on these temperatures, the measured trap frequencies are corrected to account for the effect of anharmonicity of the trap, using the coefficient β defined in the main text. Note, however, that we do not observe a significant correlation between temperature and atom number. The results are presented in Figure 7.5. A linear fit gives a slope of 0.28(70)% per million of atoms, which is consistent with the absence of a density effect. This confirms our assumption of a density independence of the oscillation frequency on the level of 1% for our standard experimental conditions.

7.7.2 Damping of Oscillations

In the main text we introduce the assumption that the damping of the CoM oscillations originates essentially from the anharmonicity of the trap: Different classes of atoms explore different regions of the trap as they oscillate, hence experiencing slightly different trap frequencies and eventually dephasing. Such a behavior would mean that the CoM oscillations that we observe result from a superposition of pure single-particle oscillations. This assumption is supported by the equal damping behavior of the two species, as pointed out in the main text, and by an estimation based on our experimental settings of the collision rate of dysprosium atoms, which yields 80 s^{-1} (a similar calculation for potassium gives a collision rate of about 90 s^{-1}). Given the radial trap frequency of about 600 Hz (2 kHz for K), the radial motion in our trapped samples is far away from the hydrodynamic regime. Here we further test our assumption on the origin of the observed damping by considering the density and temperature dependence of the damping rate of the CoM oscillations.

From the analysis of the set of experiments presented in Sec. A we also obtain the damping rate of the oscillations. Its behavior as a function of atom number is plotted in Figure 7.6. A linear fit gives a slope of $+0.008(30) \text{ s}^{-1}$ per million atom and thus does not show any significant density dependence on the 10% level for our standard atom number. This observation supports our assumption of damping being essentially due to dephasing effects.

We now turn our attention to the study of the dependence of the damping rate on the temperature. From straightforward arguments, one expects the damping rate to be proportional to the temperature. Indeed, for small oscillation amplitudes, the

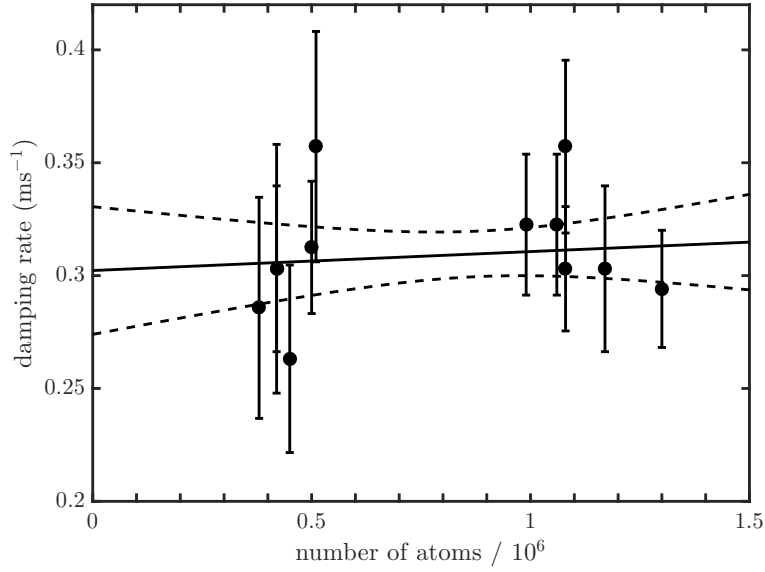


Figure 7.6: Density independence of the damping rate. The solid line is a linear fit, and the dashed lines show the 68% (1σ) confidence band.

anharmonic frequency shift of a particle in a Gaussian potential scales linearly with its energy, such that the width in Fourier space of the CoM oscillation increases linearly with the temperature of the cloud, finally leading to a linear dependence of the damping rate on the temperature. In the main text, we present a measurement of the dependence of the frequency on the temperature of the cloud (see Figure 3 in the main text). The analysis of the corresponding oscillation data also allows us to investigate the dependence of the damping rate of the oscillations on the temperature. The results are shown in Figure 7.7. We observe an increase of the damping with temperature. A linear fit without offset gives a slope of $0.409(15) \text{ ms}^{-1} \mu\text{K}^{-1}$, and a reduced χ^2 of 0.96, showing that our simple model fits well to the data. This behavior also supports our interpretation on dephasing being the main source of damping.

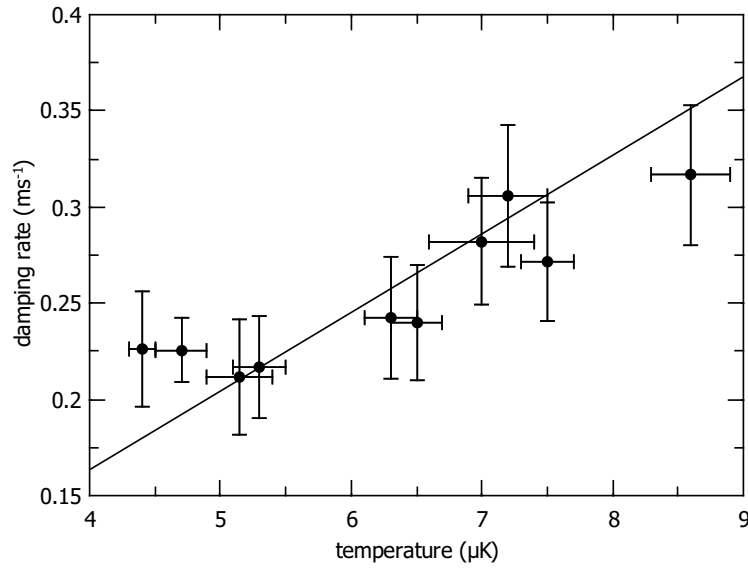


Figure 7.7: Temperature dependence of the damping time. The solid line is a linear fit without offset, with weights taking both horizontal and vertical error bars into account.

7.7.3 Error Budget of the Frequency Ratio Measurement

We measure the trap frequency ratio in two sets of data obtained on two different days. Each set of data is corrected for the residual anharmonicity, based on the anharmonicity coefficient β and on the measured temperatures of the two species. A part of the uncertainty originates from the statistical distribution of the measured frequency ratios ω_K/ω_{Dy} . The rest of the uncertainty originates from the error in the anharmonicity correction and has five contributions: the error on the anharmonicity coefficient β , and the error on the measured temperatures of the K and Dy clouds. The respective contributions to the absolute uncertainty on ω_K/ω_{Dy} are listed in Table 7.1.

The total absolute uncertainty that results from the anharmonicity correction is 0.019, and the statistical uncertainty from the 10 combined individual measurements is 0.012. These two errors are quadratically combined, which finally yields the quoted uncertainty of 0.022.

7.7.4 Measurement of the Tensor Contribution

We measure oscillation frequencies for two different orientations of the magnetic field: Always being perpendicular to the propagation axis of the trapping laser, the field is either aligned with the polarization axis of the trapping laser, or

Table 7.1: Error budget for the measurement of ω_K/ω_{Dy} .

| [p] parameter | value | uncertainty in parameter | uncertainty in frequency ratio |
|----------------|-------------------------|-----------------------------|-----------------------------------|
| T_{Dy} set 1 | 8.3 μK | 0.2 μK | 0.003 |
| T_K set 1 | 7.6 μK | 0.3 μK | 0.004 |
| T_{Dy} set 2 | 35.7 μK | 3.2 μK | 0.015 |
| T_K set 2 | 30.3 μK | 2.0 μK | 0.008 |
| β | -4.50 Hz/ μK | 0.43 Hz/ μK | 0.006 |

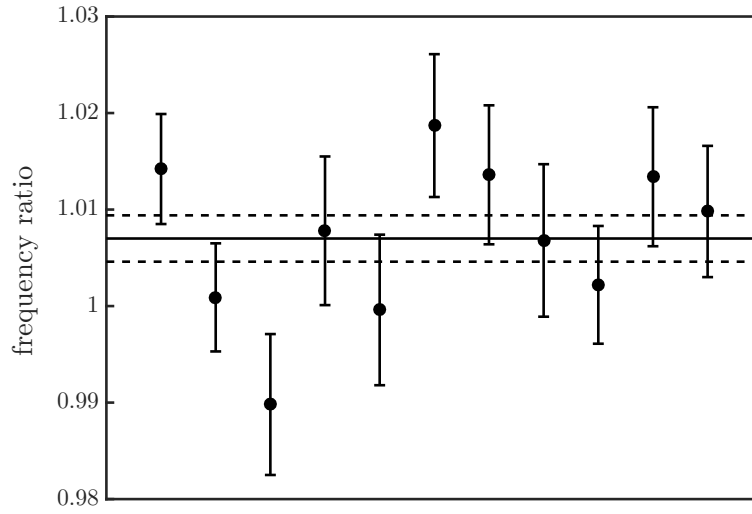


Figure 7.8: Repeated measurements of the frequency ratio $\omega_{\parallel}/\omega_{\perp}$. The first five points have been measured on one day, the remaining six ones on a second day. The solid line shows the weighted average $\omega_{\parallel}/\omega_{\perp} = 1.0070(20)$ with the dashed lines showing the corresponding statistical error range.

perpendicular to it. All other parameters are kept identical. The strength of the field is in both cases 250 mG. In the latter case we take care that the spin state of the atoms adiabatically follows the rotation of the magnetic field. We measure alternately the trap frequency for one orientation of the field, then for the other one, and repeat the procedure to eliminate systematic effects from possible slow drifts. We measure in total 11 pairs of trap frequencies over two different days, which gives us 11 values for the frequency ratio, as shown in Figure 7.8. A weighted average yields $(a_s + a_t)/(a_s - a_t/2) = 1.0140(48)$.

PUBLICATION: MEASUREMENT OF THE DYNAMIC
POLARIZABILITY OF DY ATOMS NEAR THE 626-NM
INTERCOMBINATION LINE

Published as Editor's Suggestion:

Marian Kreyer, Jeong Ho Han, Cornelis Ravensbergen, Vincent
Corre, Elisa Soave, Emil Kirilov, and Rudolf Grimm.

Phys. Rev. A **104**, 033106 (2021)

Author contribution: The author took a leading role in the process of acquiring and analyzing the data described in this publication as well as writing the manuscript.

We report on measurements of the anisotropic dynamical polarizability of Dy near the 626-nm intercombination line, employing modulation spectroscopy in a one-dimensional optical lattice. To eliminate large systematic uncertainties resulting from the limited knowledge of the spatial intensity distribution, we use K as a reference species with accurately known polarizability. This method can be applied independently of the sign of the polarizability, i.e., for both attractive and repulsive optical fields on both sides of a resonance. By variation of the laser polarization we extract the scalar and the tensorial part. To characterize the strength of the transition, we also derive the natural linewidth. We find our result to be in excellent agreement with literature values, which provide a sensitive benchmark for the accuracy of our method. In addition we demonstrate optical dipole trapping on the intercombination line, confirming the expected long lifetimes and low heating rates. This provides an additional tool to tailor optical potentials for Dy atoms and for the species-specific manipulation of atoms in the Dy-K mixture.

8.1 INTRODUCTION

Ultracold gases of submerged-shell lanthanide atoms (Dy, Ho, Er, Tm) have emerged as novel platforms for exploring the exciting many-body physics of exotic states of quantum matter under well defined and widely controllable conditions. The intriguing properties of such strongly magnetic atoms result from long-range anisotropic interactions in combination with tunability of the contact interaction. Prominent examples for novel states of matter created in the laboratory are quantum ferrofluids of Dy [236] and supersolids realized with both Dy and Er [97–99]. Progress has also been made with quantum-gas mixtures of different lanthanide atoms (Dy-Er) [122, 268] and mixtures of lanthanide and alkali-metal atoms (Dy-K) [105, 176], representing intriguing systems that offer wide potential for future applications.

Submerged-shell lanthanide atoms offer a multitude of optical transitions, which provide flexible tools for efficient laser cooling and trapping [90, 94–96] and which open up a broad range of applications based on the optical manipulation of atoms. Examples include optical pumping [269], the excitation of Rydberg states [270], realization of spin-orbit coupling [126], atomic clock applications [271], quantum-enhanced sensing [209, 272], and quantum spin models [273]. The wide range of applications has motivated theoretical [239, 240, 242, 243] and experimental [120,

124, 241, 244–247, 274] studies on the dynamic polarizability, which is the key quantity that characterizes the strength of the atomic interaction with laser light. Because of the complicated electronic structure accurate theoretical models are very challenging and can be refined based on experimental data.

In our recent work [124], we introduced a method that greatly improves the accuracy of measurements of the real part of the ground-state dynamic polarizability based on optical dipole potentials [202]. The basic principle is a comparison of the optical response of the species under investigation with the response of a reference species to the same light field [249, 250]. As the key point, this method eliminates uncertainties caused by the limited knowledge of spatial light intensity distribution. In Ref. [124] we demonstrated a polarizability measurement for Dy atoms with K atoms as a reference species by observing collective oscillations in near-infrared light. However, such a collective-excitation scheme can be applied only if the dynamical polarizabilities of both species are positive, i.e., if the laser light attracts and traps the atoms. This limitation substantially reduces the optical wavelength range where the method can be applied.

In this article, we introduce a more general scheme to measure the dynamical polarizability, which relies on the same basic principle as introduced in Ref. [124] but is independent of the sign of the polarizability. Instead of observing collective oscillations of trapped atoms, we use modulation spectroscopy in an optical lattice [275, 276], applicable for both attractive and repulsive light. As a case study, we investigate the dynamical polarizability near the 626-nm intercombination line of Dy, which is widely used for narrow-line laser cooling [96, 237] and which also offers interesting possibilities for optical dipole trapping. A particular motivation for the experiments pursued in our laboratory is the exciting prospect to realize novel superfluid states in mass-imbalanced fermion mixtures [74, 114, 225], which is the reason why we work with the fermionic isotopes ^{161}Dy and ^{40}K .

Our work is structured as follows. In Sec. 8.2, we describe the experimental procedures, including the preparation protocol and probing methods of the ultracold gas in the optical lattice. In Sec. 8.3, we discuss our main results on the dynamical polarizability of dysprosium for varying optical detunings and polarizations near the 626-nm line. We then extract the contribution of scalar and tensorial components and obtain the linewidth of the transition. In addition, we demonstrate dipole trapping and measure the heating rate and lifetime in Sec. 8.4. In Sec. 8.5, we finally summarize our results and give a brief outlook.

8.2 METHODS

In this section, we present the methods used to determine the dynamical polarizability of Dy near the 626-nm line. We start by summarizing the experimental sequence to obtain an ultracold sample of either Dy or K atoms in the lattice

(Sec. 8.2.1), after which we describe the methods to measure the lattice depth for the two species (Sec. 8.2.2) and how we use K as a well-known reference to calibrate our measurement on Dy (Sec. 8.2.3).

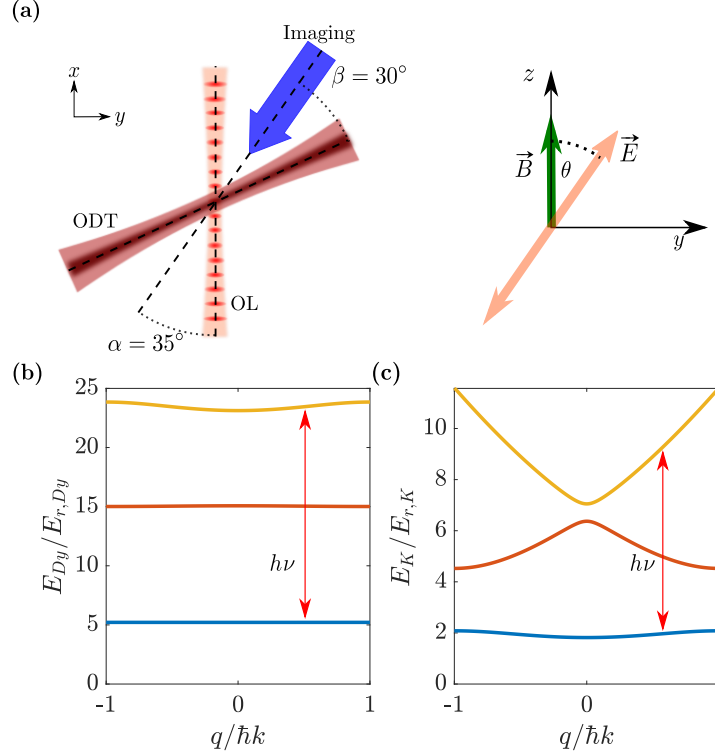


Figure 8.1: (a) Schematic of our experiment. The 1D optical lattice beam (OL) is overlapped by the optical dipole trap (ODT) and imaging beam at the sample position. The second beam of the crossed dipole trap propagates along the z direction (direction of gravity) and is not shown here. The external magnetic field \vec{B} is aligned with the gravity axis, defining the polarization angle θ for the \vec{E} field of the lattice beam. θ can be changed by rotating a half-wave plate. (b) and (c) Band structures of an optical lattice for Dy and K with a typical depth of $V_{Dy} = 30E_{r,Dy}$ and $V_K = 5E_{r,K}$, respectively. Atoms are transferred if the photon energy $h\nu$ from the modulation matches the energy difference between bands at a given quasimomentum q .

8.2.1 Sample Preparation

Our experiments begin with preparing spin-polarized degenerate Fermi gases of ^{161}Dy or ^{40}K in an optical dipole trap, following procedures described in our previous work [105]. For Dy, we rely on the evaporation of atoms in a single spin state in a crossed optical dipole trap, taking advantage of universal dipolar

collisions [89]. At the end of the evaporation, we are left with a typical atom number of $N_{\text{Dy}} = 2 \times 10^4$ in the absolute ground state $|F = 21/2, m_F = -21/2\rangle$. The mean (geometrically averaged) trapping frequency is $\bar{\omega}_{\text{Dy}}/(2\pi) = 120$ Hz, and the sample is at a temperature of $T/T_{\text{F,Dy}} = 0.1$, where $T_{\text{F,Dy}}$ is the Fermi temperature of the trapped sample.

To produce degenerate samples of K, we load Dy and K together in the crossed dipole trap. Since the trap is about 3.6 times deeper for K than for Dy [124] and the sample is nearly thermalized, essentially Dy atoms get lost during evaporation, and K is sympathetically cooled by Dy. After fully evaporating all remaining Dy atoms, we end up with a pure sample of ^{40}K in the ground state $|F = 9, m_F = -9/2\rangle$, with $N_{\text{K}} = 1 \times 10^4$, $T/T_{\text{F,K}} = 0.2$, and $\bar{\omega}_{\text{K}}/(2\pi) = 450$ Hz.

The atoms are then adiabatically loaded into a one-dimensional (1D) optical lattice generated by two counterpropagating, linearly polarized laser beams at wavelength $\lambda \approx 626$ nm with a beam waist $w_0 = 55$ μm and a power P in the range between 17 and 200 mW per beam. For normalization purposes, we define a reference power of $P_0 = 67$ mW. The lattice is superimposed with the crossed dipole trap used for evaporation [see Fig. 8.1(a)]. The lattice beams are oriented horizontally, and the quantization axis is defined by applying a small magnetic field less than 1 G along the direction of gravity. We ramp up the lattice potential

$$V_i(\mathbf{r}, \omega) = -\frac{2\pi a_0^3}{c} \tilde{\alpha}_i(\omega) I(\mathbf{r}), \quad (8.1)$$

where ω is the laser frequency, $I(\mathbf{r})$ is the laser intensity at position \mathbf{r} , a_0 is the Bohr radius, and c is the speed of light, in 200 ms to a certain lattice depth \hat{V} . As in our previous work [124], we define $\tilde{\alpha}_i(\omega)$ as the dimensionless real part of the dynamical polarizability of atomic species $i \in \{\text{Dy}, \text{K}\}$ normalized to the atomic unit of polarizability. The optical lattice depth is typically expressed in units of recoil energies $E_{r,i} = h^2/(2m_i\lambda^2)$, where h is the Planck constant and m_i is the atomic mass. After loading, because of the deeply degenerate nature of the samples, the atoms completely fill the ground band, and the fractional population of the atoms in the excited bands is measured to less than 6%, which we verified by a band mapping technique [277, 278]. We verified that ramping up the lattice intensity and then ramping it down again are possible without significant heating of the samples.

To mitigate the antitrapping effect when working with blue-detuned lattices, we ramp up the dipole trap power simultaneously with the lattice to a trapping frequency of $\bar{\omega}_{\text{Dy}}/(2\pi) = 190$ Hz and $\bar{\omega}_{\text{K}}/(2\pi) = 700$ Hz. This also helps us reduce the differential gravitational sag that the two species experience, which would result in a difference of about 5 μm in the vertical direction and therefore also a difference in lattice intensity experienced by the atoms. The deeper trap reduces the differential sag to about 1 μm .

8.2.2 Measuring the Lattice Depth of ^{161}Dy

In order to determine the lattice depth of ^{161}Dy atoms, we perform amplitude-modulation spectroscopy by sinusoidally varying the depth of the optical lattice potential for 100 to 200 ms with a relative amplitude of about 5%. In this method, the population initially filling the ground band ($n = 0$) is excited to the higher bands by absorbing the photons resonant to the energy difference between bands [see Fig. 8.1(b)]. Because of the curvature of the bands, only a specific class of quasimomenta q is resonant with the excitation frequency and can be transferred as the modulation frequency is swept [276]. The amplitude-modulation scheme predominantly drives $\Delta n = 2$ excitations because of parity conservation, coupling the ground and second excited bands with frequency ν [275].

The superimposed dipole trap mixes all spatial dimensions so that transitions to higher bands result in heating of the sample caused by the momentum being added. The transition probability is dependent on q and has a maximum at the lower band edge, where $q = 0$, and drops for larger q . We therefore expect a sharp increase in cloud size when the modulation frequency matches the resonance condition, $E_{n,q} - E_{m,q} = h\nu$ at $q = 0$. Here, $E_{n,q}$ is the energy of a particle in the n th band with quasimomentum q . To observe this effect, we ramp down the lattice (in about 2 ms), then switch off the dipole trap and measure the size of the atomic cloud using standard absorption imaging after typically 5 ms of free expansion. We then determine the size of the atomic cloud σ using a Gaussian fit.

Figure 8.2(a) shows a typical amplitude-modulation spectrum for the ^{161}Dy atoms, plotted as a function of the modulation frequency. The spectrum is fitted with a Gaussian function $\sigma(\nu) \propto e^{-((\nu-\nu_0)^2/2\Delta\nu^2)}$, where ν_0 and $\Delta\nu$ are fitting parameters, indicating the frequency position of the lower band edge for the given lattice depth. For each choice of the wavelength λ , the power of the lattice beams is set such that the lattice for ^{161}Dy is deep enough (more than $25E_{r,\text{Dy}}$) to generate flat bands. Close to resonance, the power is kept low enough to avoid heating by photon scattering. This narrows the spectroscopy signal and allows the use of a Gaussian fitting function. The typical width of the $n = 2$ band in this regime is less than 7% of the gap between the two bands. We obtain the depth of our optical lattice \hat{V}_{Dy} by matching $\nu_0 - \Delta\nu$ with the lower band edge calculated by a band structure model for an infinite, homogeneous one-dimensional lattice. We define

$$s_{\text{Dy}}(\lambda) = \frac{\hat{V}_{\text{Dy}}(\lambda, P) P_0}{E_{r,\text{Dy}} P} \quad (8.2)$$

as the power-normalized lattice depth in units of $E_{r,i}$. Here, the power normalization scales the lattice depth to the reference value P_0 . For the example in Fig. 8.2(a), we obtain $s_{\text{Dy}} = 57.9(2)$ at $\lambda = 626.174$ nm. The uncertainty given here represents the statistical fitting error.

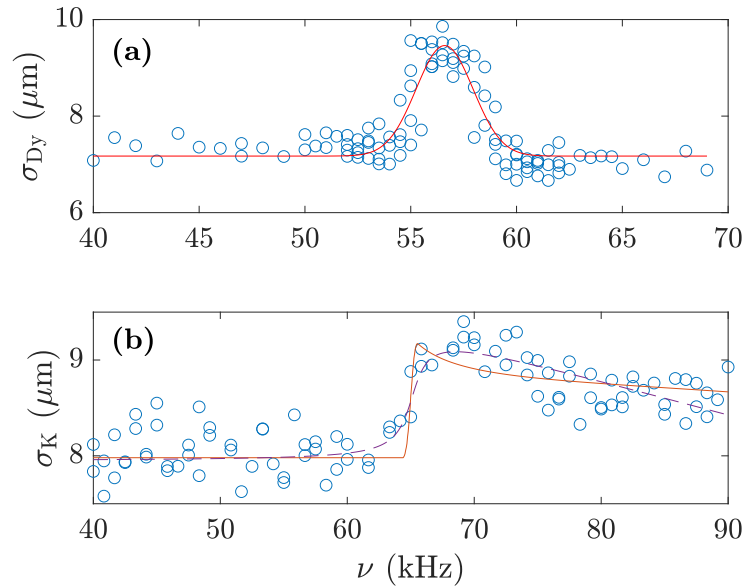


Figure 8.2: Representative amplitude-modulation spectra for an optical lattice at $\lambda = 626.174$ nm. The atomic cloud size is plotted as a function of the modulation frequency. (a) For ^{161}Dy , at a power $P = 33.5$ mW, we obtain a lattice depth of $\hat{V}_{\text{Dy}} = 28.96(9)E_{r,\text{Dy}}$ by matching $\nu_0 - \Delta\nu$, extracted from a Gaussian fit (solid line), to the band gap. (b) For ^{40}K the spectrum, taken at $P = 67$ mW, shows an asymmetric profile due to the broad band structure. We take into account systematic errors in the numerical simulation used to determine the lattice depth. The fitted simulation (solid line) yields a depth of $\hat{V}_{\text{K}} = 4.70(14)E_{r,\text{K}}$, which is consistent with the depth of $\hat{V}_{\text{K}} = 4.73(8)E_{r,\text{K}}$ obtained from an arctangent fit (dashed line). The errors given here represent the statistical fitting errors. The systematic errors are much larger (see text).

8.2.3 Calibration Measurements with Potassium

For calibration purposes we perform a similar lattice depth measurement with ^{40}K . After preparing the K sample in the lattice, we modulate the amplitude of the lattice beam for 500 ms and image the atoms after 2 ms of time of flight. The laser beam at $\lambda = 626$ nm is far detuned from the potassium transition lines, resulting in an accurately known polarizability value of $\tilde{\alpha}_{\text{K}} = -556(1)$ as a reliable reference with negligible anisotropic contributions [210]. We checked that the K lattice depth depends neither on the particular wavelength chosen close to the Dy resonance line nor on the polarization angle. We also verified the expected linear scaling of the lattice depth with the lattice power in a range between P_0 and $3P_0$.

Figure 8.2(b) exhibits an example of an amplitude-modulation spectrum for ^{40}K at the reference power $P_0 = 67$ mW. The cloud size as a function of ν shows a pronounced asymmetry, pointing to the band edge near 66 kHz. Because of the

relatively small value of $\tilde{\alpha}_K$ at $\lambda = 626$ nm and the large recoil energy $E_{r,K} \approx 4E_{r,Dy}$, the lattice depth for the potassium atoms becomes small, which leads to a broad band structure and therefore to a broader spectral response. The spectrum is further broadened for various technical reasons¹, which makes the identification of the exact location of the band gap at $q = 0$ difficult (see Appendix in Sec. 8.6). To analyze the spectra, we use a combination of analytical fitting functions and a numerical simulation based on q -dependent transition probabilities calculated between the ground and second excited bands. The uncertainty in the identification of the band edge leads to a systematic error, which we estimate to be 4%. With this model, we deduce a ^{40}K lattice depth of $s_K = 4.75(19)$ for the same conditions as used in the ^{161}Dy measurements.

Finally, the dynamical polarizability of the dysprosium atoms can be derived as

$$\tilde{\alpha}_{Dy}(\lambda) = \frac{s_{Dy}(\lambda)}{s_K} \frac{m_K}{m_{Dy}} \tilde{\alpha}_K, \quad (8.3)$$

which is the basis of our further analysis. While the main uncertainty arises from the determination of the band edge, we have identified a second possible source of systematic uncertainty. The spatial distributions of both species in the optical lattice may differ, which leads to slightly different sample-averaged lattice depths. We have modeled this effect by employing the same numerical simulation as used for K also for Dy for a range of different experimental parameters. For the effect of the spatial distribution on the determination of $\tilde{\alpha}_{Dy}$, we estimate a systematic error of 3%, which together with the band-edge uncertainty of 4% adds up to a total combined systematic error of 5%.

8.3 RESULTS

In this section we present the main results of our measurements of the anisotropic polarizability of Dy and its variation with detuning across the 626-nm resonance. Furthermore, we extract the natural linewidth of the transition.

8.3.1 Anisotropic Polarizability

The dynamical polarizability can be generally decomposed into scalar, vector, and tensor parts [207, 208], which we denote $\tilde{\alpha}_s$, $\tilde{\alpha}_v$, and $\tilde{\alpha}_t$, respectively. The present work employs linearly polarized lattice beams and, consequently, measures the scalar and tensor contributions. The dynamical polarizability of an atom in the stretched state can be expressed as a weighted sum of scalar and tensor components,

¹ Stability of the lattice intensity, quality of the absorption imaging and general stability of the experiment contribute to noise on the measurement. Furthermore, due to technical reasons, the lattice depth is modulated already when ramping up the lattice.

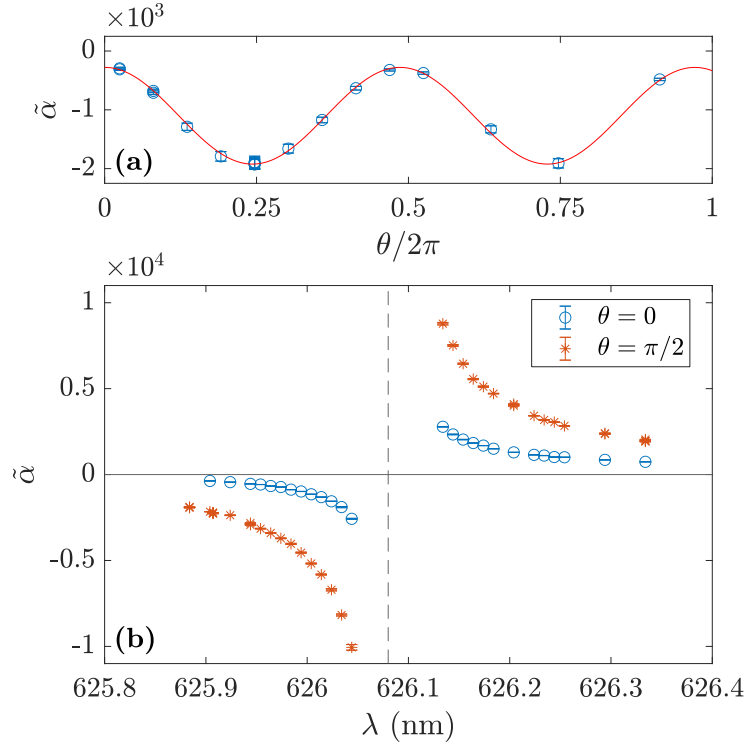


Figure 8.3: Measurements of anisotropic polarizability for ^{161}Dy . (a) Angle dependence of the polarizability at $\lambda = 625.884$ nm. The variation reveals the scalar and tensor contributions. The solid line shows a fit according to Eq. (8.4). (b) Wavelength dependence of the dynamical polarizability of ^{161}Dy near the intercombination transition line for two different polarization angles $\theta = 0, \pi/2$ (parallel and perpendicular to the quantization axis). The dashed line indicates the resonance center. In (a) the error bars represent the 1σ statistical fitting errors from the individual spectra used to determine the lattice depth. In (b) the error bars are smaller than the symbol size.

$$\tilde{\alpha}(\omega) = \tilde{\alpha}_s(\omega) + \frac{3 \cos^2 \theta - 1}{2} \tilde{\alpha}_t(\omega), \quad (8.4)$$

where θ is the polarization angle defined with respect to the quantization axis (see Fig. 8.1) and $\omega = 2\pi c/\lambda$ is the angular frequency of the laser field. In the experiment, we scan θ by rotating a half-wave plate. The quantization axis is determined by applying a small magnetic field less than 1 G along the direction of gravity (see Fig. 8.1). We experimentally confirmed that our measurements remain unaffected by an external magnetic field up to 10 G. In Fig. 8.3(a), we plot the dynamical polarizability as a function of the angle θ . The measurement was carried out at a fixed wavelength of $\lambda = 625.884$ nm, and the value of $\tilde{\alpha}_{\text{Dy}}$ is derived from the lattice depth, as discussed before. The variation of $\tilde{\alpha}_{\text{Dy}}$ shows the expected

mixing of the scalar and tensor polarizability, depending on θ . A fit according to Eq. (8.4) gives $\tilde{\alpha}_s = -1.37(1) \times 10^3$ and $\tilde{\alpha}_t = 1.10(1) \times 10^3$ (1σ statistical fitting errors). Here, at the specific wavelength chosen, the tensor component provides a contribution to the total dynamical polarizability that is comparable to the scalar component, generating the ratio $\tilde{\alpha}_t/\tilde{\alpha}_s = -0.80(1)$. Figure 8.3(b) shows the total polarizability for the two angles, $\theta = 0$ and $\pi/2$, from which we obtain $\tilde{\alpha}_s$ and $\tilde{\alpha}_t$ according to Eq. (8.4). We repeat the measurements for various detunings and observe the variation of the absolute value of $\tilde{\alpha}_{Dy}$ in a region of roughly 0.5 nm around the resonance center. The sign follows from the fact that the light field is attractive ($\tilde{\alpha}_s > 0$) for red detuning and changes sign on the blue side of the resonance.

Figure 8.4 shows the final result for the resonance behavior of $\tilde{\alpha}_s$ and $\tilde{\alpha}_t$. The polarizability can be modeled with a resonance model

$$\tilde{\alpha}(\omega) = \tilde{\alpha}_{bg} + \beta \frac{\omega_0^2}{\omega_0^2 - \omega^2}, \quad (8.5)$$

where $\tilde{\alpha}_{bg}$ is a background contribution from other resonances, the parameter β is defined as a dimensionless resonance strength, and $\omega_0 = 2\pi c/\lambda_0$ is the resonance center angular frequency. This model is applied to the data for both $\tilde{\alpha}_s$ and $\tilde{\alpha}_t$. In this case, we fit the data with a single-resonance model, although three hyperfine resonances are actually present in the fermionic isotope in the stretched state. Since the hyperfine splitting is small compared to the detuning [94, 279, 280], the deviation from the single-resonance model is negligible compared to our experimental uncertainties. We confirmed this by fitting the data with a corresponding extended model that takes hyperfine resonances into account.

Table 8.1 summarizes the fitting results. Notably, $\tilde{\alpha}_s$ includes a background of 275(13), originating from other transitions, mostly the strong blue line near 421 nm. In contrast, the background in $\tilde{\alpha}_t$ is only 8(14), which is consistent with 0. The off-resonant contributions from other lines essentially cancel each other in the tensorial part. For the 626-nm transition, from theory describing the angular part of a $J = 8 \rightarrow J' = 9$ transition [208, 210, 243], we expect a ratio between the tensor and scalar parts on resonance of

$$r \equiv \lim_{\omega \rightarrow \omega_0} \frac{\tilde{\alpha}_t(\omega)}{\tilde{\alpha}_s(\omega)} = \frac{\beta_t}{\beta_s} = -40/57 \approx -0.7018. \quad (8.6)$$

However, fitting the data with Eq. (8.5) yields a ratio of $-0.643(4)$. We attribute this deviation to a systematic error resulting from setting θ in our measurements (see Appendix in Sec. 8.7). We note that the fit results for the resonance position are inconsistent within the very small fit uncertainties. We attribute this minor discrepancy to the fact that we model the contribution of other lines with a simple constant offset $\tilde{\alpha}_{bg}$, thus ignoring the effect of a possible slope in the background.

Table 8.1: Results for the resonance parameters $\tilde{\alpha}_{bg}$, β , and $\lambda_0 = c/\omega_0$, obtained by fitting Eq. (8.5) to our data sets for $\tilde{\alpha}_s(\omega)$, $\tilde{\alpha}_t(\omega)$, and the mean polarizability $\tilde{\alpha}_0(\omega)$ according to Eq. (8.7). Numbers in parentheses give the 1σ fit uncertainties.

| Data | $\tilde{\alpha}_{bg}$ | β | λ_0 (nm) |
|--------------------|-----------------------|-----------|------------------|
| $\tilde{\alpha}_s$ | 275(13) | 1.055(3) | 626.0808(5) |
| $\tilde{\alpha}_t$ | 8(14) | -0.679(4) | 626.0794(8) |
| $\tilde{\alpha}_0$ | 278(10) | 0.885(3) | 626.0850(4) |

The exact value resulting for the fit parameter $\omega_0 = c/\lambda_0$ may be sensitive to such a slope. However, this minor inconsistency has no significant effect on the values obtained for the resonance strength parameter β .

8.3.2 Determination of the Natural Linewidth

To avoid the effect of uncertainties in θ we introduce the mean polarizability

$$\tilde{\alpha}_0 = \frac{\tilde{\alpha}(\theta = 0) + \tilde{\alpha}(\theta = \pi/2)}{2} = \tilde{\alpha}_s + \frac{1}{4}\tilde{\alpha}_t, \quad (8.7)$$

which turns out to be insensitive to small deviations of θ from the ideal values 0 and $\pi/2$ (see Appendix in Sec. 8.7). We can fit $\tilde{\alpha}_0$ with the model introduced in Eq. (8.5); the results can again be found in Table 8.1. Notably, we extract $\tilde{\alpha}_{bg} = 277(13)$, which is consistent with the offset on the scalar component given before. With the definition of $\tilde{\alpha}_0$ we find the relation

$$\beta_0 = \left(1 + \frac{r}{4}\right) \beta_s, \quad (8.8)$$

which now includes the ratio r , fixed to a theoretical value of -0.7018 . Our result for the resonance strength $\beta = 0.885(3)$ is now insensitive to systematic errors in the angle determination and combines both sets of data for $\theta = 0$ and $\pi/2$. With this method, we are left with the dominant error being the 5% uncertainty in the calibration of $\tilde{\alpha}_{Dy}$ as discussed before.

We can now extract the natural linewidth

$$\Gamma = \frac{2a_0^3\omega_0^4}{c^3} \frac{2J+1}{2J'+1} \frac{\beta_0}{1+r/4} \quad (8.9)$$

of the closed $J = 8 \rightarrow J' = 9$ transition. We calculate a linewidth of $\Gamma/2\pi = (137.9 \pm 0.4_{\text{stat}} \pm 6.9_{\text{sys}})$ kHz, which agrees well with transition probabilities obtained by radiative lifetime measurements on atomic beams [211, 281, 282]. The relative uncertainty is on par with the most precise measurement of the lifetime of $1.17(3)$ μs [281], which corresponds to a natural linewidth of (136 ± 3) kHz.

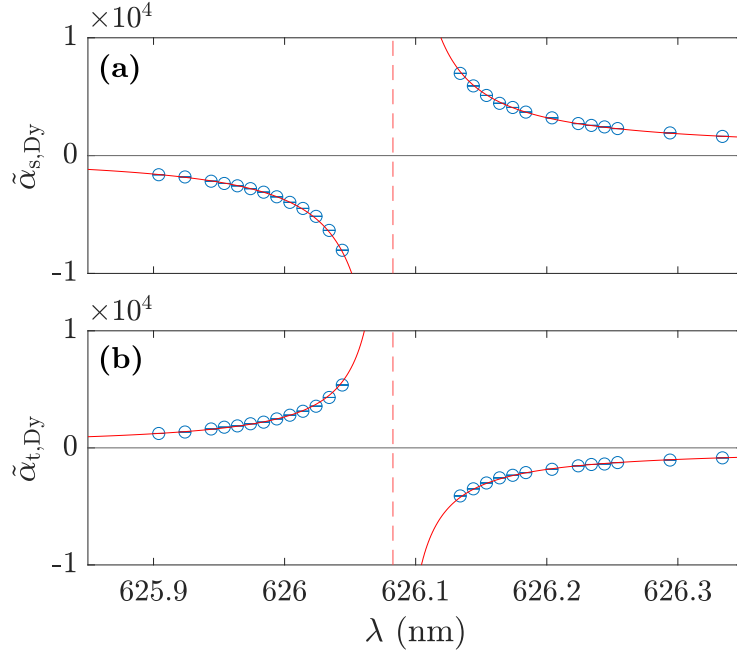


Figure 8.4: Measured (a) scalar and (b) tensor components of the dynamical polarizability of ^{161}Dy near the 626-nm line. Solid lines show a fit according to Eq. (8.5). Error bars are smaller than the symbol size.

The agreement of our result with this benchmark of a direct lifetime measurement on the level of a few percent also confirms that our indirect way to determine line strengths via measurements of dynamic polarizabilities produces accurate results. With an optimization of experimental parameters, the uncertainty in the determination of the lattice depth of K , which is the source of the dominating systematic error, could be reduced further.

8.4 DEMONSTRATION OF OPTICAL DIPOLE TRAPPING

In an additional experiment, we realize an optical dipole trap operating on the 626-nm transition and measure the lifetime and heating rate of the dysprosium atoms. We set the laser wavelength to the red-detuned side of the resonance and use one of the lattice beams, with the counterpropagating beam blocked. The polarization angle is set to $\theta = \pi/2$ to maximize the polarizability. By slowly (within 100 ms) ramping down the power of the horizontal 1064-nm dipole trap beam, we load the atoms into a bichromatic trap consisting of the horizontal 626-nm beam and the vertical 1064-nm dipole trap beam, with an average trapping frequency of $\bar{\omega}/(2\pi) = 110$ Hz. After a variable hold time, we record atom number and temperature with standard time-of-flight imaging. Since the lifetime in the

1064-nm dipole trap is two orders of magnitude larger than any other timescale of the system, we consider only the heating effect originating from the 626-nm trap.

In Fig. 8.5, the time evolution of the temperature and atom number at $\lambda = 626.334$ nm are displayed. At this detuning, we measured the polarizability to be $\tilde{\alpha} = 1.97(8) \times 10^3$, which includes also a possible deviation from the ideal angle $\theta = \pi/2$. In the measurement, we ramp the laser beam power to 170 mW, which results in a central intensity of $I_0 = 3.5 \times 10^6$ mW cm⁻². We calculate a central optical potential depth of $U_0 = -2\pi a_0^3 \tilde{\alpha} I_0 / c = k_B \times 16$ μ K, and by taking the gravitational effect into account, the potential depth is reduced to $k_B \times 4$ μ K. Initially, we observe a linear increase of the temperature. A linear fit from 0 to 1 s yields a heating rate of 311(7) nK/s, which indicates a photon scattering rate of about 0.8 s⁻¹. The calculated photon scattering rate in the middle of the trap is [202]

$$R_{\text{scatt}} = \frac{\Gamma}{\hbar\Delta} U_0, \quad (8.10)$$

where we take our result for the linewidth $\Gamma = 2\pi \times 138(7)$ kHz and where $\Delta = \omega - \omega_0$ is the frequency detuning. For our experimental parameters, we calculate a scattering rate of $R_{\text{scatt}} \approx 1.5$ s⁻¹ in the center of the optical potential. However, this model neglects that the atoms are spatially distributed in the trap and sample areas with lower intensity than in the trap center. This effect is even enhanced by the influence of gravity, which shifts the trap center out of the center of the intensity distribution. Furthermore, there is a considerable uncertainty in the measurement of the beam waist and therefore the value of I_0 . Considering these effects, the observed heating is consistent with the expected photon scattering.

For longer hold times, the heating rate is observed to decrease. This might be because the increased cloud size leads to a lower average intensity across the sample and therefore a reduced scattering rate. Another explanation is that when the temperature reaches about 500 nK, which is about a factor of 8 below the trap depth, some evaporation may set in and counteract the heating. Indeed, we observe an increased atom loss rate after 1 s of hold time [see Fig. 8.5(b)]. We use an exponential fit from 1 s onward and obtain a lifetime of $\tau = 1.9(1)$ s.

The measurement shows that dipole trapping close to the 626-nm line with a rather small wavelength detuning works as expected and provides an additional versatile tool to tailor optical potentials for Dy atoms. In particular, this may be interesting for species-selective dipole traps to manipulate mixtures of Dy with other species and can be used to optimize conditions to obtain superfluid regimes in Fermi-Fermi mixtures [176, 225].

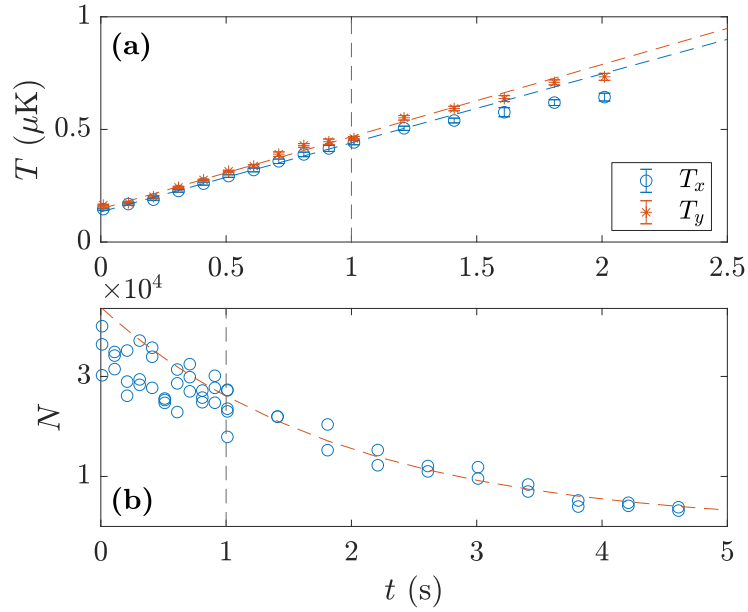


Figure 8.5: Time evolution of temperature and atom number in a bichromatic crossed dipole trap. (a) Temperature in the x and y directions with linear fits for the first 1 s (dashed vertical line). (b) Atom number and corresponding exponential fit from 1 s onward.

8.5 CONCLUSION AND OUTLOOK

We have shown that the method introduced in Ref. [124] to accurately measure the dynamic polarizability of an atom by comparison with a reference species can be generalized to light fields that act repulsively. Using modulation spectroscopy in an optical lattice, we investigated the 626-nm intercombination line of Dy and measured the scalar and the tensorial part of the anisotropic polarizability in the resonance region. As an important benchmark for our method, the line strength derived from our polarizability measurements is consistent with previous measurements of the natural transition linewidth. Our relative uncertainty of $\sim 5\%$ is already on par with the previous measurements and may be further improved by further suppressing systematic effects. The method is of particular interest for characterizing the multitude of optical transitions in submerged-shell lanthanide atoms, which have become very popular in laser cooling and quantum gas experiments.

We have also demonstrated optical dipole trapping of Dy with laser light tuned about 0.25 nm below the center of the 626-nm line. We found efficient trapping with low heating, in quantitative agreement with expectations based on the line strength derived from the polarizability measurements. This introduces optical

dipole potentials generated by laser light tuned close to this intercombination line as an interesting tool for future experiments.

For our particular goal to create a mass-imbalanced fermionic superfluid in the ^{161}Dy - ^{40}K mixture [105, 176], species-specific optical potentials [229] offer alternative handles for control. On the blue side of the 626-nm resonance, the light field will be repulsive for both species. This allows us to create boxlike trapping schemes [283–285] for the preparation of homogeneous Dy-K mixtures. At a specific detuning, the polarizability ratio will match the mass ratio, and an optical levitation scheme [223] can be realized that compensates the effect of gravity for both species simultaneously. In a harmonic trap, the phase diagram critically depends on the trap frequency ratio of both species, as investigated theoretically in Ref. [225]. Species-specific optical potentials allow us to optimize the conditions for attaining and observing the superfluid phase transition.

We thank M. Lepers for discussion. We acknowledge financial support from the Austrian Science Fund (FWF) within Project No. P32153-N36 and within the Doktoratskolleg ALM (Grant No. W1259-N27). We further acknowledge a Marie Skłodowska Curie fellowship awarded to J.H.H. by the European Union (project SIMIS, Grant Agreement No. 894429).

8.6 APPENDIX A: LATTICE DEPTH EXTRACTION FOR POTASSIUM

In general, the Hamiltonian of a lattice modulated with modulation frequency ν is given by

$$H = \frac{p^2}{2m} + V \cos(k_x x)^2 [1 + \epsilon \cos(2\pi\nu t)], \quad (8.11)$$

where ϵ denotes a small perturbation of the lattice depth and $k_x = 2\pi/\lambda$ is the wavenumber of the laser in the x direction. The calculation of transition probabilities between bands of this lattice follows Ref. [286]. According to Bloch's theorem, the eigenstates of the unperturbed system can be described in a plane-wave basis by

$$\Psi_q^{(n)}(x) = e^{iqx} \sum_K c_{K,q}^{(n)} e^{iKx}, \quad (8.12)$$

where $c_{K,q}^{(n)}$ are the Fourier coefficients to the reciprocal lattice vectors K in the n -th band. Using Fermi's golden rule, the transition probability between bands n and m of an atom with quasimomentum q is given by

$$W_q^{nm} \propto \left| \sum_K c_{K,q}^{(n)} c_{K,q}^{(m)} (q + K)^2 \right|^2. \quad (8.13)$$

By numerically diagonalizing the Hamiltonian in Eq. (8.11), the coefficients $c_{K,q}^{(n)}$ can be found for all available reciprocal lattice vectors K , the energy gap between

bands n and m can be calculated for a given q , and W_q^{nm} can be converted to $W^{nm}(\nu)$. For the transition between bands $n = 0 \rightarrow m = 2$, the resulting spectrum $W^{02}(\nu)$ exhibits a sharp edge on the lower-energy side, which corresponds to atoms with $q = 0$. However, if the cloud width σ_c and lattice beam waist w_0 are comparable and if the cloud center position is offset from the center of the lattice by r_c , the effective lattice depth will vary over the extent of the cloud, effectively smoothing out the sharp edge. In a numerical simulation we account for this by slicing the atom distribution and calculating the transition probability with the corresponding $V(r)$ for each slice, where $V(r)$ follows the Gaussian form of the lattice beam. Each spectrum of the individual slices is then weighted according to the atom distribution. In our experiment, the averaged transition probability $\bar{W}^{02}(\nu)$ manifests itself in the spectrum derived from the cloud size after time of flight $\sigma(\nu) \propto \bar{W}^{02}(\nu)$.

The value extracted for the lattice depth from such a profile depends on the particular fit model. We use numerical simulations of $\bar{W}^{02}(\nu)$ with different parameters to test various fitting functions. The best agreement of the extracted lattice depth with the simulation input is achieved with

$$\sigma(\nu) = \sigma_0 + \left(\frac{1}{2} + \frac{1}{\pi} \arctan \left(\frac{\nu - \nu_0}{\delta\nu} \right) \right) [k(\nu - \nu_0) + A], \quad (8.14)$$

where ν_0 marks the position where the cloud width increases by half of the amplitude A . $\delta\nu$ sets the width of the step, k sets the slope of the linear part above the step, and σ_0 is the cloud width below the band edge.

As a second method, we perform least-squares regression of the full numerical simulation of the experimental profiles. For this we vary w_0 , σ_c , r_c , V_0 , and a such that the sum of the squares

$$\sum_{\nu_i} [\sigma(\nu_i) - a\bar{W}^{02}(\nu_i)]^2 \quad (8.15)$$

across all measurement points ν_i is minimal. The effective lattice depth is then extracted by integrating $V(r)$ over the extent of the cloud. The results of the two methods usually agree within less than 4%.

8.7 APPENDIX B: SYSTEMATIC UNCERTAINTIES FROM ANGLE DETERMINATION

To address the issue of the impact of uncertainties in the angle determination, we rewrite Eqs. (8.4) and (8.7) as

$$\tilde{\alpha}(\theta) = \tilde{\alpha}_0 + \frac{3}{4} \tilde{\alpha}_t \cos(2\theta). \quad (8.16)$$

When measuring the polarizabilities $\tilde{\alpha}_{\parallel}$ and $\tilde{\alpha}_{\perp}$ for $\theta = 0$ and $\theta = \pi/2$, respectively, angle deviations of δ_{\parallel} and δ_{\perp} will result in measured values with systematic offsets corresponding to

$$\begin{aligned}\tilde{\alpha}'_{\parallel} &= \tilde{\alpha}_0 + \frac{3}{4}\tilde{\alpha}_t \cos(2\delta_{\parallel}) \approx \tilde{\alpha}_0 + \frac{3}{4}\tilde{\alpha}_t(1 - 2\delta_{\parallel}^2), \\ \tilde{\alpha}'_{\perp} &= \tilde{\alpha}_0 + \frac{3}{4}\tilde{\alpha}_t \cos(\pi + 2\delta_{\perp}) \approx \tilde{\alpha}_0 - \frac{3}{4}\tilde{\alpha}_t(1 - 2\delta_{\perp}^2).\end{aligned}\tag{8.17}$$

When calculating the effect on the mean polarizability

$$\tilde{\alpha}'_0 = \frac{1}{2}(\tilde{\alpha}'_{\parallel} + \tilde{\alpha}'_{\perp}) = \tilde{\alpha}_0 + \frac{3}{4}\tilde{\alpha}_t(\delta_{\perp}^2 - \delta_{\parallel}^2),\tag{8.18}$$

it becomes apparent that the errors will (partially) cancel each other. In particular, a systematic shift compared to the actual angles given by the magnetic field, such that $\delta_{\perp} = \delta_{\parallel}$, will cancel out completely. In contrast,

$$\tilde{\alpha}'_t = \frac{2}{3}(\tilde{\alpha}'_{\parallel} - \tilde{\alpha}'_{\perp}) = \tilde{\alpha}_t(1 - \delta_{\perp}^2 - \delta_{\parallel}^2)\tag{8.19}$$

is more sensitive to errors in the determination of θ .

OPTICAL POTENTIAL SHAPING WITH A DMD

To realize uniform and arbitrary trapping potentials for the atoms with a high flexibility, we employ a DMD in direct imaging configuration. I will start this chapter with a short overview over possible light tailoring techniques and the requirements for our experiment (see Sec. 9.1). A description of the setup along with the employed techniques can be found in sections 9.2-9.4. The chapter will be concluded with an overview of the results for uniform potentials and linear gradients in sections 9.5 and 9.6.

9.1 PRELIMINARY CONSIDERATIONS

In our experiment, we are mainly interested in large homogeneous traps to achieve a uniform density distribution of the atoms. To choose the most suiting technique, we try to estimate the uniformity quality that has to be achieved, and compare the advantages and disadvantages of the different approaches.

9.1.1 Uniformity Requirement

We have seen in Chapter 6 that under the LDA, see Eq. (6.9), the density follows the intensity distribution. In the case of a uniform intensity distribution, the density profile is flat. However, in a realistic scenario, at the bottom of the trap there will be a small residual modulation of the trapping potential caused by imperfections in the generation of the beam profile, which we can model as

$$V(\mathbf{r}) = V_0 + \delta V(\mathbf{r}). \quad (9.1)$$

According to Eq. (6.9), the density is then given by

$$n(r) = \frac{1}{6\pi} \left(\frac{2m}{\hbar^2} \right)^{3/2} [\mu - V_0 - \delta V(\mathbf{r})]^{3/2}. \quad (9.2)$$

At the trap bottom we can set $V_0 = 0$ and for small fluctuations $\delta V(\mathbf{r})$, we can linearly expand to

$$n(r) = n_0 \left[1 - \frac{\delta V(\mathbf{r})}{\mu} \right]^{3/2} \approx n_0 \left[1 - \frac{3}{2} \frac{\delta V(\mathbf{r})}{\mu} \right]. \quad (9.3)$$

For a zero temperature Fermi gas, the chemical potential is equal to E_F . Because no states above E_F are populated, we can set the trap depth to $V_b \geq E_F$ without losing atoms. This means that the fluctuations in the density are given by

$$\frac{\delta n(r)}{n_0} = -\frac{3}{2} \frac{\delta V(\mathbf{r})}{V_b}. \quad (9.4)$$

By requiring that the fluctuations should only be a few percent of n_0 , we can set a limit on the variation of the beam profile in its flat part.

However, in a typical experimental scenario we can reach $T/T_F \approx 0.1 - 0.2$, which means that the step at E_F is smeared out and some states above E_F are also occupied. To avoid extensive plain evaporation from these states, we have to limit E_F to about 50% of V_b . In the end, we estimate that the relative error on the trapping potential, and thus the intensity distribution, should be 3 times smaller than the required relative modulation of the density profile.¹

9.1.2 Techniques for Shaping the Intensity Distribution

The techniques to tailor the intensity distribution of light can be divided in three main categories. Each of them has been used over the years in atom trapping experiments, and has its advantages and disadvantages that have to be considered carefully to make the right choice given the requirements of the experiment. Here, only a very brief overview is given, but an extensive discussion of different techniques can be found in Ref. [218].

Acousto-optic modulators (AOMs) and deflectors (AODs) are typically used to control total power and frequency of the laser light. This is achieved by employing a radiofrequency field in a dielectric crystal that diffracts a passing laser beam. The deflection angle, and therefore also the final beam position after an imaging lens, depend on the driving frequency. By modulating the frequency faster than all relevant atomic timescales, a temporally averaged trapping potential can be painted, see Fig. 9.1(a). Alternatively, multiple frequencies can be used to generate multiple beams, for example to generate an array of micro-traps. Generally, AODs offer a high power efficiency and power threshold and therefore high trap depths, however, they can also suffer from thermal lensing. Furthermore, they lack in spatial resolution and do not perform well on larger features. The ability to produce 2D patterns also requires the addition of a second AOD, which adds complexity.

The second option is Fourier imaging of a spatial light modulator (SLM). In this case, a local phase modulation of the light is Fourier transformed to a corresponding

¹ For a BEC, the lowest single particle state of energy E_0 is macroscopically occupied, and the chemical potential has to be smaller than E_0 . For small μ , the second term in Eq. (9.3) blows up, which means that small deviations from a homogeneous potential lead to large variations in the atomic density. The quality requirement for a BEC is therefore much higher than for a DGF.

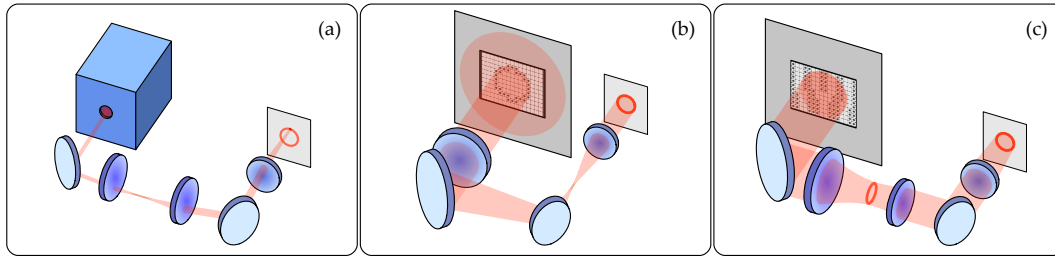


Figure 9.1: Three different techniques to generate a ring shaped potential. (a) Fast modulation of the radiofrequency of a two-directional AOM paints a time-averaged ring shape in the image plane. (b) Direct imaging of a ring shaped mask on a DMD cuts away intensity of a Gaussian beam and leaves a ring shaped potential. (c) An LC-SLM changes the phase information of a Gaussian beam in the Fourier plane such that a ring shape is produced in the image plane. Figure taken from Ref. [218].

intensity distribution in the focus of the imaging system, see Fig. 9.1(c). The phase modulation can be realized either by a static element such as a phase plate, or by an active system such as a liquid crystal (LC)-SLM or a DMD. The phase modulation method excels in power efficiency, especially in the creation of small and sharp features (e.g., micro-trap arrays in Rydberg quantum simulators). Vice versa, for the generation of large and sharp features, the Fourier approach is inefficient, because most of the high-frequency components will be close to 0. Another problem is the computational effort that is needed to derive the input field for a desired pattern. However, the Fourier approach is able to correct for aberrations resulting from the optical system.

As a third option, a DMD or dark mask can be used to locally modulate the beam intensity. A telescope is then typically used to directly image the resulting pattern onto the atoms, see Fig. 9.1(b). Amplitude modulation is inherently inefficient in terms of power, because parts of the intensity are cut out or absorbed by the beamshaping element. Furthermore, for typical applications in ultracold atom experiments, a high demagnification is needed to reach large trap depths, which poses some limitations on the optical setup. However, the method can perform well on both large and small features, and the shape of the directly imaged amplitude mask is easy to compute. Additionally, DMDs can also be used to dynamically change the trapping potential on the order of several kHz.

In our experiment, we want to generate large homogeneous traps with a high uniformity. The direct amplitude modulation technique in combination with direct imaging seems best suited for that. The requirement of a high beam quality means that we need to be able to correct for imperfections of the incoming beam and optical system. Furthermore, in the current state of the experiment, the optical access is limited, which prevents the integration of a high-resolution imaging

system needed for hard-walled traps. Additionally, without going to either the ultraviolet (UV) regime or close to a Dy transition,² it is not possible to find a wavelength where the light has a repulsive effect on both species (see Fig. 6.1). We have therefore originally decided to employ a DMD to produce red-detuned flat-top profiles [287]. Such profiles have been produced for atom trapping with extremely high quality, by a careful choice of techniques, and the employment of a well-designed optical system and a feedback algorithm [288].

9.2 BASIC METHODS AND TECHNICAL DETAILS

This section will introduce the basics of how DMDs in direct imaging configuration can produce grayscale images for homogeneous traps.

9.2.1 Digital Micromirror Devices

A DMD is a micro-opto-electro-mechanical system consisting of many microscopic movable mirrors arranged as pixels on a chip, and is used mainly in video projectors and lithography applications to project arbitrary light patterns. For an in-depth discussion of the general working principle of DMDs please refer to Refs. [218, 289]. In a nutshell, each pixel can be addressed individually to move between two stable positions, where the mirror plane is rotated by $\pm 12^\circ$ out of the chip plane. These positions can be assigned to an *on* or *off* state, where the light is reflected to the target image plane in the *on* state and elsewhere in the *off* state. Modern DMDs as the DLP9000X consist of 2560×1600 pixels, which corresponds to 4k resolution and can be driven with refresh rates of up to 12.9 kHz. Even faster refresh rates are possible for models with smaller resolution.

Because of their ability to arbitrarily shape optical potentials, DMDs recently have become popular also in the field of cold atoms, see for example Ref. [218] and references therein. However, the nature of the pixels is inherently binary, therefore, DMDs are perfectly suited for hard-walled trapping potentials like box traps, provided the imaging system has a high enough resolution. To be able to set values in between *on* and *off*, different techniques are possible. In applications like video projectors, pixels can be toggled very fast between *on* and *off* to display time-averaged shade values, since the human eye is not fast enough to sample at high frequency. When working with cold atoms, the switching frequency has to be compared to all other timescales of the system. For example, trapping frequencies can be on the order of kHz, meaning that especially older DMD models might not be fast enough and could introduce heating to the sample [290, 291].

² The characterization of the polarizability around 626 nm actually came well after the start of the DMD project. By now we could employ blue-detuned traps, but the techniques developed for red detuning translate well to other applications, such as optical levitation.

A second method to generate gray values that is used in this thesis, is to limit the resolution of the imaging system with a spatial filter, such that the point spread functions (PSFs) of the single DMD pixels overlap and multiple micromirrors contribute to one point in the image plane. A grayscale algorithm is then used to calculate which pixels have to be switched on.

9.2.2 Direct Imaging

In the direct imaging configuration, the DMD plane is imaged onto the atoms via an imaging system typically consisting of two lenses with focal lengths f_1 and f_2 , see Fig. 9.2. The DMD is placed in the focal plane of the first lens. To calculate the pattern that has to be displayed by the DMD in order to arrive at the desired intensity distribution, we look at the amplitude distribution $g(x, y)$ of the beam as it propagates through the system. Typically, the input beam intensity distribution at the position of the DMD $I_{in}(x, y) \propto |g_{in}(x, y)|^2$ will be close to a Gaussian profile. After reflection on the DMD, the amplitude distribution will be given by

$$g_1(x, y) = g_{in}(x, y)r(x, y), \quad (9.5)$$

where $r(x, y)$ is the amplitude reflectance of the DMD at position (x, y) of the individual pixels, which can be calculated by

$$r(x, y) = \sqrt{\frac{T(x, y)}{I_{in}(x, y)}}. \quad (9.6)$$

Here, $T(x, y)$ is the target function that should be imaged onto the atoms. T has to be chosen such that $r \in [0, 1]$, or $T < I_{in}$ at every point. Typically, direct imaging systems are used in high-NA applications, where the spatial bandwidth is very high. In an approximation to an ideal geometric image, this results in the output field

$$g_{out}(x, y) = \frac{1}{M}g_1(x/M, y/M), \quad (9.7)$$

where $M = -f_2/f_1$ is the magnification of the imaging system. This is best suited for hard-walled potentials such as blue-detuned box traps, because the imaging resolution does not limit the steepness of the potential barrier.

However, in reality, the bandwidth of optical systems is limited, and as a result, a single point will not be perfectly imaged but will appear washed out in the image plane. The response of an imaging system to such a point source is described by the PSF. In our system each DMD pixel contributes a more or less broad PSF. The resulting image will then be a convolution of the ideal geometric image with the PSF, and multiple pixels will contribute to the total intensity at a certain position. The optical system itself is therefore acting as a lowpass filter, allowing us to use

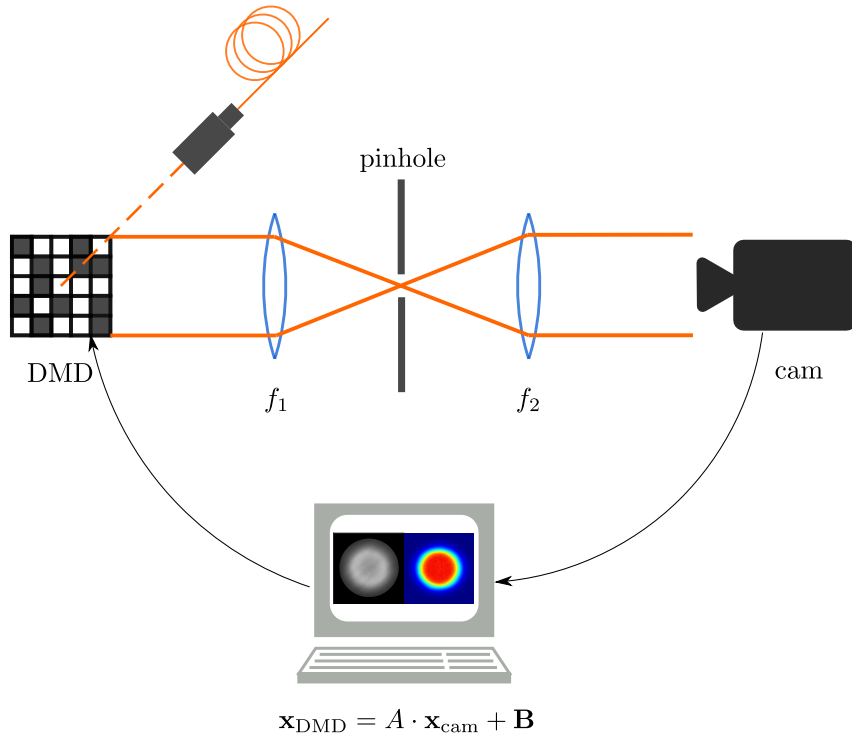


Figure 9.2: Schematic of the DMD test setup. Light is delivered to the DMD via an optical fiber. The DMD is imaged to a camera by a telescope consisting of lenses with focal lengths f_1 and f_2 . The pinhole in the Fourier plane of the telescope is used for spatial filtering. The camera acts as a beam profiler and a computer is used to analyze beam profiles, and control the DMD and upload patterns to it. In the final experiment, the image plane at the place of the camera is imaged again onto the atoms with a second imaging system.

many pixels together to set grayscale images. The cutoff frequency is set by the properties of the optical system, but can also be directly controlled by introducing a pinhole in the back focal plane of the first lens. The amplitude distribution in frequency space right behind the pinhole is given by

$$g_2(v_x, v_y) = \mathcal{F}(g_1(x, y))h(v_x, v_y), \quad (9.8)$$

where $\mathcal{F}()$ denotes the Fourier transform and $h(v_x, v_y)$ models the pinhole amplitude transmission. The cutoff frequency ν_c depends on the focal length f_1 of the first lens and the radius R_{ph} of the pinhole and is given by

$$\nu_c = \frac{R_{ph}}{\lambda f_1}. \quad (9.9)$$

After the inverse Fourier transform \mathcal{F}^{-1} caused by the second lens, the final intensity distribution is

$$I_{out} \propto |g_{out}|^2 = \left| \mathcal{F}^{-1}(\mathcal{F}(g_1(x, y))h(\nu_x, \nu_y)) \right|^2. \quad (9.10)$$

The choice of R_{ph} depends heavily on the spatial frequencies involved in $T(x, y)$. For fast varying profiles, e.g., flat traps with steep walls, a high-quality imaging system is required, and no pinhole is used. This in turn means that only a few mirrors will contribute to the total intensity at a certain position in the image, resulting in worse accuracy for I . For slowly varying profiles, however, R_{ph} can be tailored such that many pixels contribute to a single point and a high level of accuracy can be achieved.

9.2.3 Grayscale Algorithm

To obtain grayscale images from $r(x, y)$ it has to be converted to a binary pattern $DMD(x, y)$ that can be displayed by the DMD. The naive approach would be to just round $r(x, y)$ to either 0 or 1, however, the error that is made when rounding is lost, which limits the accuracy of the pattern. Instead, an error-diffusion algorithm is used [292, 293]. The idea behind this algorithm is to set a pixel at position (x, y) to 1 (0) if r for that pixel is above (below) a threshold value (typically 0.5). The algorithm then computes the pixel error

$$e(x, y) = r(x, y) - DMD(x, y), \quad (9.11)$$

and diffuses e to the reflectance of nearby pixels

$$r(x + a, y + b) = r(x + a, y + b) + c(a, b)e(x, y). \quad (9.12)$$

In this case, we use a simple algorithm that propagates the error onto four other nearby pixels (although many variations with different numbers of pixels are possible). The coefficients c at the row and column index shifts a and b are then given by

$$\begin{aligned} c(1, -1) &= -3/16, & c(1, 0) &= -5/16, \\ c(1, 1) &= -1/16, & c(0, 1) &= -7/16. \end{aligned} \quad (9.13)$$

The algorithm traverses the DMD pattern from left to right for each row, starting at the top row. An example is shown in Figure 9.3, where the grayscale algorithm was used to convert a grayscale image to a binary one. Because of the limited resolution, the binary character becomes visible only when zooming in.

It was shown that the resulting quasi-random distribution of binary values has a close to blue noise spectrum that minimizes noise at low spatial frequencies while

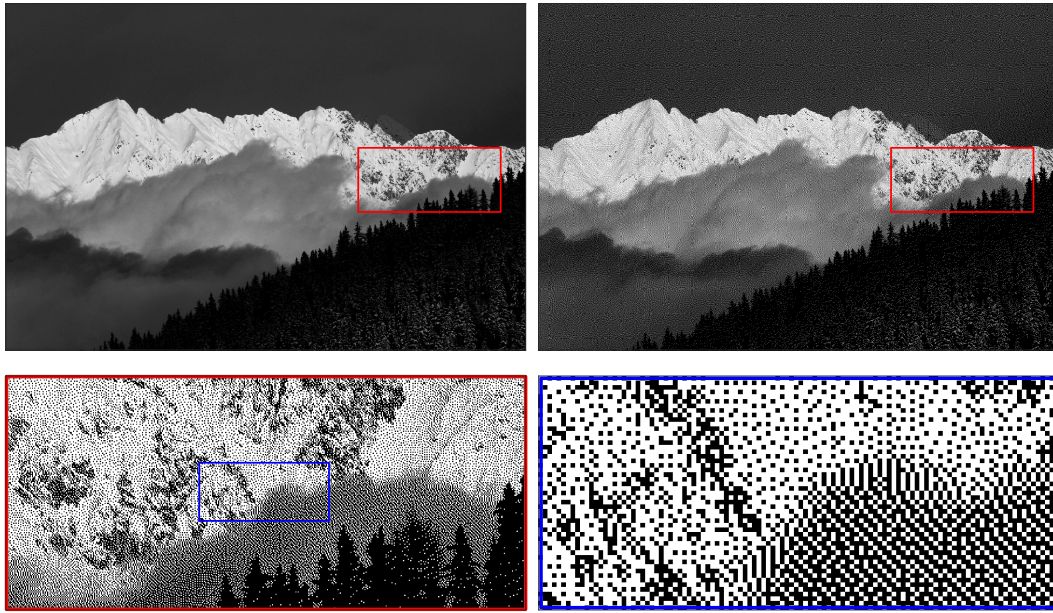


Figure 9.3: Error-diffusion on an image of the mountains close to Innsbruck [295]. Top left shows the original image, top right the error-diffusion image. The rectangles indicate the position of the magnified image sections in the lower two panels.

shifting the digitization noise to higher frequencies. In combination with the spatial filtering introduced before, which can be designed to filter out the high spatial frequencies caused by the digitization, this algorithm ensures that multiple pixel contribute to one point in the image plane, minimizing the error introduced by converting the grayscale image to a binary image [294].

9.2.4 *Input and Transformation*

For this thesis, a simple C++ software was written as an interface between the user and the system components. This includes the communication of the computer with the DMD and the camera that is used to record the beam profile. The software includes the integration of a Matlab engine to analyze the recorded profiles and to design the DMD patterns.

To calculate the reflectance $r(x, y)$, some knowledge about the intensity distribution on the DMD $I_{in}(x, y)$ is needed. For some applications, it might be enough to approximate I_{in} as an ideal Gaussian profile, with its values for center coordinates and widths estimated from beam profile measurements. However, a detailed knowledge of I_{in} will lead to higher-quality solutions for r that already account for imperfections in the initial beam.

For this, the camera in the image plane is needed, as well as a transformation from the camera coordinate system to the DMD system. An affine transformation covers rotation, translation and scaling between two coordinate systems. We can calculate the coordinates of a point \mathbf{x}_{DMD} in the DMD plane by

$$\mathbf{x}_{\text{DMD}} = A \cdot \mathbf{x}_{\text{cam}} + \mathbf{B}, \quad (9.14)$$

where A is a 2×2 matrix and \mathbf{B} is a translation vector. \mathbf{x}_{cam} are the corresponding coordinates of the point in the camera system.

A and \mathbf{B} can be found by recording a set of test points. For this, a small area of about 5×5 pixels around the coordinates $\mathbf{x}_{i,\text{DMD}}$ is displayed on the DMD and the corresponding coordinates $\mathbf{x}_{i,\text{cam}}$ are found by taking a picture in the imaging plane and fitting it with a 2D Gaussian function. Three or more points are needed to calculate the transformation.

To implement this in the control software, we use the OpenCV-package that offers extensive computer vision capabilities, including methods to find A and \mathbf{B} as well as performing the transformation. This enables us to map the intensity distribution I_c of the incoming beam to the DMD pixels such that imperfections of the beam can already be accounted for in the generation of r . Furthermore, this mapping can later be used in a feedback algorithm that maps an error function back to the DMD plane to iteratively refine the DMD pattern. A good calibration of the transformation is especially important for the feedback algorithm to work properly. In the future, it might therefore be necessary to employ higher order polynomial transformations that can include distortions caused by the imaging system.

9.2.5 Red-Detuned Flat Traps

Because of the limitations imposed by the atomic transitions and the experimental setup, we have chosen to start with red-detuned flat traps at 1064 nm.³ This is arguably harder to realize with good quality than blue-detuned traps, where it is rather straight forward to have a dark center region surrounded by sheets of light. With a DMD, a blue-detuned hollow trap is realized by cutting out a portion of a Gaussian beam [296]. For red-detuned traps on the other hand, a large region of uniform maximum intensity is required that has to satisfy the requirement imposed in section 9.1. This can be realized with a combination of direct imaging, spatial filtering, grayscaling and the right choice of target function. These techniques will also translate to the design of linear gradients for optical levitation.

³ At the starting time of this project, the Texas Instruments DLP4500NIR was the only available DMD designed for infrared applications. This particular model features a diamond geometry, and suffers from flicker noise and limited image display times, which requires some hardware modifications similar to Ref. [291].

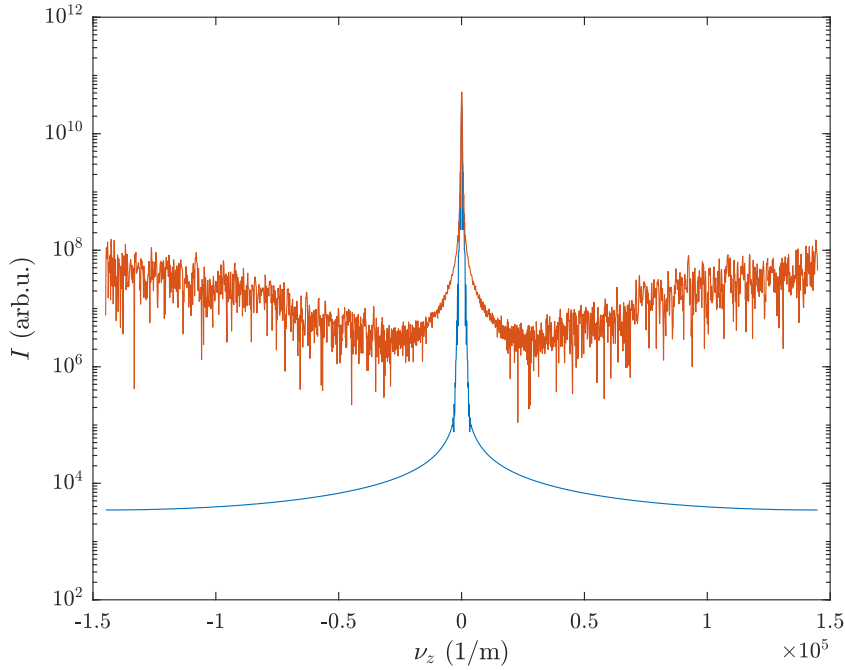


Figure 9.4: FFT spectra of a SL target function (blue) and the intensity distribution of a simulated beam directly after the DMD (red). For low spatial frequencies, the two spectra coincide, while the digitization noise introduced by the error-diffusion algorithm dominates for higher frequency components. This noise can be eliminated with spatial filtering.

For a homogeneous red-detuned trap, a target function of an 8-th order Superlorentzian (SL) form

$$SL(x, y) = \frac{A_0}{1 + \left(\frac{\sqrt{x^2 + y^2}}{r_{SL}} \right)^8} \quad (9.15)$$

has a flat-top region and is well suited to be used in combination with spatial filtering, because of its narrow spatial frequency profile compared to a perfect box function. As can be seen in Fig. 9.4, the main frequency components are located in a narrow region around 0. Also shown is a simulated beam profile directly after the DMD, displaying a realistic DMD pattern created by the grayscale algorithm. For low frequencies, it overlaps with the target SL spectrum and then starts to deviate at higher frequencies because of the introduced blue noise from the digitization. A careful choice of the cutoff frequency to the point where the two curves separate ensures a high quality beam profile. However, the SL profile can not feature particularly steep walls, as this would require frequency components that overlap with digitization noise and are cut out by spatial filtering. This trade-off

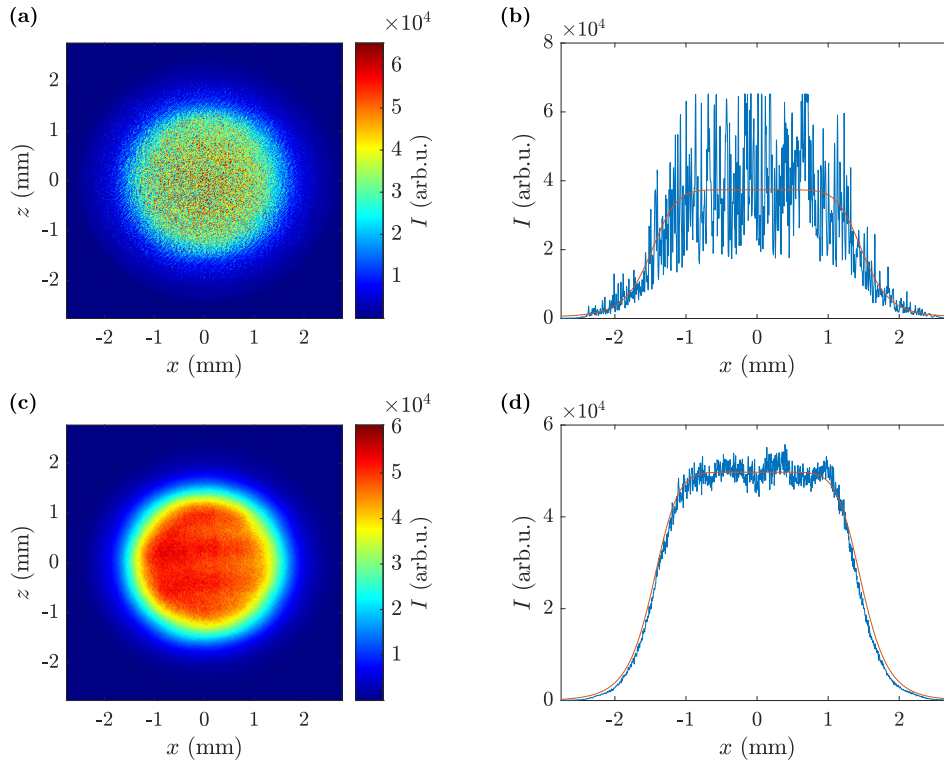


Figure 9.5: 2D profile of a first iteration SL beam without (a) and with 500 μm pinhole (c) and corresponding cut along the middle in x direction (b, d). The red line depicts a fitted SL. The exposure time of the camera was adjusted to avoid saturation, leading to a difference in amplitude between the two profiles.

has to be kept in mind when designing the target function and spatial filter cutoff frequency.

Figure 9.5 shows an experimental SL beam profile generated with the DMD, once with a 500 μm pinhole in the imaging system and once with the pinhole removed. In a first step, the profile of the incoming beam was measured with the camera by switching all DMD pixels to the *on* state. The profile was then mapped to the DMD plane to calculate r and subsequently the digitized DMD pattern. The figure shows the effect of the spatial filtering. Especially in the image without pinhole, some significant high-frequency noise is present. This is greatly reduced for the profile with the pinhole, where the digitization noise is filtered out, resulting in a much cleaner profile. As a result, the low-frequency modulation is more noticeable.

This can also be seen in Fig. 9.6, which shows a comparison of the spectra of the two profiles shown in Fig. 9.5 along with the spectrum of the target SL function. The three spectra overlap in the central blue shaded area, which shows the frequency region that is able to pass through the spatial filter. Evidently, the spectrum without the pinhole has a much higher spectral density at the mid-range of frequency

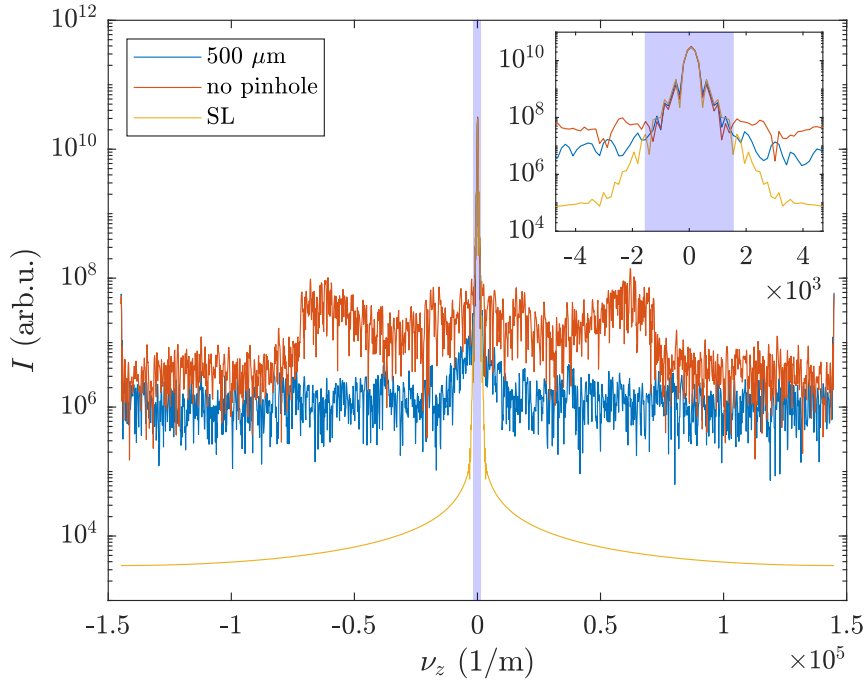


Figure 9.6: Spectra of the profiles in Fig. 9.5. The insert shows a zoom of the central region. The blue shaded area shows the frequencies that are allowed to pass through the optical low-pass filter with a pinhole diameter of 500 μm .

components, which is responsible for the lower quality of the beam profile. The step at a frequency of about $7 \times 10^4 \text{ m}^{-1}$ hints at the maximum spatial frequency of the DMD, which is given by its mirror pitch.

In the case of the 500- μm pinhole, only low-frequency components can pass through the optical system, which explains the much better quality of the profile. However, except for the center low-frequency region, the spectrum is still considerably higher than the target SL and is comparable to the unfiltered profile. From a physical view, any noise at frequencies higher than the cutoff frequency is not able to pass the pinhole, which means it has to originate somewhere after the lowpass filter. This will be discussed in more detail in the next section.

To measure the quality of the generated beam profile and to be able to compare, a root-mean-square (RMS) error

$$\epsilon_{\text{RMS}} = \sqrt{\frac{1}{N} \sum_{x,y \in \zeta} \left(\frac{I_c(x,y)}{T(x,y)} - 1 \right)^2} \quad (9.16)$$

is calculated by comparing the camera image I_c and the target function, in this case $T = SL$. ϵ_{RMS} is restricted to a mask ζ which consists of N pixels. ζ is usually

defined as the area where $T > 0.99A_0$, so that ϵ_{RMS} is only calculated over the flat part of the target function. Similarly, the maximum error is defined as

$$\epsilon_m = \max_{x,y \in \xi} \left| \frac{I_c(x,y)}{T(x,y)} - 1 \right|. \quad (9.17)$$

The profile in Fig. 9.5(a) results in $\epsilon_{\text{RMS}} = 35\%$ and $\epsilon_m = 76\%$, whereas the spatial filtering improves this to 4.9% for the RMS error and a maximum error of 52%. According to the estimations in Sec. 9.1, this would result in an average density modulation of about 15%. To improve the SL profiles, an extensive investigation of noise sources as well as the implementation of a feedback algorithm was necessary.

9.3 NOISE TREATMENT

In general we can identify three different sources that can introduce noise that deteriorates the beam quality or its measurement. Digitization noise was already introduced, with the solution being the choice of a suitable digitization algorithm, as well as spatial filtering. In this section we discuss the camera as a noise source and some methods to limit its impact, as well as the influence of the usage of coherent light.

9.3.1 Camera Noise

Every imaging sensor inherently suffers from noise, which will deteriorate the image and therefore introduce features that are physically not present. In the scope of this thesis we discuss a simplified model. The EMVA Standard 1228 [297] gives a more detailed description of the measurement and classification of imaging sensor characteristics and noise sources.

In simple words, photons incident on the sensor are converted to photo-electrons with a certain quantum efficiency QE . On readout, the resulting electrical signal gets amplified and then converted to a digital signal. In a simplification this can be described by the gain K , which includes the whole process of conversion from photon to digital signal. Furthermore, even when all light is blocked from reaching the sensor, thermal electrons accumulate in the pixel structure over time, which generates a dark current that is added to the digital signal as an offset. Different noise sources are present at all stages of this process and the noise can generally be divided in temporal and spatial components.

Temporal noise includes photon shot noise, as well as shot noise from dark electrons in the pixels, and electrons in the amplification and readout circuits. Electron shot noise dominates at low light intensity and has a dependence on temperature, which means that it can be decreased to some extent by cooling the sensor. Photon shot noise dominates at high light levels, but at the same time

decreases relative to the signal with increasing light intensity. The temporal noise component of our camera is about 1% [298] at high light levels, but can be reduced easily by averaging over N successive frames and decreases as $1/\sqrt{N}$. Typically we average 170 frames, at which point the temporal noise component is suppressed and the spatial noise component is revealed.

Spatial fixed pattern noise (FPN) originates from physical differences in the single pixels. This includes dark signal non-uniformity (DSNU) caused by different accumulation rates of dark electrons throughout the sensor's pixels, and photo response non-uniformity (PRNU). PRNU can be caused by varying QE , amplification and conversion efficiencies, resulting from imperfections in the manufacturing process, or contamination (e.g., dust) on the sensor surface or optical system. FPN can be very disturbing for a human viewer and is a big problem in applications where the photon flux is to be measured. DSNU is easily corrected by taking a dark image with the same exposure time and subtracting it from the measurement pictures. PRNU can be reduced by taking flat-field images from a homogeneous light source. K can then be calibrated for each pixel and defective or dust-covered pixels can be identified.

Since the focus of this work is on the spatial shape of the laser beam, a lot of care has to be taken to also minimize PRNU, because otherwise we can not really distinguish if the noise and deviations are on the beam itself or stem from the imaging sensor. Furthermore, any feedback algorithm will to some extent introduce the camera noise on the beam itself.

9.3.2 Flat-Field Correction

To characterize a sensor's PRNU including contaminations such as dust, and subsequently to correct for it, a light source with a very well known intensity profile, ideally completely homogeneous, is needed. Integrating spheres can be used as a spatially homogeneous light source to generate a flat intensity distribution. We use a Thorlabs 4P3 modular integrating sphere with two high-power LEDs centered at 1064 nm. Generally, the degree of flatness depends on the ratio of sizes of the output port of the sphere and the imaging sensor, as well as the ratio of port size to distance to the sensor [299]. If the distance is at least five times and the sensor size smaller than 0.8 times the size of the output port, the uniformity across the sensor should be better than 1%, however, the intensity will be strongly reduced. To reduce the effect of temporal noise, 170 frames are averaged to reveal the PRNU. An analysis of the standard deviation over the central region of the flat-field image indicates a PRNU variation of about 1.4%.

A four-stage algorithm is employed to construct a flat-field image and lookup tables that can be used to correct for PRNU. In a first step, the algorithm calculates a local-median-filtered image and compares the raw image to the filtered version.

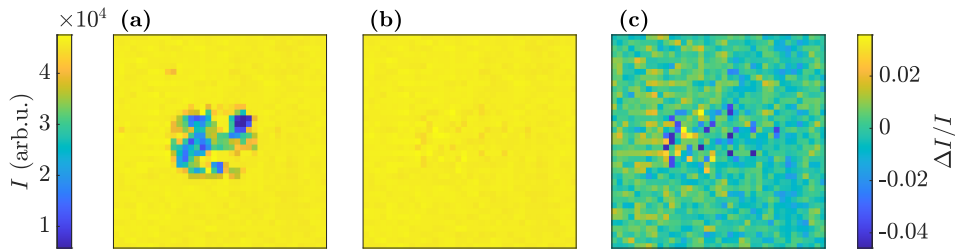


Figure 9.7: Cutout of a dust speckle in the uncorrected (a) and corrected image (b). (a) and (b) share the same color scale to show the effect of the correction. (c) shows the relative deviation to the mean of the corrected image cutout.

If pixel values are more than 5% lower than in the filtered image, the pixel is considered contaminated (for example, with a dust particle). The algorithm then substitutes the pixel value with the value of another non-contaminated pixel from a random position in its vicinity. This works well for small dust particles or single defective pixels, however, if the particle shadows several tens of pixels (comparable to the filter window size), the median value will also be substantially lower, meaning that pixels that are only partially covered will not be detected. Therefore, in the second step, the sequence is repeated with a median filter on the corrected picture. Now, almost all contaminated pixels should be identified and corrected by non-contaminated pixels nearby. The coordinates of each contaminated pixel as well as the corresponding substituted pixel are saved in a lookup table. Fig. 9.7 shows a cutout of a dust speckle in the uncorrected picture, as well as the same cutout after the correction. The dust speckle results in a reduction in intensity of up to 90%. The correction minimizes this to less than 5%, which becomes comparable to the average deviation in the rest of the cutout.

In a third step, another filtered image is calculated from the dust corrected image with smaller median filter. Then, hot pixels are identified if the pixel value of the dust corrected picture is more than 5% higher than the filtered image. These pixel values are then substituted with the median image value. The resulting picture is now corrected for contaminated and hot pixels and should represent the corrected flat-field image F that can be used to correct for PRNU. Analyzing again the central region of the corrected flat-field image results in an improved PRNU variation of about 0.8%.

To correct an image (for example from a flat-top beam), dust contaminated pixels are identified and corrected with the lookup table, and hot pixels are substituted by the local median value. The resulting dust corrected image I_{dc} should be free of contaminated and hot pixels, and the corrected flat-field image F can be used to calibrate the gain values. The final corrected image I_{fc} is calculated as

$$I_{fc} = \frac{I_{dc}m}{F}, \quad (9.18)$$

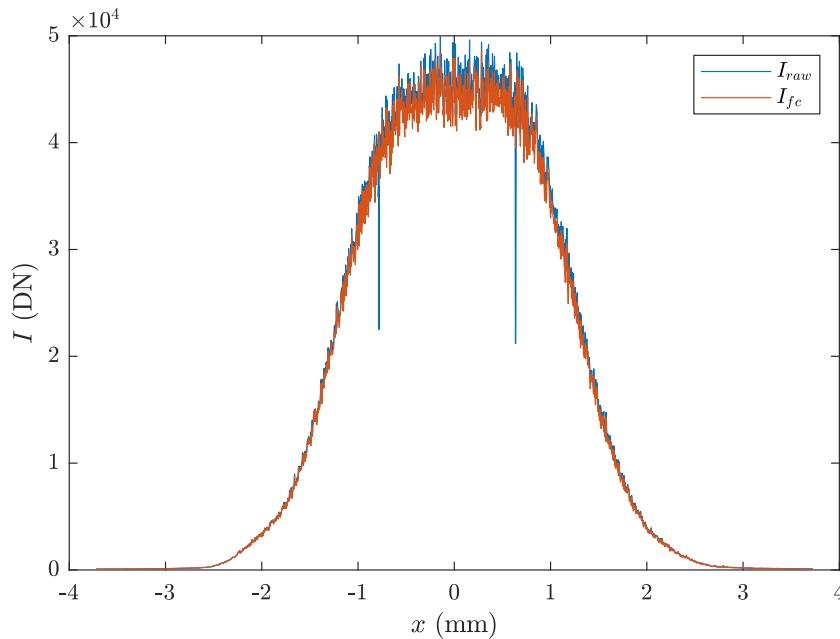


Figure 9.8: Exemplary cut through a flattop profile before and after flat-field correction. The two dips in the intensity in the raw picture I_{raw} come from dust contaminated pixels and are corrected in the flat corrected picture I_{fc} .

where m is the pixel averaged value of F . Ideally, the flat-field light source should be completely homogeneous. However, realistically, there will still be some slow variation across the sensor, and it might be necessary to replace m with a local pixel value average to account for this variation. Care has to be taken that this does not overlap with the spatial frequencies of slow variations in the sensor gain. To test this method, a second flat-field image was taken and the flat-field correction algorithm was applied to it. The standard deviation over the central region was now as low as 0.1%, which we interpret as the residual temporal noise component of the camera.

Ideally, the flat-field image is taken with the same exposure time as the one to be corrected, since it influences dark current and read error. At the same time, the intensity for both pictures should be aimed at about 70-80% of the saturation intensity of the camera, to maximize the signal-to-noise ratio. It is not always possible to achieve both simultaneously.

Figure 9.8 shows a cut through I_{raw} and I_{fc} of an image of a flat-top beam. Although the correction algorithm works very well for dust contaminated pixels and therefore greatly improves the maximum error from about 50% to about 20%, the overall effect on the RMS error is much smaller, only on the order of about 0.2%. Evidently, the corrected image still exhibits high-frequency noise that seems

to not originate from PRNU. With 170 averaged frames, there is only a residual read noise component, which is not physically present on the beam itself and could be filtered out electronically. However, other noise in the same frequency range that is present on the optical beam would also be filtered out wrongfully. It is therefore important to estimate the different contributions of other possible noise sources.

9.3.3 *Coherent Light and Interference*

Besides the camera noise, laser speckles and interference fringes can become a problem, since in atom trapping applications the light is usually generated from a narrow bandwidth laser source and is highly coherent. Analyzing the temporal behavior of single pixels over successive beam profiles shows that there is still some temporal noise present that does not come from the sensor itself. On average, this noise is about 0.5%, however in some regions the single pixel temporal noise is about 1%. Because the single profiles were averaged over 170 frames we can exclude read noise as the dominating source. Instead we suspect changing interference patterns to be the cause of the temporal behavior.

Interference fringes originate from the superposition of the original beam and a scattered spherical wave, for example originating from scatterers such as dust on the surfaces of optical components. Numerical simulations were employed to estimate the effect of scatterers and speckles on the beam quality [300]. Scatterers produce interference rings with rather low spatial frequencies in the far field. Drifts in the laser frequency or optical path length modify the phase of the interference rings temporally and cause them to move. When recording several beam profiles every few tens of seconds and calculating the standard deviation per pixel, we indeed see correlated regions of higher standard deviation corresponding to interference rings. In principle they could be corrected for with a feedback algorithm on the DMD provided they change slow enough during the measurement period.

Another concern is the appearance of speckles originating from small height changes of optical surfaces in the beam path. In our setup, speckle patterns with high spatial frequencies could possibly come from the last imaging lens. Speckles originating from before the spatial filter should be suppressed to low-frequency modulations. Modeling of speckle patterns is more difficult, as the statistical properties of the surface have to be known to infer speckle size at the position of the camera [301]. Without this information we can unfortunately not determine if the high-frequency noise on the pictures is caused by speckles.

Special care also has to be taken in the choice of camera model, since the thin layer architecture of solid-state sensors promotes interference between reflections from layer boundaries. The magnitude and shape depends on the specific design and materials used, and usually becomes more pronounced the longer the wavelength is. This interference is not present on the beam before the camera, but on the image,

and will be introduced to the beam by a feedback algorithm when not filtered out. The camera model chosen here also has its sensor protection glass removed, which would be another source for interference.

As observed by other groups [288, 302], using broadband sources or scanning the frequency of the laser greatly reduces the occurrence of interference features. However, this might not be compatible with cold atom experiments, since modulation of the light frequency can lead to parametric heating of the atomic sample if the modulation frequency is comparable to the trap frequency. Furthermore, certain applications such as the dual-species optical levitation rely on a precise detuning from a narrow atomic transition. The levitation condition would then not be met.

9.3.4 Digital Lowpass Filter

Looking at the setup in Fig. 9.2, one can arrive at the argument that noise with a frequency higher than the cutoff frequency of the spatial filter can not physically pass the optical system [294]. It therefore has to be generated somewhere after the pinhole. In Ref. [294] the noise components with frequencies higher than the cutoff frequency of the pinhole spatial filter are attributed to the camera. Subsequently a digital lowpass filter that filters noise introduced by the camera was designed for post-processing, improving their RMS error to lower than 1%.

As we observe interference that can not clearly be attributed to a single optical element or the camera, such a post-processing approach could lead to an underestimation of the error. Unfortunately, without knowledge of the statistical properties of the surface roughness of the optical elements we can not estimate an upper bound for the spatial frequency of the speckle pattern. However, we can still use a digital filter to estimate the contribution of some frequency ranges to the RMS error.

Figure 9.9 shows the effect of post-processing on a beam profile. For the original profile we observe $\epsilon_{\text{RMS}} = 4.8\%$. For a filter that reflects the maximum spatial frequency that the DMD can act upon, this reduces to 4%. Finally for a filter designed to match the pinhole transfer function we get 3.6%, which shows that, although some noise is located at frequencies higher than what the DMD supports, at this point the main contribution to the high RMS error comes from a low-frequency modulation on the beam, which can be improved by a feedback algorithm.

9.4 FEEDBACK ALGORITHM

To improve the quality of the beam profiles, different feedback algorithms have been proposed and used. In general, the camera picture is compared to the target profile and an error matrix is calculated, which can then be used to refine the pattern on the DMD. The algorithms differ in what way the feedback is employed to the

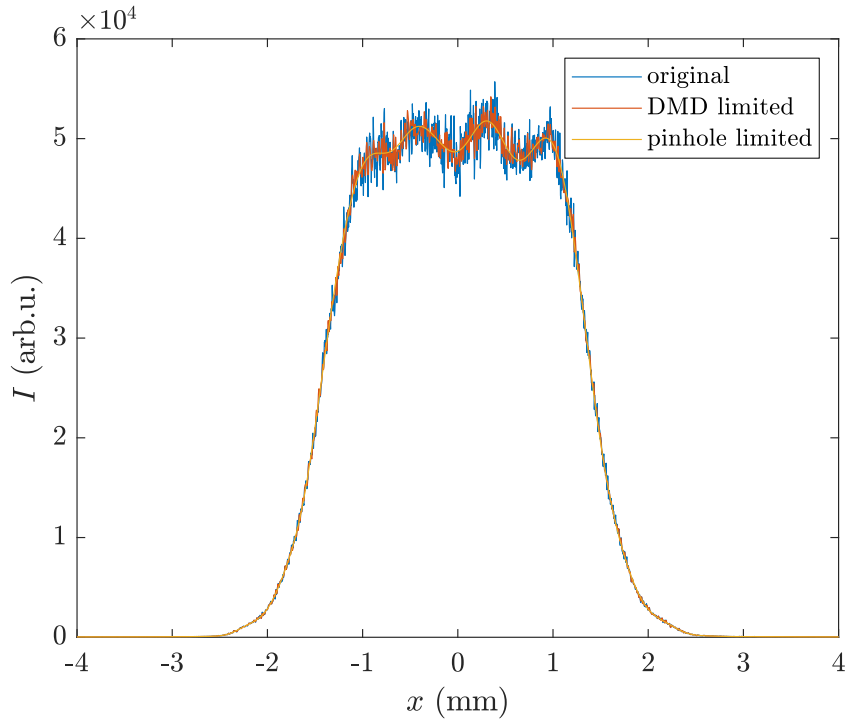


Figure 9.9: Cut through a beam profile with different digital filters.

DMD pattern. For example, a PI-feedback [303] calculates an error matrix as the difference between target and camera picture and then adds it to the last reflectivity, weighted by a proportional and integral coefficient. A new DMD pattern is then calculated by digitizing the new reflectivity, which leads to an entirely new pattern.

Here we have chosen an algorithm that works by flipping single pixels [294] with a bookkeeping approach. First, the error matrix in the camera plane $E_c(x, y)$ is calculated as the difference between target and camera image $E_c(x, y) = T(x, y) - I_c(x, y)$, and maxima and minima are identified. The algorithm then counts the number of pixels N_{on} in the *on* state in a small region S around the maxima/minima and determines the number of pixels to be flipped as

$$N = N_{\text{on}} \sum_{\{x,y\} \in S} \frac{E_c(x, y)}{T(x, y)}. \quad (9.19)$$

The shape of the original input beam is thereby accounted for by counting the number of *on* pixels that were necessary to arrive at the recorded intensity. The corresponding coordinates of the maximum/minimum on the DMD are then calculated using the affine transformation, and N pixels are switched *on* in the vicinity if $N > 0$, or vice versa if $N < 0$. This procedure is then repeated for other extrema in $E_c(x, y)$ and the resulting pattern is finally loaded to the DMD, and

the RMS error improves. In the next iteration, the size of S should be decreased to improve the accuracy of the feedback, as the size of S influences the spatial extent of the features that can be addressed. The algorithm stops when the RMS error can not be improved anymore.

As an extension to this procedure [304], if the PSF of the optical system is known, the algorithm can also check whether $E_c(x, y)$ improves after a PSF is added or subtracted from the picture at the position of the extrema, which corresponds to flipping a single pixel *on* or *off*, respectively. Supposedly, this should lead to a higher accuracy of the feedback, since smaller features can be addressed by directly computing the effect of switching a single pixel at its correct position. Although the PSF can be measured by switching only a single or a small number of mirrors *on*, we have found that this approach does not lead to better results than the bookkeeping approach in our case. We attribute this to the fact that measuring the PSF of a single pixel has to be done at extremely low light levels on the camera, which demands the adjustment of the exposure time, which in turn also influences the noise levels. Furthermore, the PSF has to be weighted by the spatial intensity variation of the input beam, which the bookkeeping routine does automatically. Also, the computational cost of adding and subtracting multiple individual PSFs per extrema in $E_c(x, y)$ is dramatically higher than flipping multiple pixels at once, especially in the first iterations of the feedback, where the RMS error is still quite large and many pixels have to be switched.

As stated before, it is important that the camera is flat-field corrected and high-frequency spatial noise originating from other sources than the beam itself is minimized. Otherwise, a single hot pixel from the camera, for example, will occur as a minimum in E_c . The algorithm will then try to flip some pixels to correct for the deviation, but since the error is originating from the camera and not dependent on the actual intensity of the beam, the algorithm will never succeed. Instead, over a few iterations, more and more pixels in this region will be set to the *off* state and a dark spot will appear in the beam.

9.5 BEST ACHIEVED FLAT PROFILE

Fig. 9.10 shows our best achieved flat-top beam after employing all of the discussed concepts including feedback. To minimize camera noise, 170-frame averages were taken and PRNU was minimized by using the flat-field correction for every image. To find the optimal cutoff frequency, the target SL was numerically filtered with different cutoff frequencies. The smallest possible cutoff that still preserved the SL shape was chosen, as to get rid of as much digitization noise as possible. The focal length of $f_1 = 150$ mm and the pinhole diameter of $500 \mu\text{m}$ were then selected accordingly. After employing the bookkeeping algorithm, the best profile resulted in $\epsilon_{\text{RMS}} = 3.2\%$ and a maximum error of $\epsilon_m = 17\%$ without digital filtering.

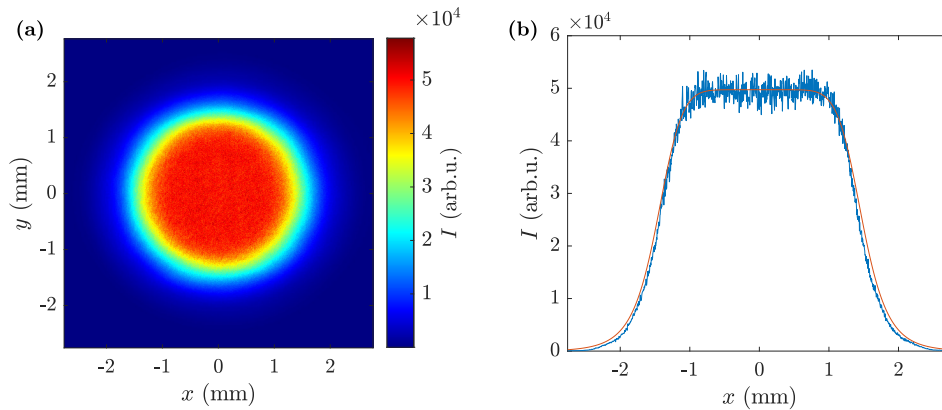


Figure 9.10: Best achieved beamprofile and cut through it. The red line indicates a fit with a SL profile.

Compared to the best reported RMS error of 0.2% in Ref. [288], our result is still an order of magnitude worse. However, as explained before, at this level it is not easy to identify the different noise sources. In Ref. [294], the argument is made that every noise component with a frequency higher than the cutoff frequency of the spatial filter can not physically pass the optical system and must have another source, therefore it can be filtered away digitally in post-processing, which results in the number given above. In our case we can not be certain that this is a valid approach, because speckle patterns with high spatial frequency can not be ruled out.

It can still be useful to employ filters to get an idea of the impact of noise in certain spatial frequency regions. A cautious choice of a 3×3 nearest-neighbor averaging filter already improves the RMS error by a factor of 2, while employing a filter reflecting the pinhole cutoff frequency would even result in $\epsilon_{\text{RMS}} = 0.53\%$. This suggests that high-frequency noise is the main contribution to the RMS error, and that the feedback algorithm got rid of most of the low-frequency deviations. The remaining low-frequency error is possibly caused by an insufficient accuracy of the determined affine transformation between camera and DMD plane.

In Ref. [288] the impact of the coherence of the light source was investigated and it was shown that the usage of incoherent light improved the beam quality. This would possibly also justify the use of a digital filter, since speckle noise can be ruled out in this case. Such an approach is unfortunately often not applicable because of the requirement of a certain light frequency, as in our case. It could still be useful to see if high-frequency noise is still present when using an incoherent source. If so, this would suggest that the camera is still limiting the performance of our system.

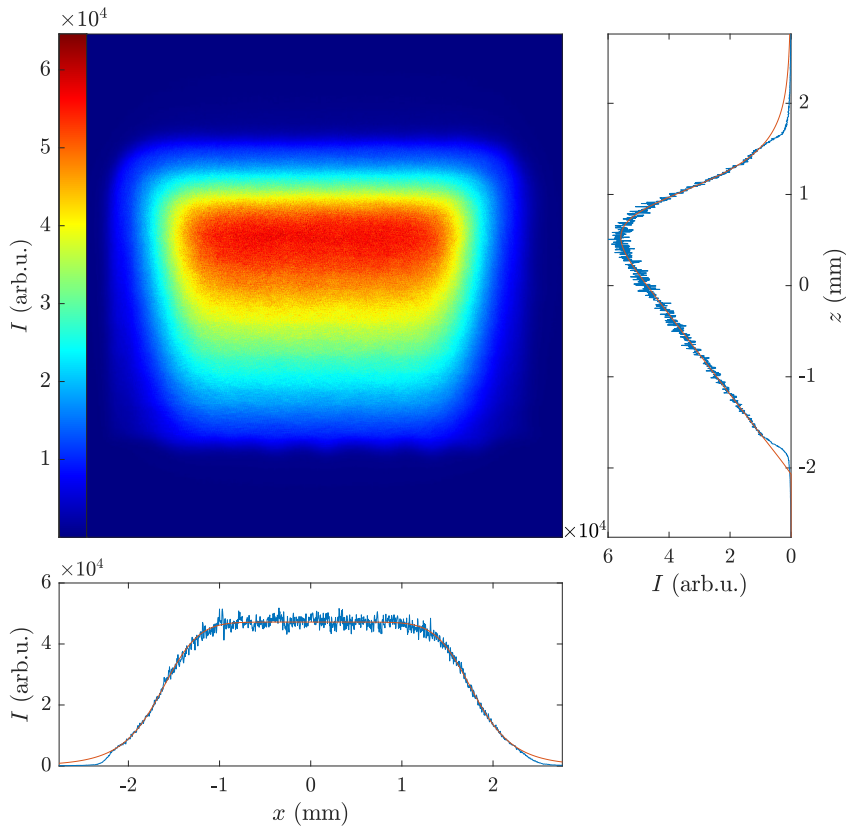


Figure 9.11: Beamprofile and cuts through a slope profile. The target function is depicted in red.

Summing up, we are confident that the RMS error of our flat-top profiles is at least 3.2% or better. According to the discussion in Sec. 9.1 this would lead to a root-mean-square density modulation in the flat part of the trap of about 10%. Ultimately, this should be tested on the atoms itself. A second imaging system is needed to image the profile in Fig. 9.10 onto the atoms. Because of the large demagnification needed to adjust the size of the trap, the high-frequency features would be scaled to sub-wavelength sizes and not be resolved anymore. In the end, the atomic density distribution should be taken as a measure of the beam quality, provided the atom imaging resolution is good enough.

9.6 LINEAR OPTICAL GRADIENTS

Some of the introduced methods can also be used to generate other beam shapes for trapping. We are mainly interested in generating linear optical gradients to compensate the gravitational potential. By requiring

$$U(z, \omega) = -\frac{2\pi a_0^3}{c} \tilde{\alpha}(\omega) I(z) \stackrel{!}{=} mgz = U_g(z), \quad (9.20)$$

we see that the optical intensity in z -direction has to have a linear slope

$$I(z) = -\frac{mgc}{2\pi a_0^3 \tilde{\alpha}(\omega)} z \quad (9.21)$$

in order to be able to levitate the atoms. This potential can be superimposed with an ordinary Gaussian trapping profile or with a uniform profile, and therefore should be as homogeneous as possible, which poses similar challenges as before.

In addition to the techniques already discussed, the choice of target function is again very important. In our experience, the easiest way is to set the target function as a combination of the linear gradient and the SL shape, as this again features a narrow spatial frequency profile centered at low frequencies. In this case, the SL is modified to a rectangular instead of circular shape. The resulting target function for the DMD (y on the DMD is z in the experiment)

$$T_s(x, y) = SL(x, y) \times k(y - y_0) \quad (9.22)$$

can be customized to fit the original Gaussian shape with the slope factor k . By changing the offset y_0 , the origin of the slope can be shifted with respect to the SL profile, thus changing the overall shape from a slope profile to a tilted-flattop-like profile.

The resulting beam profile after the bookkeeping feedback algorithm is shown in Fig. 9.11. The fitted target function T_s (red) interpolates between a high quality linear part in the central region and the SL part in the edge regions, mitigating the problems that come when spatially filtering the high-frequency components needed for a steeper cutoff. The deviation from T_s at low intensities is because the feedback algorithm was set to act only at certain intensity levels to avoid problems with the image background. Over the region where $SL > 0.99A_0$, the resulting $\epsilon_{\text{RMS}} = 3.5\%$ is very close to the reached quality for the flattop beam and should work well for compensating gravity. Similar as before, employing a digital filter simulating the pinhole (here 1 mm diameter) results in a lower error of $\epsilon_{\text{RMS}} = 1.0\%$, suggesting that we mostly exhibit the same limiting factors.

The region where $SL > 0.99A_0$ measures about $1.9 \times 1.9 \text{ mm}^2$ on the DMD, which is necessary to utilize as many of the DMD pixels as possible to achieve a high quality profile. At the same time the required total power of a square region at

the position of the atoms with length l is proportional to l^3 . As a result, to minimize the needed total power, a suiting telescope with a demagnification of about $1/80$ has to be employed, such that this region barely fully covers the trapping volume of the dipole traps. Then $\tilde{\alpha}(\omega)$, k and the initial optical power of the Gaussian beam have to be matched to l and set such that the levitation condition is fulfilled. Depending on the combination of these parameters, input powers of some W will be needed, which can be difficult to reach depending on the wavelength. One problem with this approach is that a lot of optical power of the original Gaussian beam is cut away to achieve the slope profile and is not utilized. It might therefore be better to operate the DMD in Fourier imaging, since phase modulation can be far more power efficient in cases where the target profile is similar to the input profile.

Part IV

A LOOK IN THE MIRROR AND A LOOK AHEAD

CONCLUSION

When I joined the Dy-K experiment for my Master's thesis, assembly of the the vacuum setup had just started after moving into a new lab space. After developing a laser system for the K MOT, I continued as a PhD student, at a time when we were able to realize our first dual fermionic MOT and subsequent loading of the atoms into a dipole trap, which was soon followed by the measurement of the Dy polarizability (see Chapter 7). Since this first publication, the apparatus constantly evolved to meet the new requirements imposed by the physics we wanted to explore. At the end of this thesis, I want to take a look back, to what has been achieved during my time as a PhD student, and a look ahead, to what is coming next for the Dy-K experiment in the near and far future.

My work can be roughly separated in two parts. In the first part of my work, I focused on developing a method to better understand the physical phenomena we observed in the experiment. After extensive scans over the magnetic field, we were able to identify and characterize a suitable interspecies Feshbach resonance close to 217 G that enables us to realize strongly interacting Fermi-Fermi mixtures. The Monte Carlo simulations started as a simple model to verify that the slowing effect we observed in the expansion of the interacting mixture can indeed be attributed to a high collision rate between the two species. The immediate good agreement between experiment and simulation led to a more thorough characterization of the simulation method, trials of possible expansions to the model and substantial improvements in computational efficiency. As a result, we now have a tool that serves as a fast test bed for some physical phenomena that might appear in the experiment. However, it has become clear that the simulation model does not work well in the regime where quantum statistical effects become important, which should become accessible as the experimental apparatus evolves. For a more quantitative analysis of phenomena under these conditions, more elaborate simulation models already exist [174], as well as other, better working theoretical descriptions [191, 305].

The second part is connected to the technological advances for our apparatus in terms of controlling the shape and strength of the trapping potentials. The measurement of the Dy polarizability at the standard trapping wavelength of 1064 nm led to a deeper understanding of our trap configuration and subsequently enabled us to optimize the preparation protocols used to reach the degenerate regime [105]. The measurement of the Dy polarizability close to the 626-nm intercombination line now allows us to realize traps that are blue detuned for both species simultaneously,

as well as to accurately tune the differential polarizability between Dy and K. This gives us one more handle to control the system and realize favorable conditions to access the superfluid regime [225]. A new high-power laser system for 626 nm is already in place to supply high-power beams.

In terms of controlling the shape of the potential, the DMD system is now ready to realize red-detuned homogeneous traps and linear gradients of high quality. However, currently the apparatus lacks optical access to add an imaging system with high demagnification, which would be necessary to realize traps on the length scale of the atomic sample with good quality and trap depth. One possible solution to this problem would be to add a glass science chamber to the apparatus, which would provide space for a high-resolution objective that could be used for imaging the sample and projecting the DMD patterns. There is a reserved port available on the main chamber, however this would involve substantial modifications to the current vacuum and laser setups, as well as adding a transport stage between the chambers. A second generation experiment might therefore be better suited to incorporate high-resolution imaging and DMD setups in a more customized design. As a more feasible solution in the short term, we could change to Fourier imaging and phase modulation for the optical levitation scheme. The addition of the new 626-nm laser also allows us to realize traps that are blue detuned for both species. These can also be generated with an alternative technique, for example by employing axicons [285, 306], which need less space to set up. A proof-of-principle test has been conducted with such a setup in the Dy-K experiment, and although a trapped sample was realized, the apparatus is currently lacking the imaging quality to confirm the uniformity of the potential through absorption imaging of the atoms.

CURRENT STATE AND WHAT'S NEXT FOR THE DY-K EXPERIMENT

In parallel to my thesis, several advancements were made in the experimental apparatus, some of the details are provided in Refs. [307, 308]. Ramping the magnetic field close to the 217-G resonance involves crossing many Dy intraspecies and Dy-K interspecies resonances, which leads to heating of the sample and atom loss. To circumvent these effects, a lot of time was spent on finding optimal experimental sequences that involve separating the two species by gravity during the ramp. Furthermore, the effect of induced eddy currents in our steel chamber was minimized by calculating optimized current ramps with a feed-forward technique. New power supplies with less noise were also added to the apparatus. An in-depth characterization of the dense Dy single species Feshbach spectrum was performed at low magnetic fields [224] and close to the inter-species resonances, and revealed regions with low loss, which serve as suitable preparation points for the sample.

With these advancements, we were able to identify several Dy-K resonances at lower fields [151] that were previously inaccessible because of their narrow character (in terms of magnetic field) and because we lacked field control. The observation of molecules at the BEC side of these resonances allowed us to measure the R^* parameter, and work is now underway to be able to prepare pure and cold molecular samples and ultimately a DyK molecular BEC.

More generally, recent theoretical work [225] suggests that carefully tuning the trapping potentials of K and Dy would increase the temperature where resonant superfluidity is expected to appear to experimentally feasible values. In this case, a study of the mixture across the phase diagram will provide an important benchmark for theoretical models. Ultimately, with a substantial improvement of temperature and density, our system will be a good candidate to observe the long elusive FFLO phase. With the integration of the homogeneous trapping system we will also maximize our chances to be able to observe pairing at non-zero momentum.

So far, the hydrodynamic expansion is our main signature of resonant interactions in the mixture. A colder, denser sample would also allow us to access new phenomena, for example the observation of collective oscillations, which has not yet been achieved with a mass-imbalanced Fermi-Fermi mixture. Preliminary measurements showed that we can currently only barely access the strongly damped regime between the collisionless and hydrodynamic regime for the CoM mode. With an increase of the scattering rate, we should be able to observe a locked oscillation of both species at the same frequency, different from their trapping frequencies.

BIBLIOGRAPHY

- [1] H. v. Helmholtz. *Vorträge und Reden - Erster Band*. Friedrich Vieweg und Sohn, 1896, cit. on p. v.
- [2] H. K. Onnes. *Further experiments with Liquid Helium G. On the electrical resistance of Pure Metals etc. VI. On the Sudden Change in the Rate at which the Resistance of Mercury Disappears*. Commun. Phys. Lab. Leiden 124c (1911), cit. on p. 3.
- [3] P. Kapitza. *Viscosity of Liquid Helium below the λ -Point*. Nature 141 (1938), cit. on p. 3.
- [4] J. F. Allen and A. D. Misener. *Flow Phenomena in Liquid Helium II*. Nature 142 (1938), cit. on p. 3.
- [5] F. London. *The λ -Phenomenon of Liquid Helium and the Bose-Einstein Degeneracy*. Nature 141 (1938), cit. on p. 3.
- [6] S. N. Bose. *Plancksches Gesetz und Lichtquantenhypothese*. Zeitschrift für Physik 26 (1924), cit. on p. 3.
- [7] A. Einstein. *Quantentheorie des einatomigen idealen Gases I*. Sitzungsberichte der Preussischen Akademie der Wissenschaften 21 (1924), cit. on p. 3.
- [8] E. Fermi. *Sulla quantizzazione del gas perfetto monoatomico*. Rend. Acc. Naz. Lincei 3 (1926), cit. on p. 3.
- [9] P. A. M. Dirac and R. H. Fowler. *On the theory of quantum mechanics*. Proc. R. Soc. A 112 (1926), cit. on p. 3.
- [10] J. Bardeen, L. N. Cooper, and J. R. Schrieffer. *Microscopic Theory of Superconductivity*. Phys. Rev. 106 (1957), cit. on p. 3.
- [11] J. Bardeen, L. N. Cooper, and J. R. Schrieffer. *Theory of Superconductivity*. Phys. Rev. 108 (1957), cit. on p. 3.
- [12] D. D. Osheroff, R. C. Richardson, and D. M. Lee. *Evidence for a New Phase of Solid He³*. Phys. Rev. Lett. 28 (1972), cit. on p. 3.
- [13] D. D. Osheroff, W. J. Gully, R. C. Richardson, and D. M. Lee. *New Magnetic Phenomena in Liquid He³ below 3 mK*. Phys. Rev. Lett. 29 (1972), cit. on p. 3.
- [14] A. J. Leggett. *Interpretation of Recent Results on He³ below 3 mK: A New Liquid Phase?* Phys. Rev. Lett. 29 (1972), cit. on p. 3.
- [15] W. Zwerger, ed. *The BCS-BEC Crossover and the Unitary Fermi Gas*. Springer, Berlin Heidelberg, 2012, cit. on pp. 4, 20.

- [16] D. Bailin and A. Love. *Superfluidity and superconductivity in relativistic fermion systems*. Phys. Rep. 107 (1984), cit. on p. 4.
- [17] K.-H. Bennemann and J. B. Ketterson. *Novel Superfluids: Volume 2*. Oxford University Press, Oxford, 2015, cit. on p. 4.
- [18] B. C. Barrois. *Superconducting quark matter*. Nucl. Phys. B 129 (1977), cit. on p. 4.
- [19] R. Casalbuoni and G. Nardulli. *Inhomogeneous superconductivity in condensed matter and QCD*. Rev. Mod. Phys. 76 (2004), cit. on pp. 4, 6.
- [20] T. Schäfer and D. Teaney. *Nearly perfect fluidity: from cold atomic gases to hot quark gluon plasmas*. Rep. Prog. Phys. 72 (2009), cit. on pp. 4, 6.
- [21] E. Snider, N. Dasenbrock-Gammon, R. McBride, X. Wang, N. Meyers, K. V. Lawler, E. Zurek, A. Salamat, and R. P. Dias. *Synthesis of Yttrium Superhydride Superconductor with a Transition Temperature up to 262 K by Catalytic Hydrogenation at High Pressures*. Phys. Rev. Lett. 126 (2021), cit. on p. 4.
- [22] C. H. Townes. *Nobel Lecture: Production of Coherent Radiation by Atoms and Molecules* (1964), cit. on p. 4.
- [23] W. D. Phillips. *Nobel Lecture: Laser cooling and trapping of neutral atoms*. Rev. Mod. Phys. 70 (1998), cit. on p. 4.
- [24] S. Chu. *Nobel Lecture: The manipulation of neutral particles*. Rev. Mod. Phys. 70 (1998), cit. on p. 4.
- [25] C. N. Cohen-Tannoudji. *Nobel Lecture: Manipulating atoms with photons*. Rev. Mod. Phys. 70 (1998), cit. on p. 4.
- [26] M. H. Anderson, J. R. Ensher, M. R. Matthews, C. E. Wieman, and E. A. Cornell. *Observation of Bose-Einstein condensation in dilute atomic vapor*. Science 269 (1995), cit. on p. 5.
- [27] K. B. Davis, M. O. Mewes, M. R. Andrews, N. J. van Druten, D. S. Durfee, D. M. Kurn, and W. Ketterle. *Bose-Einstein condensation in a gas of sodium atoms*. Phys. Rev. Lett. 75 (1995), cit. on p. 5.
- [28] B. DeMarco and D. S. Jin. *Onset of Fermi Degeneracy in a Trapped Atomic Gas*. Science 285 (1999), cit. on p. 5.
- [29] A. G. Truscott, K. E. Strecker, W. I. McAlexander, G. B. Partridge, and R. G. Hulet. *Observation of Fermi Pressure in a Gas of Trapped Atoms*. Science 291 (2001), cit. on p. 5.
- [30] F. Schreck, L. Khaykovich, K. L. Corwin, G. Ferrari, T. Bourdel, J. Cubizolles, and C. Salomon. *Quasipure Bose-Einstein Condensate Immersed in a Fermi Sea*. Phys. Rev. Lett. 87 (2001), cit. on p. 5.

- [31] S. Inouye, M. R. Andrews, J. Stenger, H.-J. Miesner, D. M. Stamper-Kurn, and W. Ketterle. *Observation of Feshbach resonances in a Bose-Einstein condensate*. Nature 392 (1998), cit. on p. 5.
- [32] C. Chin, R. Grimm, P. S. Julienne, and E. Tiesinga. *Feshbach resonances in ultracold gases*. Rev. Mod. Phys. 82 (2010), cit. on pp. 5, 15, 17, 20, 23, 31, 36.
- [33] C. C. Bradley, C. A. Sackett, and R. G. Hulet. *Bose-Einstein condensation of lithium: Observation of limited condensate number*. Phys. Rev. Lett. 78 (1997), cit. on p. 5.
- [34] E. A. Donley, N. R. Clausen, S. L. Cornish, J. L. Roberts, E. A. Cornell, and C. E. Wieman. *Dynamics of Collapsing and Exploding Bose-Einstein Condensates*. Nature 412 (2001), cit. on p. 5.
- [35] J. L. Roberts, N. R. Clausen, S. L. Cornish, E. A. Donley, E. A. Cornell, and C. E. Wieman. *Controlled collapse of a Bose-Einstein condensate*. Phys. Rev. Lett. 86 (2001), cit. on p. 5.
- [36] P. O. Fedichev, M. W. Reynolds, and G. V. Shlyapnikov. *Three-Body recombination of ultracold atoms to a weakly bound s level*. Phys. Rev. Lett. 77 (1996), cit. on p. 5.
- [37] B. D. Esry, C. H. Greene, and J. P. Burke. *Recombination of Three Atoms in the Ultracold Limit*. Phys. Rev. Lett. 83 (1999), cit. on p. 5.
- [38] T. Weber, J. Herbig, M. Mark, H.-C. Nägerl, and R. Grimm. *Three-Body Recombination at Large Scattering Lengths in an Ultracold Atomic Gas*. Phys. Rev. Lett. 91 (2003), cit. on pp. 5, 37.
- [39] K. Dieckmann, C. A. Stan, S. Gupta, Z. Hadzibabic, C. H. Schunck, and W. Ketterle. *Decay of an Ultracold Fermionic Lithium Gas near a Feshbach Resonance*. Phys. Rev. Lett. 89 (2002), cit. on pp. 5, 26, 37.
- [40] S. Jochim, M. Bartenstein, A. Altmeyer, G. Hendl, C. Chin, J. Hecker Denschlag, and R. Grimm. *Pure Gas of Optically Trapped Molecules Created from Fermionic Atoms*. Phys. Rev. Lett. 91 (2003), cit. on pp. 5, 6.
- [41] J. Cubizolles, T. Bourdel, S. J. J. M. F. Kokkelmans, G. V. Shlyapnikov, and C. Salomon. *Production of Long-Lived Ultracold Li₂ Molecules from a Fermi Gas*. Phys. Rev. Lett. 91 (2003), cit. on pp. 5, 6.
- [42] D. S. Petrov, C. Salomon, and G. V. Shlyapnikov. *Weakly bound dimers of fermionic atoms*. Phys. Rev. Lett. 93 (2004), cit. on pp. 5, 20, 27.
- [43] K. M. O'Hara, S. L. Hemmer, M. E. Gehm, S. R. Granade, and J. E. Thomas. *Observation of a Strongly Interacting Degenerate Fermi Gas*. Science 298 (2002), cit. on pp. 5, 66.
- [44] C. A. Regal, C. Ticknor, J. L. Bohn, and D. S. Jin. *Creation of Ultracold Molecules from a Fermi Gas of Atoms*. Nature 424 (2003), cit. on p. 6.

- [45] K. E. Strecker, G. B. Partridge, and R. G. Hulet. *Conversion of an Atomic Fermi Gas to a Long-Lived Molecular Bose Gas*. Phys. Rev. Lett. 91 (2003), cit. on p. 6.
- [46] S. Jochim, M. Bartenstein, A. Altmeyer, G. Hendl, S. Riedl, C. Chin, J. Hecker Denschlag, and R. Grimm. *Bose-Einstein Condensation of Molecules*. Science 302 (2003), cit. on p. 6.
- [47] M. Greiner, C. A. Regal, and D. S. Jin. *Emergence of a Molecular Bose-Einstein Condensate from a Fermi Gas*. Nature 426 (2003), cit. on p. 6.
- [48] M. W. Zwierlein, C. A. Stan, C. H. Schunck, S. M. F. Raupach, S. Gupta, Z. Hadzibabic, and W. Ketterle. *Observation of Bose-Einstein Condensation of Molecules*. Phys. Rev. Lett. 91 (2003), cit. on p. 6.
- [49] C. A. Regal, M. Greiner, and D. S. Jin. *Observation of Resonance Condensation of Fermionic Atom Pairs*. Phys. Rev. Lett. 92 (2004), cit. on pp. 6, 90.
- [50] M. Bartenstein, A. Altmeyer, S. Riedl, S. Jochim, C. Chin, J. Hecker Denschlag, and R. Grimm. *Collective Excitations of a Degenerate Gas at the BEC-BCS Crossover*. Phys. Rev. Lett. 92 (2004), cit. on p. 6.
- [51] J. Kinast, S. L. Hemmer, M. E. Gehm, A. Turlapov, and J. E. Thomas. *Evidence for Superfluidity in a Resonantly Interacting Fermi Gas*. Phys. Rev. Lett. 92 (2004), cit. on p. 6.
- [52] T. Bourdel, L. Khaykovich, J. Cubizolles, J. Zhang, F. Chevy, M. Teichmann, L. Tarruell, S. J. J. M. F. Kokkelmans, and C. Salomon. *Experimental Study of the BEC-BCS Crossover Region in Lithium 6*. Phys. Rev. Lett. 93 (2004), cit. on p. 6.
- [53] M. W. Zwierlein, J. R. Abo-Shaeer, A. Schirotzek, C. H. Schunck, and W. Ketterle. *Vortices and Superfluidity in a Strongly Interacting Fermi Gas*. Nature 435 (2005), cit. on p. 6.
- [54] C. Chin, M. Bartenstein, A. Altmeyer, S. Riedl, S. Jochim, J. Hecker Denschlag, and R. Grimm. *Observation of the Pairing Gap in a Strongly Interacting Fermi Gas*. Science 305 (2004), cit. on p. 6.
- [55] T.-L. Ho. *Universal Thermodynamics of Degenerate Quantum Gases in the Unitarity Limit*. Phys. Rev. Lett. 92, 090402 (2004), cit. on p. 6.
- [56] M. Horikoshi, S. Nakajima, M. Ueda, and T. Mukaiyama. *Measurement of universal thermodynamic functions for a unitary Fermi gas*. Science 327 (2010), cit. on p. 6.
- [57] N. Navon, S. Nascimbène, F. Chevy, and C. Salomon. *The Equation of State of a Low-Temperature Fermi Gas with Tunable Interactions*. Science 328 (2010), cit. on p. 6.

- [58] M. J. H. Ku, A. T. Sommer, L. W. Cheuk, and M. W. Zwierlein. *Revealing the Superfluid Lambda Transition in the Universal Thermodynamics of a Unitary Fermi Gas*. Science 335 (2012), cit. on p. 6.
- [59] D. E. Miller, J. K. Chin, C. A. Stan, Y. Liu, W. Setiawan, C. Sanner, and W. Ketterle. *Critical Velocity for Superfluid Flow across the BEC-BCS Crossover*. Phys. Rev. Lett. 99, 070402 (2007), cit. on p. 6.
- [60] M. K. Tey, L. A. Sidorenkov, E. R. S. Guajardo, R. Grimm, M. J. H. Ku, M. W. Zwierlein, Y.-H. Hou, L. Pitaevskii, and S. Stringari. *Collective Modes in a Unitary Fermi Gas across the Superfluid Phase Transition*. Phys. Rev. Lett. 110 (2013), cit. on p. 6.
- [61] L. A. Sidorenkov, M. K. Tey, R. Grimm, Y.-H. Hou, L. Pitaevskii, and S. Stringari. *Second sound and the superfluid fraction in a Fermi gas with resonant interactions*. Nature 498 (2013), cit. on p. 6.
- [62] A. Schirotzek, C.-H. Wu, A. Sommer, and M. W. Zwierlein. *Observation of Fermi polarons in a tunable Fermi liquid of ultracold atoms*. Phys. Rev. Lett. 102 (2009), cit. on p. 6.
- [63] N. B. Jørgensen, L. Wacker, K. T. Skalmstang, M. M. Parish, J. Levinsen, R. S. Christensen, G. M. Bruun, and J. J. Arlt. *Observation of Attractive and Repulsive Polarons in a Bose-Einstein Condensate*. Phys. Rev. Lett. 117 (2016), cit. on p. 6.
- [64] P. Massignan, M. Zaccanti, and G. M. Bruun. *Polarons, dressed molecules and itinerant ferromagnetism in ultracold Fermi gases*. Rep. Prog. Phys. 77 (2014), cit. on p. 6.
- [65] M. W. Zwierlein, A. Schirotzek, C. H. Schunck, and W. Ketterle. *Fermionic Superfluidity with Imbalanced Spin Populations*. Science 311 (2006), cit. on p. 7.
- [66] G. B. Partridge, W. Li, R. I. Kamar, Y. Liao, and R. G. Hulet. *Pairing and Phase Separation in a Polarized Fermi Gas*. Science 311 (2006), cit. on pp. 7, 90.
- [67] Y. Shin, C. H. Schunck, A. Schirotzek, and W. Ketterle. *Phase diagram of a two-component Fermi gas with resonant interactions*. Nature 451 (2008), cit. on pp. 7, 90.
- [68] P. Fulde and R. A. Ferrell. *Superconductivity in a Strong Spin-Exchange Field*. Phys. Rev. 135 (1964), cit. on pp. 7, 20.
- [69] A. I. Larkin and Y. N. Ovchinnikov. *Inhomogeneous state of superconductors*. Sov. Phys. JETP 20 (1965), cit. on pp. 7, 20.
- [70] J. E. Baarsma, K. B. Gubbels, and H. T. C. Stoof. *Population and mass imbalance in atomic Fermi gases*. Phys. Rev. A 82 (2010), cit. on pp. 7, 28, 102.

- [71] M. M. Parish, F. M. Marchetti, A. Lamacraft, and B. D. Simons. *Finite-temperature phase diagram of a polarized Fermi condensate*. Nature Physics 3 (2007), cit. on p. 7.
- [72] H. Mayaffre, S. Krämer, M. Horvatić, C. Berthier, K. Miyagawa, K. Kanoda, and V. F. Mitrović. *Evidence of Andreev bound states as a hallmark of the FFLO phase in κ -(BEDT-TTF) $_2$ Cu(NCS) $_2$* . Nature Physics 10 (2014), cit. on p. 7.
- [73] R. Lortz, Y. Wang, A. Demuer, P. H. M. Böttger, B. Bergk, G. Zwicknagl, Y. Nakazawa, and J. Wosnitza. *Calorimetric Evidence for a Fulde-Ferrell-Larkin-Ovchinnikov Superconducting State in the Layered Organic Superconductor κ -(BEDT-TTF) $_2$ Cu(NCS) $_2$* . Phys. Rev. Lett. 99 (2007), cit. on p. 7.
- [74] J. Wang, Y. Che, L. Zhang, and Q. Chen. *Enhancement effect of mass imbalance on Fulde-Ferrell-Larkin-Ovchinnikov type of pairing in Fermi-Fermi mixtures of ultracold quantum gases*. Sci. Rep. 7 (2017), cit. on pp. 8, 20, 102, 111.
- [75] J. Levinsen and D. Petrov. *Atom-dimer and dimer-dimer scattering in fermionic mixtures near a narrow Feshbach resonance*. Eur. Phys. J. D 65 (2011), cit. on pp. 8, 20.
- [76] M. Taglieber, A.-C. Voigt, T. Aoki, T. W. Hänsch, and K. Dieckmann. *Quantum Degenerate Two-Species Fermi-Fermi Mixture Coexisting with a Bose-Einstein Condensate*. Phys. Rev. Lett. 100, 010401 (2008), cit. on p. 8.
- [77] T. G. Tiecke, M. R. Goosen, A. Ludewig, S. D. Gensemer, S. Kraft, S. J. J. M. F. Kokkelmans, and J. T. M. Walraven. *Broad Feshbach resonance in the ^6Li - ^{40}K mixture*. Phys. Rev. Lett. 104 (2010), cit. on pp. 8, 20.
- [78] F. M. Spiegelhalder, A. Trenkwalder, D. Naik, G. Kerner, E. Wille, G. Hendl, F. Schreck, and R. Grimm. *All-optical production of a degenerate mixture of ^6Li and ^{40}K and creation of heteronuclear molecules*. Phys. Rev. A 81 (2010), cit. on p. 8.
- [79] A. Trenkwalder, C. Kohstall, M. Zaccanti, D. Naik, A. I. Sidorov, F. Schreck, and R. Grimm. *Hydrodynamic Expansion of a Strongly Interacting Fermi-Fermi Mixture*. Phys. Rev. Lett. 106 (2011), cit. on pp. 8, 20, 26, 66.
- [80] M. Jag, M. Zaccanti, M. Cetina, R. S. Lous, F. Schreck, R. Grimm, D. S. Petrov, and J. Levinsen. *Observation of a Strong Atom-Dimer Attraction in a Mass-Imbalanced Fermi-Fermi Mixture*. Phys. Rev. Lett. 112 (2014), cit. on pp. 8, 20.
- [81] M. Jag, M. Cetina, R. S. Lous, R. Grimm, J. Levinsen, and D. S. Petrov. *Lifetime of Feshbach dimers in a Fermi-Fermi mixture of ^6Li and ^{40}K* . Phys. Rev. A 94 (2016), cit. on pp. 8, 9, 20, 36.

- [82] D. Naik, A. Trenkwalder, C. Kohstall, F. M. Spiegelhalder, M. Zaccanti, G. Hendl, F. Schreck, R. Grimm, T. Hanna, and P. Julienne. *Feshbach resonances in the ^6Li - ^{40}K Fermi-Fermi mixture: Elastic versus inelastic interactions*. Eur. Phys. J. D 65 (2011), cit. on pp. 8, 20.
- [83] B. Naylor, A. Reigue, E. Maréchal, O. Gorceix, B. Laburthe-Tolra, and L. Vernac. *Chromium dipolar Fermi sea*. Phys. Rev. A 91 (2015), cit. on p. 8.
- [84] B. J. DeSalvo, M. Yan, P. G. Mickelson, Y. N. Martinez de Escobar, and T. C. Killian. *Degenerate Fermi Gas of ^{87}Sr* . Phys. Rev. Lett. 105 (2010), cit. on p. 8.
- [85] T. Fukuhara, Y. Takasu, M. Kumakura, and Y. Takahashi. *Degenerate Fermi gases of ytterbium*. Phys. Rev. Lett. 98 (2007), cit. on p. 8.
- [86] K. Aikawa, A. Frisch, M. Mark, S. Baier, R. Grimm, and F. Ferlaino. *Reaching Fermi Degeneracy via Universal Dipolar Scattering*. Phys. Rev. Lett. 112 (2014), cit. on pp. 8, 21.
- [87] M. Lu, N. Q. Burdick, and B. L. Lev. *Quantum Degenerate Dipolar Fermi Gas*. Phys. Rev. Lett. 108 (2012), cit. on pp. 8, 21, 47, 95.
- [88] M. A. Baranov, M. Dalmonte, G. Pupillo, and P. Zoller. *Condensed Matter Theory of Dipolar Quantum Gases*. Chemical Reviews 112 (2012). PMID: 22877362, cit. on p. 8.
- [89] J. L. Bohn, M. Cavagnero, and C. Ticknor. *Quasi-universal dipolar scattering in cold and ultracold gases*. New J. Phys. 11 (2009), cit. on pp. 8, 47, 113.
- [90] M. Lu, S. H. Youn, and B. L. Lev. *Trapping Ultracold Dysprosium: A Highly Magnetic Gas for Dipolar Physics*. Phys. Rev. Lett. 104 (2010), cit. on pp. 8, 110.
- [91] K. Baumann, N. Q. Burdick, M. Lu, and B. L. Lev. *Observation of low-field Fano-Feshbach resonances in ultracold gases of dysprosium*. Phys. Rev. A 89 (2014), cit. on pp. 8, 22.
- [92] A. Frisch, M. Mark, K. Aikawa, F. Ferlaino, J. L. Bohn, C. Makrides, A. Petrov, and S. Kotochigova. *Quantum chaos in ultracold collisions of gas-phase erbium atoms*. Nature 507 (2014), cit. on p. 8.
- [93] A. J. Berglund, J. L. Hanssen, and J. J. McClelland. *Narrow-Line Magneto-Optical Cooling and Trapping of Strongly Magnetic Atoms*. Phys. Rev. Lett. 100 (2008), cit. on p. 9.
- [94] M. Lu, S. H. Youn, and B. L. Lev. *Spectroscopy of a narrow-line laser-cooling transition in atomic dysprosium*. Phys. Rev. A 83 (2011), cit. on pp. 9, 88, 110, 118.
- [95] A. Frisch, K. Aikawa, M. Mark, A. Rietzler, J. Schindler, E. Zupanič, R. Grimm, and F. Ferlaino. *Narrow-line magneto-optical trap for erbium*. Phys. Rev. A 85 (2012), cit. on pp. 9, 110.

- [96] T. Maier, H. Kadau, M. Schmitt, A. Griesmaier, and T. Pfau. *Narrow-line magneto-optical trap for dysprosium atoms*. Opt. Lett. 39 (2014), cit. on pp. 9, 97, 110, 111.
- [97] L. Tanzi, E. Lucioni, F. Famà, J. Catani, A. Fioretti, C. Gabbanini, R. N. Bisset, L. Santos, and G. Modugno. *Observation of a Dipolar Quantum Gas with Metastable Supersolid Properties*. Phys. Rev. Lett. 122 (2019), cit. on pp. 9, 110.
- [98] F. Böttcher, J.-N. Schmidt, M. Wenzel, J. Hertkorn, M. Guo, T. Langen, and T. Pfau. *Transient Supersolid Properties in an Array of Dipolar Quantum Droplets*. Phys. Rev. X 9 (2019), cit. on pp. 9, 110.
- [99] L. Chomaz et al. *Long-Lived and Transient Supersolid Behaviors in Dipolar Quantum Gases*. Phys. Rev. X 9 (2019), cit. on pp. 9, 110.
- [100] M. L. González-Martínez and P. S. Żuchowski. *Magnetically tunable Feshbach resonances in Li+Er*. Phys. Rev. A 92 (2015), cit. on pp. 9, 21.
- [101] V. Barbé, A. Ciamei, B. Pasquiou, L. Reichsöllner, F. Schreck, P. S. Żuchowski, and J. M. Hutson. *Observation of Feshbach resonances between alkali and closed-shell atoms*. Nat. Phys. 14 (2018), cit. on p. 9.
- [102] A. Green, H. Li, J. H. See Toh, X. Tang, K. C. McCormick, M. Li, E. Tiesinga, S. Kotochigova, and S. Gupta. *Feshbach Resonances in p-Wave Three-Body Recombination within Fermi-Fermi Mixtures of Open-Shell ^6Li and Closed-Shell ^{173}Yb Atoms*. Phys. Rev. X 10 (2020), cit. on p. 9.
- [103] B. Mukherjee, M. D. Frye, and J. M. Hutson. *Feshbach resonances and molecule formation in ultracold mixtures of Rb and Yb(3P) atoms*. Phys. Rev. A 105 (2022), cit. on p. 9.
- [104] E. Neri, A. Ciamei, C. Simonelli, I. Goti, M. Inguscio, A. Trenkwalder, and M. Zaccanti. *Realization of a cold mixture of fermionic chromium and lithium atoms*. Phys. Rev. A 101 (2020), cit. on p. 9.
- [105] C. Ravensbergen, V. Corre, E. Soave, M. Kreyer, E. Kirilov, and R. Grimm. *Production of a degenerate Fermi-Fermi mixture of dysprosium and potassium atoms*. Phys. Rev. A 98 (2018), cit. on pp. 11, 21, 22, 28, 31–34, 36, 47, 110, 112, 123, 153.
- [106] *Stable diffusion online*, cit. on p. 13.
- [107] W. Ketterle and M. W. Zwierlein. *Making, probing and understanding ultracold Fermi gases*. Rivista del Nuovo Cimento 31 (2008), cit. on pp. 15, 17, 47.
- [108] J. J. Sakurai and S. F. Tuan. *Modern Quantum Mechanics*. Addison-Wesley Publishing Company, Inc., 1994, cit. on p. 15.
- [109] D. S. Petrov. *Three-boson problem near a narrow Feshbach resonance*. Phys. Rev. Lett. 93 (2004), cit. on pp. 17, 36.

- [110] M. Inguscio, W. Ketterle, and C. Salomon, ed. *Ultra-cold Fermi Gases: Proceedings of the International School of Physics "Enrico Fermi", Course CLXIV, Varenna, 2006*. IOS Press, 2008, cit. on p. 20.
- [111] L. Pitaevskii and S. Stringari. *Bose-Einstein Condensation and Superfluidity*. Oxford University Press, 2016, cit. on pp. 20, 76.
- [112] G. C. Strinati, P. Pieri, G. Röpke, P. Schuck, and M. Urban. *The BCS-BEC crossover: From ultra-cold Fermi gases to nuclear systems*. Phys. Rep. 738 (2018), cit. on p. 20.
- [113] K.-H. Bennemann and J. B. Ketterson. *Novel Superfluids: Volumes 1 and 2*. Oxford University Press, Oxford, 2013, 2014, cit. on p. 20.
- [114] K. Gubbels and H. Stoof. *Imbalanced Fermi gases at unitarity*. Phys. Rep. 525 (2013), cit. on pp. 20, 41, 111.
- [115] K. B. Gubbels, J. E. Baarsma, and H. T. C. Stoof. *Lifshitz Point in the Phase Diagram of Resonantly Interacting ^6Li - ^{40}K Mixtures*. Phys. Rev. Lett. 103 (2009), cit. on pp. 20, 28.
- [116] L. Radzihovsky and D. E. Sheehy. *Imbalanced Feshbach-resonant Fermi gases*. Rep. Prog. Phys. 73 (2010), cit. on p. 20.
- [117] D. S. Petrov, C. Salomon, and G. V. Shlyapnikov. *Scattering properties of weakly bound dimers of fermionic atoms*. Phys. Rev. A 71, 012708 (2005), cit. on pp. 20, 27.
- [118] D. S. Petrov, C. Salomon, and G. V. Shlyapnikov. *Diatom molecules in ultracold Fermi gases - novel composite bosons*. J. Phys. B 38 (2005), cit. on pp. 20, 27.
- [119] E. Wille et al. *Exploring an ultracold Fermi-Fermi mixture: Interspecies Feshbach resonances and scattering properties of ^6Li and ^{40}K* . Phys. Rev. Lett. 100, 053201 (2008), cit. on p. 20.
- [120] M. Lu, N. Q. Burdick, S. H. Youn, and B. L. Lev. *Strongly Dipolar Bose-Einstein Condensate of Dysprosium*. Phys. Rev. Lett. 107 (2011), cit. on pp. 21, 95, 96, 110.
- [121] K. Aikawa, A. Frisch, M. Mark, S. Baier, A. Rietzler, R. Grimm, and F. Ferlaino. *Bose-Einstein Condensation of Erbium*. Phys. Rev. Lett. 108 (2012), cit. on pp. 21, 95.
- [122] A. Trautmann, P. Ilzhöfer, G. Durastante, C. Politi, M. Sohmen, M. J. Mark, and F. Ferlaino. *Dipolar Quantum Mixtures of Erbium and Dysprosium Atoms*. Phys. Rev. Lett. 121 (2018), cit. on pp. 21, 110.
- [123] S. Baier, D. Petter, J. H. Becher, A. Patscheider, G. Natale, L. Chomaz, M. J. Mark, and F. Ferlaino. *Realization of a Strongly Interacting Fermi Gas of Dipolar Atoms*. Phys. Rev. Lett. 121 (2018), cit. on p. 21.

- [124] C. Ravensbergen, V. Corre, E. Soave, M. Kreyer, S. Tzanova, E. Kirilov, and R. Grimm. *Accurate Determination of the Dynamical Polarizability of Dysprosium*. Phys. Rev. Lett. 120 (2018), cit. on pp. 21, 22, 110, 111, 113, 122.
- [125] A. Petrov, E. Tiesinga, and S. Kotochigova. *Anisotropy induced Feshbach resonances in a quantum dipolar gas of magnetic atoms*. Phys. Rev. Lett. 109 (2012), cit. on p. 21.
- [126] N. Q. Burdick, Y. Tang, and B. L. Lev. *Long-Lived Spin-Orbit-Coupled Degenerate Dipolar Fermi Gas*. Phys. Rev. X 6 (2016), cit. on pp. 22, 37, 95, 110.
- [127] M. Arndt, M. Ben Dahan, D. Guéry-Odelin, M. W. Reynolds, and J. Dalibard. *Observation of a Zero-Energy Resonance in Cs-Cs Collisions*. Phys. Rev. Lett. 79 (1997), cit. on pp. 22, 24.
- [128] M. E. Gehm, S. L. Hemmer, K. M. O'Hara, and J. E. Thomas. *Unitarity-limited elastic collision rate in a harmonically trapped Fermi gas*. Phys. Rev. A 68 (2003), cit. on pp. 22, 24.
- [129] M. Anderlini, D. Ciampini, D. Cossart, E. Courtade, M. Cristiani, C. Sias, O. Morsch, and E. Arimondo. *Model for collisions in ultracold-atom mixtures*. Phys. Rev. A 72 (2005), cit. on pp. 24, 45, 55, 56, 71.
- [130] C. A. Regal, M. Greiner, and D. S. Jin. *Lifetime of Molecule-Atom Mixtures near a Feshbach Resonance in K*. Phys. Rev. Lett. 92, 083201 (2004), cit. on pp. 26, 37.
- [131] T. Bourdel, J. Cubizolles, L. Khaykovich, K. M. F. Magalhães, S. J. J. M. F. Kokkelmans, G. V. Shlyapnikov, and C. Salomon. *Measurement of the Interaction Energy near a Feshbach Resonance in a ${}^6\text{Li}$ Fermi Gas*. Phys. Rev. Lett. 91 (2003), cit. on pp. 26, 37.
- [132] S. Jochim. *Bose-Einstein Condensation of Molecules*. PhD thesis. Innsbruck University, 2004, cit. on pp. 26, 37.
- [133] G. Barontini, C. Weber, F. Rabatti, J. Catani, G. Thalhammer, M. Inguscio, and F. Minardi. *Observation of heteronuclear atomic Efimov resonances*. Phys. Rev. Lett. 103 (2009), cit. on p. 27.
- [134] R. A. W. Maier, M. Eisele, E. Tiemann, and C. Zimmermann. *Efimov Resonance and Three-Body Parameter in a Lithium-Rubidium Mixture*. Phys. Rev. Lett. 115 (2015), cit. on p. 27.
- [135] L. J. Wacker, N. B. Jørgensen, D. Birkmose, N. Winter, M. Mikkelsen, J. Sherson, N. Zinner, and J. J. Arlt. *Universal Three-Body Physics in Ultracold KRb Mixtures*. Phys. Rev. Lett. 117 (2016), cit. on p. 27.
- [136] R. S. Bloom, M.-G. Hu, T. D. Cumby, and D. S. Jin. *Tests of Universal Three-Body Physics in an Ultracold Bose-Fermi Mixture*. Phys. Rev. Lett. 111 (2013), cit. on p. 27.

- [137] R. Pires, J. Ulmanis, S. Häfner, M. Repp, A. Arias, E. D. Kuhnle, and M. Weidemüller. *Observation of Efimov Resonances in a Mixture with Extreme Mass Imbalance*. Phys. Rev. Lett. 112 (2014), cit. on p. 27.
- [138] S.-K. Tung, K. Jiménez-García, J. Johansen, C. V. Parker, and C. Chin. *Geometric Scaling of Efimov States in a ${}^6\text{Li}$ – ${}^{133}\text{Cs}$ Mixture*. Phys. Rev. Lett. 113 (2014), cit. on p. 27.
- [139] J. Ulmanis, S. Häfner, R. Pires, F. Werner, D. S. Petrov, E. D. Kuhnle, and M. Weidemüller. *Universal three-body recombination and Efimov resonances in an ultracold Li-Cs mixture*. Phys. Rev. A 93 (2016), cit. on p. 27.
- [140] R. S. Lous, I. Fritsche, M. Jag, F. Lehmann, E. Kirilov, B. Huang, and R. Grimm. *Probing the Interface of a Phase-Separated State in a Repulsive Bose-Fermi Mixture*. Phys. Rev. Lett. 120 (2018), cit. on pp. 27, 69.
- [141] S. Tzanova. *Realization and characterization of two unconventional ultracold mixtures*. PhD thesis. University of Innsbruck, 2020, cit. on p. 27.
- [142] M. W. Zwierlein, A. Schirotzek, C. H. Schunck, and W. Ketterle. *Direct observation of the superfluid phase transition in ultracold Fermi gases*. Nature 442 (2006), cit. on p. 28.
- [143] A. D. Lange, K. Pilch, A. Prantner, F. Ferlaino, B. Engeser, H.-C. Nägerl, R. Grimm, and C. Chin. *Determination of atomic scattering lengths from measurements of molecular binding energies near Feshbach resonances*. Phys. Rev. A 79 (2009), cit. on p. 29.
- [144] K. Jachymski and P. S. Julienne. *Analytical model of overlapping Feshbach resonances*. Phys. Rev. A 88 (2013), cit. on pp. 29, 31.
- [145] K. M. O'Hara, S. L. Hemmer, S. R. Granade, M. E. Gehm, J. E. Thomas, V. Venturi, E. Tiesinga, and C. J. Williams. *Measurement of the zero crossing in a Feshbach resonance of fermionic ${}^6\text{Li}$* . Phys. Rev. A 66 (2002), cit. on p. 31.
- [146] S. Jochim, M. Bartenstein, G. Hendl, J. Hecker Denschlag, R. Grimm, A. Mosk, and W. Weidemüller. *Magnetic Field Control of Elastic Scattering in a Cold Gas of Fermionic Lithium Atoms*. Phys. Rev. Lett 89 (2002), cit. on p. 31.
- [147] A. Mosk, S. Kraft, M. Mudrich, K. Singer, W. Wohlleben, R. Grimm, and M. Weidemüller. *Mixture of ultracold lithium and cesium atoms in an optical dipole trap*. Appl. Phys. B 73 (2001), cit. on pp. 31, 32, 34, 56.
- [148] J. R. Taylor. *An Introduction to Error Analysis*. University Science Books, 1997, cit. on p. 32.
- [149] C. Lobo, A. Recati, S. Giorgini, and S. Stringari. *Normal State of a Polarized Fermi Gas at Unitarity*. Phys. Rev. Lett. 97 (2006), cit. on p. 41.
- [150] A. Gezerlis, S. Gandolfi, K. E. Schmidt, and J. Carlson. *Heavy-light fermion mixtures at unitarity*. Phys. Rev. Lett. 103 (2009), cit. on pp. 41, 102.

- [151] Z.-X. Ye, A. Canali, E. Soave, M. Kreyer, Y. Yudkin, C. Ravensbergen, E. Kirilov, and R. Grimm. *Observation of low-field Feshbach resonances between ^{161}Dy and ^{40}K* . Phys. Rev. A 106 (2022), cit. on pp. 45, 68, 155.
- [152] G. A. Bird. *Approach to Translational Equilibrium in a Rigid Sphere Gas*. Phys. Fluids 6 (1963), cit. on p. 45.
- [153] G. Bird. *Molecular gas dynamics*. Oxford University Press, 1976, cit. on pp. 45, 46, 48.
- [154] G. A. Bird. *The DSMC method*. CreateSpace Independent Publishing Platform, 2013, cit. on p. 45.
- [155] B. J. Alder and T. E. Wainwright. *Studies in Molecular Dynamics. I. General Method*. J. Chem. Phys. 31 (1959), cit. on pp. 45, 46, 48.
- [156] D. C. Rapaport. *The Art of Molecular Dynamics Simulation*. 2nd ed. Cambridge University Press, 2004, cit. on p. 45.
- [157] B. J. Alder, D. M. Gass, and T. E. Wainwright. *Studies in Molecular Dynamics. VIII. The Transport Coefficients for a Hard-Sphere Fluid*. J. Chem. Phys. 53 (1970), cit. on p. 45.
- [158] L. Wilets and J. S. Cohen. *Fermion molecular dynamics in atomic, molecular, and optical physics*. Contemp. Phys. 39 (1998), cit. on p. 45.
- [159] E. Oran, C. Oh, and B. Cybyk. *DIRECT SIMULATION MONTE CARLO: Recent Advances and Applications*. Annu. Rev. Fluid Mech. 30 (1998), cit. on pp. 45, 82.
- [160] V. Shariati, M. H. Ahmadian, and E. Roohi. *Direct Simulation Monte Carlo investigation of fluid characteristics and gas transport in porous microchannels*. Sci. Rep. 9 (2019), cit. on p. 45.
- [161] R. Horstmann, L. Hecht, S. Kloth, and M. Vogel. *Structural and Dynamical Properties of Liquids in Confinements: A Review of Molecular Dynamics Simulation Studies*. Langmuir 38 (2022), cit. on p. 45.
- [162] Hospital, Adam, J. R. Goñi, M. Orozco, and J. L. Gelpí. *Molecular dynamics simulations: advances and applications*. Adv. Appl. Bioinform. Chem. 8 (2015), cit. on p. 45.
- [163] H. Wu, E. Arimondo, and C. J. Foot. *Dynamics of evaporative cooling for Bose-Einstein condensation*. Phys. Rev. A 56 (1997), cit. on pp. 45, 55, 72, 81.
- [164] A. C. J. Wade, D. Baillie, and P. B. Blakie. *Direct simulation Monte Carlo method for cold-atom dynamics: Classical Boltzmann equation in the quantum collision regime*. Phys. Rev. A 84 (2011), cit. on pp. 45, 48.
- [165] T. Lepers, D. Davesne, S. Chiacchiera, and M. Urban. *Numerical solution of the Boltzmann equation for the collective modes of trapped Fermi gases*. Phys. Rev. A 82 (2010), cit. on pp. 45, 76, 77, 81, 82.

- [166] V. V. Aristov. *Direct methods for solving the Boltzmann equation and study of nonequilibrium flows*. Fluid mechanics and its applications. New York: Springer, 2001, cit. on p. 46.
- [167] J. Von Neumann. *Various techniques used in connection with random digits*. Appl. Math Ser 12 (1951), cit. on p. 46.
- [168] A. Frisch. *Dipolar Quantum Gases of Erbium*. PhD thesis. University of Innsbruck, 2014, cit. on p. 47.
- [169] E. Meiburg. *Comparison of the molecular dynamics method and the direct simulation Monte Carlo technique for flows around simple geometries*. Phys. Fluids 29 (1986), cit. on p. 48.
- [170] W. Wagner. *A convergence proof for Bird's direct simulation Monte Carlo method for the Boltzmann equation*. J. Stat. Phys. 66 (1992), cit. on p. 48.
- [171] Z.-X. Sun, Z. Tang, Y.-L. He, and W.-Q. Tao. *Proper cell dimension and number of particles per cell for DSMC*. Comput. Fluids 50 (2011), cit. on p. 48.
- [172] O. Goulko, F. Chevy, and C. Lobo. *Boltzmann equation simulation for a trapped Fermi gas of atoms*. New J. Phys. 14 (2012), cit. on p. 48.
- [173] S. Chapman and T. G. Cowling. *The Mathematical Theory of Non-uniform Gases - An Account of the Kinetic Theory of Viscosity, Thermal Conduction and Diffusion in Gases*. Cambridge: Cambridge University Press, 1990, cit. on p. 54.
- [174] P.-A. Pantel, D. Davesne, and M. Urban. *Numerical solution of the Boltzmann equation for trapped Fermi gases with in-medium effects*. Phys. Rev. A 91 (2015), cit. on pp. 55, 76, 81, 153.
- [175] M. Anderlini and D. Guéry-Odelin. *Thermalization in mixtures of ultracold gases*. Phys. Rev. A 73 (2006), cit. on pp. 56, 71.
- [176] C. Ravensbergen, E. Soave, V. Corre, M. Kreyer, B. Huang, E. Kirilov, and R. Grimm. *Resonantly Interacting Fermi-Fermi Mixture of ^{161}Dy and ^{40}K* . Phys. Rev. Lett. 124 (2020), cit. on pp. 60, 61, 110, 121, 123.
- [177] I. Shvarchuck, C. Buggle, D. S. Petrov, M. Kemmann, W. von Klitzing, G. V. Shlyapnikov, and J. T. M. Walraven. *Hydrodynamic behavior in expanding thermal clouds of ^{87}Rb* . Phys. Rev. A 68 (2003), cit. on p. 66.
- [178] Y. Kagan, E. L. Surkov, and G. V. Shlyapnikov. *Evolution of a Bose gas in anisotropic time-dependent traps*. Phys. Rev. A 55 (1997), cit. on p. 66.
- [179] P. Pedri, D. Guéry-Odelin, and S. Stringari. *Dynamics of a classical gas including dissipative and mean-field effects*. Phys. Rev. A 68 (2003), cit. on p. 66.
- [180] S. Gupta, Z. Hadzibabic, M. W. Zwierlein, C. A. Stan, K. Dieckmann, C. H. Schunck, E. G. M. van Kempen, B. J. Verhaar, and W. Ketterle. *Radio-Frequency Spectroscopy of Ultracold Fermions*. Science 300 (2003), cit. on p. 69.

- [181] M. Bartenstein et al. *Precise determination of ${}^6\text{Li}$ cold collision parameters by radio-frequency spectroscopy on weakly bound molecules*. Phys. Rev. Lett. 94 (2005), cit. on p. 69.
- [182] C.-H. Wu, I. Santiago, J. W. Park, P. Ahmadi, and M. W. Zwierlein. *Strongly interacting isotopic Bose-Fermi mixture immersed in a Fermi sea*. Phys. Rev. A 84 (2011), cit. on p. 69.
- [183] I. Fritsche, C. Baroni, E. Dobler, E. Kirilov, B. Huang, R. Grimm, G. M. Bruun, and P. Massignan. *Stability and breakdown of Fermi polarons in a strongly interacting Fermi-Bose mixture*. Phys. Rev. A 103 (2021), cit. on p. 69.
- [184] M. Mudrich. *Interactions in an optically trapped mixture of ultracold lithium and cesium atoms: Thermalization, spin-exchange collisions and photoassociation*. PhD thesis. University of Heidelberg, 2003, cit. on p. 71.
- [185] W. C. Swope, H. C. Andersen, P. H. Berens, and K. R. Wilson. *A computer simulation method for the calculation of equilibrium constants for the formation of physical clusters of molecules: Application to small water clusters*. J. Chem. Phys. 76 (1982), cit. on p. 72.
- [186] J. Stenger, S. Inouye, D. M. Stamper-Kurn, H.-J. Miesner, A. P. Chikkatur, and W. Ketterle. *Spin domains in ground-state Bose-Einstein condensates*. Nature 396 (1998), cit. on p. 76.
- [187] S. B. Papp, J. M. Pino, and C. E. Wieman. *Tunable Miscibility in a Dual-Species Bose-Einstein Condensate*. Phys. Rev. Lett. 101 (2008), cit. on p. 76.
- [188] G. Orso, L. P. Pitaevskii, and S. Stringari. *Equilibrium and dynamics of a trapped superfluid Fermi gas with unequal masses*. Phys. Rev. A 77 (2008), cit. on p. 77.
- [189] D. Guéry-Odelin, F. Zambelli, J. Dalibard, and S. Stringari. *Collective oscillations of a classical gas confined in harmonic traps*. Phys. Rev. A 60 (1999), cit. on p. 77.
- [190] F. Toschi, P. Capuzzi, S. Succi, P. Vignolo, and M. P. Tosi. *Transition to hydrodynamics in colliding fermion clouds*. J. Phys. B: At. Mol. Opt. Phys. 37 (2004), cit. on p. 77.
- [191] Y. Asano, S. Watabe, and T. Nikuni. *Dipole oscillation of a trapped Bose-Fermi-mixture gas in collisionless and hydrodynamic regimes*. Phys. Rev. A 101 (2020), cit. on pp. 77, 153.
- [192] L. Vichi and S. Stringari. *Collective oscillations of an interacting trapped Fermi gas*. Phys. Rev. A 60 (1999), cit. on p. 77.
- [193] S. D. Gensemer and D. S. Jin. *Transition from Collisionless to Hydrodynamic Behavior in an Ultracold Fermi Gas*. Phys. Rev. Lett. 87 (2001), cit. on p. 77.

- [194] G. Ferrari, M. Inguscio, W. Jastrzebski, G. Modugno, G. Roati, and A. Simoni. *Collisional Properties of Ultracold K-Rb Mixtures*. Phys. Rev. Lett. 89 (2002), cit. on p. 77.
- [195] L. W. Nordheim. *On the kinetic method in the new statistics and application in the electron theory of conductivity*. Proc. R. Soc. Lond. A 119 (1928), cit. on p. 81.
- [196] E. A. Uehling and G. E. Uhlenbeck. *Transport Phenomena in Einstein-Bose and Fermi-Dirac Gases. I*. Phys. Rev. 43 (1933), cit. on p. 81.
- [197] G. F. Bertsch, H. Kruse, and S. D. Gupta. *Boltzmann equation for heavy ion collisions*. Phys. Rev. C 29 (1984), cit. on p. 81.
- [198] G. Bertsch and S. Das Gupta. *A guide to microscopic models for intermediate energy heavy ion collisions*. Phys. Rep. 160 (1988), cit. on p. 81.
- [199] E. Cerboneschi, C. Menchini, and E. Arimondo. *Monte Carlo simulations of Bose-Einstein condensation of trapped atoms*. Phys. Rev. A 62 (2000), cit. on p. 81.
- [200] A. L. Garcia and W. Wagner. *Direct simulation Monte Carlo method for the Uehling-Uhlenbeck-Boltzmann equation*. Phys. Rev. E 68 (2003), cit. on p. 81.
- [201] S. Riedl, E. R. Sánchez Guajardo, C. Kohstall, A. Altmeyer, M. J. Wright, J. Hecker Denschlag, R. Grimm, G. M. Bruun, and H. Smith. *Collective oscillations of a Fermi gas in the unitarity limit: Temperature effects and the role of pair correlations*. Phys. Rev. A 78, 053609 (2008), cit. on p. 81.
- [202] R. Grimm, M. Weidemüller, and Y. B. Ovchinnikov. *Optical dipole traps for neutral atoms*. Adv. At. Mol. Opt. Phys. 42 (2000), cit. on pp. 85, 94, 96, 111, 121.
- [203] T. Walker and P. Feng. *Measurements of Collisions Between Laser-Cooled Atoms*. Adv. At. Mol. Opt. Phys. 34 (1994), cit. on p. 85.
- [204] D. W. Sesko, T. G. Walker, and C. E. Wieman. *Behavior of neutral atoms in a spontaneous force trap*. J. Opt. Soc. Am. B 8 (1991), cit. on p. 85.
- [205] S. Stellmer, B. Pasquiou, R. Grimm, and F. Schreck. *Laser Cooling to Quantum Degeneracy*. Phys. Rev. Lett. 110, 263003 (2013), cit. on p. 85.
- [206] D. E. Pritchard. *Cooling Neutral Atoms in a Magnetic Trap for Precision Spectroscopy*. Phys. Rev. Lett. 51 (1983), cit. on p. 85.
- [207] I. H. Deutsch and P. S. Jessen. *Quantum control and measurement of atomic spins in polarization spectroscopy*. Opt. Commun. 283 (2010), cit. on pp. 86, 88, 95, 116.
- [208] F. Le Kien, P. Schneeweiss, and A. Rauschenbeutel. *Dynamical polarizability of atoms in arbitrary light fields: general theory and application to cesium*. Eur. Phys. J. D 67 (2013), cit. on pp. 86, 88, 116, 118.

- [209] T. Chalopin, C. Bouazza, A. Evrard, V. Makhalov, D. Dreon, J. Dalibard, L. A. Sidorenkov, and S. Nascimbene. *Quantum-enhanced sensing using non-classical spin states of a highly magnetic atom*. Nat. Commun. 9 (2018), cit. on pp. 88, 110.
- [210] M. S. Safronova, U. I. Safronova, and C. W. Clark. *Magic wavelengths for optical cooling and trapping of potassium*. Phys. Rev. A 87 (2013), cit. on pp. 88, 97, 103, 115, 118.
- [211] M. Wickliffe, J. Lawler, and G. Nave. *Atomic transition probabilities for Dy I and Dy II*. J. Quant. Spectrosc. Radiat. Transf. 66 (2000), cit. on pp. 88, 119.
- [212] J. Wang, H. Guo, and Q. Chen. *Exotic phase separation and phase diagrams of a Fermi-Fermi mixture in a trap at finite temperature*. Phys. Rev. A 87 (2013), cit. on p. 90.
- [213] H. Caldas and Q. Chen. *The Gor'kov and Melik-Barkhudarov Correction to the Mean-Field Critical Field Transition to Fulde-Ferrell-Larkin-Ovchinnikov States*. Ann. Phys. 532 (2020), cit. on p. 90.
- [214] K. Yang. *Realization and Detection of Fulde-Ferrell-Larkin-Ovchinnikov Superfluid Phases in Trapped Atomic Fermion Systems*. Phys. Rev. Lett. 95 (2005), cit. on p. 90.
- [215] M. Greiner, C. A. Regal, J. T. Stewart, and D. S. Jin. *Probing Pair-Correlated Fermionic Atoms through Correlations in Atom Shot Noise*. Phys. Rev. Lett. 94 (2005), cit. on p. 90.
- [216] M. Pini, P. Pieri, and G. C. Strinati. *Strong Fulde-Ferrell Larkin-Ovchinnikov pairing fluctuations in polarized Fermi systems*. Phys. Rev. Res. 3 (2021), cit. on p. 90.
- [217] N. Navon, R. P. Smith, and Z. Hadzibabic. *Quantum gases in optical boxes*. Nat. Phys. 17 (2021), cit. on pp. 90, 91.
- [218] G. Gauthier, T. A. Bell, A. B. Stilgoe, M. Baker, H. Rubinsztein-Dunlop, and T. W. Neely. *Chapter One - Dynamic high-resolution optical trapping of ultracold atoms*. Ed. by L. F. Dimauro, H. Perrin, and S. F. Yelin. Adv. At. Mol. Opt. Phys. Academic Press, 2021, cit. on pp. 91, 128–130.
- [219] L. Amico et al. *Roadmap on Atomtronics: State of the art and perspective*. AVS Quantum Science 3 (2021), cit. on p. 91.
- [220] F. Nogrette, H. Labuhn, S. Ravets, D. Barredo, L. Béguin, A. Vernier, T. Lahaye, and A. Browaeys. *Single-Atom Trapping in Holographic 2D Arrays of Microtraps with Arbitrary Geometries*. Phys. Rev. X 4 (2014), cit. on p. 91.
- [221] A. Mazurenko, C. S. Chiu, G. Ji, M. F. Parsons, M. Kanász-Nagy, R. Schmidt, F. Grusdt, E. Demler, D. Greif, and M. Greiner. *A cold-atom Fermi-Hubbard antiferromagnet*. Nature 545 (2017), cit. on p. 91.

- [222] M. Lebrat, P. Grišins, D. Husmann, S. Häusler, L. Corman, T. Giamarchi, J.-P. Brantut, and T. Esslinger. *Band and Correlated Insulators of Cold Fermions in a Mesoscopic Lattice*. Phys. Rev. X 8 (2018), cit. on p. 91.
- [223] K. Shibata, H. Ikeda, R. Suzuki, and T. Hirano. *Compensation of gravity on cold atoms by a linear optical potential*. Phys. Rev. Research 2 (2020), cit. on pp. 91, 123.
- [224] E. Soave, V. Corre, C. Ravensbergen, J. Han, M. Kreyer, E. Kirilov, and R. Grimm. *Low-Field Feshbach Resonances and Three-Body Losses in a Fermionic Quantum Gas of ^{161}Dy* . Ukr. J. Phys. 67 (2022), cit. on pp. 92, 155.
- [225] M. Pini, P. Pieri, R. Grimm, and G. C. Strinati. *Beyond-mean-field description of a trapped unitary Fermi gas with mass and population imbalance*. Phys. Rev. A 103 (2021), cit. on pp. 92, 111, 121, 123, 154, 155.
- [226] K. D. Bonin and V. V. Kresin. *Electric-dipole polarizabilities of atoms, molecules, and clusters*. World Scientific, 1997, cit. on p. 94.
- [227] J. Mitroy, M. S. Safronova, and C. W. Clark. *Theory and applications of atomic and ionic polarizabilities*. J. Phys. B: At. Mol. Opt. Phys. 43 (2010), cit. on p. 94.
- [228] H. H. Stroke. *Advances in atomic, molecular, and optical physics*. Gulf Professional Publishing, 2005, cit. on p. 94.
- [229] L. J. LeBlanc and J. H. Thywissen. *Species-specific optical lattices*. Phys. Rev. A 75 (2007), cit. on pp. 94, 123.
- [230] A. D. Ludlow, M. M. Boyd, J. Ye, E. Peik, and P. O. Schmidt. *Optical atomic clocks*. Rev. Mod. Phys. 87 (2015), cit. on p. 94.
- [231] V. Galitski and I. B. Spielman. *Spin-orbit coupling in quantum gases*. Nature 494 (2013), cit. on p. 95.
- [232] D. Sukachev, A. Sokolov, K. Chebakov, A. Akimov, S. Kanorsky, N. Kolachevsky, and V. Sorokin. *Magneto-optical trap for thulium atoms*. Phys. Rev. A 82 (2010), cit. on p. 95.
- [233] K. Aikawa, S. Baier, A. Frisch, M. Mark, C. Ravensbergen, and F. Ferlaino. *Observation of Fermi surface deformation in a dipolar quantum gas*. Science 345 (2014), cit. on p. 95.
- [234] J. Miao, J. Hostetter, G. Stratis, and M. Saffman. *Magneto-optical trapping of holmium atoms*. Phys. Rev. A 89 (2014), cit. on p. 95.
- [235] B. Hemmerling, G. K. Drayna, E. Chae, A. Ravi, and J. M. Doyle. *Buffer gas loaded magneto-optical traps for Yb, Tm, Er and Ho*. New J. Phys. 16 (2014), cit. on p. 95.
- [236] H. Kadau, M. Schmitt, M. Wenzel, C. Wink, T. Maier, I. Ferrier-Barbut, and T. Pfau. *Observing the Rosensweig instability of a quantum ferrofluid*. Nature 530 (2016), cit. on pp. 95, 110.

- [237] D. Dreon, L. Sidorenkov, C. Bouazza, W. Maineult, J. Dalibard, and S. Nascimbène. *Optical cooling and trapping of highly magnetic atoms: the benefits of a spontaneous spin polarization*. J. Phys. B 50 (2017), cit. on pp. 95, 97, 111.
- [238] X. Cui, B. Lian, T.-L. Ho, B. L. Lev, and H. Zhai. *Synthetic gauge field with highly magnetic lanthanide atoms*. Phys. Rev. A 88 (2013), cit. on p. 95.
- [239] V. A. Dzuba, V. V. Flambaum, and B. L. Lev. *Dynamic polarizabilities and magic wavelengths for dysprosium*. Phys. Rev. A 83 (2011), cit. on pp. 95, 97, 98, 102, 103, 110.
- [240] M. Lepers, J.-F. Wyart, and O. Dulieu. *Anisotropic optical trapping of ultracold erbium atoms*. Phys. Rev. A 89 (2014), cit. on pp. 95, 110.
- [241] D. Sukachev, S. Fedorov, I. Tolstikhina, D. Tregubov, E. Kalganova, G. Vishnyakova, A. Golovizin, N. Kolachevsky, K. Khabarova, and V. Sorokin. *Inner-shell magnetic dipole transition in Tm atoms: A candidate for optical lattice clocks*. Phys. Rev. A 94 (2016), cit. on pp. 95, 96, 111.
- [242] H. Li, J.-F. Wyart, O. Dulieu, S. Nascimbène, and M. Lepers. *Optical trapping of ultracold dysprosium atoms: transition probabilities, dynamic dipole polarizabilities and van der Waals C_6 coefficients*. J. Phys. B: At. Mol. Opt. Phys. 50 (2017), cit. on pp. 95, 97, 98, 101–103, 110.
- [243] H. Li, J.-F. Wyart, O. Dulieu, and M. Lepers. *Anisotropic optical trapping as a manifestation of the complex electronic structure of ultracold lanthanide atoms: The example of holmium*. Phys. Rev. A 95 (2017), cit. on pp. 95, 110, 118.
- [244] A. A. Golovizin, E. Kalganova, D. Sukachev, G. Vishnyakova, D. Tregubov, K. Khabarova, V. Sorokin, and N. Kolachevsky. *Methods for determining the polarisability of the fine structure levels in the ground state of the thulium atom*. Quantum Electron. 47 (2017), cit. on pp. 95, 96, 111.
- [245] T. Maier. *Interactions in a quantum gas of dysprosium atoms*. PhD thesis. University of Stuttgart, 2015, cit. on pp. 95, 96, 111.
- [246] M. Schmitt. *A self-bound dilute quantum liquid of dysprosium atoms*. PhD thesis. University of Stuttgart, 2017, cit. on pp. 95, 111.
- [247] J. H. Becher, S. Baier, K. Aikawa, M. Lepers, J.-F. Wyart, O. Dulieu, and F. Ferlaino. *Anisotropic polarizability of erbium atoms*. Phys. Rev. A 97 (2018), cit. on pp. 95, 96, 102, 111.
- [248] A. Khramov, A. H., W. Dowd, R. J. Roy, C. Makrides, A. Petrov, S. Kotochigova, and S. Gupta. *Ultracold Heteronuclear Mixture of Ground and Excited State Atoms*. Phys. Rev. Lett. 112 (2014), cit. on p. 96.
- [249] B. Neyenhuis, B. Yan, S. A. Moses, J. P. Covey, A. Chotia, A. Petrov, S. Kotochigova, J. Ye, and D. S. Jin. *Anisotropic Polarizability of Ultracold Polar $^{40}\text{K}^{87}\text{Rb}$ Molecules*. Phys. Rev. Lett. 109 (2012), cit. on pp. 96, 111.

- [250] J. G. Danzl, M. J. Mark, E. Haller, M. Gustavsson, R. Hart, J. Aldegunde, J. M. Hutson, and H.-C. Nägerl. *An ultracold high-density sample of rovibronic ground-state molecules in an optical lattice*. Nat. Phys. 6 (2010), cit. on pp. 96, 111.
- [251] M. S. Safronova. private communication. 2017, cit. on p. 97.
- [252] D. Fernandes, F. Sievers, N. Kretzschmar, S. Wu, C. Salomon, and F. Chevy. *Sub-Doppler laser cooling of fermionic ^{40}K atoms in three-dimensional gray optical molasses*. Europhys. Lett. 100 (2012), cit. on p. 97.
- [253] F. Dalfovo, S. Giorgini, L. P. Pitaevskii, and S. Stringari. *Theory of Bose-Einstein condensation in trapped gases*. Rev. Mod. Phys. 71 (1999), cit. on p. 98.
- [254] V. Flambaum and M. Dzuba. private communication. 2017, cit. on p. 102.
- [255] M. Lepers and O. Dulieu. private communication. 2017, cit. on p. 102.
- [256] L. D. Carr, D. DeMille, R. V. Krems, and J. Ye. *Cold and ultracold molecules: Science, technology and applications*. New J. Phys. 11 (2009), cit. on p. 102.
- [257] G. Quéméner and P. S. Julienne. *Ultracold Molecules under Control!* Chem. Rev. (2012), cit. on p. 102.
- [258] E. B. Norrgard, D. J. McCarron, M. H. Steinecker, M. R. Tarbutt, and D. DeMille. *Submillikelvin Dipolar Molecules in a Radio-Frequency Magneto-Optical Trap*. Phys. Rev. Lett. 116 (2016), cit. on p. 102.
- [259] E. Chae, L. Anderegg, B. L. Augenbraun, A. Ravi, B. Hemmerling, N. R. Hutzler, A. L. Collopy, J. Ye, W. Ketterle, and J. M. Doyle. *One-dimensional magneto-optical compression of a cold CaF molecular beam*. New J. Phys. 19 (2017), cit. on p. 102.
- [260] P. Soldan, P. S. Zuchowski, and J. M. Hutson. *Prospects for sympathetic cooling of polar molecules: NH with alkali-metal and alkaline-earth atoms - a new hope*. Faraday Discuss. 142 (2009), cit. on p. 102.
- [261] J. Lim, M. D. Frye, J. M. Hutson, and M. R. Tarbutt. *Modeling sympathetic cooling of molecules by ultracold atoms*. Phys. Rev. A 92 (2015), cit. on p. 102.
- [262] M. L. González-Martínez and J. M. Hutson. *Ultracold Hydrogen Atoms: A Versatile Coolant to Produce Ultracold Molecules*. Phys. Rev. Lett. 111 (2013), cit. on p. 102.
- [263] W. V. Liu and F. Wilczek. *Interior Gap Superfluidity*. Phys. Rev. Lett. 90 (2003), cit. on p. 102.
- [264] M. Iskin and C. A. R. Sá de Melo. *Two-Species Fermion Mixtures with Population Imbalance*. Phys. Rev. Lett. 97, 100404 (2006), cit. on p. 102.

- [265] M. M. Parish, F. M. Marchetti, A. Lamacraft, and B. D. Simons. *Polarized Fermi Condensates with Unequal Masses: Tuning the Tricritical Point*. Phys. Rev. Lett. 98 (2007), cit. on p. 102.
- [266] M. A. Baranov, C. Lobo, and G. V. Shlyapnikov. *Superfluid pairing between fermions with unequal masses*. Phys. Rev. A 78 (2008), cit. on p. 102.
- [267] J. Braun, J. E. Drut, and D. Roscher. *Zero-Temperature Equation of State of Mass-Imbalanced Resonant Fermi Gases*. Phys. Rev. Lett. 114 (2015), cit. on p. 102.
- [268] G. Durastante, C. Politi, M. Sohmen, P. Ilzhöfer, M. J. Mark, M. A. Norcia, and F. Ferlaino. *Feshbach resonances in an erbium-dysprosium dipolar mixture*. Phys. Rev. A 102 (2020), cit. on p. 110.
- [269] M. Schmitt, E. A. L. Henn, J. Billy, H. Kadau, T. Maier, A. Griesmaier, and T. Pfau. *Spectroscopy of a narrow-line optical pumping transition in atomic dysprosium*. Opt. Lett. 38 (2013), cit. on p. 110.
- [270] J. Hostetter, J. D. Pritchard, J. E. Lawler, and M. Saffman. *Measurement of holmium Rydberg series through magneto-optical trap depletion spectroscopy*. Phys. Rev. A 91 (2015), cit. on p. 110.
- [271] A. Golovizin, E. Fedorova, D. Tregubov, D. Sukachev, K. Khabarova, V. Sorokin, and N. Kolachevsky. *Inner-shell clock transition in atomic thulium with a small blackbody radiation shift*. Nat. Commun. 10 (2019), cit. on p. 110.
- [272] A. Evrard, V. Makhalov, T. Chalopin, L. A. Sidorenkov, J. Dalibard, R. Lopes, and S. Nascimbene. *Enhanced Magnetic Sensitivity with Non-Gaussian Quantum Fluctuations*. Phys. Rev. Lett. 122 (2019), cit. on p. 110.
- [273] V. Makhalov, T. Satoor, A. Evrard, T. Chalopin, R. Lopes, and S. Nascimbene. *Probing Quantum Criticality and Symmetry Breaking at the Microscopic Level*. Phys. Rev. Lett. 123 (2019), cit. on p. 110.
- [274] T. Chalopin et al. *Anisotropic light shift and magic polarization of the intercombination line of dysprosium atoms in a far-detuned dipole trap*. Phys. Rev. A 98 (2018), cit. on p. 111.
- [275] J. Hecker Denschlag, J. E. Simsarian, H. Häffner, C. McKenzie, A. Browaeys, D. Cho, K. Helmerson, S. L. Rolston, and W. D. Phillips. *A Bose-Einstein condensate in an optical lattice*. J. Phys. B 35 (2002), cit. on pp. 111, 114.
- [276] J. Heinze, S. Götze, J. S. Krauser, B. Hundt, N. Fläschner, D.-S. Lühmann, C. Becker, and K. Sengstock. *Multiband Spectroscopy of Ultracold Fermions: Observation of Reduced Tunneling in Attractive Bose-Fermi Mixtures*. Phys. Rev. Lett. 107 (2011), cit. on pp. 111, 114.

- [277] A. Kastberg, W. D. Phillips, S. L. Rolston, R. J. C. Spreeuw, and P. S. Jessen. *Adiabatic Cooling of Cesium to 700 nK in an Optical Lattice*. Phys. Rev. Lett. 74 (1995), cit. on p. 113.
- [278] M. Greiner, I. Bloch, O. Mandel, T. W. Hänsch, and T. Esslinger. *Exploring Phase Coherence in a 2D Lattice of Bose-Einstein Condensates*. Phys. Rev. Lett. 87 (2001), cit. on p. 113.
- [279] E. R. Eliel, W. Hogervorst, G. J. Zaal, K. A. H. van Leeuwen, and J. Blok. *A study of the spectrum of natural dysprosium with the laser-atomic-beam technique. II. Hyperfine structure*. J. Phys. B: Atom. Mol. Phys. 13 (1980), cit. on p. 118.
- [280] D. Dreon. *Designing and building an ultracold Dysprosium experiment: a new framework for light-spin interaction*. PhD thesis. Paris Sciences Lettres Research University, 2017, cit. on p. 118.
- [281] M. Gustavsson, H. Lundberg, L. Nilsson, and S. Svanberg. *Lifetime measurements for excited states of rare-earth atoms using pulse modulation of a cw dye-laser beam*. J. Opt. Soc. Am. 69 (1979), cit. on p. 119.
- [282] J. J. Curry, E. A. D. Hartog, and J. E. Lawler. *Radiative lifetimes of Dy I and Dy II*. J. Opt. Soc. Am. B 14 (1997), cit. on p. 119.
- [283] Y. B. Ovchinnikov, I. Manek, and R. Grimm. *Surface Trap for Cs atoms based on Evanescent-Wave Cooling*. Phys. Rev. Lett. 79 (1997), cit. on p. 123.
- [284] A. L. Gaunt, T. F. Schmidutz, I. Gotlibovych, R. P. Smith, and Z. Hadzibabic. *Bose-Einstein Condensation of Atoms in a Uniform Potential*. Phys. Rev. Lett. 110 (2013), cit. on p. 123.
- [285] B. Mukherjee, Z. Yan, P. B. Patel, Z. Hadzibabic, T. Yefsah, J. Struck, and M. W. Zwierlein. *Homogeneous Atomic Fermi Gases*. Phys. Rev. Lett. 118 (2017), cit. on pp. 123, 154.
- [286] B. Hundt. *Momentum-Resolved Optical Lattice Modulation Spectroscopy on Bose-Fermi Mixtures*. Diploma thesis. University of Hamburg, 2011, cit. on p. 123.
- [287] J. Liang, R. N. Kohn, M. F. Becker, and D. J. Heinzen. *1.5% Root-Mean-Square Flat-Intensity Laser Beam Formed Using a Binary-Amplitude Spatial Light Modulator*. Appl. Opt. 48 (2009), cit. on p. 130.
- [288] J. Liang, M. F. Becker, R. N. Kohn, and D. J. Heinzen. *Homogeneous one-dimensional optical lattice generation using a digital micromirror device-based high-precision beam shaper*. J. Micro/ Nanolithogr. MEMS MOEMS 11 (2012), cit. on pp. 130, 144, 147.
- [289] Y.-X. Ren, R.-D. Lu, and L. Gong. *Tailoring light with a digital micromirror device*. Ann. Phys. 527 (2015), cit. on p. 130.

- [290] G. Gauthier, I. Lenton, N. M. Parry, M. Baker, M. J. Davis, H. Rubinsztein-Dunlop, and T. W. Neely. *Direct imaging of a digital-micromirror device for configurable microscopic optical potentials*. *Optica* 3 (2016), cit. on p. 130.
- [291] K. Hueck, A. Mazurenko, N. Luick, T. Lompe, and H. Moritz. *Note: Suppression of kHz-frequency switching noise in digital micro-mirror devices*. *Rev. Sci. Instrum.* 88 (2017), cit. on pp. 130, 135.
- [292] R. Floyd and L. Steinberg. *An adaptive algorithm for spatial grey scale*. In: *Proceedings of the Society for Information Display*. Ed. by M. R. Douglass and L. J. Hornbeck. Vol. 17. International Society for Optics and Photonics. SPIE, 1976, cit. on p. 133.
- [293] C. Dorrer and J. D. Zuegel. *Design and analysis of binary beam shapers using error diffusion*. *J. Opt. Soc. Am. B* 24 (2007), cit. on p. 133.
- [294] M. F. Becker, J. Liang, R. N. K. Jr., and D. J. Heinzen. *High-precision laser beam shaping using binary-amplitude DLP spatial light modulators*. In: *Emerging Digital Micromirror Device Based Systems and Applications II*. Ed. by M. R. Douglass and L. J. Hornbeck. Vol. 7596. International Society for Optics and Photonics. SPIE, 2010, cit. on pp. 134, 144, 145, 147.
- [295] Peter Buchebner. online, cit. on p. 134.
- [296] J.-L. Ville. *Quantum gases in box potentials : sound and light in bosonic Flatland*. PhD thesis. Université Paris sciences et lettres, 2018, cit. on p. 135.
- [297] European Machine Vision Association (EMVA). *EMVA Standard 1288: Standard for Characterization of Image Sensors and Cameras, Release 4.0*. 2021, cit. on p. 139.
- [298] FLIR Integrated Imaging Solutions Inc. *EMVA 1288 IMAGING PERFORMANCE FLIR BLACKFLY S BFS-U3-88S6*. 2018, cit. on p. 140.
- [299] Labsphere, Inc. *Technical Guide: Integrating Sphere Theory and Applications*. 2017, cit. on p. 140.
- [300] G. A. Phelps. *A dipolar quantum gas microscope*. PhD thesis. Harvard University, 2019, cit. on p. 143.
- [301] J. W. Goodman. *Speckle Phenomena in Optics: Theory and Applications, Second Edition*. SPIE, 2020, cit. on p. 143.
- [302] F. Etzold. *Laser Beam Shaping with a Digital Micromirror Device*. Diploma thesis. Johannes Gutenberg-Universität, Mainz, 2010, cit. on p. 144.
- [303] G. Del Pace. *Tailored optical potentials for experiments with atomic superfluids*. PhD thesis. Università degli studi di Firenze, 2018, cit. on p. 145.
- [304] J. Liang, S.-Y. Wu, R. N. Kohn, M. F. Becker, and D. J. Heinzen. *Grayscale laser image formation using a programmable binary mask*. *Opt. Eng.* 51 (2012), cit. on p. 146.

- [305] M. Narushima, S. Watabe, and T. Nikuni. *Density and spin modes in imbalanced normal Fermi gases from collisionless to hydrodynamic regime*. J. Phys. B: At. Mol. Opt. Phys. 51 (2018), cit. on p. 153.
- [306] I. Manek, Y. Ovchinnikov, and R. Grimm. *Generation of a hollow laser beam for atom trapping using an axicon*. Opt. Commun. 147 (1998), cit. on p. 154.
- [307] C. Ravensbergen. *Creation of a Fermi-Fermi mixture of dysprosium and potassium with resonant interactions*. PhD thesis. University of Innsbruck, 2020, cit. on p. 155.
- [308] E. Soave. *Interaction Properties of an Ultracold Fermi-Fermi Mixture of Dysprosium and Potassium Atoms*. PhD thesis. University of Innsbruck, 2022, cit. on p. 155.

How you climb a mountain is more important than reaching the top.

— Yvon Chouinard

ACKNOWLEDGEMENT

As I reach the final pages of this thesis, I would like to take the opportunity to express my gratitude to all the people who have contributed to making this project possible. First, I would like to thank Rudi Grimm for welcoming me in his group, first as a master student, and then also giving me the opportunity to carry on with a doctoral thesis. It has been exciting to work in a completely new experiment and I really appreciate the freedom to pursue the technical challenges that seemed interesting to me. I have personally learned a lot while working on these side projects that were maybe not immediately helpful to the experiment at the time.

After all these years of working together, I also want to thank my colleagues, the past and current members of the Dy-K experiment: Cornee, Slava, Vincent, Elisa, Emil, Jeong Ho, Yaakov, Zhuxiong and Alberto. In particular, thank you to Cornee, for building the Dy-K machine with his just-do-it attitude, an area where I could and can still learn a lot, and to Alberto for numerous discussions about the simulations and the manuscript. My gratitude also goes to Tracy Northup for support and feedback as my second supervisor, and Emil and Vincent for their corrections and thoughts on the manuscript.

I also want to thank the rest of the Grimm group, the FeLiKx team, for stimulating discussions and support, as well as Christine and Verena for their administrative support. Special thanks also to Gregor for his patience when pointing me in the right direction whenever I needed help with electronics or coding. Last and not least I also want to thank the whole ultracold group in Innsbruck for creating a stimulating environment for interesting science.

As the exceptional climber (and later also Nobel prize laureate in physics) Mike Kosterlitz once said: "Where I got my best ideas, [...] was sitting somewhere on a cliff holding a rope." I consider myself fortunate to have found a great climbing partner and friend in my postdoc Vincent, with whom I was lucky to share not only the lab, but also a rope in short afternoon sessions in the crag or more extensive trips to Sardinia, Brittany and the Dolomites (and the one or the other beer). This extends to my many other friends and partners in sport, that were always complicit in fleeing university to go climbing, skiing or biking, whenever I became stuck somewhere and needed to clear my mind to make room for fresh ideas. Thanks for the many small and big adventures together! Let me also not forget the Fensterbankler-Gruppe. The daily exchange in all matters Führungskräfte has

become a tradition that hopefully will outlive our academic careers and time in Innsbruck.

At last, but most importantly, I want to thank my family! To my parents Christiane and Tom, and to my favorite human Kathrin, thank you for always believing in me, kicking my butt when I lost motivation, but also celebrating the little successes, and supporting me throughout the last years. This thesis would not have been possible without you!

COLOPHON

This document was typeset using the typographical look-and-feel `classicthesis` developed by André Miede and Ivo Pletikosić. The style was inspired by Robert Bringhurst's seminal book on typography "*The Elements of Typographic Style*". `classicthesis` is available for both \LaTeX and \LyX :

<https://bitbucket.org/amiede/classicthesis/>